

# Infrared studies of impurity states and ultrafast carrier dynamics in semiconductor quantum structures

Dominik Stehr

Juli 2007



Wissenschaftlich-Technische Berichte  
**FZD-477**  
Juli 2007

Dominik Stehr

**Infrared studies of impurity states  
and ultrafast carrier dynamics in  
semiconductor quantum structures**

Bibliothek D 120



100079908



**Forschungszentrum  
Dresden Rossendorf**

Institut für Ionenstrahlphysik und Materialforschung  
Forschungszentrum Dresden-Rossendorf

# **Infrared studies of impurity states and ultrafast carrier dynamics in semiconductor quantum structures**

Dissertation

zur Erlangung des akademischen Grades  
Doctor rerum naturalium (Dr. rer. nat.)

vorgelegt der Fakultät Mathematik und Naturwissenschaften  
der Technischen Universität Dresden

von  
Dominik Stehr  
geboren am 12.08.1978 in Erlangen

Dresden 2007

Gutachter:

1. Prof. Dr. Manfred Helm
2. Prof. Dr. Karl Leo
3. Prof. Dr. Thomas Dekorsy

Verteidigt am 11.07.2007

## Abstract

This thesis deals with infrared studies of impurity states, ultrafast carrier dynamics as well as coherent intersubband polarizations in semiconductor quantum structures such as quantum wells and superlattices, based on the GaAs/AlGaAs material system.

In the first part it is shown that the  $2p_z$  confined impurity state of a semiconductor quantum well develops into an excited impurity band in the case of a superlattice. This is studied by following theoretically the transition from a single to a multiple quantum well or superlattice by exactly diagonalizing the three-dimensional Hamiltonian for a quantum well system with random impurities. Intersubband absorption experiments, which can be nearly perfectly reproduced by the theory, corroborate this interpretation, showing that at low temperatures in the low doping density regime all optical transitions originate from impurity transitions. These results also require reinterpretation of previous experimental data.

The relaxation dynamics of interminiband transitions in doped GaAs/AlGaAs superlattices in the mid-IR are studied. This involves single-color pump-probe measurements to explore the dynamics at different wavelengths, which is performed with the Rossendorf free-electron laser (FEL), providing picosecond pulses in a range from 3-200  $\mu\text{m}$  and are used for the first time within this thesis. In these experiments, a fast bleaching of the interminiband transition is observed followed by thermalization and subsequent relaxation, whose time constants are determined to be 1-2 picoseconds. This is followed by an additional component due to carrier cooling in the lower miniband. In the second part, two-color pump-probe measurements are performed, involving the FEL as the pump source and a table-top broad-band tunable THz source for probing the transmission changes. These measurements allow a separate specification of the cooling times after a strong excitation, exhibiting time constants from 230 ps to 3 ps for different excitation densities and miniband widths. In addition, the dynamics of excited electrons *within the minibands* is explored and their contribution quantitatively extracted from the measurements.

Intersubband absorption experiments of photoexcited carriers in single quantum well structures, measured directly in the time-domain, i.e. probing *coherently* the polarization between the first and the second subband, are presented. From the data we can directly extract the density and temperature dependence of the intersubband dephasing time between the two lowest subbands, ranging from 50 up to 400 fs. This all optical approach gives us the ability to tune the carrier concentration over an extremely wide range which is not accessible in a doped quantum well sample. By varying the carrier density, many-body effects such as the depolarization and their influence on the spectral position as well as on the lineshape on the intersubband dephasing are studied. Also the difference of excitonic and free-carrier type excitation is discussed, and indication of an excitonic intersubband transition is found.



## Kurzfassung

Gegenstand dieser Arbeit ist die Untersuchung von Übergängen zwischen Störstellen-niveaus und die ultraschnelle Ladungsträgerdynamik in Halbleiter-Quantenstrukturen im infraroten Spektralbereich.

In dieser Arbeit wird gezeigt, dass sich der quantisierte  $2p_z$  Störstellenzustand innerhalb eines dotierten Quantentrogens beim Übergang zu einer Übergitterstruktur zu einem Störstellenband ausbildet. Die Ausbildung dieses Störstellenbandes wird anhand von theoretischen Simulationen, basierend auf einer annähernd exakten Diagonalisierung des dreidimensionalen Hamilton-Operators, nachvollzogen, indem die Anzahl der gekoppelten Quantentröge sukzessive erhöht wird. Intersubband Absorptions-Messungen, die nahezu perfekt mit dem theoretischen Modell übereinstimmen, untermauern diese Interpretation, nämlich dass bei tiefen Temperaturen alle optischen Übergänge von Störstellen-Übergängen herrühren. Diese Ergebnisse erfordern teilweise eine Neu-Interpretation bisheriger experimenteller Ergebnisse, bei denen die Ausbildung eines resonanten Störstellenbandes nicht in Betracht gezogen wurde.

Mit Hilfe von Anrege-Abfrage Experimenten, sowohl unter Verwendung des Freielektronen Lasers (FEL) in Rossendorf, der Infrarot-Pulse mit einer Dauer von 1-5 Pikosekunden im Bereich von 3-200  $\mu\text{m}$  liefert, als auch einer breitbandigen, ultrakurzen THz-Lichtquelle, wird die Ladungsträgerdynamik in dotierten GaAs/AlGaAs Übergittern untersucht. In Einfarben-Experimenten, in denen nur der FEL verwendet wird, wird ein schnelles Ausbleichen der Interminiband Absorption beobachtet, gefolgt von schneller Relaxation und Thermalisierung auf einer Zeitskala von 1-2 Pikosekunden. Eine zusätzliche Komponente, die dem Abkühlen der heißen Ladungsträger zuzuordnen ist, wird im Anschluss an diese Prozesse beobachtet. Unter Einbezug der zweiten, synchronisierten infraroten Lichtquelle wird die Abkühl-dynamik separat untersucht. Hierzu werden die FEL Pulse als Anrege-, und breitbandige THz Pulse als Abfragestrahl eingesetzt, was Mehrfarben-Experimente über einen weiten Spektralbereich erlaubt. Dazu wird der THz-Strahl auf eine stark temperaturabhängige Resonanz eingestellt, was es ermöglicht, sehr sensitiv die dynamische Elektronentemperatur mittels der Transmissionänderung des Abfragestrahls zu bestimmen. Es werden Abkühlzeiten von 3-230 ps beobachtet, stark abhängig von den jeweiligen energetischen Breiten der Minibänder und der verwendeten Anregungsleistung. Diese Messungen erlauben zusätzlich eine quantitative Bestimmung der Beiträge von Übergängen *innerhalb* der einzelnen Minibänder zu den beobachteten Ergebnissen.

Die zeitliche Entwicklung der Polarisation zwischen dem ersten und zweiten Subband eines zuvor optisch angeregten, undotierten symmetrischen GaAs/AlGaAs Quantentrogens wird mittels ultra-breitbandiger THz Strahlung während und nach der Anregung untersucht. Diese Messungen erfolgen in der Zeit-Domäne, was die direkte Messung der kohärenten Polarisations-Dynamik erlaubt. Unter Variation der optischen Anregungslei-

tung und der Gittertemperatur können die wesentlichen Komponenten, die zum Zerfall der Polarisation beitragen, bestimmt werden. Den wesentlichen Teil zu dieser "Dephasierung", die im Bereich von 50 bis 400 Femtosekunden stattfindet, trägt dabei die Elektron-Elektron Streuung bei. Zusätzlich werden dynamische Vielteilchen-Effekte, wie die Depolarisationsverschiebung beobachtet und theoretisch diskutiert. Des Weiteren wurde der Einfluss von gebundenen Elektron-Loch Paaren auf die Intersubband-Polarisation untersucht und Hinweise auf einen exzitonischen Intersubband Übergang gefunden.



# Contents

<b>1</b>	<b>Introduction</b>	<b>1</b>
<b>2</b>	<b>Basic electronic and optical properties of quantum wells and superlattices</b>	<b>7</b>
2.1	Confined states in semiconductor heterostructures . . . . .	7
2.2	Shallow impurity states in semiconductors . . . . .	9
2.3	Optical transitions and their selection rules . . . . .	13
2.4	Standing wave pattern in waveguide geometries . . . . .	19
2.5	Dynamic description of many-level systems . . . . .	21
2.6	Ultrafast processes . . . . .	25
2.7	Nonlinear optics . . . . .	27
<b>3</b>	<b>Properties of resonant impurity states in semiconductor heterostructures and their influence on the intersubband absorption spectra</b>	<b>29</b>
3.1	Introduction . . . . .	29
3.2	Basic properties of confined impurity states . . . . .	30
3.3	Method of calculation . . . . .	32
3.4	Results for the double quantum well . . . . .	34
3.5	Quadruple quantum well . . . . .	40
3.6	Towards the superlattice . . . . .	42
3.7	Summary and outlook . . . . .	47
<b>4</b>	<b>Ultrafast spectroscopy in the infrared</b>	<b>49</b>
4.1	The Rossendorf Free-Electron Lasers . . . . .	49
4.1.1	Working principle . . . . .	49
4.1.2	Slippage effect and cavity detuning . . . . .	53
4.1.3	Characteristics of the FEL radiation . . . . .	55
4.2	Measurement techniques . . . . .	66
4.2.1	Pump-probe spectroscopy . . . . .	66
4.2.2	Two-color FEL pump-probe setup using phase matched second harmonic generation . . . . .	67
4.3	Broadband Terahertz radiation using GaSe . . . . .	70
4.3.1	10 fs Ti:Sapphire lasersystem . . . . .	71
4.3.2	Principle of phase matched difference frequency mixing . . . . .	72
4.3.3	Method of detection and characterization of ultra-broadband THz pulses . . . . .	76
4.3.4	Tunability . . . . .	86
4.3.5	Synchronization to external light sources . . . . .	87

---

<b>5</b>	<b>Ultrafast dynamics of inter- and intra-miniband transitions in doped superlattices</b>	<b>91</b>
5.1	Single color pump-probe results . . . . .	91
5.2	FEL-pump broadband THz-probe experiments . . . . .	102
5.3	Discussion . . . . .	114
5.4	Outlook . . . . .	124
<b>6</b>	<b>Coherent dynamics of intersubband transitions in single quantum wells</b>	<b>125</b>
6.1	Experimental description and realization . . . . .	126
6.2	Results . . . . .	130
6.3	Discussion . . . . .	137
6.4	Outlook . . . . .	146
	<b>Bibliography</b>	<b>147</b>
	<b>Acknowledgement</b>	<b>159</b>

# 1 Introduction

Upon the rising request for fast and efficient electronic devices such as microprocessors and fast optical modulators allowing high rate data transfer in computer technology, the miniaturization in semiconductor physics will proceed to size dimensions of active components such as a transistor gate of only a few tens of nanometers already within the next years [1, 2] – eventually approaching the quasiparticle de-Broglie wavelength of carriers in the devices. In this regime quantum size effects will become important and new physical phenomena will occur. However, Arakawa and Sakaki predicted in 1982 that the reduction of the dimensionality for the free carrier motion [3] will lead to improved performance of semiconductor optoelectronic devices.

Already in 1970, Esaki and Tsu [4] proposed semiconductor structures that consist of two different semiconductor materials, exhibiting different band gaps, that are deposited alternately on top of each other. This gives rise to a one-dimensional confinement in the direction of growth, resulting in semiconductor quantum wells that first have been realized by Dingle *et al.* in 1974 [5]. The advent of high-quality epitaxial growth of these structures down to a single atomic layer allowed direct bandgap engineering to precisely adjust the quantized energy levels in the confinement direction. Repeating the alternate growth over many periods results in the formation of an artificial solid with tunable periodicity and coupling strength, known as superlattices.

The quantization of electronic states in these low-dimensional semiconductors results in the formation of a subband structure which consists of a series of valence and conduction subband states with a respective energy spacing much smaller than fundamental bandgap (for an illustration, see Fig 1.1).

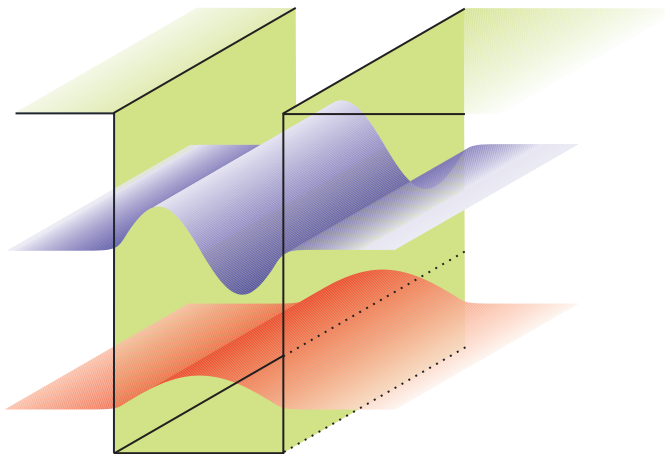


**Figure 1.1:** Scheme of the conduction band configuration of a quantum well, e.g. a GaAs layer sandwiched between two AlGaAs layers. Also shown are the two lowest resulting confined subband states within the conduction band.

In strong contrast to the broad absorption spectrum between the valence- and conduction band of a semiconductor, the absorption spectrum between subbands (intersubband absorption) is spectrally much narrower, giving rise to a sharp absorption peak. After the first demonstration of an intersubband transition in a quantum well 1985 by West and Eglash [6], the photon energy (or wavelength) range accessible with intersubband transitions today spans from 1.5  $\mu\text{m}$  [7] up to 200  $\mu\text{m}$  [8]. The covered wavelength range is of large technical interest for applications, such as sensing and optical data communication. Especially the interest in the long-wavelength regime, also denoted as the THz spectral region which is mostly not covered by standard optical technology, has triggered a large research effort to exploit the optical properties of semiconductor nanostructures in order to develop new opto-electronic device structures. Most prominently, this research cumulated in the realization of efficient quantum well infrared detectors (QWIP) [9] and of unipolar, electrically driven intersubband lasers, called quantum-cascade (QC) lasers, which nowadays provide coherent radiation ranging from 190  $\mu\text{m}$  (1.6 THz) [10, 11] down to 3.1  $\mu\text{m}$  (97 THz) [12, 13, 14].

In particular, QC lasers are the only mid-infrared semiconductor lasers capable of continuous-wave operation at room temperature, and they are playing an ever-increasing role in many sensing applications. Similarly, QWIPs offer excellent performance in infrared thermal imaging and additionally are finding new applications utilizing their high-speed response.

However, thorough understanding of the mechanisms governing the optical and electronic properties of semiconductor nanostructures are mandatory for further performance improvements and development of future applications. This requires a detailed analysis of the properties of the confined electronic states itself as well as their dynamic behavior.

With respect to fundamental research, quantum wells and superlattices have attracted much attention, since they provide an almost ideal quantum mechanical system allowing the studies of basic quantum and many-body effects. Purely quantum mechanical effects in a quasi-steady state [15] and the effect of a one-dimensional confinement on the low-temperature transport [16, 17] and optical properties [18] as well as on interaction processes that occur among the carriers on an ultrafast timescale was explored with quantum wells [19, 20, 21]. Recently, also confinement effects on excitons, representing a bound state of an electron in the conduction band and its corresponding hole in the valence band, have attracted much interest with respect to their influence on the subband states [22]. The possibility of Bose-Einstein-condensation [23, 24] – due to the bosonic nature of excitons – has triggered a renewed interest in these relatively simple structures.

Superlattices on the other hand, consisting of many quantum wells coupled by thin barriers, exhibit a more complex subband structure [4], giving rise to so-called minibands *within* the conduction or valence band. The optical transitions between these minibands lie, just like in quantum wells, in the mid-infrared to far-infrared region and have been

---

studied intensely over the last decade along with their transport properties [25]. Most prominently, the nonlinear transport mechanisms within a miniband, exhibiting negative differential resistance that is caused by Bloch oscillations, has attracted many research groups in the past [26, 27]. Since the frequency of these Bloch oscillations lie within the THz range and depends linearly on the applied static electric field, such systems could represent an easily tunable THz source and hence are still of large interest today [28, 29].

Generally, intersubband absorption in quantum wells and superlattices usually requires the presence of doping atoms, inevitably giving rise to disorder by randomly distributed hydrogenic impurity states (Coulomb potentials). In this thesis a theoretical framework is developed to describe quasi-two-dimensional electrons in the presence of a strong disorder potential as induced by doping. Starting from the microscopic distribution of the positively charged dopants, the resulting potential fluctuations acting on the electron system are determined. The set of localized quantum states, formed in this random potential, is computed numerically for a mesoscopic lateral segment of the system. Based on the realistic electron states, obtained by this full 3D-model, the spectra of optical intersubband transitions are calculated within an independent-particle model. For the first time, this method is extended to coupled multi-quantum wells and even superlattices. From there we obtain a deep insight into the relevance of localized states on the resulting absorption spectra. Moreover, we find that in the low-density-regime ( $n^{(2)} < 5 \times 10^{10} \text{cm}^{-2}$ ), intersubband spectra are completely dominated by impurity-transitions at low temperatures that lead to a drastic change in the absorption behavior for systems with two or more quantum wells. For the case of superlattices we found evidence of the presence of resonant impurity bands that are attached to their corresponding excited minibands. Within this model, hitherto unexplained absorption data of a quadruple quantum well and of superlattices data could be reproduced, indicating that the presence of impurities has to be taken into account for a precise prediction of intersubband and interminiband resonances.

As already mentioned above, also the dynamics play a major role in intersubband devices such as the QC laser. Since the timescale of the interactions among the carriers and between the carriers and the lattice can be as short as a few tens to hundreds of femtoseconds ( $1 \text{ fs} = 10^{-15} \text{ s}$ ), ultrafast spectroscopy represents a perfect tool to investigate these processes [19], since it allows the coherent preparation of a well-defined nonequilibrium state and the subsequent time-dependent monitoring of the relaxation back to equilibrium. Over the last decades, ultrafast spectroscopy in the mid-infrared spectral range has attracted considerable interest, since it has a broad potential for the study of the ultrafast dynamics of elementary excitations in condensed matter [30, 31, 32].

In this work, we explore the dynamics in two different types of heterostructures, i.e. superlattices and quantum wells, by two different methods of ultrafast spectroscopy:

(i): Picosecond dynamics of interminiband- and intra-miniband transitions in superlattices:

Semiconductor superlattices are an essential component of novel infrared devices such as detectors and quantum cascade lasers and additionally represent the first solid-state system where Bloch oscillations were observed. However, unlike for quantum well structures where considerable knowledge on the intersubband relaxation dynamics has been obtained, so far no experimental work has been done on the interminiband relaxation dynamics in superlattices. First, we performed degenerate ( $\lambda_{\text{pump}} = \lambda_{\text{probe}}$ ) pump-probe experiments on the mid-infrared interminiband transitions in doped superlattices exhibiting fast components due to relaxation of the bleached interminiband absorption and slower components due to cooling of the hot-carrier distribution.

The fast component decays typically in around 1-2 ps, in reasonable agreement with published theoretical values [33]. The slower component due to cooling shows time constants from 3 to 230 ps and exhibits a strong temperature and excitation density dependence. This behavior is consistent with the temperature dependence of the linear absorption spectrum, i.e. yielding higher or lower transmission for increasing electron temperature at the respective wavelength. We show that this effect provides an internal thermometer for the miniband electrons on a picosecond timescale.

To separate the relaxation from the cooling effects, we have also performed two-color mid-infrared pump-probe experiments with a novel two-color setup utilizing a high-repetition free-electron laser and a synchronized femtosecond near-infrared oscillator. This allowed us a detailed analysis of the dynamics of carrier cooling for a well-defined excitation density. From there we find that at high excitation densities, cooling is mainly triggered by LO-phonon emission, whereas for low excitation densities carrier-carrier and carrier-impurity scattering dominate the cooling process.

(ii): Coherent polarization dynamics of photoinduced intersubband transitions:

As briefly discussed above, single quantum wells represent an ideal quantum mechanical system to investigate the role of carrier-carrier interaction as well as excitonic effects. Here we aim to investigate the dephasing mechanisms of intersubband excitations by means of time-domain THz spectroscopy in combination with ultrafast optical excitation. While the latter allows one to vary the carrier density and the type of excitation, THz time-domain spectroscopy permits to study the coherent response after excitation with an ultrashort THz pulse with a time resolution of about 50 fs. By this the influence of the carrier density on the intersubband dephasing as well as different types of optical excitation, i.e. the generation of a free electron-hole plasma or the generation of bound electron-hole

---

states, is studied. In the latter case we found a distinct increase of the dephasing time and asymmetric lineshapes, indicating that the role of bound electron-hole states do have an influence also on the intersubband absorption behavior.

This thesis is organized as follows. In Chapter 2 the basic properties of quantum semiconductor structures are presented, based on a single-particle model and a one-dimensional Schrödinger equation. From there we derive the energy spectrum and the density of states. Subsequently we discuss the properties of shallow impurities and the main mechanisms of interband, intersubband and interminiband absorption; also different line-broadening effects and many-body effects as well as the electromagnetics of the investigated samples are addressed. Then an overview of the different mechanisms and their typical timescales that dominate the response to a resonant ultrashort excitation is given and we present a simple model to describe their dynamics. We also briefly introduce the basics of nonlinear optics.

In Chapter 3 a detailed analysis of impurity transitions in quantum wells and superlattices is presented. After an introduction on ionized donors in semiconductor heterostructures we derive a fully three-dimensional Hamiltonian where the one-dimensional quantum well potential and the three-dimensional impurity-potential are treated in a unified framework. With this model, the influence of resonant impurity states is analyzed by calculation of the resulting absorption spectra for different temperatures, doping densities and for their relative lateral location within coupled quantum wells. Finally we present calculations that are able to explain hitherto unexplained experimental data.

Chapter 4 is devoted to ultrafast spectroscopy in the infrared. First we give an introduction to the different ultrafast light sources necessary for the experiments. This includes the free-electron lasers at Rossendorf which have been used for the first time for time-resolved experiments within this thesis, and an ultra-broadband THz light source based on nonlinear frequency conversion of a near-infrared table-top laser. Ultrafast THz pulses can be detected by interferometric correlation techniques and by electro-optic sampling. Both techniques are discussed and the synchronization to the FELs is demonstrated, providing a high repetition rate, fully tunable two-color pump-probe experiment. Also the different methods used for pump-probe spectroscopy, such as single color- and two-color experiments and their specifications are addressed.

We present the results from pump-probe experiments on interminiband transitions in superlattices in Chapter 5, giving a deep insight on the relaxation and cooling dynamics, and subsequently the dominating mechanisms are evaluated. Finally we give an outlook on different issues that could be addressed in the near future.

In Chapter 6 we investigate the ultrafast dephasing mechanisms of photoinduced intersubband transitions, measured by application of femtosecond THz time-domain spectroscopy. We discuss the sample properties as well as previous measurements and our experimental concept. Then we present excitation-density as well as excitation-type and temperature dependent ultrafast dephasing experiments. The main contributions to the observed intersubband dephasing are discussed and finally an outlook on future experiments and remaining questions is given.



## 2 Basic electronic and optical properties of quantum wells and superlattices

In this chapter the basic properties of the electronic eigenstates of a quantum well system are derived from a one-dimensional Schrödinger equation and the main properties of shallow impurities in semiconductors and semiconductor heterostructures are discussed. Based on the solutions of the one-dimensional Schrödinger equation we proceed by evaluating the optical properties of quantum wells and superlattices in the dipole approximation. From there we find that intersubband- and interminiband absorption only takes place if the incoming light exhibits an electric field component parallel to the growth direction. The consequence is that a special sample geometry is required for intersubband absorption, which will be discussed. Then we will address the the dynamic description of a two-level system as well as ultrafast processes that play a role in quantum wells and superlattices. This is followed by a short introduction in nonlinear optics.

### 2.1 Confined states in semiconductor heterostructures

The Schrödinger equation for a semiconductor including an additional potential  $V(\mathbf{r})$  can be written as:

$$\left( \frac{\mathbf{p}^2}{2m} + U(\mathbf{r}) + V(\mathbf{r}) \right) \psi_{\nu,n}(\mathbf{r}) = E_{\nu} \psi_{\nu,n}(\mathbf{r}) \quad (2.1)$$

where  $U(\mathbf{r})$  denotes the periodic potential of the crystal lattice. The total wave function  $\psi_{\nu,n}(\mathbf{r})$  can be decomposed into an *envelope* function  $\zeta_n(\mathbf{r})$ , which varies slowly over one lattice period and the lattice periodic Bloch function  $u_{\nu}(\mathbf{r})$ . Assuming this Bloch function to be the same in all materials of the heterostructure results in a Schrödinger equation only for the envelope function in an effective mass approach:

$$\left( \frac{\mathbf{p}^2}{2m^*} + V(\mathbf{r}) \right) \zeta_n(\mathbf{r}) = E_{\mu} \zeta_n(\mathbf{r}) \quad (2.2)$$

In the case of quantum wells and superlattices where we define  $z$  as the growth direction, we can separate  $\zeta_n(\mathbf{r})$  into

$$\zeta_{n,\mathbf{k}_{\perp}}(\mathbf{r}) = \frac{1}{\sqrt{A}} e^{i\mathbf{k}_{\perp} \cdot \mathbf{r}} \varphi_n(z) \quad (2.3)$$

Where  $\mathbf{k}_{\perp}$  denotes the two-dimensional vector  $(k_x, k_y)$ ,  $\mathbf{r} = (x, y)$  represents the coordinates perpendicular to the growth direction and  $A$  is the sample area.

This yields the one-dimensional Schrödinger equation of the form

$$\left(-\frac{\hbar^2}{2m^*} \frac{\partial^2}{\partial z^2} + V(z)\right) \varphi_n(z) = E_n \varphi_n(z) \quad (2.4)$$

Depending on the structure of  $V(z)$ , this equation can be solved analytically or numerically with these boundary conditions at the interfaces ( $z_n = z_0, z_1$ , etc.):

$$\varphi^A(z_n) = \varphi^B(z_n) \quad \text{and} \quad \frac{1}{m_A^*} \frac{\partial \varphi^A}{\partial z}(z_n) = \frac{1}{m_B^*} \frac{\partial \varphi^B}{\partial z}(z_n) \quad (2.5)$$

Here  $m_A^*$  and  $m_B^*$  are the respective effective masses of the two different semiconductor materials.

### Quantum well

In a quantum well, the solution of Eqn.(2.2) yields the eigenvalues of the form

$$E_{n,\mathbf{k}_\perp} = E_n + \frac{\hbar^2 \mathbf{k}_\perp^2}{2m^*}. \quad (2.6)$$

Directly connected with the energy spectrum of a quantum structure is the density of states (DOS). In Fig. 2.1 the densities of states in a bulk semiconductor, a quantum well, and a superlattice are schematically depicted. Generally the density of electron and hole states gives a measure of the number of states  $N$  in an energetic interval  $\epsilon$  and hence can be expressed as:

$$\text{DOS} = \frac{dN}{d\epsilon} \propto E^{(\xi/2)-1} \quad (2.7)$$

where  $\xi$  is the system's dimensionality. The resulting density of states for a quantum well system reads

$$\frac{dN}{d\epsilon} = \frac{m^*}{\pi \hbar^2} \sum_n \theta(\epsilon - E_n). \quad (2.8)$$

### Superlattice

In superlattices, ideally consisting of an infinite number of periods of the same quantum well structure, due to the coupling of the barriers, the degeneracy of the eigenstates in each quantum well is lifted and *minibands* are formed.

The  $z$ -dependent part of the envelope wavefunction, can now, similar to the transition from Eqn.(2.1) to Eqn.(2.2), be decomposed into a Bloch part which is periodic in the superlattice period and a slowly varying plane-wave part

$$\varphi_n(z) = e^{ik_z z} u_n(z) \quad \text{with} \quad u_n(z) = u_n(z + d) \quad (2.9)$$

where  $d$  is the superlattice period. In the tight-binding approximation, where only nearest neighbors are taken into account, an analytical solution to Eqn.(2.2) can be obtained and leads to a modified dispersion relation:

$$E_n(\mathbf{k}) = \epsilon_n + \frac{\Delta_n}{2} (1 \pm \cos(k_z d)) + \frac{\hbar^2 \mathbf{k}_\perp^2}{2m^*} \quad (2.10)$$

where  $\Delta_n$  denotes the width of the specific miniband. Here the minus sign holds for odd minibands ( $n = 1, 3, \dots$ ) and the plus sign for the even ones ( $n = 2, 4, \dots$ ). The exact solution can be derived from a Kronig-Penney model of a one-dimensional lattice with periodic boundary conditions and results in a slight deviation from cosine-like dispersion obtained from the tight-binding approximation.

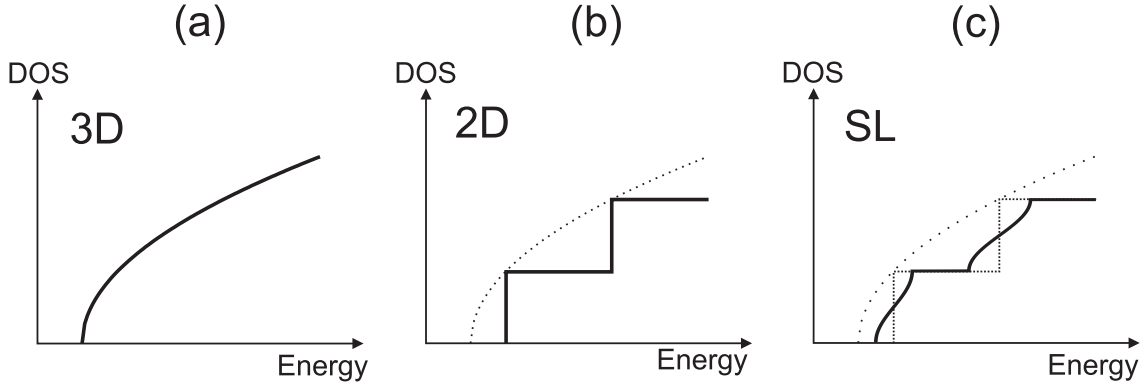


**Figure 2.1:** Schematic of the density of states in a bulk semiconductor, a quantum well and a superlattice.

The resulting density of states is schematically drawn in Fig. 2.1(c). There we see that superlattices exhibit a density of states that lies between the case of a quasi two-dimensional electron gas such as a quantum well with abrupt steps and that of a bulk semiconductor, showing a monotonic increase.

## 2.2 Shallow impurity states in semiconductors

A common method to provide electrons in the conduction or valence band within a semiconductor is to insert a shallow donor or acceptor atom in the semiconductor matrix, where they directly replace an original atom (no defects!). On the other hand, these ionized or neutral dopant atoms give rise to a long range Coulomb potential which modifies the bare lattice potential. In an infinite crystalline material it is not necessary to know the exact position of the dopant atom, since the binding energy will not differ for different positions within the lattice. If the impurity wavefunction extends over many periods in the crystal, one can, similar to the case of heterostructures, treat this problem within a three-dimensional envelope-function formalism. These impurity envelope functions have to fulfill the following Schrödinger-equation, representing a standard hydrogen problem within the effective mass approximation:

$$\left[ \frac{\mathbf{p}^2}{2m^*} - \frac{e^2}{4\pi\epsilon\epsilon_0 |\mathbf{r}|} \right] \psi(\mathbf{r}) = E_n \psi(\mathbf{r}) \quad (2.11)$$

where  $m^*$  is the respective effective mass and  $\epsilon_0$  is the dielectric constant of the chosen semiconductor material. The ground state of this problem is the 1s hydrogenic wavefunc-

tion

$$\psi(\mathbf{r})_{1s} = \frac{1}{\sqrt{\pi (a_0^*)^3}} \exp\left(-\frac{r}{a_0^*}\right) \quad (2.12)$$

where  $a_0^*$  is the effective Bohr-radius, defined as:

$$a_0^* = \frac{4\pi\epsilon\epsilon_0\hbar^2}{m^*e^2} = \frac{\epsilon}{m^*}a_0 \quad (2.13)$$

with  $a_0 = 0.53 \text{ \AA}$ , the Bohr radius of the hydrogen atom. For GaAs, where  $\epsilon \approx 12.5$  and the effective mass of the electron in the conduction bands is  $m^* \approx 0.068 m_e$  we find an effective Bohr radius of  $a_0^* \approx 100 \text{ \AA}$ , which is about 20 times the lattice period of GaAs. Hence the envelope-function formalism is justified.

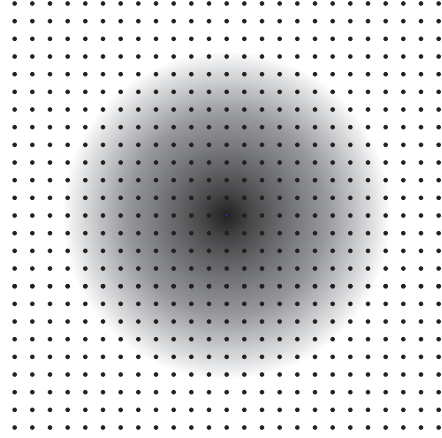


**Figure 2.2:** Schematic of the 1s hydrogen wavefunction in a semiconductor matrix. Typically the wavefunction extends over many lattice periods of the host crystal, justifying an envelope-function formalism.

This situation is also schematically shown in Fig. 2.2, where the 1s hydrogenic wavefunction extends over many lattice periods of the host crystal.

Similar to the effective Bohr radius, also the binding energy is modified:

$$E_n = \frac{-e^2}{8\pi\epsilon\epsilon_0 a_0^*} \frac{1}{n^2} = \text{Ryd}^* \frac{1}{n^2} \quad (2.14)$$

Here it is convenient to define an effective Rydberg  $\text{Ryd}^* = \frac{m^*}{m_e} \text{Ryd}$  where Ryd is the 1s binding energy of the hydrogen atom (Ryd = 13.6 eV). Assuming again GaAs as the host crystal, we find a binding energy of only 5.8 meV. Hence, at room temperature, all donors are completely ionized whereas at very low temperatures the electrons remain localized in the impurity states. As already indicated by the 1s-notation of the ground state of the impurity, in bulk semiconductors the classification fully corresponds to the hydrogen case. Thus, impurity states are classified by the quantum numbers  $N$ ,  $l$  (angular momentum) and  $m$  (magnetic quantum number). These are: 1s, 2s, 2p ( $m = 0, \pm 1$ ), 3s, 3p ( $m = 0, \pm 1$ ), 3d ( $m = 0, \pm 1, \pm 2$ ), etc. From this series, the most important states are schematically shown on the left part of Fig. 2.3.

In contrast to bulk materials, a semiconductor heterostructure is characterized by the lack of translational invariance along the growth axis. Hence the impurity binding energy

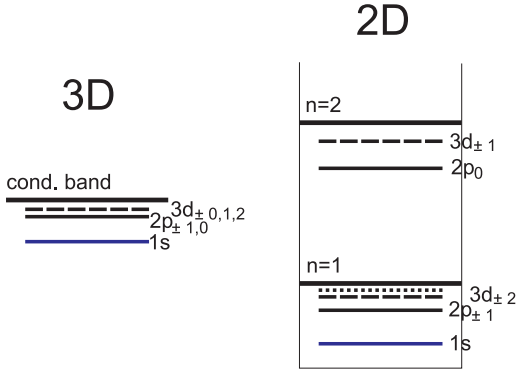


**Figure 2.3:** Classification of the impurity states within a bulk semiconductor (left) and a quantum well (right).

explicitly depends on its precise location relative to the heterostructure potential, e.g. it can be placed either directly at an interface, within the quantum wells or within the barriers.

Also the binding energy depends strongly on the dimensions of the quantum well or superlattice system, e.g. the thickness of the quantum well. In the exactly two-dimensional case (a single infinitely thin quantum well) the impurity-problem can still be solved analytically, yielding the energy series of the 2D hydrogen atom [34]:

$$E_n^{2D} = \frac{\text{Ryd}^{3D}}{\left(n - \frac{1}{2}\right)^2} \quad (2.15)$$

Hence the binding energy of the ground state  $E_1^{2D} = 4 \cdot \text{Ryd}^{3D}$  in two dimensions is four times larger than for bulk systems. For a realistic quantum well, the binding energy lies in between these two limits. The classification of the impurity states also changes for two dimensions. States that had a  $z$ -symmetry are now absent, leading to a two-fold degeneracy of the  $p$  and  $d$  states, respectively. In real quantum wells, the classification, as was the binding energy, is a mixture of both. Generally, the Hamiltonian for a quantum well or superlattice system, including the impurity potential, reads:

$$H = H_0 + V_{\text{imp}} = \frac{\mathbf{p}}{2m^*} + V_{\text{QW}}(z) + V_{\text{imp}}(\mathbf{r}) \quad (2.16)$$

where

$$V_{\text{imp}}(\mathbf{r}) = V_{\text{imp}}(x, y, z) = -\frac{e^2}{4\pi\epsilon\epsilon_0\sqrt{x^2 + y^2 + (z - z_i)^2}} \quad (2.17)$$

is the impurity potential of the impurity located at  $z_i$ . The Schrödinger equation with the Hamiltonian from Eqn.(2.16) is not solvable with analytical methods. Usually the impurity-problem in heterostructures is solved with a variational ansatz, where some assumptions of the the shape of the impurity wavefunctions have to be made in advance [35]. However, in this thesis we circumvent such assumptions and treat the quantum well and impurity potential in a unified framework and exactly solve the impurity problem for different kinds of heterostructures (see Chap.(3)). Apart from this, we can make already some statements on the effect of the quantum well width and the respective position of

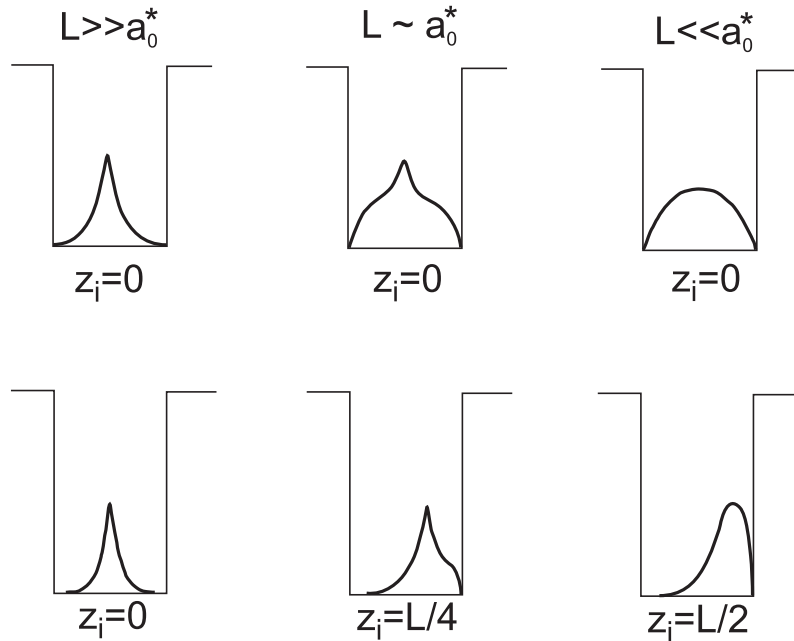


**Figure 2.4:** Schematic evolution of the shape of the impurity ground state wavefunction in a quantum well of decreasing width for an on-center impurity (upper part) and with the impurity position in a thick well at different positions (lower part). Graph reproduced from [35].

the impurity inside the quantum well. In Fig. 2.4 the shape of the impurity wavefunction with respect to the  $z$ -coordinate is sketched. In the upper part, the impurity wavefunction is shown for different quantum well thicknesses ( $L$ ), decreasing from left to right. The impurity is located in the center of the quantum well. For thick wells ( $L \gg a_0^*$ ) the on-center impurity wavefunction resembles that of the bulk system. With decreasing well width, the impurity wavefunction approaches the shape of the ground state wavefunction in a square well. This is because the impurity wavefunction can only slightly penetrate into the barrier, hence its  $z$ -part becomes confined by the quantum well potential. This leads to an impurity wavefunction that looks similar to that of the ground state wavefunction of the quantum well itself. In case of a wide well, shown in the lower part of Fig. 2.4, the impurity wavefunction only changes its shape once the impurity location is moved towards the interface of the heterostructure. The reason for this is again that the impurity wavefunction has only a small penetration depth into the barrier. In thin quantum wells, when the impurity approaches the barrier, its binding energy is reduced [8].

As already indicated in the text, the impurity states with magnetic quantum number  $m = 0$  are strongly influenced by a narrow quantum well potential and the degeneracy of their original series ( $p$ ,  $d$ , etc.) is partially removed [36]. In a quantum well, states with  $m = 0$  become pinned to higher quantum well states, where they form an additional hydrogenic series attached to it [37]. This is illustrated in the right part Fig. 2.3, where the most important impurity levels are shown in combination with the quantum well states  $n = (1, 2)$ . There we find that the most important impurity levels pinned to the first

subband are the  $1s$ ,  $2p_{\pm 1}$  and near the second subband  $2p_0$  and  $3d_{\pm 1}$ , respectively. The  $3d_0$  state is located near the third subband (not shown). It has been demonstrated that optical transitions are allowed for the  $1s-2p_0$  transition with the same selection rule as for the transition between the quantum well states. Hence, it can contribute to a measured absorption spectrum. Exactly this will be the topic of Chap.(3), where the influence of impurity states on the absorption spectra of various heterostructures is studied in detail.

## 2.3 Optical transitions and their selection rules

Apart from impurity transitions, in principle there are two main mechanisms of optical transitions in semiconductor heterostructures, the transition between the valence band and the conduction band, *interband*-transitions, and transitions within the bands, *intraband*-transitions. This work focusses mainly on the intraband transitions in the conduction band, which are called intersubband transitions for a quantum well and interminiband transitions for the case of a superlattice. Due to the fact that the subbands are parallel with respect to  $\mathbf{k}_{\perp}$  in a simplified picture, intersubband transitions appear only at a specific photon energy, strongly in contrast to their interband counterparts, where all photons with a higher energy than the bandgap energy can be absorbed. Let us start with

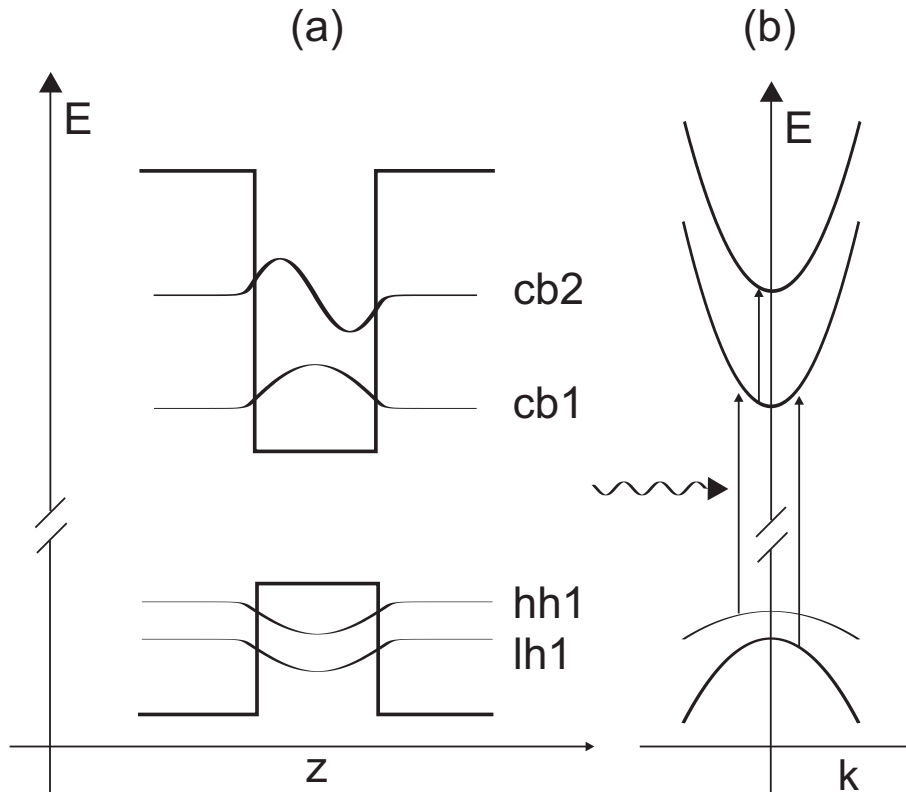


**Figure 2.5:** (a) Variation of the conduction- and valence band profile along the growth-axis  $z$  with the most important electron and hole wavefunctions. (b) Schematic energy dispersion of the subband levels as a function of  $k_{\perp}$  according to the free motion of carriers perpendicular to the growth direction.

the full Hamiltonian, incorporating the quantum well potential  $V(\mathbf{r})$  and the interaction with an electromagnetic field:

$$H = \frac{1}{2m^*} (\mathbf{p} - e\mathbf{A})^2 + V(\mathbf{r}) \quad (2.18)$$

with  $\mathbf{A}$  as the vector potential. By neglecting the nonlinear term in  $\mathbf{A}$ , Eqn.(2.18) can be separated into an unperturbed part  $H_0$  and the perturbation arising from the incident electromagnetic field  $H'$ :

$$H = H_0 + H' = \frac{\mathbf{p}^2}{2m^*} + V(\mathbf{r}) + \frac{e}{2m^*} (\mathbf{A} \cdot \mathbf{p} + \mathbf{p} \cdot \mathbf{A}) \quad (2.19)$$

In the *dipole approximation*, which implies that the wavelength used is much larger than any structural parameter, i.e.  $\text{div}\mathbf{A} = 0$ , the vector potential  $\mathbf{A}$  commutes with  $\mathbf{p}$ , yielding  $H' = (e/m^*)\mathbf{A} \cdot \mathbf{p}$ .

Using  $\mathbf{A} = \mathbf{e}A$ , where  $\mathbf{e}$  represents the polarization vector, and  $E_0 = -\dot{A}$  the perturbation term can be transformed into

$$H' = \frac{ie^2}{2m^*\omega} E_0 e^{i(\mathbf{q}\mathbf{r} - \omega t)} \mathbf{e} \cdot \mathbf{p} \quad (2.20)$$

where  $\mathbf{E}(t) = \frac{1}{2}\mathbf{e}E_0 \cdot e^{i(\mathbf{q}\mathbf{r} - \omega t)} + \text{c.c.}$  describes the incoming light.

In a simple picture, the transition rate for an optical transition from state  $i$  to state  $f$  in semiconductors can be calculated with *Fermi's Golden Rule*:

$$W_{if} = \frac{2\pi}{\hbar} |\langle \Psi_f | H' | \Psi_i \rangle|^2 \delta(E_f - E_i - \hbar\omega) \quad (2.21)$$

Here the  $\delta$ -function accounts for the energy conservation, while the first term describes matrix overlap of the respective states regarding to the perturbation.

For evaluation of Eqn.(2.21) with respect to transitions between the valence and conduction band as well as transitions within the same band one has to use the three-dimensional wavefunctions  $\psi_{\mu,n}(\mathbf{r})$  introduced in Eqn.(2.1), consisting of a slowly varying part  $\zeta_n(\mathbf{r})$  and the lattice periodic Bloch function  $u_\nu(\mathbf{r})$ . Then the momentum matrix element for the entire crystal volume  $\Omega$  reads:

$$\langle \psi_i(\mathbf{r}) | \mathbf{e} \cdot \mathbf{p} | \psi_f(\mathbf{r}) \rangle = \mathbf{e} \cdot \int_{\Omega} d^3r \psi_i^*(\mathbf{r}) \mathbf{p} \psi_f(\mathbf{r}) \quad (2.22)$$

Due to the fact that  $u_\nu(\mathbf{r})$  varies rapidly over the length  $k_{\perp}^{-1}$  or over the characteristic lengths of variation of  $\zeta_n(\mathbf{r})$ , one can expand Eqn.(2.22) into<sup>1</sup>:

$$\begin{aligned} \mathbf{e} \cdot \int_{\Omega} d^3r \psi_i^*(\mathbf{r}) \mathbf{p} \psi_f(\mathbf{r}) &= \mathbf{e} \cdot \int_{\Omega} d^3r \zeta_n^*(\mathbf{r}) u_{\mu}^*(\mathbf{r}) [\zeta_n(\mathbf{r}) \mathbf{p} u_{\nu}(\mathbf{r}) + u_{\nu}(\mathbf{r}) \mathbf{p} \zeta_n(\mathbf{r})] \\ &\stackrel{1}{=} \mathbf{e} \cdot \int_{\Omega_0} d^3r u_{\mu}^*(\mathbf{r}) \mathbf{p} u_{\nu}(\mathbf{r}) \int_{\Omega} d^3r \zeta_i^*(\mathbf{r}) \zeta_f(\mathbf{r}) \\ &+ \mathbf{e} \cdot \delta_{\nu\mu} \int_{\Omega} d^3r \zeta_i^*(\mathbf{r}) \mathbf{p} \zeta_f(\mathbf{r}) \end{aligned} \quad (2.23)$$

<sup>1</sup>The slowly varying part  $\zeta_n(\mathbf{r})$  can be extracted from the integral over the crystal, since they can be assumed to be constant with respect to the lattice periodic functions  $u_{\nu}(\mathbf{r})$ .



Here  $\Omega_0$  reflects the volume of a the elementary cell of the materials involved in the structure. In Eqn.(2.23) the first part describes the interband transitions and the second one transitions within the same band. The first part consists of the interband absorption between the valence and conduction band Bloch functions, with an additional subband-selection rule. The latter implies that interband-transition can only take place between subbands that exhibit identical parity. Hence, the transition from the heavy hole ground state hh1 to the conduction band ground state cb1 is allowed, whereas the transition from hh1 to cb2 is forbidden.

The second term in Eqn.(2.23) describes the transition within the conduction or valence band. Using the wavefunctions  $\zeta_n(\mathbf{r}) = |n, \mathbf{k}_\perp\rangle$  from above we now can evaluate the matrix element which is responsible for the selection rules of transitions within the conduction or valence band, i.e. intersubband transitions,

$$\langle n, \mathbf{k}_\perp | \mathbf{e} \cdot \mathbf{p} | n', \mathbf{k}_\perp \rangle \quad (2.24)$$

where  $(n, n')$  reflects the respective subband. The above matrix element can be transformed into [35]:

$$\langle n, \mathbf{k}_\perp | \mathbf{e} \cdot \mathbf{p} | n', \mathbf{k}_\perp \rangle = \mathbf{e}_\perp \hbar \mathbf{k}_\perp \delta_{n,n'} + e_z \langle n | p_z | n' \rangle \quad (2.25)$$

The first term accounts for transitions within a single subband at a constant  $\mathbf{k}_\perp$ -position, thus reflecting a Drude-like absorption of free carriers at  $\omega = 0$ .

From the second term of Eqn.(2.25), however, we see clearly that intersubband transitions are only allowed if the incoming light has a  $z$ -component. Due to this a special geometry has to be applied for the infrared experiments, which will be discussed later.

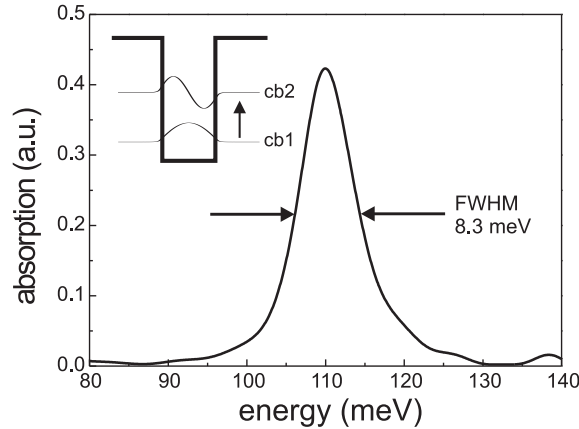


**Figure 2.6:** Experimental absorption spectrum of a GaAs/Al<sub>0.3</sub>Ga<sub>0.7</sub>As Quantum well with a well width of 8.3 nm at  $T=300$  K. It clearly shows a Lorentzian line shape with a FWHM of 8.3 meV.

For the intraband (intersubband) absorption coefficient, which is simply a measure of the fraction of the electromagnetically absorbed energy, we also have to account for the Fermi-Dirac occupation probabilities of the initial and final states  $f_n(E_n(\mathbf{k}_\perp))$  and  $f_{n'}(E_{n'}(\mathbf{k}_\perp))$

[37]:

$$\alpha_{2D} = \frac{\hbar\omega}{IA} \sum_{n,n'} \sum_{\mathbf{k}_\perp} |\langle n|p_z|n'\rangle|^2 [f_n(E_n(\mathbf{k}_\perp)) - f_{n'}(E_{n'}(\mathbf{k}_\perp))] \delta(E_{n'}(\mathbf{k}_\perp) - E_n(\mathbf{k}_\perp) - \hbar\omega) \quad (2.26)$$

Here  $I$  reflects the intensity of the incoming radiation and  $A$  the area of incidence, respectively. If we assume a parabolic in-plane dispersion, the summation or integration over the Fermi-Dirac distributions (with  $E_F$  as the Fermi energy) can be performed analytically and one obtains:

$$\alpha_{2D} \propto \sum_{n,n'} f_{n,n'} \ln \left[ \frac{1 + \exp((E_F - E_n)/k_B T)}{1 + \exp((E_F - E_{n'})/k_B T)} \right] \delta(E_{n'} - E_n - \hbar\omega) \quad (2.27)$$

Here we introduced the dimensionless oscillator strength, which is widely used in optical spectroscopy:

$$f_{n,n'} = \frac{2}{m^* \hbar \omega_{n,n'}} |\langle n|p_z|n'\rangle|^2 \quad (2.28)$$

where  $\hbar\omega_{n,n'}$  is the intersubband transition energy. The oscillator strength obeys the sum rule:

$$\sum_{n'} f_{n,n'} = 1 \quad (2.29)$$

being the sum over all final states  $n'$ .

So far we have used the  $\delta$ -function to account for the energy conservation during an optical transition. This would unrealistically result in an infinitesimal sharp absorption peak in the case of a single quantum well. To account for the broadening effects discussed below we therefore simply replace the  $\delta$ -function by a Lorentzian with a phenomenological broadening parameter  $\Gamma$ , representing the half width at half maximum:

$$\delta(E_{n'} - E_n - \hbar\omega) \rightarrow \frac{\Gamma/\pi}{(E_{n'} - E_n - \hbar\omega)^2 + \Gamma^2}$$

Fig. 2.6 shows a typical intersubband absorption spectrum taken from a 8.3 nm wide GaAs quantum well in  $\text{Al}_{0.30}\text{Ga}_{0.70}\text{As}$ . The carrier density, introduced by optical interband-excitation, was  $5 \times 10^{10} \text{ cm}^{-2}$ . It nicely shows a Lorentzian lineshape with a full width at half maximum of 8.3 meV.

Apart from the single particle approach described above the spectral position of the intersubband resonance and its linewidth depends on the following effects:

### Homogeneous broadening

Scattering mechanisms such as electron-electron interaction, electron-phonon scattering and disorder (impurity-)scattering result in a damping of a macroscopic intersubband polarization. These broadening effects lead to a Lorentzian-like shape absorption line.

### Inhomogeneous broadening

The assumption of a pure two-level system cannot be justified in most cases. Fluctuations due to disorder, either induced by randomly placed dopants in the quantum wells or variations of the thickness or composition of the different layers may lead to an inhomogeneous distribution of resonances and thus to enhanced broadening of the intersubband absorption line [38]. The simple model of purely parabolic subbands also breaks down for higher  $k_{\perp}$ -values. This nonparabolicity (e.g. the increase of the effective masses with higher  $k_{\perp}$ -values) not only leads to broadening but also to a slight redshift of the intersubband resonance [39].

### Many-body effects

The picture of independent two-level systems as presented above is an approximation. In particular at high carrier concentrations, the coupling of different oscillators via the Coulomb interaction has to be taken into account. This changes the behavior of the system with respect to the interaction with an electromagnetic wave leading to a change in the shape, width, and position of the intersubband absorption line. A prominent many-body effect is the depolarization shift [40]. A collective charge density oscillation in  $z$ -direction induced by a coherent excitation leads to an oscillating charge separation. Consequently, the Coulomb-interaction among the carriers results in an additional back-driving force for the carriers and shifts the transition frequency to higher energies (blue shift)[39]. Many-body effects are very significant in case of wide wells, i.e., large intersubband dipoles, and high carrier concentrations. Here, the mere single-particle picture is not adequate to describe the position and width of the intersubband line.

### Absorption in superlattices

The absorption process for intersubband transitions, as well as the selection rules are also valid for transitions in a superlattice, where transitions between minibands in the conduction band are then called interminiband transitions.

Interminiband transitions are generally calculated in the same manner as in Eqn.(2.26), except that we are now dealing with a three-dimensional system. Therefore we have to integrate over  $k_x$ ,  $k_y$ , and  $k_z$  and take the energy dispersion in  $k_z$  direction into account. Again we can perform the integration  $k_x$  and  $k_y$  direction assuming parabolic bands. Then, considering only the two lowest minibands in a superlattice, the absorption coefficient reads:

$$\alpha \propto \int_0^{\pi/d} dk_z |\langle 1, k_z | p_z | 2, k_z \rangle|^2 \ln \left[ \frac{1 + \exp((E_F - E_1(k_z))/k_B T)}{1 + \exp((E_F - E_2(k_z))/k_B T)} \right] \delta(E_2(k_z) - E_1(k_z) - \hbar\omega) \quad (2.30)$$

The mechanism of absorption in superlattices is depicted in Fig. 2.7. The inset shows schematically the dispersion relation for the two lowest minibands, both of them showing

an approximate cosine-like behavior. In the case of occupation of the lower miniband, provided either by  $n$ -type doping or interband-excitation, the interminiband absorption is allowed all over the mini-Brillouin-zone ranging from  $k_z = 0$  to  $k_z = \pi/d$ . However, due to the  $k_z$ -dependent *curvature* of the miniband, the oscillator-strength also varies over the mini-Brillouin-zone. This can be understood by extending the oscillator sum rule (2.29) for energy bands [37], which then reads

$$\sum_{n'} f_{n,n'}(k_z) + \frac{m^*}{\hbar^2} \frac{\partial^2 E_{n'}(k_z)}{\partial k_z^2} = 1. \quad (2.31)$$

To fulfill this sum rule, it is necessary that  $f_{n,n'}$  is reduced at positive curvatures ( $k_z = 0$ ) and enhanced at negative curvatures ( $k_z = \pi/d$ ), which leads to a maximum absorption at the mini-Brillouin-zone edge, assuming an equally occupied lower miniband, realized at high temperatures or high doping. This effect gets stronger for thinner coupling barriers, whereas for thick barriers  $f_{n,n'}(k_z)$  remains constant as for single quantum wells.

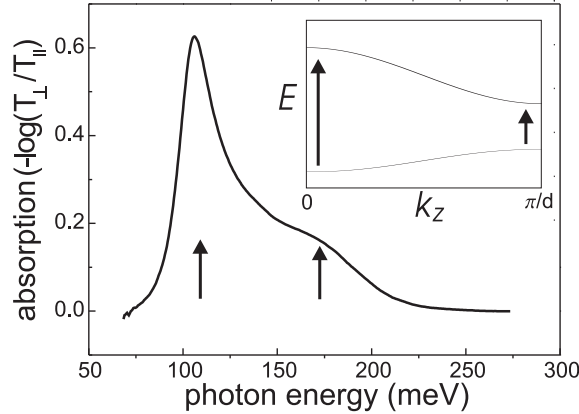


**Figure 2.7:** Experimental absorption spectrum of a GaAs/Al<sub>0.3</sub>Ga<sub>0.7</sub>As superlattice with a well width of 7.5 nm and a barrier width of 2.5 nm, respectively. The temperature is  $T=300$  K.

However, the absorption spectrum of a superlattice not only depends on the oscillator strength and the occupation factor, but also on the joint density of states (JDOS), which is simply the  $k_z$ -integration of the  $\delta$ -function in Eq.(2.30). Previous works [41] demonstrated that the JDOS has two van-Hove-singularities, at the center and the edge of the mini-Brillouin-zone. Due to its one-dimensional character, it exhibits a  $\omega^{-1/2}$  divergence.

Fig. 2.7 shows the experimental absorption curve of a typical GaAs/Al<sub>0.3</sub>Ga<sub>0.7</sub>As superlattice ( $d_{\text{well}}=7.5$  nm,  $d_{\text{barr}}=2.5$  nm) at a lattice temperature of 300 K. It clearly shows a prominent maximum at 109 meV and a shoulder at 180 meV, reflecting the relatively weak zone center transition, while the transition at 109 meV refers to the transition at  $k_z = \pi/d$ . Since the spectrum is taken at room temperature, one can assume that all states in the lower miniband are sufficiently occupied, leading to an absorption spectrum which nicely agrees with the expectations described above.

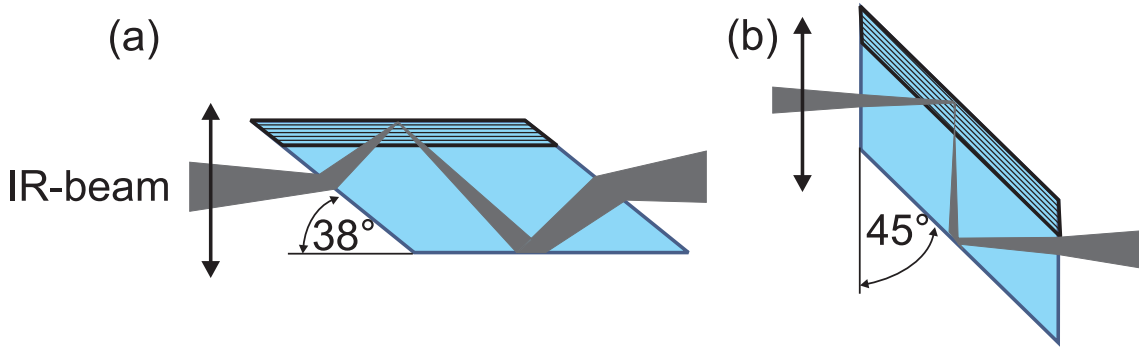


**Figure 2.8:** Different waveguide geometries used in the intersubband absorption experiments. (a) Single-pass waveguide with a facet polished under an angle of  $38^\circ$ . (b) Single-pass waveguide with a facet under  $45^\circ$ .

## 2.4 Standing wave pattern in waveguide geometries

For spectroscopy, it is necessary to achieve a strong coupling of the infrared or THz light field to the intersubband transition dipoles. As was shown earlier, the selection rule for intersubband transitions requires an electric field component perpendicular to the quantum well layers. Thus, nonstandard geometries have to be used for absorption measurements, which in turn require a careful consideration of the spatial distribution of the electromagnetic field in the sample [37].

In a standard geometry, where the light is incident perpendicular to the sample surface, the electric field has no component in the growth direction and thus does not couple to the intersubband transition dipoles. The simplest way to overcome this problem is to shine the light on the sample at Brewster's angle ( $\theta_B = \arctan(\eta) = 73^\circ$  for GaAs with a refractive index of  $\eta = 3.3$  at IR wavelengths). However, due to the high refractive index, the angle of incidence within the sample is still rather small ( $\theta = 17^\circ$  for GaAs), leading to a small intersubband-active electric-field component. The electric-field component interacting with the intersubband transition is  $E_z = E_0 \sin(\theta)$ , which gives a factor  $\sin^2(\theta)$  for the absorbed intensity. However, the effective interaction length of the radiation with the quantum well structure is then increased by  $1/\cos(\theta)$ , so that the effective coupling factor is  $\sin^2(\theta)/\cos(\theta) = 0.09$  for GaAs. Hence, usually the Brewster's angle geometry is only used in highly doped samples with many layers.

To obtain a much stronger coupling, the samples here are processed into a waveguide, in which the light beam enters through side facets and thus can travel under a small, even grazing angle with respect to the quantum well layers. In principle, there are two slightly different waveguide systems that are commonly used. In one geometry, the facets are polished at an angle of  $45^\circ$ . Then in a 1 mm long sample with a thickness of  $500 \mu\text{m}$ , one has one internal reflection, leading to a coupling strength of  $2 \times \sin^2(45^\circ)/\cos(45^\circ) = \sqrt{2} = 1.41$ , since the incoming light passes the active layers twice. Fig. 2.8(b) shows the geometry of such a waveguide. The advantage of this method is that for absorption

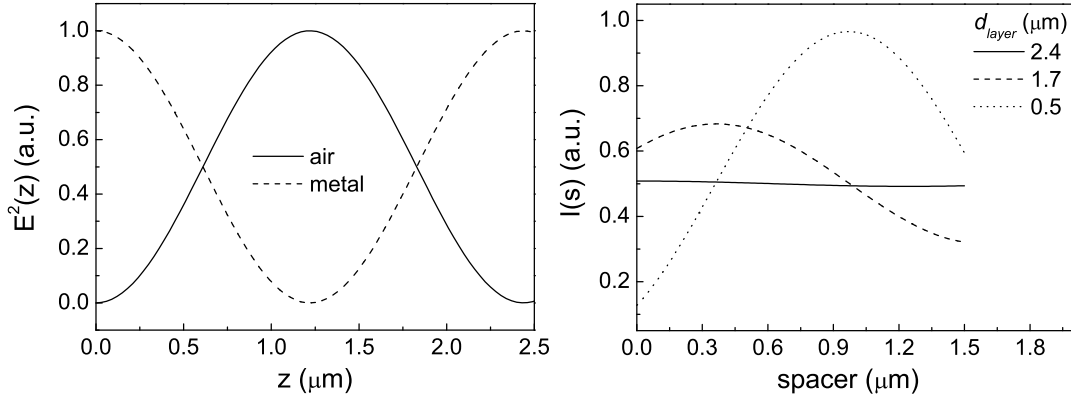


**Figure 2.9:** Left hand side: intersubband-active intensity pattern at a wavelength of  $11 \mu\text{m}$  for a semiconductor-air interface (full line) and a semiconductor-metal interface (dashed). As semiconductor material GaAs with  $\eta=3.3$  is chosen. Right side: integrated intensity at a wavelength of  $11 \mu\text{m}$  for different layer thicknesses as a function on the spacer-thickness  $s$ .

measurements, where the transmission of  $p$ -polarized light (which is intersubband-active!) is normalized to the  $s$ -polarization, one gets identical reflection losses at the entry and the exit of the sample for both polarizations. The disadvantage, however, is that the IR beam undergoes a vertical displacement, depending on the length of the waveguide.

An alternative method for a waveguide is to polish the facets at an angle of  $\alpha = 38^\circ$  (see Fig. 2.8(a)). Then the internal angle is given by

$$\theta = \alpha + \arcsin\left(\frac{90^\circ - \alpha}{\eta}\right). \quad (2.32)$$

By choosing  $\alpha = 38^\circ$  we find that the IR beam travels parallel to the entrance facet. In this case the coupling strength is more than 2, so even stronger than for the  $45^\circ$ -waveguide model.

However, to calculate the absorption of an electromagnetic wave in a waveguide structure, it is also necessary to consider the situation at the sample surface, i.e., the semiconductor-air interface. Due to interference of the incoming and reflected wave, a standing-wave intensity pattern of the field component  $E_z$  will form along the  $z$ -direction having a periodicity of  $\lambda/2\eta \cos(\theta)$  [42]. Thus, it is clear that the absorption strongly depends on the position of the quantum wells relative to the position of the intensity nodes and antinodes, if the total thickness of the structure is smaller than this standing-wave period. In Fig. 2.9 (left) the electric-field distribution near the semiconductor-air interface is shown. In case of the  $45^\circ$  waveguide the light is incident from inside the semiconductor at an angle of  $\theta = 45^\circ$ . According to Fresnel's law, the totally reflected wave will undergo a phase shift of  $168^\circ$ , which corresponds to an almost complete phase reversal, eventually leading to a node of the electric field at the semiconductor surface. Thus, for thin layers such as single quantum wells, there is virtually no interaction of the incoming light with the intersubband transition. Hence, the active layer must be moved towards an antinode of

the standing wave pattern, requiring a spacer layer towards the surface. A different possibility is to evaporate a thin metallic film on top of the active layer, which changes the boundary conditions in such a way that the standing-wave pattern exhibits an antinode on the sample surface. This gives a well-defined interaction of light with the intersubband transition.

Fig. 2.9 shows the intensity for different thicknesses of the spacer layer, integrated over the active layer for a given layer thickness. The wavelength was  $11 \mu\text{m}$ :

$$I(s) = \int_s^{s+d_{\text{layer}}} E^2(z, \lambda) dz \quad (2.33)$$

where  $E^2(z, \lambda) = \sin^2(2\pi z \eta \cos(\theta)/\lambda)$  is the electric-field intensity inside the waveguide. For comparison, the curves are normalized to the thickness of their respective layers. We find that for thick layers ( $2.4 \mu\text{m}$ ) the intensity remains nearly constant for varying spacer thickness. However, this changes for small structures with a thickness of  $1.7 \mu\text{m}$  and  $0.5 \mu\text{m}$ , respectively. In the latter case, the integrated intensity can be enhanced by a factor of 10, simply by choosing the proper spacer thickness.

In the experiments involving superlattices that consist of 300 periods, the intensities of the standing wave averages out making no metallic layer necessary. Their growth parameters and calculated electronic properties, obtained from a one-dimensional Kronig-Penny model, are listed in Table 2.1.

However, in Chapter 6, we probe the intersubband transition of a thin multi-quantum well structure ( $d_{\text{layer}} = 1.71 \mu\text{m}$ ), in which carriers are generated via interband excitation at the sample surface. In this structure a spacer layer of  $300 \text{ nm}$  is additionally implemented during the growth process to secure a high interaction strength.

## 2.5 Dynamic description of many-level systems

Up to now we have treated the intersubband absorption time-independently by simply calculating the transition matrix element by Fermi's Golden Rule with stationary states. However, once pulsed light sources interact with the system, this method becomes no longer applicable. In this case, the coherent and incoherent interaction of light with the system is generally analyzed for an ensemble of non-interacting many-level systems. In a simple approximation, such a model, mostly known from atomic physics, can be applied to semiconductor physics as well. However, it remains only valid as long the corresponding states do not interact.

A formalism that facilitates the treatment of such a system in a compact manner, is the density-matrix-formalism [43]. Under circumstance the precise state of the system is unknown, the density matrix formalism can be used to describe the system in a statistical sense. For this we introduce the density matrix:

$$\rho(t) = (|n\rangle \rho_{nm}(t) \langle m|)_{n,m \in \{1..N\}} \quad (2.34)$$

Sample		G757	G998	G999	H171	H175
Well width	$d_{\text{well}}$	90	85	85	68	77
Barrier width	$d_{\text{barr}}$	25	31	31	11.3	21
Al-content	%	30	30	30	40	33
Lower miniband	$E_1^1 - E_1^2$	29-41	34-43	34-43	33-81	35-55
Lower miniband-width	$\Delta_1$	12	9	9	48	20
Second miniband	$E_2^1 - E_2^2$	117-166	131-172	131-172	165-325	144-223
Second miniband-width	$\Delta_2$	49	41	41	160	79
Zone-edge transition	ZET ( $k_z = \pi/d$ )	76	88	88	84	89
Zone-center transition	ZCT ( $k_z = 0$ )	137	138	138	292	188
Doping density (3D)	$n^{(3)}$	0.6	1	2	1	1.5
Doping thickness	$d_{\text{dope}}$	60	50	50	40	40
Sheet density (2D)	$n^{(2)}$	2	5	10	2	6

**Table 2.1:** Structure parameters and calculated energy-values of the respective miniband and transition energies of the investigated superlattice samples. The calculations were done with a Kronig-Penney model.



Here  $|n\rangle$  and  $|m\rangle$  represent the eigenstates of the Hamiltonian  $H_0$ :

$$H_0|n\rangle = \hbar\omega_n|n\rangle$$

Then, the mean value of an observable  $X$  of the system is given by

$$\langle X \rangle = \sum_{nm} \rho_{nm} X_{mn} = \text{tr}(\rho X). \quad (2.35)$$

The diagonal elements  $\rho_{nn}$  represent the probability to find the system in its eigenstates and thus gives a measure of the *population*. The off-diagonal elements  $\rho_{n,m}$  ( $n \neq m$ ) describe the coherent superposition of the corresponding states, i.e. the macroscopic *polarization*.

If a time-dependent electric field  $E(t)$  is applied, the density matrix evolves according to the von Neumann equation:

$$i\hbar \frac{\partial \rho}{\partial t} = [H_0, \rho] + [W(t), \rho] + i\hbar \underbrace{\left( \frac{\partial \rho}{\partial t} \right)_{rel}}_A \quad (2.36)$$

Here  $W(t) = -\hat{\mu}E(t)$  denotes the dipolar interaction of  $E(t)$  where  $\hat{\mu}$  is the dipole operator. The relaxation term  $A$  represents the scattering processes and can be written in the form

$$\left( \frac{\partial \rho}{\partial t} \right)_{rel} = \hat{\Gamma} (\rho_{nm}(t) - \rho_{nm}(t_0)) \quad t_0 = t \rightarrow -\infty \quad (2.37)$$

phenomenologically leading to an exponential decay of the population of the excited states ( $T_1$ ) and the coherent polarization ( $T_2$ ). The latter is also connected to population relaxation and therefore has two components, where  $T_2^*$  reflects the pure dephasing time:

$$\frac{1}{T_2} = \frac{1}{2T_1} + \frac{1}{T_2^*} \quad (2.38)$$

However, in most cases  $T_1$  is much longer than  $T_2$ , so that the off-diagonal elements of  $\rho(t)$  decay faster than the diagonal elements.

As a model system we now consider a single quantum well, containing only two subbands with an energy spacing  $E_{21}$  of 100 meV, representing an ideal two-level system with the eigenstates  $|1\rangle$  and  $|2\rangle$ .

Generally, we can describe the state of the entire system based on the states  $|1\rangle, |2\rangle$  that form a complete orthonormal basis:

$$|\psi(t)\rangle = \sum_{n=1,2} c_n(t)|n\rangle \quad (2.39)$$

Note that in the density matrix formalism  $C(t) = c_1^*(t)c_2(t)$  reflects the non-diagonal elements  $\rho_{12}$  and  $\rho_{21} = C^*(t)$ . Evaluating the von Neumann equation for this two-level

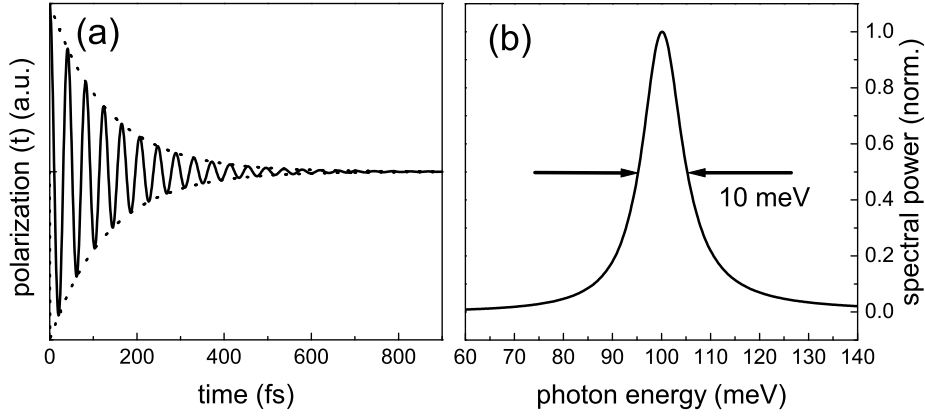


**Figure 2.10:** (a) Schematic oscillation of the macroscopic intersubband polarization at  $E_{21} = 100$  meV with a oscillation period corresponding to the intersubband resonance ( $T_{osc} = h/E_{21} = 41.4$  fs) and a damping time-constant of 132 fs. (b) Resulting power spectrum, showing a Lorentzian with a full width at half maximum of 10 meV.

system gives the coupled differential equations for the population and the coherence. For now, we are only interested in the the coherence:

$$\begin{aligned}
 i\hbar \frac{d}{dt} \rho_{12}(t) &= H_{21} \rho_{11} + H_{22} \rho_{12}(t) - \rho_{12} H_{11} - \rho_{22} H_{12} \\
 &= (H_{22} - H_{11}) \rho_{12}(t) + H_{12} (1 - 2\rho_{22}) \\
 &= E_{21} \rho_{12}(t) + H_{12} (1 - 2\rho_{22})
 \end{aligned} \tag{2.40}$$

Hence, in absence of the perturbation term  $H_{12}$ ,  $\rho_{12}$  simply oscillates with the resonance energy of the two-level system

$$\rho_{12}(t) = e^{i \frac{E_{21}}{\hbar} t}. \tag{2.41}$$

Assuming now that we have prepared the two-level system such that both states are occupied to some degree by an ultrashort coherent excitation with a resonant light pulse, we find the system in a coherent superposition of both eigenstates (with  $E_1 \equiv 0$ ):

$$|\psi(t)\rangle = \frac{1}{\sqrt{2}} \left( |1\rangle + |2\rangle e^{i(\frac{E_{21}}{\hbar} t + \Phi)} \right) \tag{2.42}$$

This results in an oscillatory behavior of  $|\psi(t)\rangle$  with the period  $T_{osc} = h/E_{21}$ . Assuming the presence of relaxation mechanisms of the phase relation we than have an exponentially damped oscillation between state  $|1\rangle$  and  $|2\rangle$

$$\Psi(t) \propto e^{-t/T_2} \cos(\omega_{osc} t + \Phi). \tag{2.43}$$

Its Fourier transform yields a Lorentzian

$$\tilde{F}_{\Psi}(\omega) = \frac{1/T_2}{(1/T_2)^2 + (\omega - \omega_{21})^2}$$

with a full width at half maximum of  $2/T_2 = 2\Gamma$ . This behavior is schematically shown in Fig. 2.10, where the exponentially damped oscillation and the corresponding power spectrum is plotted. Note that it is simply the assumption of a single exponential decay in Eqns.(2.37) and (2.43) that leads to the well known Lorentzian lineshape of homogeneously broadened intersubband resonances.

## 2.6 Ultrafast processes

The application of ultrafast optical experiments, such as pump-probe spectroscopy and four-wave mixing, to the field of semiconductor heterostructures has led to a deep insight into the dynamics of intersubband transitions. In these experiments the system undergoes several relaxation mechanisms back to the thermodynamic equilibrium after an ultrafast, coherent excitation that leads to a state far from equilibrium[31]. The subsequent relaxation can be classified into four main processes, which, depending on the specific sample, can also temporally overlap (see Fig. 2.11). We restrict ourselves to the general case of a typical quantum well system, based on the GaAs/AlGaAs material system and subband (miniband) spacings far above the longitudinal optical (LO) phonon energy ( $\hbar\omega_{\text{LO}} = 36$  meV) as well as to low electron concentrations, where many-body interactions are negligible.

- **Coherent polarization and dephasing**

The interaction of a coherent ultrashort light pulse, resonant with the intersubband spacing, creates a macroscopic optical polarization between optically coupled states with equal in-plane momenta (Fig. 2.11(a)). This polarization can be understood as a nonstationary superposition of the involved subbands with a rigid phase relation to the electric field of the incident pulse (compare Eqn.(2.42)). In addition, an occupation of the electronic states in the formerly unoccupied upper subband is generated by the absorption.

In two-level intersubband systems with a subband spacing in the range from 100-200 meV the polarization decays on timescale of a few hundreds of femtoseconds (*dephasing*) [44, 45]. Due to various scattering processes the relative phase between the ground state and the excited state gets destroyed. The main dephasing mechanisms are electron-electron, intrasubband LO-phonon and impurity (hole)-scattering and lead to *homogeneous* broadening of the intersubband resonance. Since the population relaxation is usually longer (0.5-2 picoseconds, [46]), it plays only a minor role for the dephasing.

Structural defects or intrinsic disorder, leading to an ensemble of different intersubband oscillators, provide another dephasing mechanism. These mechanisms lead to an inhomogeneous broadening of the intersubband resonance. The initially ro-

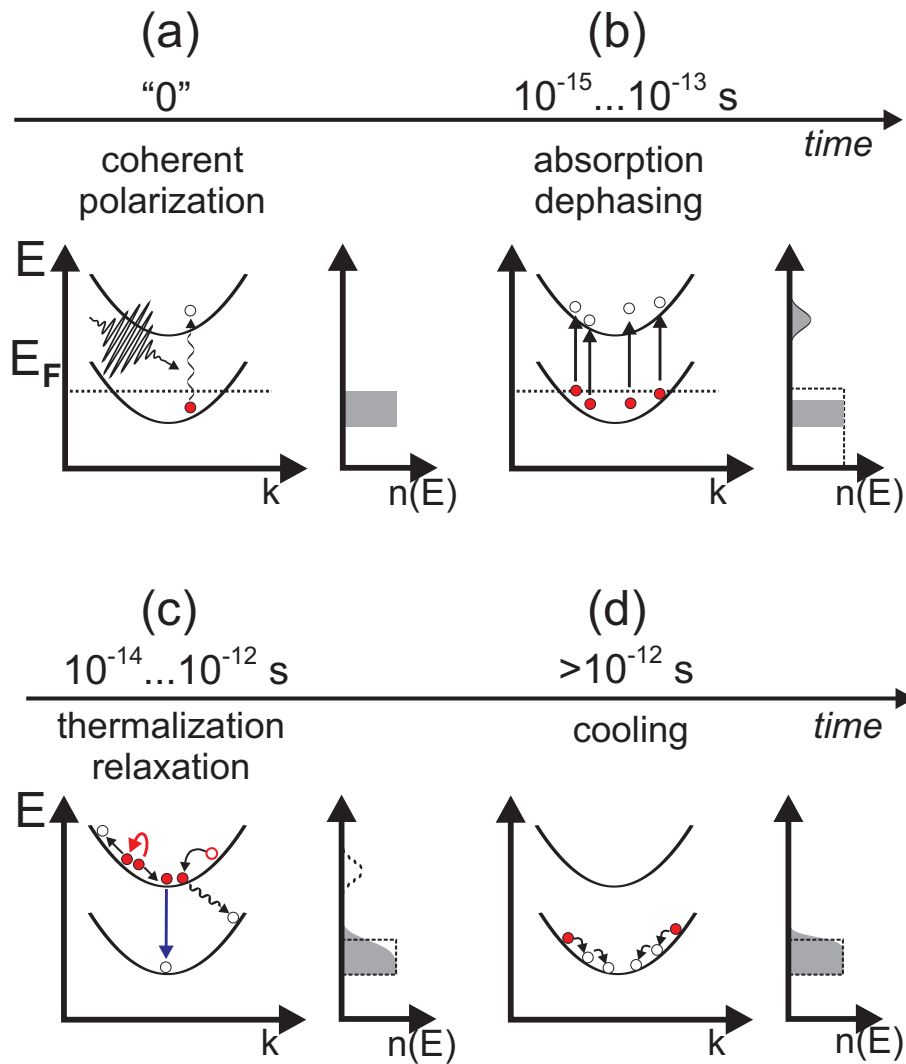


**Figure 2.11:** Hierarchy of processes and their timescales for intersubband transitions after an ultrafast excitation. See details in the text.

bust polarization gets destroyed due the different time evolution of these oscillators with different resonance frequencies. However, assuming a high quality of the sample, which is nowadays mostly achieved in the GaAs/AlGaAs material system, its contribution to the dephasing is rather small.

- **Relaxation and thermalization**

Carriers that have been promoted to the excited level by the incoming radiation are able to relax down to the ground state either by carrier-carrier scattering or by interaction with the lattice in terms of phonon-scattering (compare Fig. 2.11(c)). Of course, also the (re)emission of the formerly absorbed photon is possible. In case of phonon-scattering it is important if the subband spacing is below or above the LO-phonon energy. Below this energy only relaxation via acoustical phonons and carrier-carrier scattering is possible and leads to typical relaxation times of 10-100

picoseconds. In case of a large subband spacing ( $\Delta E > \hbar\omega_{\text{LO}}$ ) the relaxation via LO-phonons is very efficient and thus has the largest contribution. Due to its  $1/q$ -dependence, where  $q$  is the momentum transfer, the relaxation time is dependent of the subband spacing. The relaxation is faster if the subband spacing equals (multiples of) the phonon energy than somewhere in between. LO-phonon relaxation times are in the order of 1-2 ps.

Since in most cases the subband spacing does not match the phonon-resonance, relaxed carriers 'arrive' in the lower subband at higher  $k$ -values (see Fig. 2.11(c)) and lead to an athermal carrier distribution. Subsequent scattering mechanisms, again such as interaction with phonons and other carriers, cause additional heating of the electrons in the lower subband. Therefore the time-constants depend strongly on the carrier-concentration. After thermalization the electrons remain in a quasi-Fermi-distribution with a higher temperature than the lattice.

- **Cooling**

After the carriers have reached the quasi-Fermi-distribution with a temperature  $T_e > T_L$ , the Fermi-gas cools down to the lattice temperature by phonon or carrier-carrier interaction, as shown in Fig. 2.11(d). Typical cooling times that have been observed range from a few picoseconds up to 100 ps.

## 2.7 Nonlinear optics

Generally, the interaction of an electromagnetic wave  $\vec{E}(\vec{r}, t)$  with matter leads to a polarization  $\vec{P}(\vec{r}, t)$ , which will serve itself as a source for new electromagnetic waves. In a non-quantum-mechanical treatment, which will be appropriate in our case, this is well described by the wave-equation:

$$\vec{\nabla} \times \vec{\nabla} \times \vec{E}(\vec{r}, t) - \epsilon_0 \mu_0 \frac{\partial^2 \vec{E}(\vec{r}, t)}{\partial t^2} = \mu_0 \frac{\partial^2 \vec{P}(\vec{r}, t)}{\partial t^2} \quad (2.44)$$

In nonlinear optics, the polarization  $\vec{P}(\vec{r}, t)$  can be expanded into a power series of the electrical field:

$$\begin{aligned} \vec{P}(\vec{r}, t) &= \epsilon_0 \underline{\chi}^{(1)} \vec{E}(\vec{r}, t) + \epsilon_0 \underline{\chi}^{(2)} \vec{E}^2(\vec{r}, t) + \epsilon_0 \underline{\chi}^{(3)} \vec{E}^3(\vec{r}, t) + \dots \\ &= \vec{P}^{(1)}(\vec{r}, t) + \vec{P}^{(2)}(\vec{r}, t) + \vec{P}^{(3)}(\vec{r}, t) + \dots \end{aligned} \quad (2.45)$$

where  $\underline{\chi}^{(1)}$  is the linear optical susceptibility tensor in the time representation,  $\underline{\chi}^{(2)}$  is the second-order nonlinear optical susceptibility tensor, and so on. Since the susceptibility drastically become smaller at higher orders, it can be assumed at small electrical fields that the polarization is directly proportional to the incident field, representing linear optics:

$$\vec{P}(\vec{r}, t) = \epsilon_0 \underline{\chi}^{(1)} \vec{E}(\vec{r}, t) \quad (2.46)$$

However, at higher intensities terms of higher order have to be taken into account. The effect of the second order polarization will be demonstrated for a simple case, assuming the superposition of two planar waves ( $E_1 \sin(\omega_1 t), E_2 \sin(\omega_2 t)$ ) incident to a (nonlinear) medium in a single spatial dimension. Then, according to Eqn.(2.45), we find for the second order polarization:

$$\begin{aligned}
 P^{(2)}(t) = \frac{1}{2} \epsilon_0 \chi \quad [ & E_1^2 + E_2^2 \\
 & - E_1^2 \cos(2\omega_1 t) - E_2^2 \cos(2\omega_2 t) \\
 & - 2E_1 E_2 \cos((\omega_1 + \omega_2)t) \\
 & + 2E_1 E_2 \cos((\omega_1 - \omega_2)t)] \quad (2.47)
 \end{aligned}$$

In Eqn.(2.47) we see that different new electromagnetic waves can have different frequencies. Line 1 shows a static part, representing the sum of intensities, known as *optical rectification*. The terms in line 2 oscillate at twice the frequency of the incoming radiation, thus showing the process of *second harmonic generation* (SHG). As seen in line 3 and 4 of Eqn.(2.47), there also exist terms with frequencies as the sum of the incoming frequencies (*sum-frequency generation*) and as their difference (*difference-frequency generation*). This simple picture is also valid for pulsed light sources, which will be shortly presented for the case of optical rectification. Therefore we assume a single, ultrashort laser pulse in the near infrared with a duration of only  $\tau \approx 10$  fs. The second order polarization for optical rectification reads

$$P^{(2)}(t) = \epsilon_0 \chi^{(2)} E(t) E^*(t) = \epsilon_0 \chi^{(2)} I(t). \quad (2.48)$$

Thus, the polarization follows the intensity envelope function of the incoming laser pulse. This polarization results in the emission of a quasi-single cycle pulse, while its frequency spectrum can be obtained by a Fourier-transformation. For instance, a time-period of 10 fs results in a frequency of about 30 THz (10  $\mu\text{m}$ ).

# 3 Properties of resonant impurity states in semiconductor heterostructures and their influence on the intersubband absorption spectra

In this chapter we present a theory of impurity states in quantum wells and superlattices which treats the confining heterostructure potential and the random impurity potential on the same footing. The relevant 3D Hamiltonian is diagonalized in the low-doping regime. The results are used to calculate infrared absorption spectra which contain contributions of impurity and intersubband transitions. We mainly discuss the excited impurity states, which are pinned to higher subbands and are resonant states in the continuum. After a detailed analysis of a coupled quantum well system, we study the transition to a superlattice. In particular, we are able to reproduce existing experimental data on a quadruple quantum well and superlattices, which had not been understood in the past.

This chapter has been published in *Physical Review Letters* **95**, 257401 (2005), and *Physical Review B* **74**, 85311 (2006).

## 3.1 Introduction

A fundamental problem in semiconductor physics is the existence of localized states in addition to extended band states, which are unavoidable due to disorder and doping, and give rise to a metal insulator transition as a function of doping density [47]. In an effective-mass framework, the limit of low doping and zero compensation is equivalent to a system of isolated hydrogen atoms, resulting in the well known shallow impurity levels located below the conduction band (see Sec.(2.2) on page 9). At higher doping densities, impurity bands are formed due to the interaction between doping atoms and eventually the impurity band develops into a band tail of localized states. The metal-insulator transition (MIT) usually occurs while the Fermi energy is located in the impurity band [48]. In a slightly metallic semiconductor, the MIT can be induced by a magnetic field, which leads to stronger confinement of the wavefunctions and thus to localization [49].

For many applications structures doped with electrons are required. Important examples are "band-structure engineered" infrared devices making use of intersubband transitions such as quantum cascade lasers (QCL) or quantum well infrared photodetectors (QWIP)

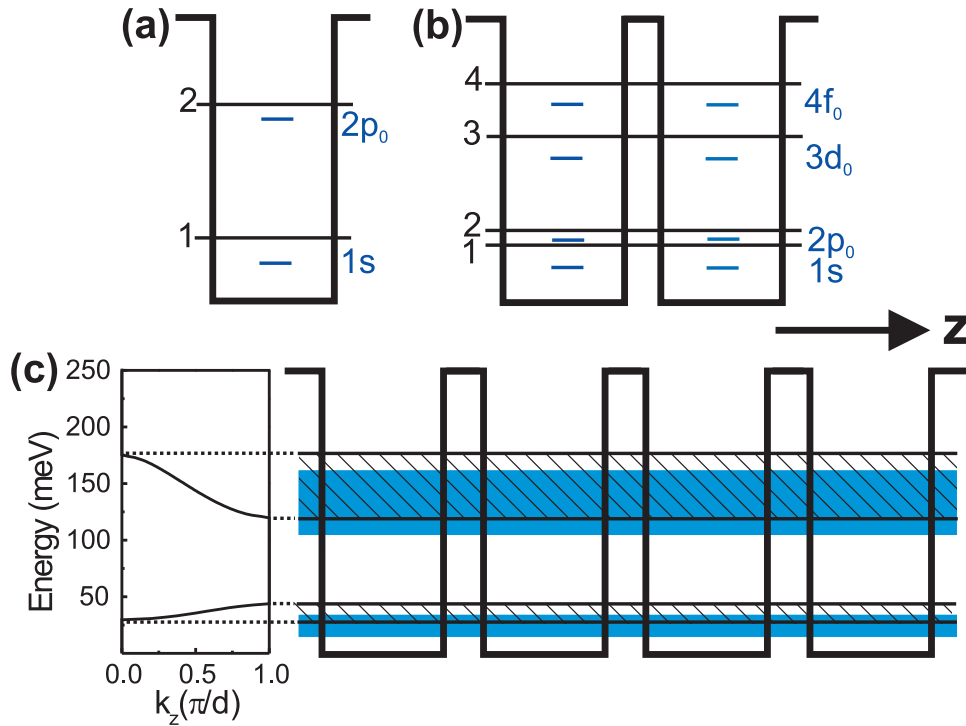


**Figure 3.1:** Sketch of the subband levels and most important impurity levels (blue) for a single (a) and double (b) quantum well. In (c) the minibands (hatched) and impurity bands (blue bars) for a superlattice are shown.

[50]. Consequently the properties of shallow impurity levels in quantum wells and superlattices have first been studied twenty five years ago [34, 51], and some detailed understanding has been achieved [52, 53]. Most theoretical work has been concerned with variational approaches, considering only selected, and often low-lying impurity states. In this work we present a calculation of the energy levels of the combined quantum well and random-impurity system, where quantum well potential and impurity potential are treated on the same footing. We will show that this approach leads to considerable insight and unveils some features which have not been noticed in the past. In order to facilitate comparison with experimental data, we use the results to calculate infrared absorption spectra, exhibiting intersubband and impurity transitions according to the thermal occupation of the respective energy levels. The nature of the states – impurity-like or band-like – is analyzed by looking at the wavefunctions in the planes of the confined layers.

## 3.2 Basic properties of confined impurity states

In a bulk semiconductor the energy levels of shallow donors can be well described in the usual scheme for hydrogen atoms with the quantum numbers  $N$ ,  $l$  (angular momentum),  $m$  (magnetic quantum number), i.e. the  $1s$ ,  $2s$ ,  $2p$  ( $m=\pm 1, 0$ ),  $3s$ ,  $3p$  ( $m=\pm 1, 0$ ),  $3d$  ( $m=\pm 2, \pm 1, 0$ ), etc. states with ground-state binding energy of one effective Rydberg,  $\text{Ryd}^*$ . In two dimensions, the binding energy is four times higher, and also the level



classification is different, e.g., the  $2p$  state is only two-fold degenerate. The exact two-dimensional limit corresponds to a situation with a single subband, and is only of limited relevance for realistic QWs. In a quasi-2D system with several subbands it is still possible and useful to employ the 3D classification, which however becomes modified by the QW potential (see Sec.(2.2)). The breaking of the translation symmetry in growth ( $z$ -) direction removes the degeneracy of some states [36], which become pinned to higher QW subbands<sup>1</sup>. Detailed analysis shows that states with low  $|m|$  quantum numbers, which are the ones with largest extension in  $z$ -direction, are pushed up farthest, in particular the states  $1s$  and  $2p_{\pm 1}$  are associated with the ground ( $n=1$ ) subband, the states  $2p_0$ ,  $3d_{\pm 1}$  etc. with the  $n=2$  subband, the states  $3d_0$ ,  $4f_{\pm 1}$  with the  $n=3$  subband etc. The relation expressing the exact assignment of an impurity state ( $N, l, m$ ) to a subband  $n$  reads  $n = l - |m| + 1$  [54]. The "most important" states are the  $m=0$  states ( $1s, 2p_0, 3d_0, \dots$ ) having  $z$ -symmetry (except of course the  $1s$ ), which become the ground states of a 2-dimensional hydrogenic series attached to each subband. This is illustrated for a single quantum well in Fig. 3.1(a). It should be pointed out again that this labelling of the quasi 2D states with the 3D atomic notation is mainly a matter of convenience, but can be justified with the one-to-one correspondence [54].

The optical transition between the attached impurity ground levels, ( $1s-2p_0$ ), follows the same selection rule as the usual intersubband transition, i.e., the exciting light needs to have an electric-field component parallel to the growth axis  $z$ . Due to the slightly larger binding energy of the  $1s$  state with respect to the  $n=1$  subband, as compared to the  $2p_0$  state with respect to the  $n=2$  subband, the  $1s-2p_0$  transition occurs at a slightly higher photon energy than the  $1 \rightarrow 2$  intersubband transition, and can thus be regarded as an "impurity-shifted" intersubband transition. It is easier to observe in wide QWs, where the relative shift (relative to the intersubband energy) is larger [55]; in narrower quantum wells ( $<10$  nm) it has only been observed recently [56]. Helm *et al.* [41, 25] have shown that in strongly coupled superlattices the  $1s-2p_0$  transition can be observed very clearly, since it is spectrally well separated from the van Hove singularities of the inter-miniband absorption spectra due to the finite miniband width. In this connection it is interesting to observe how an isolated quantum well evolves into a superlattice, consisting of many coupled quantum wells. This is best studied by looking at a coupled double-quantum well system, which can, on the one hand, be analyzed as one quantum mechanical entity with twice as many subbands as a single QW, but can also be regarded as a precursor to a superlattice. In this latter case the lower-state doublet ( $n=1,2$ ) evolves into the first miniband and the upper-state doublet ( $n=3,4$ ) into the second miniband (see Fig. 3.1 (b) and (c).). The  $1 \rightarrow 4$  and  $2 \rightarrow 3$  transitions in the coupled QW would thus correspond to the superlattice transitions at the mini-Brillouin center ( $k_z=0$ ) and edge ( $k_z=\pi/d$ ), respectively. The terminology for

<sup>1</sup>In addition, the binding energy becomes  $z$ -dependent, which however won't be discussed here further, since we assume all impurities to be located in the center of a quantum well. Compare Sec.2.2

the impurity states, however, then acquires some ambiguity: Looking from the "one entity" perspective [57], the main impurity states associated with the  $n=1.4$  subband would be  $1s$ ,  $2p_0$ ,  $3d_0$ ,  $4f_0$ , respectively (see Fig. 3.1(b)). From the SL perspective, on the other hand, the  $3d_0$  (and  $4f_0$ ) state would rather be called a  $2p_0$  state (or band). We will show below that the  $1s$ - $3d_0$  transition, which is dipole forbidden in a single quantum well, is actually allowed in a (strongly coupled) double QW, in contrast to the corresponding  $1 \rightarrow 3$  intersubband transition, a fact understandable from the SL perspective.

### 3.3 Method of calculation

Previous calculations of impurity levels in quantum wells were often based on variational approaches [34, 51, 52, 36, 58, 8], which usually require some apriori assumptions concerning the impurity states. Also mostly low-lying levels have been investigated in the past. Yet already in 1984 Priester *et al.* [58] had shown that each 2D subband has an impurity band associated with it. Ghazali *et al.* [59, 60] performed calculations of the density of states (DOS) in a multiple-scattering approach, and obtained also excited impurity levels [61], however they did not extend their calculation to continuum states. Kortus and Monecke [62] demonstrated the evolution of impurity states into 2D subbands in  $\delta$ -doped layers without an external confining potential, while Hofmann *et al.* [63] calculated the DOS in a 2D system with random impurities and investigated the Coulomb gap. Recent calculations investigated a double QW, but only near the lowest subband doublet [57], or reported an analytical approach for resonant impurity states in QWs [64].

Here we treat quantum well and impurity potentials in a unified framework and follow the method introduced in Ref. [65]. Our goal is to solve the 3D Schrödinger equation for the single particle quantum states:

$$\hat{H}(x, y, z)\Psi^{(i)}(x, y, z) = E^{(i)}\Psi^{(i)}(x, y, z). \quad (3.1)$$

The Hamiltonian can be decomposed into a purely  $z$ -dependent part  $\hat{H}_0$  and a "perturbation"  $\Delta\hat{H}$ :

$$\hat{H}(x, y, z) = \hat{H}_0(z) + \Delta\hat{H}(x, y, z). \quad (3.2)$$

The  $z$ -part determines the 1D states of the undoped multiple quantum well system,

$$\hat{H}_0(z) = \frac{p_z^2}{2m} + V_{\text{qw}}(z), \quad (3.3)$$

while the perturbation contains the lateral kinetic energy and the random 3D Coulomb potential of the impurities:

$$\Delta\hat{H}(x, y, z) = \frac{p_{xy}^2}{2m} + V_{\text{imp}}(x, y, z). \quad (3.4)$$

We first compute the 1D subband states of the undoped system:

$$\hat{H}_0(z)\varphi_n(z) = \epsilon_n\varphi_n(z). \quad (3.5)$$

As solutions of a Schrödinger equation, the subband wavefunctions  $\varphi_n(z)$  form a complete, orthonormal set. Since they already incorporate the strong potential  $V_{\text{qw}}(z)$  of the multi quantum well system, this set is especially well suited for expanding perturbed states of the system with respect to the  $z$ -coordinate.

In order to treat the  $x$ - $y$ -directions, we assume an artificial lateral periodicity of the impurity arrangement. Ideally, the linear dimension of the unit cell (in our case 100 nm) is chosen much larger than the average distance between nearest-neighbor impurities. This allows us the use of plane waves as lateral basis functions. Thus, the complete expansion of our 3D wavefunctions reads:

$$\Psi^{(i)}(x, y, z) = \sum_{k_x k_y n} G_{k_x k_y n}^{(i)} e^{ik_x x} e^{ik_y y} \varphi_n(z). \quad (3.6)$$

Inserting Eqn.(3.6) into Eqn.(3.1) transforms the continuum Schrödinger equation into a discrete matrix eigenvalue problem:

$$\sum_{k'_x k'_y n'} H_{k_x k_y n, k'_x k'_y n'} G_{k'_x k'_y n'}^{(i)} = E^{(i)} G_{k_x k_y n}^{(i)}. \quad (3.7)$$

For its numerical solution, the fundamentally infinite number of basis states is truncated to a tractable number of order 1000. The Hamilton matrix to be diagonalized is given by:

$$\begin{aligned} H_{k_x k_y n, k'_x k'_y n'} &= \delta_{k_x k_y n, k'_x k'_y n'} \left[ \epsilon_n + \frac{\hbar^2(k_x^2 + k_y^2)}{2m} \right] \\ &+ \langle k_x k_y n | V^{(imp)} | k'_x k'_y n' \rangle. \end{aligned} \quad (3.8)$$

In principle, the optical transition between two quantum states ( $i$ ) and ( $j$ ) can directly be computed from the resulting coefficients  $G_{k_x k_y n}^{(i)}$  and  $G_{k_x k_y n}^{(j)}$ , respectively. However, it is often instructive to back-transform the states into real-space representation. For this purpose, we first introduce the definition of lateral wavefunctions  $g_n^{(i)}(x, y)$  attached to the different subbands  $n$ :

$$g_n^{(i)}(x, y) = \sum_{k_x k_y} G_{k_x k_y n}^{(i)} e^{ik_x x} e^{ik_y y}. \quad (3.9)$$

We can then write the expansion Eq.(3.6) in the more intuitive form

$$\Psi^{(i)}(x, y, z) = \sum_n \varphi_n(z) g_n^{(i)}(x, y). \quad (3.10)$$

This expression shows the possibility of subband mixing arising from the (impurity-related) 2D lateral functions  $g_n^{(i)}(x, y)$ , which is of crucial importance in the case of energetically close subbands like in coupled quantum wells and superlattices. In case of a narrow single quantum well, where the subbands are largely separated in energy, this can be neglected [66]. Note that this method, namely the exact solution of the complete 3D-system and treatment of impurity potential and QW-potential on the same footing, differs

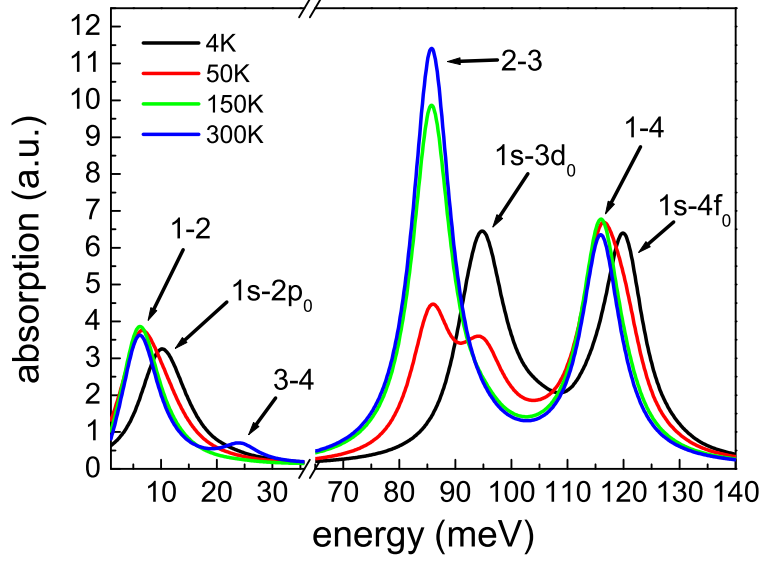


**Figure 3.2:** Calculated absorption of a double quantum well for different temperatures. The transitions are identified according to Fig. 3.1.

significantly from variational methods, which have been the main tool to describe impurity states especially in confined systems in the past, and where certain preassumptions have to be made beforehand.

With the resulting wavefunctions  $\Psi^{(i)}(x, y, z)$  (several hundreds for a double QW and up to thousands for a SL) we then proceed in calculating the absorption coefficient  $\alpha$  for light polarized in  $z$ -direction via Fermi's Golden Rule in dipole approximation:

$$\alpha(\hbar\omega) \propto \sum_{i,f} |\langle \Psi_f | p_z | \Psi_i \rangle|^2 (f_i - f_f) \delta(E_f - E_i - \hbar\omega) \quad (3.11)$$

Here  $f_i$  and  $f_f$  are the Fermi-Dirac occupation probabilities of the initial and final state. In order to remove artifacts due to one specific impurity configuration, and to obtain data directly comparable to real absorption measurements, we finally average this result over several (up to ten) additional random impurity configurations. The absorption spectra are obtained by using a Lorentzian lineshape for each transition with a phenomenological broadening parameter  $\Gamma$ , representing the half width at half maximum.

### 3.4 Results for the double quantum well

In this part we discuss the calculated absorption spectra of a lightly doped (few  $10^{10} \text{cm}^{-2}$ ) coupled GaAs/ $\text{Al}_x\text{Ga}_{1-x}\text{As}$  double QW ( $d_{\text{well}} = 9.0 \text{ nm}$ ,  $d_{\text{barr}} = 2.5 \text{ nm}$ ) in the mid-infrared (MIR) and far-infrared (FIR) regions. We will also vary the thickness of the coupling barrier and the electron density, and show the effects of directly placed dopants.

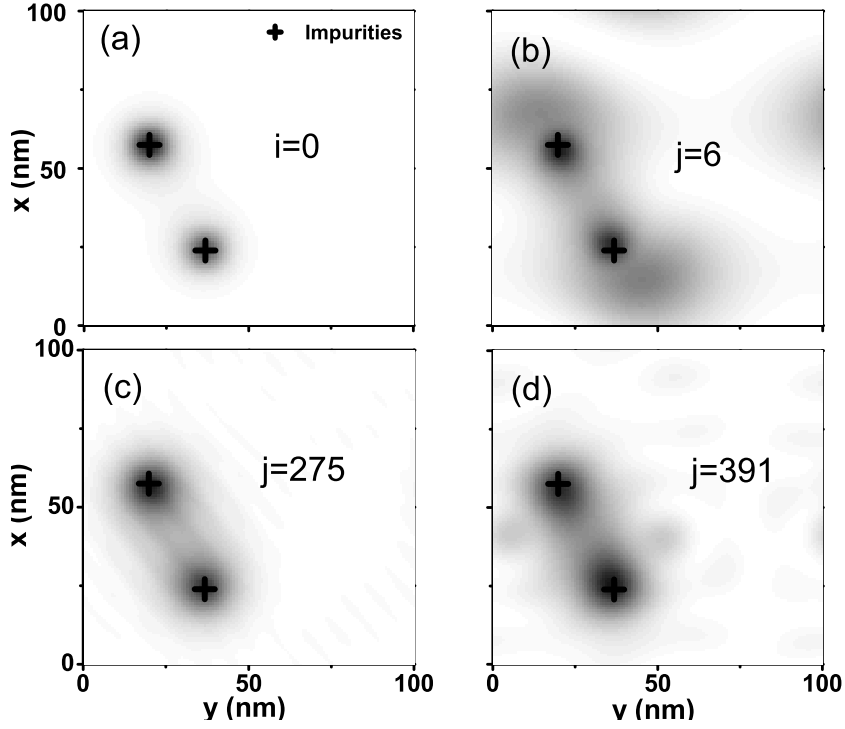


**Figure 3.3:** Wavefunctions of the initial (a) and final states (b),(c),(d) that contribute the spectrum of the DQW at  $T=4$  K.

Fig. 3.2 shows the absorption spectra calculated for different lattice temperatures and a phenomenological broadening of  $\Gamma=4$  meV. The doping was set to  $1 \times 10^{10} \text{cm}^{-2}$  per QW, corresponding to one impurity in a  $100 \times 100 \text{nm}^2$  area, and put in the center of each QW in  $z$ -direction. It was checked that at 4 K the Fermi energy is below the lowest extended (subband) state, this implies that all transitions observed at 4 K are due to impurity transitions. Shown are the FIR region ( $< 20$  meV), dominated by transitions to states near the first subband doublet of the double QW, and the MIR region (here 70-140 meV), dominated by transitions to states near the second doublet. Let us first analyze the spectrum at  $T=4$  K. It consists of three peaks, one in the FIR and two in the MIR. As we will show below, both MIR peaks can be attributed to transitions between localized states, the one at 95 meV to the  $1s-3d_0$  and the one at 120 meV to the  $1s-4f_0$  transition. Both final states have slightly lower energy than their corresponding subband states 3 and 4. Upon increasing the lattice temperature, we observe drastic changes in the spectrum:

(i): The high-energy peak at 120 meV slightly shifts towards lower energy (116 meV). This is due to decreasing localization of the corresponding wavefunctions, leading finally to a pure intersubband transition  $1 \rightarrow 4$ .

(ii): The peak at 95 meV disappears rapidly with rising temperature and an additional peak at 85 meV becomes dominant. This is due to thermal occupation of the second subband, leading to absorption into the third subband.

(iii): Also the low-energy peak gets red shifted, again reflecting the transition from im-

4 K					300 K				
$i$	$\rightarrow$	$j$	$f_{ij}$	$\epsilon_{ij}$ (meV)	$i$	$\rightarrow$	$j$	$f_{ij}$	$\epsilon_{ij}$ (meV)
1	$\rightarrow$	272	0.35	94.3	17	$\rightarrow$	286	0.022	85.75
<b>0</b>	$\rightarrow$	<b>275</b>	0.31	95.9	...		...	...	...
0	$\rightarrow$	<b>391</b>	0.28	119.6	10	$\rightarrow$	<b>415</b>	0.012	115.85
1	$\rightarrow$	392	0.27	120.6	...		...	...	...
0	$\rightarrow$	<b>6</b>	0.16	9.3	28	$\rightarrow$	<b>44</b>	0.005	6.0

**Table 3.1:** List of strongest transitions at  $T=4$  K (left) and  $T=300$  K (right). Listed are the initial ( $i$ ) and final ( $j$ ) states of each transition, their respective oscillator strengths,  $f_{ij}$ , and energies,  $\epsilon_{ij}$ . The transition in the third line at  $T=300$  K is the strongest around 116 meV, but only the 23rd overall. The wavefunctions of the bold states are plotted in Fig. 3.3 and Fig. 3.4.

purity states to extended (subband) states with rising temperature. The peak at 6 meV denotes the  $1 \rightarrow 2$  transition.

(*iv*): Finally, at  $T=300$  K another peak shows up at 24 meV; at this high temperature, even the third subband becomes slightly occupied resulting in the transition into the fourth subband.

Tab. 3.1 shows the most important transitions at 4 K and 300 K that contribute to each absorption spectrum. Note that now the system consists of hundreds to thousands of states, numbered ( $i, j$ ) with increasing eigen-energy (as opposed to the simple subband numbering,  $n=1..4$ ). We find that at low temperatures the spectrum is dominated by a *few* impurity transitions with *large* oscillator strength, whereas at room temperature it consists of hundreds (we only show one for each peak) of transitions between extended states with much *weaker* oscillator strength<sup>2</sup>. The wavefunctions of the ground and final states corresponding to the three strongest transitions at  $T=4$  K, integrated over the  $z$ -coordinate, are plotted in Fig. 3.3. The ground state and all final states are clearly localized.

The same analysis can be made for the strongest transitions at 300 K. As an example we plotted the wavefunctions of the final states  $j=44$ , and  $j=415$  in Fig. 3.4, marking the final states of the  $1 \rightarrow 2$  and  $1 \rightarrow 4$  transitions, respectively. Since initial and final states have almost the same shape (integrated over the  $z$ -coordinate), we omit here a detailed analysis for all contributing states. However, from Table 3.1 and Fig. 3.4 we see that at high temperatures the spectrum is dominated by many transitions between extended states.

### Barrier thickness dependence

Now we want to discuss the influence of the barrier thickness that separates the two wells. Therefore we have calculated the low-temperature absorption spectra using a very – unrealistically – small broadening parameter ( $\Gamma=0.5$  meV) to follow exactly its evolution

<sup>2</sup>At low temperature Tab. 3.1 shows two almost identical transitions for each spectral position, deriving from the presence of two impurities in the complete system.

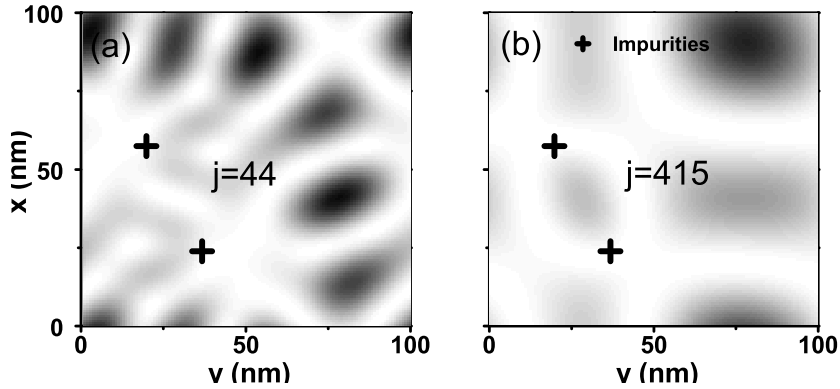


**Figure 3.4:** Final states of the most important transitions contributing to the absorption spectrum of the DQW at  $T=300$  K.

from a single quantum well behavior to the one of a typical DQW with fixed well thicknesses of 9.0 nm. The results are shown in Fig. 3.5. We start with the comparison of a single-QW spectrum to the DQW spectrum with a barrier thickness of 9.0 nm. Since the barrier is wide, the wells act independently of each other leaving the line position unchanged, but doubling the strength, since we have two impurities in the DQW and only one in the single QW. In the case of very strong coupling ( $d_{\text{barr}} = 2$  nm) we observe two peaks at 94 meV and 124 meV, respectively, each of which is split again by a very small amount. Whereas the two large features correspond to the  $1s - 3d_0$  and  $1s - 4f_0$  transitions, the small splitting is probably due to a slightly different impurity configuration in the two QWs, and only visible due to the unrealistically high resolution. At intermediate coupling-barrier thickness ( $d_{\text{barr}} = 4$  nm) the low-energy doublet at  $\approx 99$  meV is already well established, whereas the high-energy transitions are not clearly developed. This can most likely be attributed to the fact that for this barrier thickness the  $z$ -coupling strength (as measured by the splitting of the corresponding  $n=3,4$  subbands) is of the same order as the Coulomb binding energy ( $\text{Ryd}^* \approx 10$  meV). I.e., when the coupling strength is larger than one  $\text{Ryd}^*$ , both subbands acquire their own impurity state, and for the opposite case of weak coupling there is only one impurity state below the exited subband manifold. In the intermediate range, all states (subband and impurity) are heavily mixed, defying a clear classification.

### Doping concentration dependence

Also interesting is the effect of higher doping concentration, which we increased up to  $3 \times 10^{10} \text{cm}^{-2}$ . The integral absorption is proportional to the electron density, so we plotted the absorption behavior for doping densities of  $1, 2, 3 \times 10^{10} \text{cm}^{-2}$  normalized to  $1 \times 10^{10} \text{cm}^{-2}$  in Fig. 3.6 for three different temperatures. Since impurity states play a role mostly at low temperatures, we would expect the strongest differences in this regime. In fact, this is what we observe in Fig. 3.6. At a temperature of 4 K, the absorption peak at 95 meV obtains an additional shoulder on the low-energy side, becoming stronger with

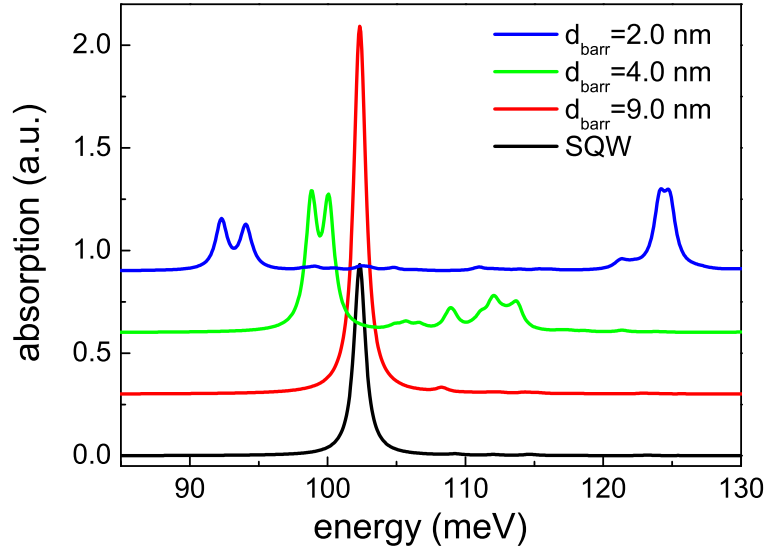


**Figure 3.5:** Absorption spectra for the DQW with different barrier thicknesses and of a single QW for comparison at  $T=4$  K. The spectra are vertically shifted for clarity.

increasing density. Obviously, the ground states of the additional impurity transitions are slightly higher in energy than that of a single impurity (i.e., more weakly bound), leading to a broader absorption line. At 50 K, however, this effect seems to be more pronounced. The  $1s-3d_0$  transition becomes enhanced and broader with increasing doping density, since it now consists of several impurity transitions, leading to inhomogeneous broadening. Interestingly, the  $1s-4f_0$  transition gets weaker at the same time, while the regular  $2 \rightarrow 3$  transition remains unchanged. At high temperature, where transitions between impurity states become less important compared to the regular intersubband transitions, no significant changes in the absorption spectrum can be determined, which is in agreement with our previous expectations. So with increased doping we find that the impurity-related peaks in the spectrum become broader, and that the  $1s-3d_0$  transition gets stronger compared to the intersubband transitions. Since we are limited to the low doping regime we cannot explore this phenomenon further, but it will be an interesting aspect once electron-electron interaction can be included in our model.

### Impurity location dependence

Up to this point we were distributing the impurities in each QW randomly. While this method reflects the experimental case most realistically, we also want to show what happens if we place the single dopant atoms in each quantum well at different distances from each other in the  $(x, y)$ -plane. This is not feasible with current experimental technologies, but since real samples will exhibit a random distribution of impurity separations, it is useful to understand the separation effects. Note the absolute position inside the well is



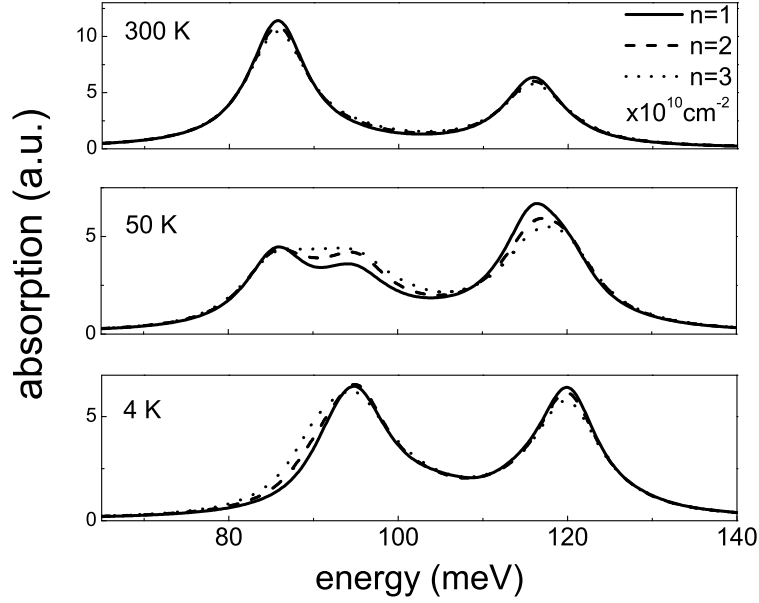


**Figure 3.6:** Calculated normalized absorption of a double quantum well for different electron densities and temperatures.

irrelevant due to the periodic boundary conditions, which also limits the maximum separation. We calculated the absorption coefficient at a temperature of 4 K for different distances (0.01.. 70 nm) of the impurities in the  $(x, y)$ -plane. The carrier density was set to  $1 \times 10^{10} \text{cm}^{-2}$ , so that we have again one impurity per QW. The results of this calculation are shown in Fig. 3.7.

At a distance of more than 30 nm, we see the regular absorption spectrum deriving from impurity transitions in each well with three absorption peaks (at 10, 95 and 120 meV), just like before in Fig. 3.2. Once we reduce the distance in the  $(x, y)$ -plane (note that both impurities are always separated in  $z$ -direction by 11.5 nm), we see drastic changes of the absorption behavior. While the spectral position of the peak at 120 meV does not change, both other peaks get shifted. Amazingly, the peak at 10 meV not only broadens and blueshifts, but also completely vanishes at very small distances. Apparently this transition becomes symmetry forbidden once the impurity levels start to couple in  $z$ -direction. We also observe major changes of the  $1s-3d_0$  transition, namely a large red-shift of  $\approx 10$  meV and a strong increase by a factor of two. Thus, in the same way as the doublets in a DQW are obtained by moving two QWs closer together, now the impurity levels are split. To clarify this we plotted the energetic level of the ground state for various distances in the inset of Fig. 3.7. We see that the ground state (i.e.  $1s$ ) gets lowered in energy by  $\approx 8$  meV, indicating that the formerly independent  $1s$ -states of each impurity now are split into a doublet. Of course this effect not only acts on the ground states but for all impurity states and thus leads to these drastic changes of the absorption spectrum. However, due to the

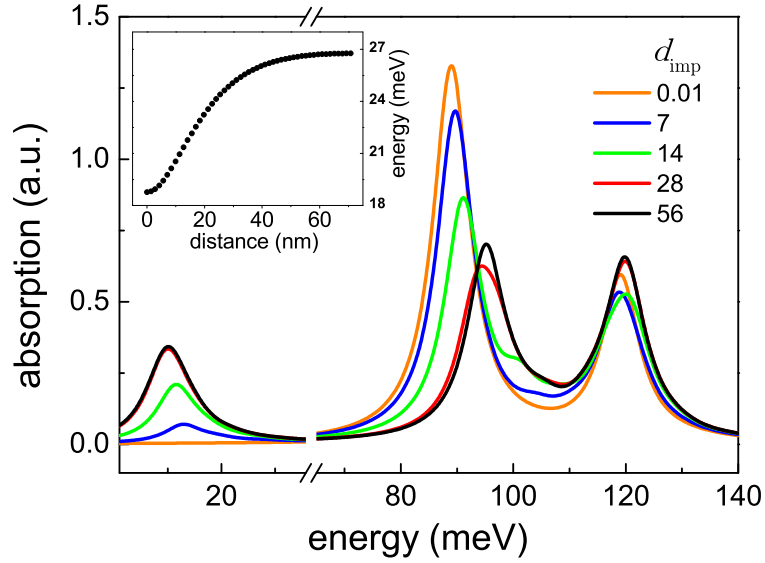


**Figure 3.7:** Calculated absorption of a double quantum well for different lateral distances of the donors in each well at an electron temperature of 4 K. The inset shows the energy level of the ground state for different distances.

complexity we omit a detailed study of all states contributing to the spectra as was done above. But as already mentioned, although this calculation is not directly comparable to a real absorption experiment, it still shows the possibility of an additional effect, that can lead to an enhanced broadening of some absorption peaks, if the donor density is high enough that some impurities have a similar  $(x, y)$ -position.

### 3.5 Quadruple quantum well

It is now most interesting to increase the number of coupled wells and track the evolution into a superlattice. In the following we will calculate the absorption spectrum of a quadruple quantum well (QQW) that will be compared to experimental data, leading to an almost perfect agreement. After this we will increase the number of wells further up to 20, which will serve as a superlattice, and compare their absorption spectra.

So let us now turn to the case of a QQW. The experimental data of such a structure was provided by M.C. Wanke, who has grown the sample at Bell Laboratories, New Jersey (USA) and provided us with the absorption spectra. The QQW sample consists of 6.8 nm wide GaAs-wells separated by 2.5 nm thin  $\text{Al}_{0.32}\text{Ga}_{0.68}\text{As}$  barriers. This structure is repeated 120 times and separated by an undoped 20 nm thick  $\text{Al}_{0.32}\text{Ga}_{0.68}\text{As}$  layer [67]. The average doping density over the four QWs with coupling barriers was  $3 \times 10^{16} \text{cm}^{-3}$ , resulting in a sheet density per QW of  $2.6 \times 10^{10} \text{cm}^{-2}$ . The experimental absorption spectra for different temperatures are shown in Fig. 3.8(a) [67].

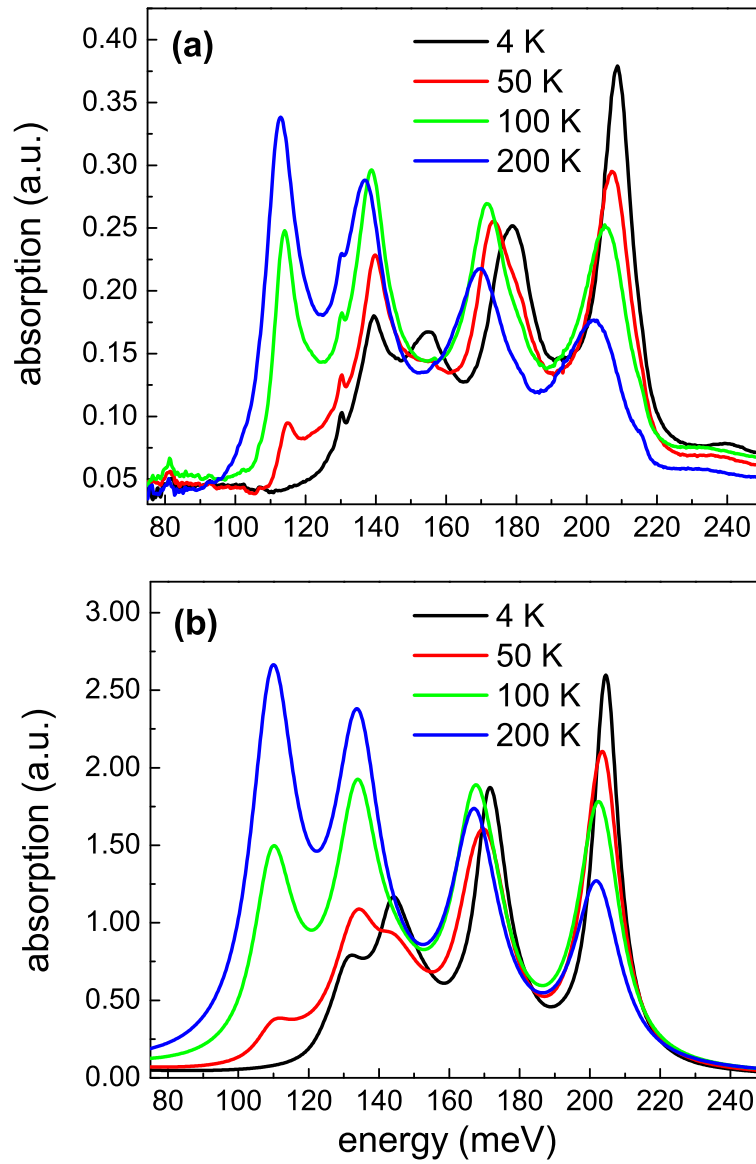


**Figure 3.8:** Experimental (a) and calculated (b) absorption spectra of a quadruple quantum well shown for different temperatures.

At all temperatures, we observe four prominent peaks in the spectrum, however, their spectral position and strength drastically changes for different temperatures. At  $T=200$  K, starting on the low energy side, they can be attributed to the  $4\rightarrow 5$ ,  $3\rightarrow 6$ ,  $2\rightarrow 7$ , and  $1\rightarrow 8$  transitions in the structure. At  $T=4$  K, as for DQW, we can assign all peaks to transitions between localized states, namely impurity states.

This can be proven by a direct comparison to calculated absorption spectra for different temperatures, using the same structure parameters as for the grown sample. This is shown in Fig. 3.8(b). To account for the different linewidths with varying the temperature, we adjusted the broadening parameter  $\Gamma$  from 4 meV at 4 K to 6 meV at 200 K. By comparing the experimental and theoretical results we observe excellent agreement in the peak positions and strengths, clearly demonstrating the validity of our model.

### 3.6 Towards the superlattice

While this – the presence of impurity states associated with the upper subbands (5-8) – may not be surprising for itself, it bears consequences for the situation in a superlattice, where it would correspond to a resonant impurity state associated with the *upper edge* of the second miniband<sup>3</sup>. To investigate this regime we now increase the number of wells further and follow the system’s evolution into a superlattice. Therefore we use the same parameters as for the double quantum well calculations ( $d_{\text{well}}=9.0$  nm,  $d_{\text{barr}}=2.5$  nm) and a doping density of  $1\times 10^{10}\text{cm}^{-2}$ , so that we have one impurity per QW.

Let us first analyze the change of the absorption at  $T=300$  K with increasing number of wells from 4 to 20. The results are shown in Fig. 3.9(a). For four wells, we observe a similar absorption shape as for the QQW above, having the strongest absorption at the  $4\rightarrow 5$  transition. By increasing the number of wells, this behavior remains and at 20 periods we see a smooth absorption spectrum. This reveals the typical absorption spectrum of a superlattice [41, 25], reflecting the van-Hove singularities in the joint density of states at the edge of the mini-Brillouin-zone ( $k_z = \pi/d$ ) and at its center ( $k_z = 0$ ), respectively (see Fig. 3.1(c)). The integrated absorption strength is proportional to the number of quantum wells.

We performed the same calculations for  $T=4$  K, shown in Fig. 3.9(b). With only four periods, we see four clearly separated peaks that all derive from transitions between localized states, as mentioned above. Increasing the number of periods, the individual peaks merge into a broad spectrum that contains two pronounced maxima at 90 and 135 meV, respectively. The low-energy maximum is sharper due to the higher density of transitions, while the high-energy maximum becomes discernible only for more than ten periods. By increasing the number of periods, the formerly separated impurity states in each quantum well start to form impurity bands, that are attached to each miniband. Note, however, that

<sup>3</sup>Fertig and Das Sarma[68] predicted localized states near the upper miniband, however, in a completely different context.

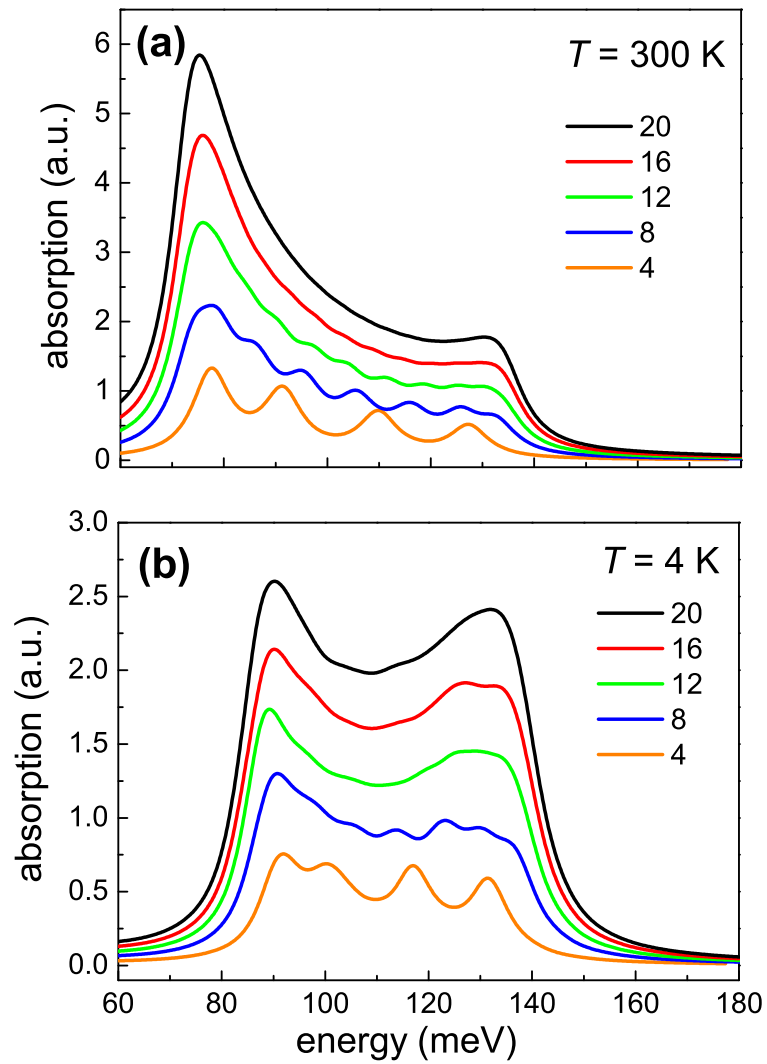


**Figure 3.9:** Calculated absorption spectra at (a)  $T=300$  K and (b) at  $T=4$  K for different numbers of quantum wells.

this results from coupling in  $z$ -direction and not through wavefunction overlap in the  $(x, y)$ -plane, the latter corresponding to the common notion of impurity bands [69]. As for single impurity states, they are slightly lower in energy than their corresponding minibands [70]. This is depicted in Fig. 3.1(c) as the blue area. To prove this assumption, we have plotted

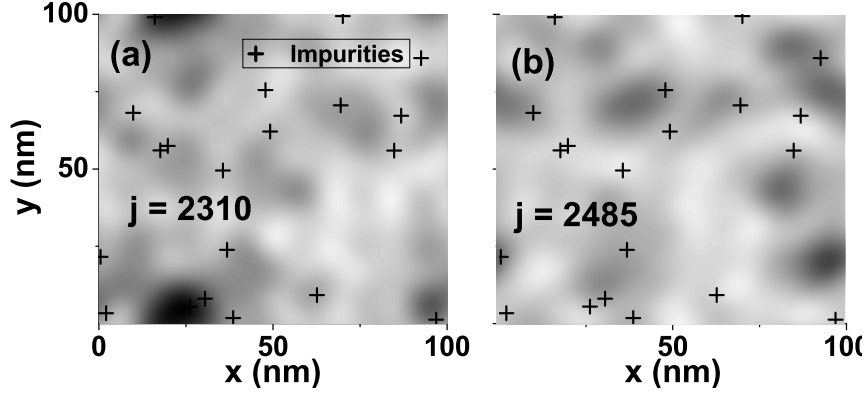


**Figure 3.10:** Wavefunctions of the final states contributing to a transition at 135 meV at 4 K (a) and to a transition at 132 meV at  $T=300$  K (b).

the excited states that contribute to the absorption spectrum near 130 meV for low and high temperatures in Fig. 3.10. While the state 2310 in Fig. 3.10(a) is mainly localized around an impurity on the bottom left, there is no correlation between the wavefunction and the impurity locations for state 2485 in Fig. 3.10(b). This clearly demonstrates that also for superlattices at low temperature we only have transitions between impurity states, in fact a broad absorption band. This modifies the previous assumption [41, 25], where only the lower-energy peak (here at 90 meV) was ascribed to an impurity transition and the higher-energy one to a miniband transition (at  $k_z=0$ ). A full temperature-dependent absorption spectrum of the same superlattice, that is approximated by 20 QW's (with the same parameters as above, i.e. well width 9 nm, barrier thickness 2.5 nm) is shown in Fig. 3.11(a). The impurities are distributed over 1 nm of the QW center with a density of  $n = 1 \times 10^{10} \text{cm}^{-2}$  per QW (the binding energy varies negligibly over this 1 nm range and is very close to the bulk value). Upon lowering the temperature the low-energy peak disappears due to thermal depopulation of the first miniband. What remains is a peak at 90 meV, which has previously been assigned to an impurity transition [41]. This interpretation remains valid by performing a similar analysis as for the double QW.

Let us analyze the higher energy peak at 133 meV. As stated above, at high temperature this corresponds to the interminiband transition at  $k_z=0$ . At low temperature, however, where it simply appears to become stronger, both the comparison with the double QW and the analysis of the wavefunctions show that this is again an impurity transition, namely *from the ground state to the impurity state associated with the upper edge of the second miniband*. In fact the whole spectrum (from 90 to 133 meV) at  $T=4$  K is due to impurity transitions, and reflects a band of resonant states, partly overlapping the second miniband (see Fig. 3.1(c)); these states are de facto localized, yet strictly they are resonant

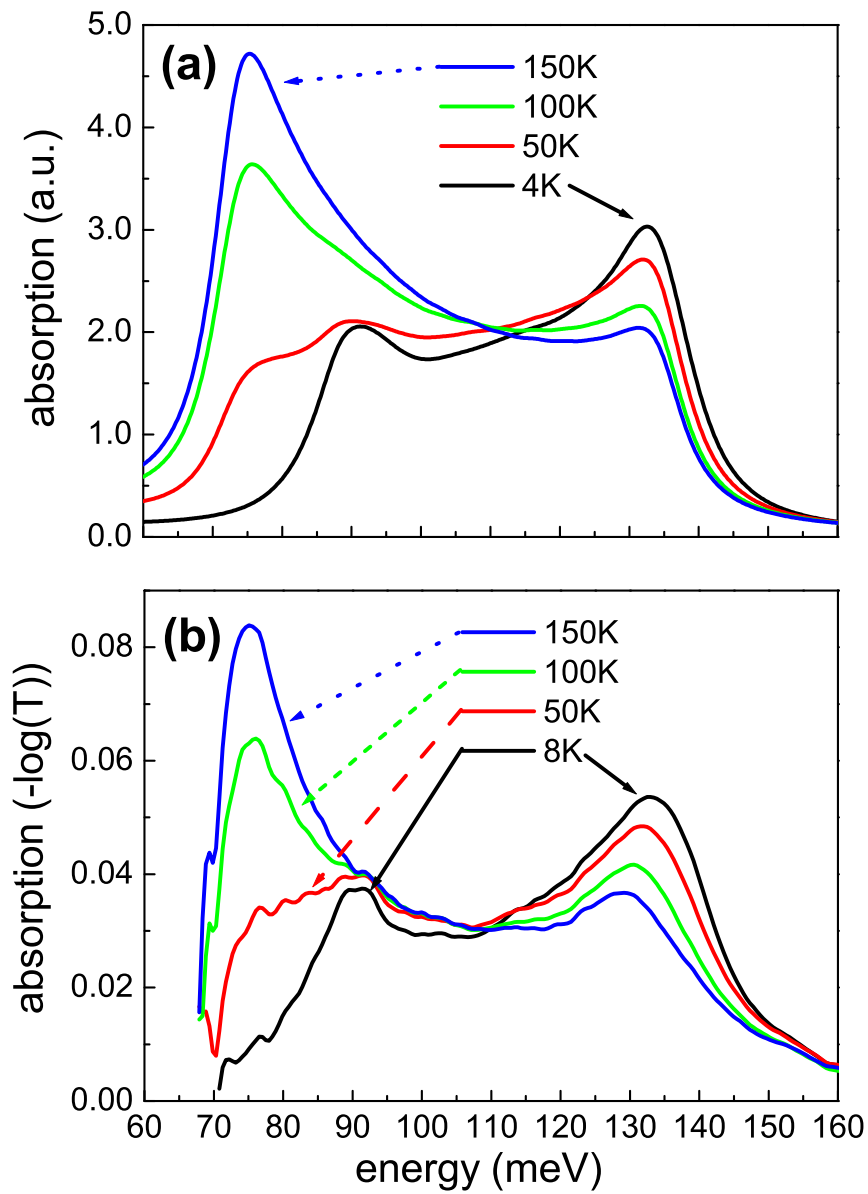


**Figure 3.11:** (a): Calculated infrared absorption spectra of a superlattice for different temperatures as indicated. (b): Experimental infrared absorption spectrum of a GaAs/Al<sub>0.3</sub>Ga<sub>0.7</sub>As superlattice with 9 nm well width and 2.5 nm barrier thickness (G757, see Table 2.1). The cut-off at 70 meV is due to the detector employed in the measurement.

states which can decay into the continuum). Note that this is not an impurity band in the usual meaning (arising from interacting impurity ions), but results from the large number of QWs, just like the miniband. Hence it cannot be decided by simply looking at the experimental spectrum whether the 133 meV peak is a miniband or an impurity transition! The calculation shows that the Fermi energy at  $T=4$  K lies slightly below the bottom of the first miniband. Thus clearly, the appearance of this peak is *not* an indication for the Fermi energy lying in the first miniband, as has been falsely assumed in the past [71]. Also, this peak will *not* disappear, when a metallic sample is driven into an insulating state via a strong magnetic field – a fact which has been observed but not understood in the past [71].

In order to demonstrate the validity of the present calculation also for the case of superlattices, we have measured the interminiband absorption in a GaAs/Al<sub>0.3</sub>Ga<sub>0.7</sub>As superlattice (well width 9 nm, barrier width 2.5 nm, 300 periods), doped with  $n \approx 2 \times 10^{10} \text{ cm}^{-2}$  in the center of each QW (corresponding to a bulk density of  $1.7 \times 10^{16} \text{ cm}^{-3}$ ). The sample has been prepared in a multiple-total-reflection waveguide geometry and the absorption spectra (measured in a Fourier-transform spectrometer) are obtained by normalizing the  $p$ -polarized signal by the  $s$ -polarized one. The result is displayed in Fig. 3.11(b) for different temperatures. Comparison with the theoretical spectra in Fig. 3.11(a) shows an amazing agreement of the lineshapes and their temperature dependence. Low-temperature magnetotransport shows a marginally metallic behavior, with a MIT being induced by magnetic fields above 4 T. This behavior is consistent with an impurity-band metal, where the Fermi energy at low temperature lies in the impurity band [69].

Another experimental proof that at low temperatures all transitions which contribute to the absorption spectrum are due to impurity transitions are magneto-transmission experiments that have been performed previously [72]: In that work a superlattice (well width 7.5 nm, barrier width 2.5 nm) with doping concentration of  $6 \times 10^{16} \text{ cm}^{-3}$  was studied. Magnetotransport experiments revealed a magnetic-field-induced metal-insulator transition in this sample, and far-infrared cyclotron and impurity resonance experiments proved that at  $B > 6$  T the Fermi energy at low temperature was in the impurity band [71]. Interminiband absorption experiments on this sample were performed in a magnetic field along the  $z$ -direction, in a 7 T split-coil magnet optical cryostat equipped with ZnSe windows [72]. Assuming that the Fermi energy drops from the miniband into the impurity band at some magnetic field below 6 T one would expect that the high-energy peak – if ascribed to the  $k_z=0$  interminiband transition – would disappear. However, the resulting spectra, displayed in Fig. 3.12, remain completely unchanged between  $B=0$  and  $B=7$  T. Their shape is similar to Fig.3.11 and 3.9(b), only the energy scale is different due to the different sample parameters. This behavior *can only be explained assuming that the whole spectrum, including the high-energy peak, is due to an impurity transition*. This is a further striking prove of the existence of the above described impurity bands, attached to each miniband.



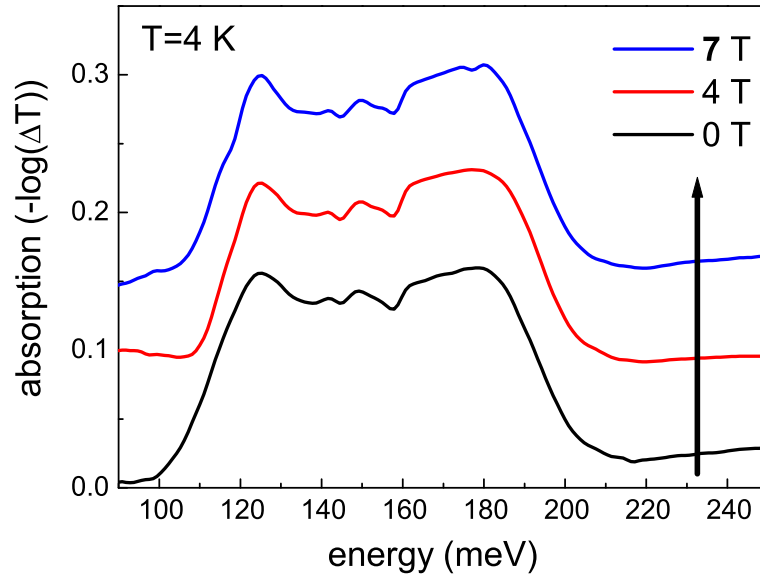


**Figure 3.12:** Absorption spectra of a superlattice for magnetic fields  $B=0, 4,$  and  $7$  T, exhibiting no change with magnetic field.  $\Delta T$  is the ratio of  $p$ - and  $s$ -polarized transmission, the curves are vertically shifted for clarity. The fine structure around  $150$  meV is probably due to some traces of organic solvents on the sample surface and not relevant here.

### 3.7 Summary and outlook

In summary, we have presented a unified theory of confined impurity states in heterostructures, which is able to describe the infrared optical properties of a quantum wells and superlattices treating the quantum well potential and the random impurity potential on the same footing. Calculation of infrared absorption spectra has provided insight into the interplay between impurity and subband states and facilitated the interpretation of experimental data. i.e. the occurrence of impurity bands in the continuum has been demonstrated, explaining experimentally observed spectra. By including electron-electron interaction and/or a magnetic field in the calculation, it should be possible in the future to study the metal-insulator transition as a function of doping density or induced by a magnetic field.



# 4 Ultrafast spectroscopy in the infrared

## 4.1 The Rossendorf Free-Electron Lasers

The linear electron accelerator ELBE, located at the Forschungszentrum Dresden-Rossendorf, delivers electrons with energies up to 36<sup>1</sup> MeV with an electron bunch charge of up to 77 pC. Since it consists of superconducting rf-acceleration cavities, it can deliver these electrons at a high repetition rate, which is usually set to 13 MHz. The relativistic electrons are used directly in nuclear physics experiments or to generate secondary radiation such as x-rays, positrons and neutrons. However, its main application is the operation of the free-electron laser (FEL). To cover a large wavelength-range in the infrared, two FELs have been realized. Since the FEL was used for time-resolved experiments for the first time within this thesis, in this section we will discuss the main working mechanism of an FEL, followed by a full characterization of the optical pulses, including the available wavelength-range, the temporal shape of single IR-pulses and the spatial profile of the IR-beam used in the experiments.

### 4.1.1 Working principle

Free-electron lasers differ from conventional lasers in several ways. Usually lasers consist of a gain medium, which generates stimulated emission of coherent light under strong optical or electrical excitation and an optical cavity which acts as a resonator [73]. In FELs this gain medium is replaced by a relativistic electron beam and the stimulated emission does not occur on transitions between bound electron states like in solid-state or gas lasers, but upon the interaction of the free electrons generated by an accelerator with a spatially periodic magnetic field, the so-called *undulator*. This is schematically shown in Fig. 4.1. By entering the periodic magnetic potential  $\mathbf{B} = \hat{\mathbf{y}}B \cos \frac{2\pi z}{\lambda_u}$ , which is provided by a row of alternately poled magnets in  $z$ -direction, the relativistic electrons start to perform a *wiggling* motion transverse to the magnetic field due to the Lorentz force. This phenomenon is widely used to generate synchrotron radiation.

The wavelength of the emitted radiation is determined by the energy of the relativistic electrons,  $\gamma m_e c^2$  where  $\gamma = (1 - (v/c)^2)^{-\frac{1}{2}}$ , and by the undulator parameters, in particular its period  $\lambda_u$ . This is also known as the resonance condition (for details see various

---

<sup>1</sup>This is valid only at a reduced repetition rate. At a repetition rate of 13 MHz, the maximum electron energy is 33 MeV.

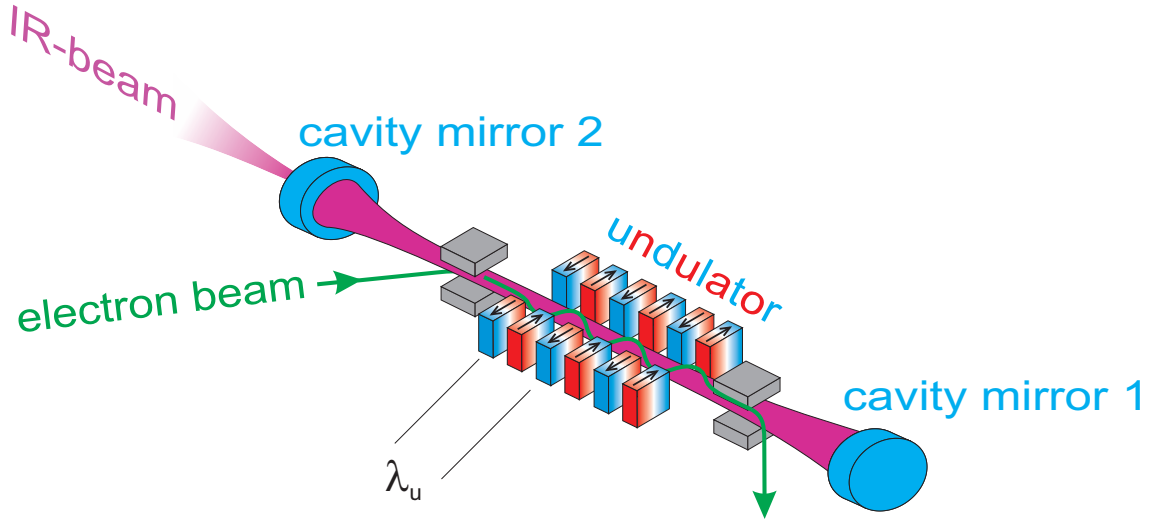


**Figure 4.1:** Schematic of an FEL oscillator. After acceleration of the electron bunches to relativistic energies, they are injected into a spatially periodic magnetic field, the undulator. The emitted radiation, caused by the wiggling motion of the electrons due to the magnetic field forces, is amplified by successive electron bunches during several round trips between the cavity mirrors. One cavity mirror contains a small hole (1.5 - 7 mm) to couple out a certain amount of the radiation inside the cavity.

textbooks, such as [74, 75, 76])

$$\lambda_0 = \frac{\lambda_u}{2\gamma^2} \left( 1 + \frac{K^2}{2} \right) \quad (4.1)$$

where  $K$  is the dimensionless undulator parameter

$$K = \frac{\lambda_u e B}{2\pi m_e c}$$

Here we see that FELs, in contrast to conventional lasers, can have a large tuning range, simply by variation of the electron energy and strength of the magnetic field. At a given wavelength  $\lambda_0$ , Eqn.(4.1) also determines the *resonance energy*  $\gamma_r m_e c^2$  of the electrons:

$$\gamma_r^2 = \frac{\lambda_u}{2\lambda_0} \left( 1 + \frac{K^2}{2} \right)$$

For later purpose we define  $\Delta\gamma$  as the energy detuning from the resonance energy:

$$\gamma = \gamma_r + \Delta\gamma \quad \text{and} \quad \Delta\gamma \ll \gamma_r$$

The working principle of the gain mechanism can be understood by a Lorentz transformation to the rest frame of the electrons in a fully classical way, corresponding to a periodic pendulum [74, 75]. In this frame the undulator acts as an electromagnetic wave propagating towards the electrons and leads to Compton scattering in backward direction with the frequency

$$\omega' = \gamma \frac{2\pi c}{\lambda_u}.$$

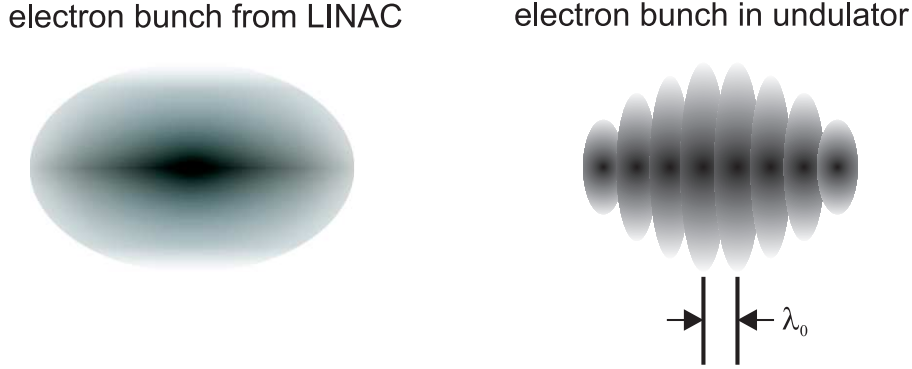


**Figure 4.2:** Principle of microbunching of the electron bunch inside the undulator, leading to a coherent buildup of radiation of subsequent bunches.

Transforming back into the laboratory frame, this emitted wave appears with a Doppler-shift:

$$\omega'' = 2\gamma\omega' = 2\gamma^2 \frac{2\pi c}{\lambda_u}; \quad \lambda_0 = \frac{\lambda_u}{2\gamma^2} \quad (4.2)$$

In the electron frame, the scattered wave and the original undulator wave combine to form a standing wave pattern. The ponderomotive force of this standing wave pattern influences the spatial distribution of the electrons and leads to the formation of microbunches, giving rise to enhanced stimulated scattering. The microbunch-spacing equals the radiation wavelength, ensuring that the radiation generated by an electron bunch adds *coherently* to the radiation generated by another bunch. This process, taking place in the undulator, is schematically shown in Fig. 4.2.

The gain inside an undulator was found to be the first derivative of the spontaneous emission. It was first described by Madey [77] and is depicted in Fig. 4.3.

The intensity of the spontaneous emission at  $\omega_0 = 2\pi \frac{c}{\lambda_0}$  at a fixed electron energy reads [74]

$$I(\Delta\omega) \propto \left[ \frac{\sin\left(\pi N_u \frac{\Delta\omega}{\omega_0}\right)}{\pi N_u \frac{\Delta\omega}{\omega_0}} \right]^2 = \text{sinc}\left(\pi N_u \frac{\Delta\omega}{\omega_0}\right) \quad (4.3)$$

Note that the *width* of the spontaneous emission is inversely proportional to the number of undulator periods  $N_u$ . According to Eqn.(4.2) we can transform the argument in Eqn.(4.3) into

$$\pi N_u \frac{\Delta\omega}{\omega_0} = \frac{2\pi N_u}{\gamma} \Delta\gamma$$

The spontaneous emission, depending on  $\Delta\gamma$ , is schematically illustrated in Fig. 4.3(a). Its first derivative after  $\Delta\gamma$ , the gain, is depicted in 4.3(b), showing an asymmetric curve around the resonance energy. Due to this asymmetric gain curve the wavelength of the resulting radiation is slightly larger than the original resonance wavelength, since only the long-wavelength part of the spontaneous emission gives rise to stimulated emission. The shorter-wavelength part will be absorbed from the electrons in successive round trips inside the optical cavity. In general it should be mentioned that the main advantage of

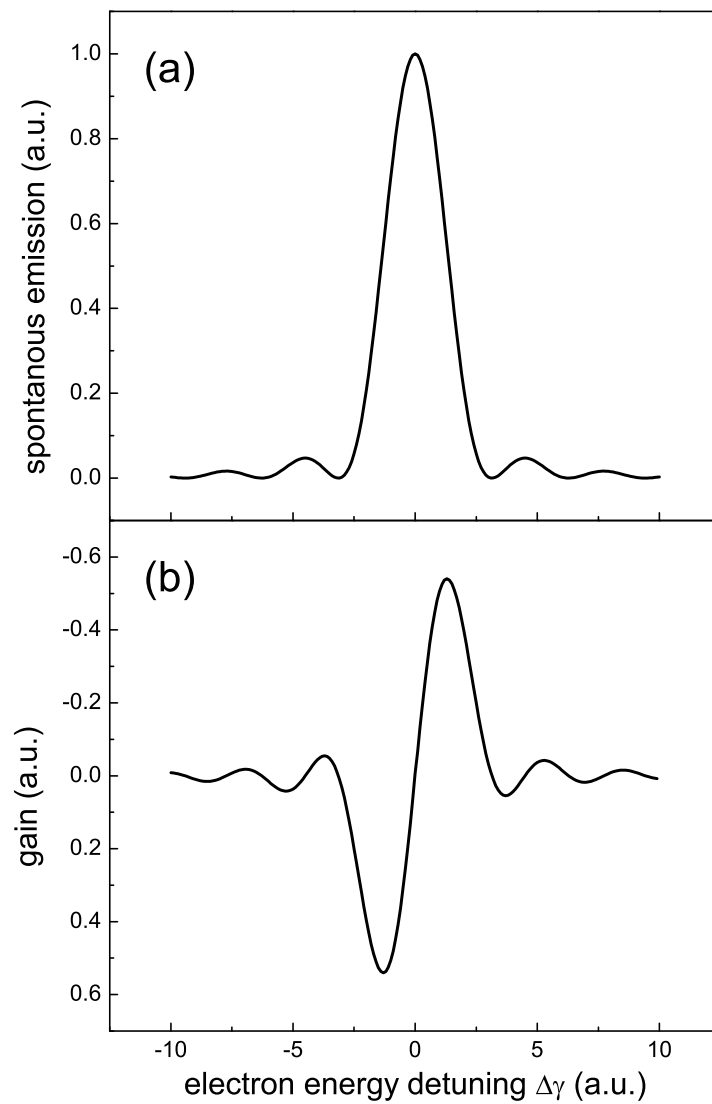


**Figure 4.3:** (a) Spontaneous emission around the resonance energy inside the undulator and (b) its associated gain curve. Note that there is no gain directly at the resonance energy (or resonance wavelength, respectively).

the free-electron laser is that it can, in principle, operate at any wavelength, simply by suitable choice of the parameters in Eqn.(4.1). Since there is no "real" gain medium as for instance in solid state lasers, a very powerful output can be generated, because the electron beam can carry a high energy load without the risks of damaging the laser medium or of too much power dissipation in the laser structure. However, powerful FELs require state-of-the art rf-linacs with a high brilliance and high electron bunch charges.

#### 4.1.2 Slippage effect and cavity detuning

Due to the different velocities of the electromagnetic light wave and the electron beam, the positions of the electron microbunches shift continuously along the undulator with respect to the travelling wave. It can be shown [78] that this shift ( $\Delta z$ ) equals one wavelength  $\lambda_0$  per undulator period of the length  $L$ :

$$\Delta z \approx L/(2\gamma^2) = \lambda_0$$

Thus, at the end of an undulator with  $N$  periods, the electromagnetic wave is  $N\lambda_0$  ahead of the electron bunch, which we define as the *slippage* distance  $L_s$ . Note that the slippage effect is very important for the coherent buildup of microbunching [79, 80]. The result of slippage is that each electron interacts only with a portion of the radiation field of length  $L_s$ , while each position of the propagating wave field is in turn influenced by electrons in a length  $L_s$  of the electron beam. For the buildup of radiation inside the undulator the length of the electron bunch now becomes important. In case that the electron bunch is long compared to the slippage distance, a large part of the optical pulse develops as if the electron beam were continuous. However, at the beginning and the end there will be portions of the pulse that do not overlap along the complete transit through the undulator. The front of the optical pulse interacts with electrons only at the beginning, while its trailing edge is influenced only by the last electrons just before they leave the undulator. By use of an optical cavity, where the optical pulse undergoes several round trips and is amplified by fresh electrons, these end-effects accumulate and become noticeable even for electron bunches that are much shorter than the slippage length.

In combination with the buildup of microbunching during the transit through the undulator, which influences strongly the gain<sup>2</sup>, these end effects lead to the fact that mostly the rear of the optical pulse gets amplified. The leading part does not grow in successive round trips. However, this lack of gain can partly be compensated by a slight *shortening* of the optical cavity, so-called *cavity detuning*. That is, instead of adjusting the optical cavity length in such a way that the round trip time of the optical pulses exactly matches the repetition time of the electron pulses, the length of the optical cavity is decreased by a small amount  $\Delta L_{cav}$  from its synchronous value.

<sup>2</sup>The undulator gain depends also on the density of the electron bunch. Due to its pulsed structure a microbunched electron bunch has a much higher gain than a homogeneous bunch since the peak electron density is much higher.

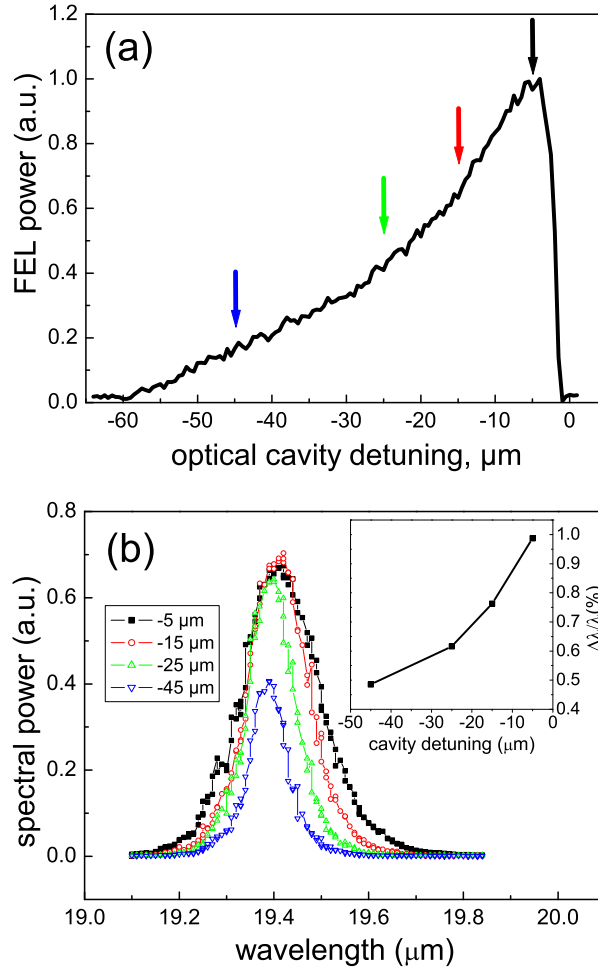


**Figure 4.4:** (a) Detuning curve of the undulator U27 at a lasing wavelength of  $19.4 \mu\text{m}$ . (b) Wavelength spectra at different cavity detuning; Inset: spectral width for different detuning points.

Thus, the optical pulse arrives on its second trip at the entrance of the undulator with a small offset with respect to the electron pulse. In this way the part of the optical pulse that had only small or no gain is now in front of the electron pulse in the next round trips. Then the electron pulse experiences a larger optical field already in the beginning of the undulator. This leads to improved microbunching and the optical pulse can grow further without its maximum getting continuously shifted backward. In addition, the combination of a reduced group velocity and a slightly shorter cavity-length leads to an effective synchronism between the optical and electron pulses, and the optical pulse can develop into a stable shape that grows uniformly[79].

It is predicted that the FEL reaches its highest saturated intensity at a cavity length that is only slightly ( $\Delta L_{\text{cav}} \approx -\lambda_0/5$ ) detuned from the synchronous value [81], while the highest net gain per pass occurs around  $-\lambda_0$ . However, the operation at larger cavity detuning



leads to a very stable operation since the micropulse energy saturates quickly [79]. This behavior was observed with both FELs at ELBE. In Fig. 4.4 the detuning curve of the U27 at a lasing wavelength of  $19.8 \mu\text{m}$  and the respective optical spectra are shown: Fig. 4.4(a) shows the average power of the FEL for different detunings of the optical cavity. As expected, within a fraction of the wavelength,  $\Delta L_{\text{cav}} \approx -\lambda_0/5 = -4 \mu\text{m}$  the FEL power increases rapidly and drops slowly towards extinction at a detuning of  $-60 \mu\text{m}$ . At the indicated points of the detuning curve, the optical spectrum has been measured with a grating spectrometer; the results are shown in Fig. 4.4(b). It can clearly be seen that the spectral width is reduced with increased shortening of the cavity length, which will be discussed later.

### 4.1.3 Characteristics of the FEL radiation

In this section we will discuss the main parameters of the FEL radiation used in the further experiments. First of all, this will be the determination of the optical pulse length and simultaneous measurement of the spectrum. While for the latter only a grating spectrometer with appropriate detectors and gratings is needed, the measurements of the optical pulse length was performed with a non-collinear second-order autocorrelator [82, 83].

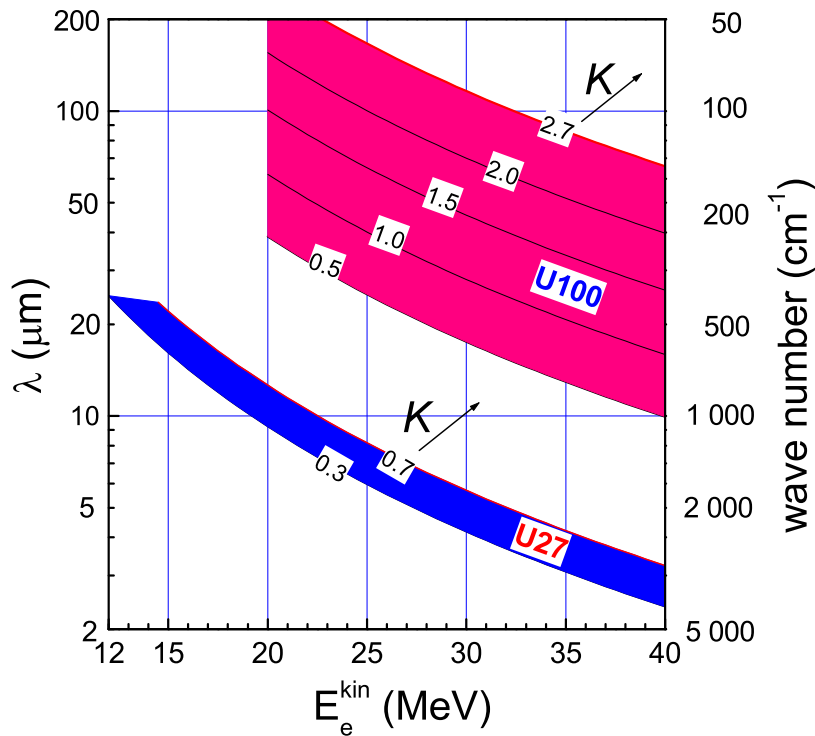


**Figure 4.5:** Schematic of the accessible wavelength range of the two undulators U27 (lower part) and U100 (upper part) for different electron energies and  $K$ -parameters as indicated.

In order to cover a wide wavelength range, there are two different undulators available for

operation, undulators U27 and U100, respectively. The number specifies the undulator period in mm, their complete specifications are listed in Table 4.1. From these values and the electron energies which are available one can now estimate the operation range of the FELs according to Eqn.(4.1). The results are shown in Fig. 4.5. From this graph we find that with the undulator U27 wavelengths ranging from 3 to 22  $\mu\text{m}$  should be possible, while the U100 covers a large range from 20  $\mu\text{m}$  up to 200  $\mu\text{m}$ .

After its first lasing in May 2004 [84], the properties of the U27 have been investigated intensively with respect to the tuning range and its pulse lengths [85]. By variation of the

		U27	U100
Undulator period	$\lambda_u$	27.3 mm	100 mm
Number of periods	$N_u$	$2 \times 34$	38
Undulator parameter	K	0.3-0.7	0.5-2.7

**Table 4.1:** Specifications of the undulators U27 and U100.

electron energy between 15 and 33 MeV and the undulator parameter, the U27 today can continuously be tuned between 3  $\mu\text{m}$  and 22  $\mu\text{m}$ <sup>3</sup>, which is illustrated in Fig. 4.6. The energy of the optical pulses reaches up to 1  $\mu\text{J}$  (depending on the wavelength), yielding in an average optical power of 13 Watts. The pulse length measurements have been performed at a wavelength of 11  $\mu\text{m}$ .

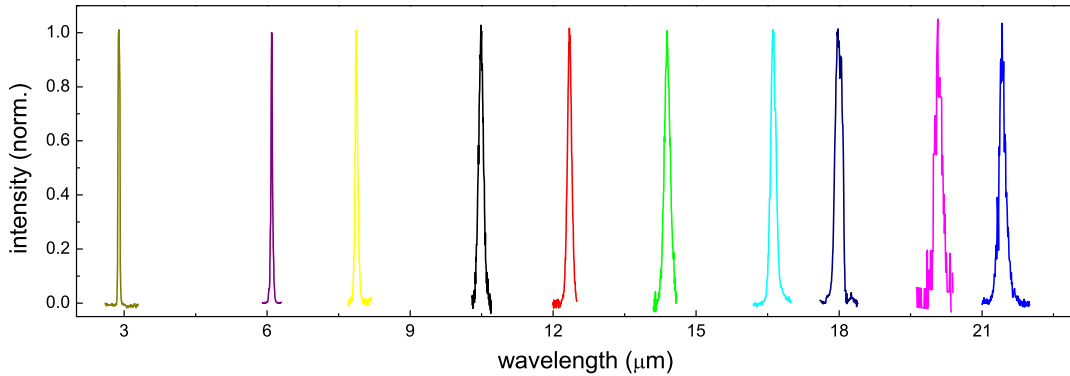


**Figure 4.6:** Wavelength range of undulator U27. The spectrum spans from 3  $\mu\text{m}$  up to 22  $\mu\text{m}$ .

The setup for the pulse-length measurements, based on second harmonic generation (SHG), is schematically shown in Fig. 4.7. The original FEL pulse first passes a beamsplitter, yielding two synchronous pulses with equal intensity. While one of the pulses is directly focused onto the nonlinear crystal, where the second harmonic of the incoming radiation is generated, the second pulse undergoes an adjustable time delay. This time delay is realized

<sup>3</sup>Note that for a larger tuning range one would need a stronger magnetic field, which – with nowadays available permanent magnets – would lead to a too small undulator gap for the infrared radiation.

by a mechanical translation stage that can precisely move a retroreflector back and forth. By control of the mirror position the arrival time of the second pulse on the crystal with respect to the first can be selected. Once both pulses arrive at the same time at the crystal (or significantly overlap in time), apart from the two pulses a third beam is generated, containing only the SHG-wavelength, which propagates in the direction between the two original beams ( $\mathbf{k}_{\text{SHG}} = \mathbf{k}_1 + \mathbf{k}_2$ ). This effect relies on the conservation of energy *and momentum* in the SHG-process. The advantage of the non-collinear beam alignment is that the SHG-signal can be detected background-free. In addition it is very common to place an aperture and an additional short-pass filter in front of the detector to reduce the noise during a measurement. The principle described above is basically applicable for

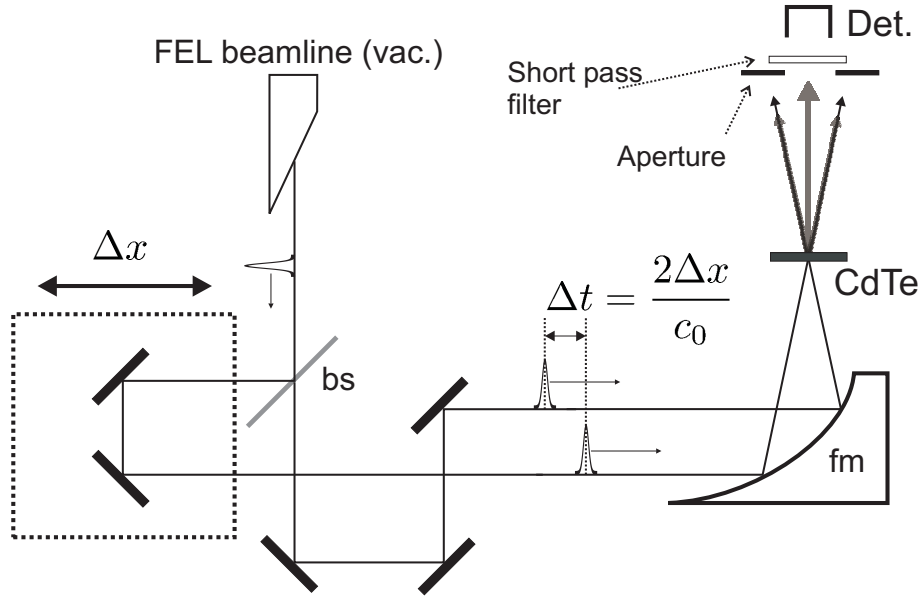


**Figure 4.7:** Schematic of the setup used for the autocorrelation measurements; fm=focusing mirror, bs=beamsplitter.

all wavelengths (from ultraviolet to the far-infrared), however, a nonlinear crystal that meets the wavelength-specific requirements (transparency, high nonlinear coefficient) has to be found. In all our experiments measuring the pulse length, a  $z$ -cut (non-birefringent) CdTe-crystal has been used [86]. It has a wide transparency range (1-35  $\mu\text{m}$ )[87] and a very high damage threshold, making it suitable for pulse-length measurements of a high power and tunable infrared light source such as the FEL.

The second-order intensity autocorrelation of an electric field is given by

$$A(\Delta t) = \int_{-\infty}^{\infty} E^2(t)E^2(t - \Delta t)dt = \int_{-\infty}^{\infty} I(t)I(t - \Delta t)dt \quad (4.4)$$

Note that  $A(\Delta t)$  is symmetric in time, which can simply be seen by the substitution  $t = t' + \Delta t$ , and we find

$$\int_{-\infty}^{\infty} I(t)I(t - \Delta t)dt = \int_{-\infty}^{\infty} I(t')I(t' + \Delta t)dt'$$

	Gaussian pulse shape	Hyperbolic secant pulse shape
$I(t)$	$e^{\left(-2\sqrt{\ln(2)}\frac{t}{\tau_{pulse}}\right)^2}$	$\text{sech}^2\left(\frac{1.7627t}{\tau_{pulse}}\right)=1/\cosh^2\left(\frac{1.7627t}{\tau_{pulse}}\right)$
$A(\tau_{AC})$	$e^{\left(-2\sqrt{\ln(2)}\frac{t}{\tau_{AC}}\right)^2}$	$\frac{-3(\tau_{AC}\coth(\tau_{AC})-1)}{\sinh^2(\tau_{AC})}$
$\tau_{AC}/\tau_{pulse}$	$\sqrt{2}$	1.54
$\tau_{pulse}\Delta\nu$	0.441	0.315

**Table 4.2:** Characteristics of Gaussian and  $\text{sech}^2$  pulses: from top to bottom: intensity  $I(t)$ , autocorrelation function  $A(\tau_{AC})$ , ratio of the autocorrelation length and the pulse length (FWHM)  $\tau_{AC}/\tau_{pulse}$ , and time-bandwidth-product for transform limited pulses  $\tau_{pulse}\Delta\nu$ .  $\tau_{pulse}$  represents the FWHM of the optical pulse.

Due to the fact that the autocorrelation function is always symmetric, this method lacks the possibility to fully characterize the temporal shape of the FEL pulse, with respect to its phase and possible temporal asymmetry. However, from its shape one can define its intrinsic intensity profile to some extent. Usually ultrashort lasers deliver either Gaussian or  $\text{sech}^2$  pulses. Their characteristics are listed in Table 4.2.

The results of the pulse-length measurements at 11  $\mu\text{m}$  for different detuning of the optical cavity are shown in Fig. 4.8 (left hand side). On the right side the corresponding power spectra are shown. The shortest pulse length is measured at a small cavity detuning of only  $-1 \mu\text{m}$ . The autocorrelation trace has a FWHM of 1.74 ps, corresponding to a pulse length of 1.23 ps, if a Gaussian pulse shape is assumed. The solid lines in the autocorrelation traces represent a best fit with a Gaussian pulse (compare Table 4.2). The power spectrum has a relative width ( $\Delta\lambda/\lambda$ ) of about 1.2%, yielding a time-bandwidth product of  $\tau\Delta\nu = 0.4$ , which lies in between the values of a transform-limited Gaussian (0.441) and a  $\text{sech}^2$  pulse (0.315). However, it is closer to the Gaussian value. With further increase of the cavity detuning, the optical pulse clearly becomes longer, and reaches a duration of 2.4 ps for  $\Delta L = -10 \mu\text{m}$ . Since the FEL was not operating at longer detuning, we could not go to longer pulse lengths. However, it has been shown before that at large cavity detuning, the optical pulses become significantly longer [79]. The reason for this is that at large detuning values the optical pulse is quickly driven away from the electron bunch in successive round trips (see Sec.(4.1.2)), and is exactly the reason for the observed lengthening of the optical pulse. In addition, at large detunings, the FEL reaches its power-saturation level very quickly, which is low compared to small a detuning (compare Fig. 4.4).

As already observed in Fig. 4.4, with larger detuning the spectral width of the optical pulses decreases, while the pulse length increases.

With the pulse length and the spectral width measured simultaneously, it is possible to calculate the time-bandwidth product over the detuning range. Fig. 4.9 shows the results of

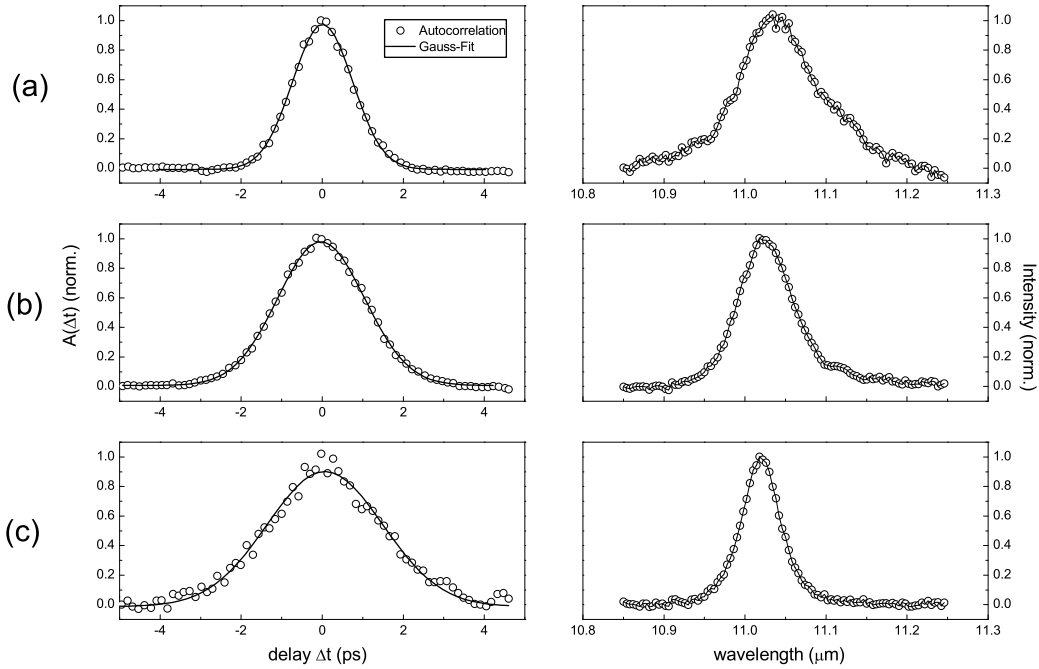


**Figure 4.8:** Second-order autocorrelation traces (left) with their respective power spectra (right), recorded for three different detuning of the optical cavity: (a)  $\Delta L = -1 \mu\text{m}$ , (b)  $\Delta L = -4 \mu\text{m}$ , (c)  $\Delta L = -10 \mu\text{m}$ . The solid lines represent a best fit of the autocorrelation traces with a Gaussian pulse. The derived pulse durations from (a) to (c) are 1.23 ps, 1.78 ps, and 2.37 ps, respectively.

a measurement series taken over a broad detuning range ( $\Delta L \approx [0..3\lambda]^4$ ). At a very short detuning value we determine a time-bandwidth product (TBP) of 0.46 which is very close the transform-limit of a Gaussian pulse. With increasing detuning, the TBP slightly rises and eventually drops continuously towards larger detuning, with its last value being close to a transform-limited  $\text{sech}^2$ -pulse. This is an interesting behavior and has been observed in FELs in a similar way before [79]. However, it is worth mentioning that the quality of the obtained autocorrelation traces drastically drops towards large cavity detuning, since second harmonic generation is a  $\chi^{(2)}$ -process and thus depends quadratically on the optical intensity. Not only the drop of average power, but also the reduced *peak*-intensity (due to longer pulses) reduces the signal-to-noise ratio in this regime significantly. Therefore, at large cavity detuning, it is not possible to distinguish between a Gaussian or  $\text{sech}^2$ -pulse, although the latter is indicated from the TBP-perspective. Another effect leading to the reduced TBP might be the presence of chirped optical pulses, i.e. that the different frequencies inside an optical pulse do not have the same phase. While this effect might be generated by large cavity detunings, it is again not possible to make a precise statement on this since the employed autocorrelation technique always measures symmetrical traces. However, in other FEL facilities an asymmetrical pulse-shape has been observed at large

<sup>4</sup>The shortest pulse length is now longer than in the previous measurements, however, this FEL configuration allowed a longer cavity detuning.

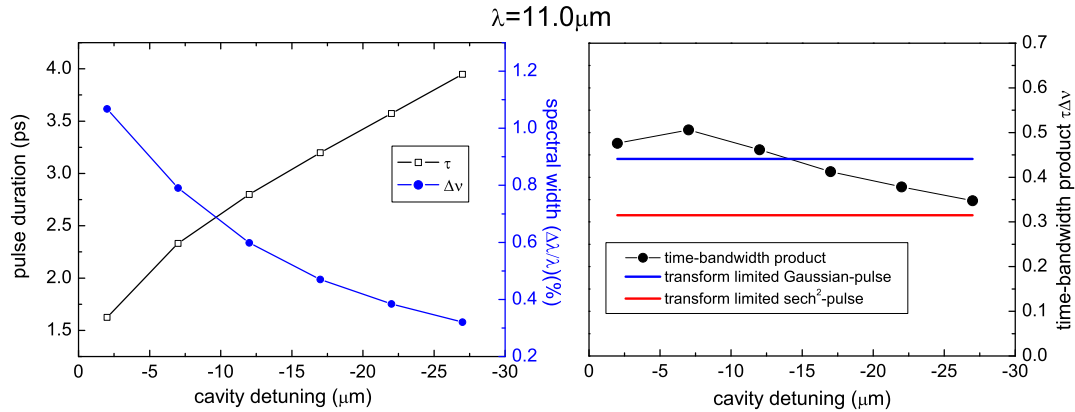


**Figure 4.9:** Optical pulse lengths and spectral widths measured at a lasing wavelength of 11 μm for different cavity detuning (left), and the resulting time-bandwidth product  $\tau\Delta\nu$  (right), assuming a Gaussian pulse. The time-bandwidth-product of transform limited Gaussian and  $\text{sech}^2$  pulses are shown as constants.

cavity-detunings [88, 89], measured with a different technique.

### Shortest optical pulse from FELBE

The ELBE accelerator is equipped with a special element, the so called "chicanery". This element, inserted in the beamline of the relativistic electrons, is able to manipulate the phase space of the electrons [90]. Virtually speaking, with the chicanery it is possible to turn the electron bunch by 90 degrees from a horizontal to a vertical standing ellipse. Thus it makes the electron bunch shorter in time and also with respect to the  $z$ -axis in the undulator. Shorter electron pulses are capable of producing also shorter optical pulses in the FEL.

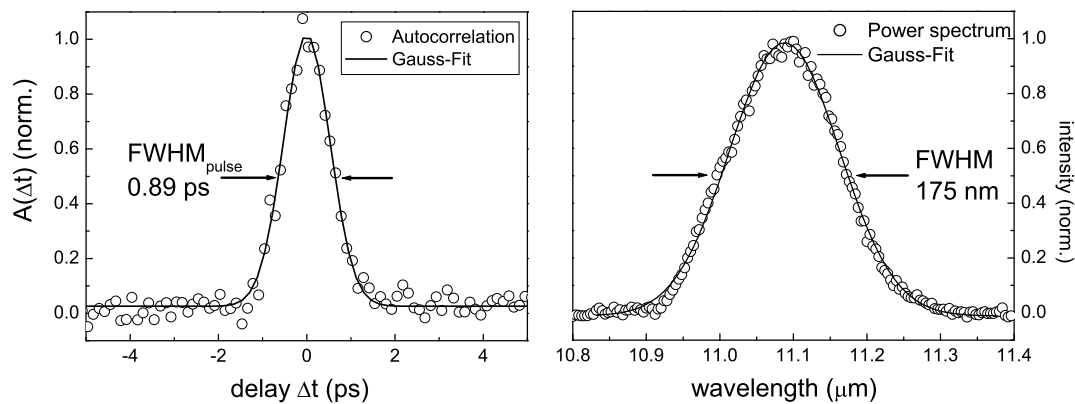


**Figure 4.10:** Autocorrelation (left) of the shortest measured optical pulse and its power spectrum (right) at 11 μm by use of the chicanery in the electron beam path.

In this experiment, first the duration of the electron pulses has been minimized by use of a Martin-Puplett-Interferometer[91]. Subsequently, the shortest electron pulses were fed into the FEL. And in fact, with these optimized electron pulses, the shortest optical pulses with a duration of less than one picosecond could be generated. While this work's aim is not the investigation of this phenomenon, we will only present its results, which are shown in Fig. 4.10. The autocorrelation trace and the power spectrum can be fitted with a Gaussian very well, and the resulting TBP of 0.38 indicates again operation close to the Fourier-limit.

In August 2006 first lasing was demonstrated with the second undulator U100 installed at ELBE. Due to the increased wavelength range (20-200  $\mu\text{m}$ ), the optical resonator of the U100 consists of a partial waveguide, ensuring good overlap with the electron bunches even for very long wavelengths, where free propagating modes (as used for the U27) would be spatially too large, leading to large intrinsic undulator gaps. Hence, without the vertical waveguide one would need much stronger magnetic fields, eventually reducing the accessible wavelength range. A cartoon of the optical cavity of the U100 is shown in Fig. 4.11.

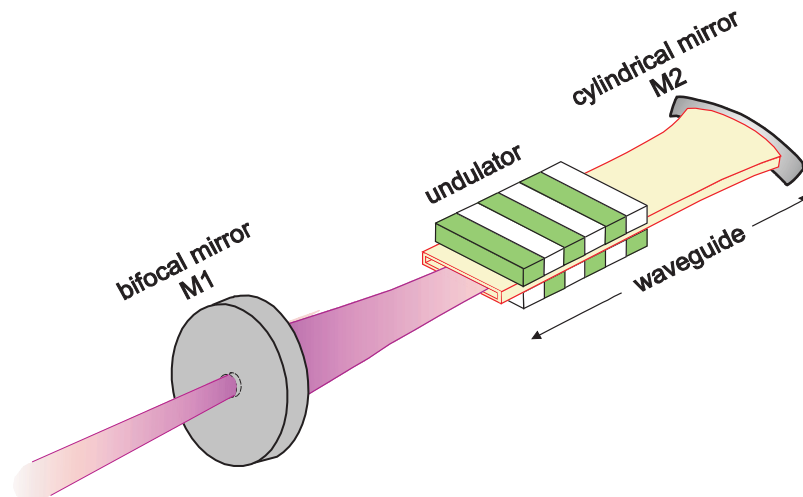


**Figure 4.11:** Schematic of the optical cavity of the long-wavelength undulator U100, consisting of a partial waveguide, a cylindrical mirror and a bifocal mirror.

Since its first lasing the U100 had five weeks of operation, and thus such an extensive characterization as for the U27 could not be performed yet. Lasing was demonstrated from 20  $\mu\text{m}$  up to 200  $\mu\text{m}$  (compare Fig. 4.12).

The average optical power achieved in quasi-cw mode is in the order of 10 W, throughout all available wavelengths<sup>5</sup>, yielding pulse energies of the micro pulses of up to 1  $\mu\text{J}$ . Due to the lack of an appropriate nonlinear crystal at the longest wavelengths, the time structure of the micro-pulses has been investigated at a wavelength of 24  $\mu\text{m}$ . For these measurements the same setup as described before was used, however, different filters and detectors

<sup>5</sup>For wavelengths above 150  $\mu\text{m}$  the power gradually drops towards about 1 W.

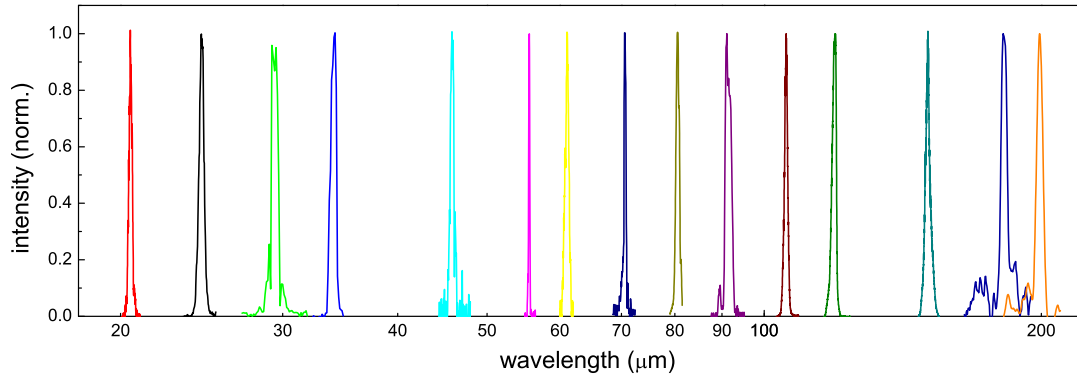


**Figure 4.12:** Wavelengths that have been generated by the U100.

were chosen. The fundamental wavelength was blocked by bulk ZnSe (thickness 3 mm), while the SHG signal was recorded again with a liquid-nitrogen-cooled HgCdTe-detector (*Judson-J15D16-M204-S01M-60*) with a cutoff-wavelength of 16  $\mu\text{m}$ .

First, an autocorrelation trace was recorded at a small cavity detuning of only  $\Delta L = -2 \mu\text{m}$  and a pulse energy of 0.37  $\mu\text{J}$ , which is depicted in Fig. 4.13. The measured data

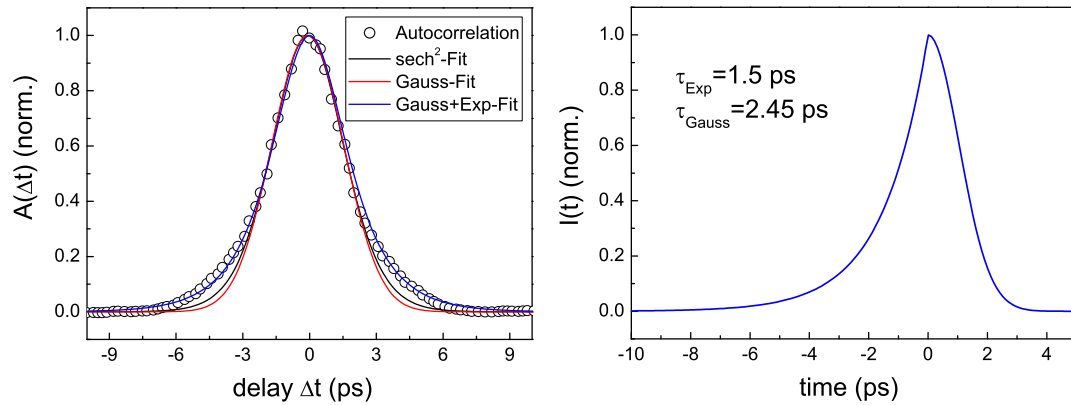


**Figure 4.13:** Second-order autocorrelation trace of the U100 at a wavelength of 24  $\mu\text{m}$  (left hand side). The open circles represent the measured signal, while the full lines are fits assuming a gaussian pulse (red), a  $\text{sech}^2$ -pulse (black), and a combination of a Gaussian pulse with an exponential rising pulse (blue). The figure on the right plots the time-evolution of the Gaussian-exponential-pulse with its best fit parameters for the measured autocorrelation.

are given by open circles, while the full lines represent various fits. A few picoseconds away from zero time-delay, Gaussian and  $\text{sech}^2$ -pulses do not show an acceptable overlap with the measured curve, although the latter agrees slightly better. In other FEL facilities (Stanford FEL, FELIX), it has been observed (by a cross-correlation experiment with an additional synchronized near-infrared laser with a pulse duration of only 10 femtoseconds), that the optical pulses generated by an FEL have an asymmetric time dependency [88]. In fact, it was found that the pulses rise exponentially, while it decays like a regular Gaussian



pulse:

$$I(t) = \begin{cases} e^{\frac{-t}{\tau_{exp}}} & \text{for } t < 0 \\ e^{\left(-\frac{2\sqrt{\ln(2)t}}{\tau_{pulse}}\right)^2} & \text{for } t > 0 \end{cases} \quad (4.5)$$

The temporal profile of such a pulse is shown in the right hand side of Fig. 4.13. It has an exponential rise-time of 1.5 ps and a Gaussian pulse width of 2.45 ps. The autocorrelation of this pulse has been calculated and is shown as the blue solid line in Fig. 4.13 (left). It clearly shows a better agreement with the observed autocorrelation signal than a Gaussian or  $\text{sech}^2$  fit. Although this is not a clear evidence for such a pulse shape, the comparison with data from other infrared FELs gives a strong indication that this is most likely the case. However, to solve this question also cross-correlation experiments have to be performed. The pulse length (FWHM) that can be deduced from the autocorrelation, is then 2.27 ps. However, it is not convenient for a quick estimate of the pulse length, since it includes two individual time-constants. Therefore, since the fit with a  $\text{sech}^2$ -pulse gives better agreement than a Gaussian, we deduce the pulse length from the autocorrelation by assuming this pulse shape. In this case, a pulse duration of 2.47 ps can be extracted. As was done for the U27, a series of autocorrelation traces was recorded for different cavity detuning ( $\Delta L = -[2..24] \mu\text{m}$ ) simultaneously to its power spectrum. The results are shown in Fig. 4.14 for  $\Delta L = -2 \mu\text{m}$  (a),  $\Delta L = -14 \mu\text{m}$  (b), and  $\Delta L = -24 \mu\text{m}$  (c).

The autocorrelation traces were fitted with a  $\text{sech}^2$ -pulse, and (apart from Fig. 4.14(a)) showed good agreement with the measured data. As observed for the U27, by increasing the cavity detuning, the pulses become longer (up to 5.85 ps at  $\Delta L = -24 \mu\text{m}$ ), while simultaneously the power spectrum narrows. This behavior is in agreement with the data obtained at the U27. The time-bandwidth product was then extracted from these measurements and was calculated from assumption of a Gaussian and  $\text{sech}^2$ -pulse. The result is shown in Fig. 4.15 for different cavity detuning.

The TBP first rises with increasing cavity detuning and eventually drops towards the long detuning values. Comparing the obtained values to ideally transform-limited Gaussian and  $\text{sech}^2$  pulses one finds that the calculated data show better agreement if we assume a Gaussian pulse. Especially at the largest detuning it almost perfectly matches its ideal value. However, these values are calculated in assumption of a symmetrical pulse, which might not be the case, and thus it is difficult to make a final statement about the actual pulse shape. The results must be confirmed with a different technique such as electro-optic sampling [88].

The bottomline of the pulse-length measurement is, that we obtain pulse lengths on the order of 1-4 ps of the U27 at 11  $\mu\text{m}$  and 2-6 ps for the U100 at 24  $\mu\text{m}$  in regular operation. Incorporating the chicanery gives the possibility to reduce the pulse-length additionally to some extent, however, its operation has proven not trivial and additionally the duration of the electron bunches has to be monitored simultaneously. In all measurements we have

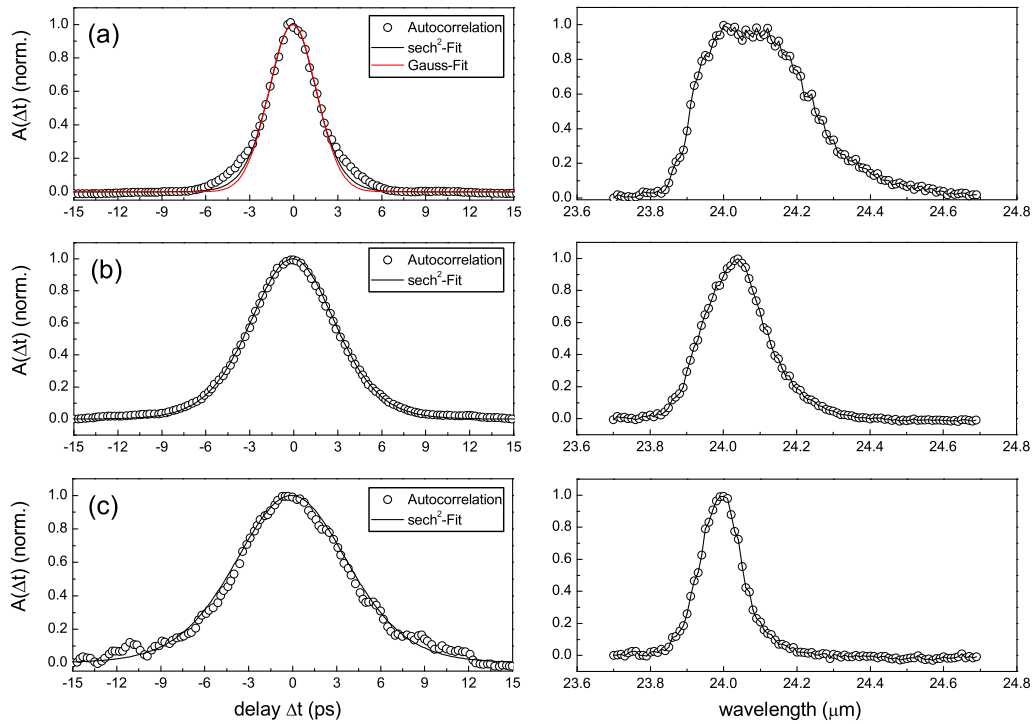


**Figure 4.14:** Second-order autocorrelation traces (left) with their respective power spectra (right) of the U100, recorded for three different detuning of the optical cavity: (a)  $\Delta L = -2 \mu\text{m}$ , (b)  $\Delta L = -14 \mu\text{m}$ , (c)  $\Delta L = -24 \mu\text{m}$ . The solid lines represent a best fit of the autocorrelation traces with a sech<sup>2</sup> pulse. The derived pulse durations (assuming a sech<sup>2</sup>-pulse) from (a) to (c) are 2.47 ps, 4.42 ps, and 5.85 ps, respectively.

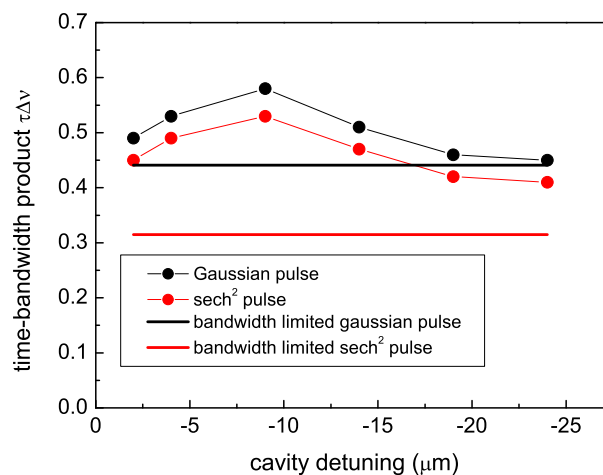


**Figure 4.15:** Calculated time-bandwidth product at 24  $\mu\text{m}$  at different cavity detuning. A Gaussian pulse (black) and a sech<sup>2</sup> pulse (red) was used to extract the pulse length  $\Delta\tau$  from the FWHM of the second order autocorrelation. The time-bandwidth products of transform-limited Gaussian and sech<sup>2</sup> pulses are drawn as constants.

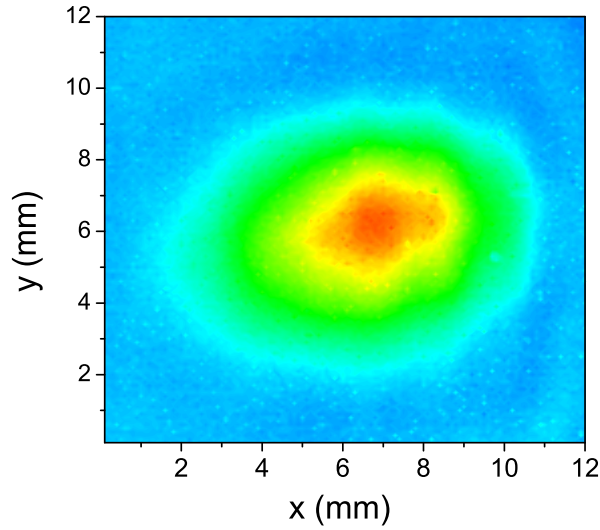


**Figure 4.16:** Spatial profile of the FEL recorded at a wavelength of  $11 \mu\text{m}$ .

observed a narrowing of the power spectrum when the pulses become longer. Thus, as for user experiments, it should be possible to extract the actual pulse length of the FEL from its power-spectrum within an error of 15%. In case the pulse length required for the specific experiment must be known more accurately, it has to be measured directly at the experimental setup with the techniques described above. While this method is still relatively simple, it was demonstrated that, due to its implicit symmetry, it has the disadvantage that the actual pulse shape cannot be retrieved and thus some guesses have to be made. To solve this question it is desirable to measure the pulse shape by cross-correlation or electro-optic sampling with a synchronized near infrared ultrafast laser to alleviate these drawbacks.

### Spatial profile

Another important aspect, particularly for nonlinear spectroscopy, is the spatial mode of the FEL, commonly known as the beam profile. The best focusing quality is obtained when the beam exhibits a Gaussian profile.

In Fig. 4.16 we show the beam profile at a wavelength of  $11 \mu\text{m}$  as measured by an infrared camera consisting of a  $12.4 \times 12.4 \text{ mm}^2$  large pyroelectric array with a pixel size of  $100 \times 100 \mu\text{m}^2$  (*Spiricon Pyrocam III*). The profile exhibits a smooth shape and almost Gaussian like profile in both orientations. However, the overall shape is elliptical to some degree, so that astigmatism will become an issue once the FEL pulse is focused. Hence, careful analysis of the individual spots in the time-resolved experiments is mandatory to ensure a homogenous excitation area.

## 4.2 Measurement techniques

### 4.2.1 Pump-probe spectroscopy

Pump-probe measurements are a widely used technique to study the temporal decay of an excited system back to equilibrium after an ultrafast excitation. Its simplest implementation is to monitor a macroscopic parameter that changes due to an ultrafast excitation, such as the reflection or transmission of the investigated sample. For instance, the absorption of a system changes due to a strong resonant excitation, due to the depletion of the ground state and simultaneous occupation of the excited state.

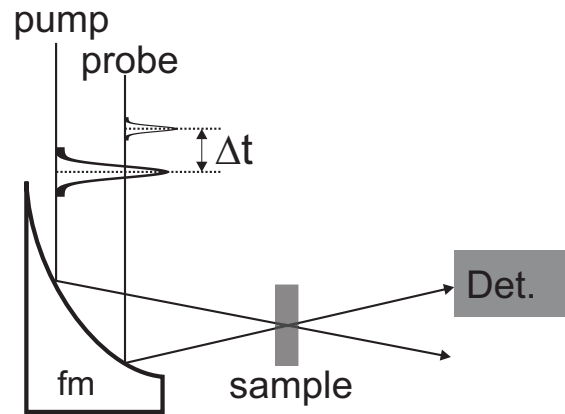


**Figure 4.17:** Schematic setup of the pump-probe measurements in transmission configuration. An intense pump pulse first excites the sample. The resulting change in transmission is then recorded with a weak probe pulse as a function of the time-delay  $\Delta t$ . Both pulses are focused on the sample with a gold-coated off-axis parabolic focusing mirror (fm).

The pump-probe setup used for the single color experiments is shown in Fig. 4.17. As was schematically shown already in the setup for the autocorrelation experiments (Fig. 4.7), a beamsplitter first divides the original FEL pulse into an intense pump-pulse and a weak probe pulse. The pump pulse gets directly focused onto the sample using an off-axis-parabolic gold mirror. Note that its power, excitation area and the intrinsic reflectivity of the sample determines the density of the excited carriers by a given absorption rate and ground state carrier concentration. By use of a motorized linear translation stage with a retroreflector the probe pulse undergoes an adjustable temporal delay  $\Delta t$  with respect to the pump pulse. Note that due to the different effective focal lengths the presented configuration ensures that the excitation area of the pump is always larger than that of the probe pulse, providing a homogeneously excited area with respect to the probe pulse. The change in transmission can then be recorded as a function of  $\Delta t$ . The temporal resolution in this experiment is given only by the duration of the original FEL pulse and the accuracy of the linear stage, while the probe intensity can be detected with a relatively slow but sensitive detector. In our experiments we used liquid nitrogen-cooled HgCdTe-detectors. Since their sensitivity drops significantly towards longer cutoff-wavelengths, detectors with the highest sensitivity at the respective wavelengths were employed. To obtain a good

signal-to-noise-ratio, usually the pump pulse is modulated using an mechanical chopper. Due to the relatively large beam size of the FEL ( $d = 10\text{-}20$  mm), a chopper wheel with only 6 open slits had to be used, so that the modulation frequency was usually set to  $f_{\text{chopp}} = 350$  Hz. Then, to filter out only the pump-induced signal, the detector signal is connected to a Lock-In amplifier with  $f_{\text{chopp}}$  as the reference frequency. The output of the Lock-In amplifier is then digitally recorded by a Labview-program that also controls the linear stage. This was the main method to investigate the relaxation behavior of miniband transitions in doped superlattices.

### 4.2.2 Two-color FEL pump-probe setup using phase matched second harmonic generation

In some cases it is useful not only to perform pump-probe experiments at a single wavelength but to excite the system with an intense pulse and subsequently probe its transmission at a different wavelength. A simple solution for such problems is the use of the fundamental from the FEL as pump light and its second-harmonic for the probe pulse. Of course, this method cannot be applied in many systems, since both frequencies have to match the resonances of interest. However, in semiconductor quantum well structures and superlattices, the intersubband transitions can be tuned in many ways so that this method becomes applicable. Naturally, a major limiting factor is that the reverse experiment, i.e. exciting strongly with the second harmonic and probing at its fundamental, is very difficult since the net-conversion efficiency is usually only a few percent<sup>6</sup>. While regular second harmonic generation, as used for the autocorrelation measurements above, has usually only very low efficiencies in the order of 0.1% or less, it is possible to increase the SHG-intensity by taking advantage of *phase matching* of the fundamental and its second harmonic. In the case of phase matching both beams travel coherently along a nonlinear crystal with length  $L$ . Thus, the phase matching condition in the case of SHG simply means that the wavelength-dependent indices of refraction  $n(\lambda)$  of both beams have to be equal. However, this condition can only be fulfilled in birefringent crystals, where  $n(\lambda)$  differs for ordinary (polarization normal to the principal plane of the crystal) and extraordinary (polarization parallel to the principal plane) beams (see Fig. 4.18). This also implies that the fundamental and its second harmonic have perpendicular polarization. In GaSe, which is a negatively uniaxial crystal (which means that  $n_o > n_{eo}$ ), the fundamental has to be an ordinary beam while its second harmonic is an extraordinary beam (Type I phase matching):  $o + o \rightarrow eo$ . Then the phase matching condition simply reads

$$n_o(\lambda) = n_{eo}(\lambda/2), \quad (4.6)$$

<sup>6</sup>This is valid for infrared pulses with peak intensities smaller than  $1 \text{ GW/cm}^2$ .

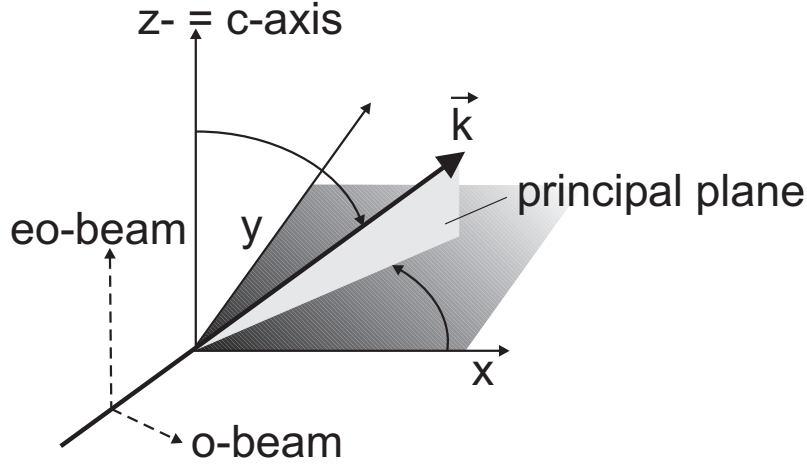


**Figure 4.18:** Polar coordinate system for description of the refraction properties of a uniaxial crystal.  $\vec{k}$  is the propagation direction of the incident light,  $z$  is the optical axis,  $\theta$  and  $\phi$  depict the coordinate angles. Light polarized normal to the principal plane is called the ordinary beam, while light polarized parallel is called the extraordinary beam.

while  $n_{eo}(\lambda)$  can additionally be tuned by the internal phase matching angle  $\theta_{\text{int}}$ , representing the angle between the *eo*-beam and the principal plane (compare Fig. 4.18):

$$n_{eo}(\lambda, \theta_{\text{int}}) = \frac{1}{\sqrt{\frac{\cos^2(\theta_{\text{int}})}{n_o(\lambda)} + \frac{\sin^2(\theta_{\text{int}})}{n_{eo}(\lambda)}}} \quad (4.7)$$

For a given wavelength  $\lambda_0$  and refractive indices  $n_o(\lambda)$  and  $n_{eo}(\lambda)$ , the required internal phase-matching angle  $\theta_{\text{int}}$  can be calculated. The *external* phase-matching angle is then obtained via Snell's law:

$$\frac{\sin(\theta_{\text{int}})}{\sin(\theta_{\text{ext}})} = \frac{1}{n_o(\lambda)} \quad (4.8)$$

In GaSe, whose refractive indices are given by a regular Sellmeier equation [92], phase matching can be achieved in the range from 2.5 to 14.5  $\mu\text{m}$ , as shown in Fig. 4.19. Since SHG is a  $\chi^{(2)}$  process, its resulting power depends quadratically on the intensity  $I_0$  of the incoming beam, while its efficiency  $\eta$  increases linearly with  $I_0$ . Additionally it depends on the length of the nonlinear crystal. We use the following simple approximation for the efficiency [93], while other effects such as depletion and absorption of the pump beam as well as a walk-off of the interacting beams are neglected:

$$\eta = 2\pi^2 d_{\text{eff}}^2 \frac{L^2 \text{sinc}\left(|\Delta k(\theta)| \frac{L}{2}\right)}{\epsilon_0 c_0 n_o^2(\lambda) n_{eo}(\frac{\lambda}{2}, \theta) \left(\frac{\lambda}{2}\right)^2} \cdot I_0 \quad (4.9)$$

Here  $\Delta k(\theta)$  is the phase mismatch:  $\Delta k(\theta) = \frac{2\pi}{\lambda/2} [n_o(\lambda) - n_{eo}(\lambda/2, \theta)]$ . By applying formula (4.9) to a 2 mm thick GaSe crystal ( $d_{\text{eff}} = \cos(\theta) \sin(3\phi) \times 54 \text{ pm/V}$ ) and an intensity of 100  $\text{MW/cm}^2$ , we achieve an efficiency of about 9% at a wavelength of 13  $\mu\text{m}$ . However, it was demonstrated that the above losses have to be taken into account, leading to a drastic lowering of the efficiency by one order of magnitude [94]. There an efficiency of 1% was measured in a 6.5 mm long GaSe crystal at 12  $\mu\text{m}$  at about 100  $\text{MW/cm}^2$ .

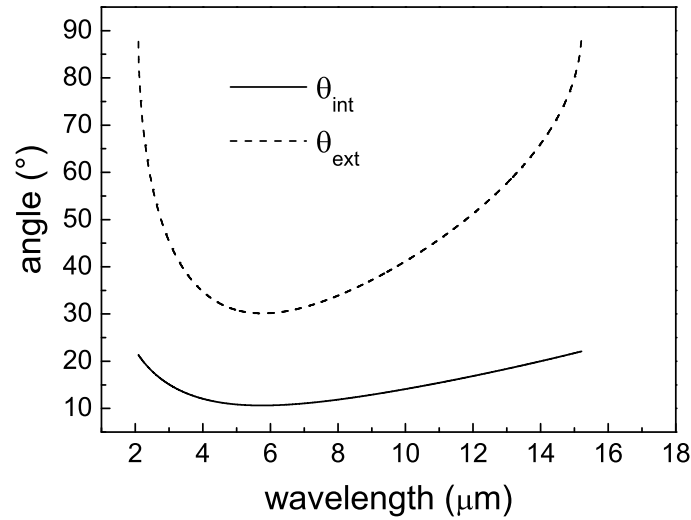


**Figure 4.19:** Internal (black) and external (red) phase matching angles for SHG in GaSe as a function of the fundamental wavelength. Phase matching is possible from 2.5-14.5  $\mu\text{m}$ .

In this work second harmonic radiation has been generated using the mid-IR FEL at ELBE, operating at 13  $\mu\text{m}$  and a 2 mm long GaSe crystal. The SHG crystal was placed between two off-axis parabolic mirrors with a focal length of 150 mm and the SHG power was measured with a thermopile powermeter with an accuracy of 0.1 mW. Before the powermeter, the fundamental wavelength was blocked by an appropriate filter and additionally the second harmonic radiation was selected by a wire-grid polarizer set to the SHG polarization. The generated SHG power was measured for different pump intensities, ranging from 15 to 110  $\text{MW}/\text{cm}^2$ . The result is shown in Fig. 4.20. It can be seen that the measured values fit nicely onto the parabolic curve drawn as a full black line. Thus, the output power increases quadratically with the intensity of the incoming pulse. The inset shows the extracted efficiency of the SHG-process, calculated from the SHG power and the transmitted power of the fundamental,  $\eta = P_{\text{SHG}}/P_{\text{trans}}$ . As expected, the efficiency shows a more linear dependency on the incident intensity.

Overall, the obtained SHG efficiency surely enables us to perform pump-probe measurements using the fundamental as pump pulse and the SHG as a probe pulse. The reverse experiment does not seem adequate, although at shorter wavelengths higher efficiencies (up to a factor of two) should be achievable. For time resolved experiments with the fundamental and its second harmonic, a compact system consisting of two KBr-lenses ( $f=100$  mm) and a rotary unit for the GaSe crystal can easily be installed in the beam path of either the pump or the probe pulse.

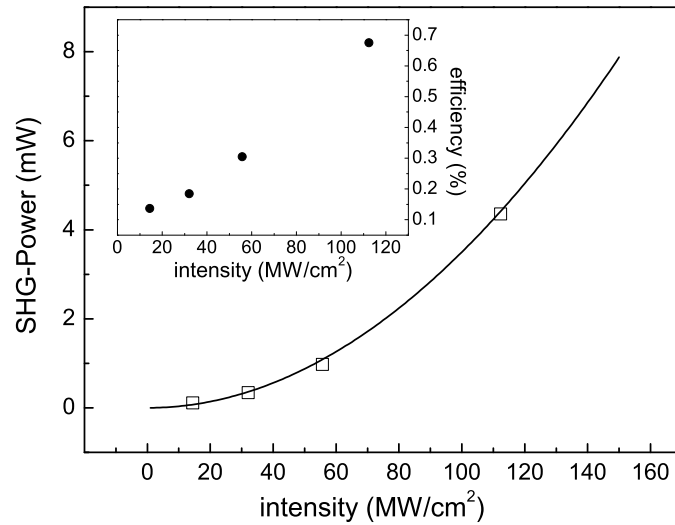


**Figure 4.20:** Second harmonic power generated at 13  $\mu\text{m}$  in a 2 mm long GaSe crystal at a phase-matching angle of  $\theta = 58^\circ$ . The inset shows the conversion efficiency,  $P_{\text{SHG}}/P_{\text{trans}}$ .

### 4.3 Broadband Terahertz radiation using GaSe

For investigations of the response of a system after an intense ultrashort excitation in the time *and* in the frequency-domain *simultaneously*, it is necessary to have another fully tunable light source that is synchronized to the pump laser source [95, 96, 97]. While in the near-infrared remarkably good two-color systems have been developed based on mode-locked Ti:Sapphire lasers [98, 99], it remains a challenge to achieve this in the mid-infrared or THz-regime, at least for high power systems. The most common way is to use a single Ti:Sapphire amplifier, which produces ultrashort near-IR pulses (25-150 fs) with pulse energies up to 5 mJ at kHz repetition rates. To generate intense mid-IR radiation, these pulses are used to pump an optical parametric amplifier (OPA), where two infrared pulses (signal and idler) with wavelengths from 1.3-2.5  $\mu\text{m}$  are generated at the first stage. These pulses are then mixed in another nonlinear crystal for difference frequency generation (DFG). The resulting mid-IR pulses range from 4-18  $\mu\text{m}$  and have a pulse energy of about 1  $\mu\text{J}$ . To perform frequency and time-resolved experiments usually two OPA's are pumped by a single amplifier, eventually delivering synchronous mid-IR pulses that are independently tunable. However, due to the relatively low repetition rate and the long series of nonlinear processes involved in its generation, the signal-to-noise ratio in pump-probe experiments is expected to be much lower than compared to the FEL (operating at 13 MHz) or Ti:Sapphire oscillators (60-100 MHz). In addition, in most systems the beam direction of the DFG-pulse changes for every chosen wavelength, which needs to be compensated in a frequency resolved pump-probe experiment. Nevertheless,



this principle is the only way to achieve time-resolution on the order of 200 fs (i.e. the usual pulse duration from OPAs) since the individual pulses have almost no timing jitter, whereas two individual lasers that are phase-locked to each other usually have a timing jitter of 1-2 picoseconds [100, 101]. To achieve a very small timing-jitter in experiments with FELs one would have to split the electron beam into two parts, each of them driving an FEL oscillator, or to use two different undulators within a single optical cavity [102]. But these methods are rather complex and cost intensive, and are currently not planned for the Rossendorf FELs.

In this work we use a different approach to combine high repetition rates, large tunability and a high resolution in time as well. For this an ultrafast Ti:Sapphire laser oscillator with a repetition frequency of 78 MHz is actively synchronized to the FEL clock. Instead of feeding an amplifier with these synchronized pulses, the oscillator pulses themselves are used to generate broadband tunable mid-IR and THz pulses, since the spectral width of the near-IR pulses allows difference frequency mixing with central wavelengths of up to 7.3  $\mu\text{m}$ . In the case of ultra-broadband pulses the spectral region extends to 6  $\mu\text{m}$  (41 THz). As appropriate nonlinear crystal GaSe is chosen, thus the long-wavelength cut-off of this process is given by its reststrahlenband starting at 35  $\mu\text{m}$  (8.5 THz).

In this section, we will first give an introduction to the ultrafast lasers system used, then we describe the principle of phase matched difference frequency generation. The resulting THz pulses have been detected by various methods and their tuning range has been explored. Finally the synchronization to the FEL or other lasers is illustrated.

#### 4.3.1 10 fs Ti:Sapphire lasersystem

Over the last one and a half decades Titanium-doped sapphire ( $\text{Ti}^{3+}:\text{Al}_2\text{O}_3$ ) has become the most important laser medium in femtosecond technology. The main reason for this is its extremely broad fluorescence spectrum, ranging from 650 up to 1000 nm [103] with a maximum around 780 nm. Its high third-order nonlinear coefficient additionally implies that ultrashort pulses via Kerr lens mode locking can be generated without the help of an additional nonlinear optical element. In this scheme the active lasing medium acts as a lens with a focal length depending on the instantaneous power of the laser beam, known as the Kerr effect. The power-dependent change in the spatial profile of the beam is then transformed into a passive amplitude modulation through an aperture of suitable diameter. The simplest embodiment of this technique utilizes the (soft) aperture which is formed by the pumped volume in the gain medium itself. The rapid technological development of ultrafast Ti:Sapphire lasers culminated in near-infrared pulses with only 4 fs duration [104].

The schematic setup of the Kerr-lens modelocked laser (*Femtolasers Scientific sPro*) used in this work is shown in Fig. 4.21. Its cavity contains a 2 mm long Ti:Sa crystal, which is optically pumped by a 5 W Nd:YVO<sub>4</sub> laser (*Coherent Verdi V5*) and inserted at Brewster's angle. While the mirrors M1 and M5 have a high transparency at the pump wavelength

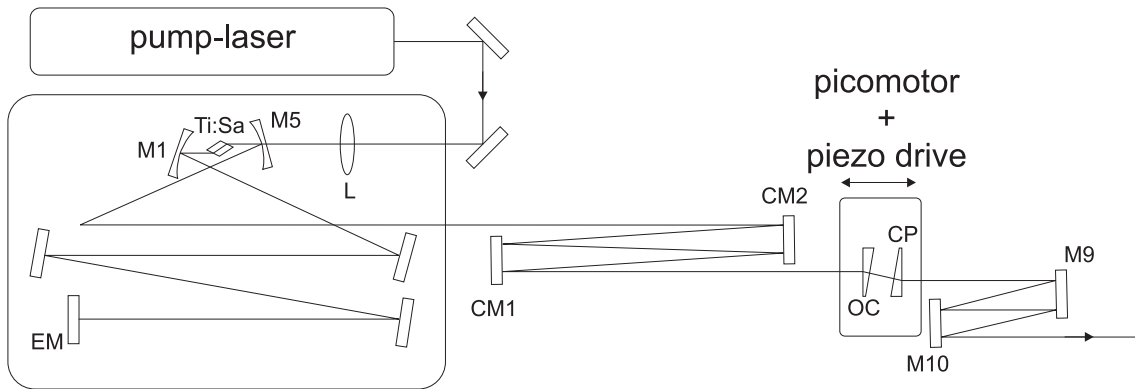


**Figure 4.21:** Schematic layout of the laser oscillator (*Femtosource Scientific sPro, Femtolasers GmbH*). The light-amplifying Ti:sapphire crystal is pumped by a continuous-wave Nd:YVO4 laser (*Coherent Verdi V5*) via a focusing lens L. The linear optical resonator is formed by the end mirror EM and the slightly transmitting output coupler OC. The focusing mirrors M1 and M5 are responsible for a high power density in the crystal thus enhancing the Kerr effect. Chirped mirrors CM1 and CM2 compensate for the group-velocity dispersion accumulated by 1 pulse roundtrip in the resonator. All beams are incident on the Ti:Sapphire crystal under Brewster's angle to minimize losses, and the orientation of M1 and M5 is chosen to compensate for the astigmatism introduced by the Ti:Sapphire crystal. The OC has the shape of a double-wedge (compensating plate CP) to avoid multiple reflections into and out of the resonator. The external cavity dispersion control consists of 2 chirped mirrors (M9, M10) where each double reflection compensates for the dispersion introduced by a 1 mm thick plate of BK7 glass.

(532 nm) they have a high reflectivity in the emission range of the Ti:Sa crystal. Most of the other mirrors installed in the cavity introduce a negative dispersion in order to compensate for the positive group velocity dispersion (chirp) accumulated inside the laser cavity by air and the Ti:Sa crystal. OC denotes the output coupler, which transmits 20 % of the intra-cavity power. Mirrors M9 and M10 provide additional negative dispersion and can be combined with the compensation-plate (CP) to fine-tune the output pulse duration. For active synchronization, the output coupler and the compensation plate are mounted on a linear stage, which contains a picomotor and a piezo-drive for precise matching of the repetition rate of the oscillator to an external clock. The oscillator operates at 78 MHz and delivers an output power of 400 mW in daily operation, which corresponds to a pulse energy of 5 nJ. The laser spectrum and its interferometric second-order autocorrelation trace are shown in Fig. 4.22.

The power spectrum is centered at 801 nm and exhibits a FWHM of 105 nm. The pulse duration was measured using an interferometric second-order autocorrelator (*Femtolasers Femto AC*) and found to be 10.7 fs. This yields a time-bandwidth product of  $\Delta\nu\Delta\tau = 0.51$ , indicating operation close to the Fourier limit.

### 4.3.2 Principle of phase matched difference frequency mixing

The experimental setup described in this section provides a high repetition source of nearly bandwidth-limited THz-pulses in the range from 10-50 THz. These pulses are generated

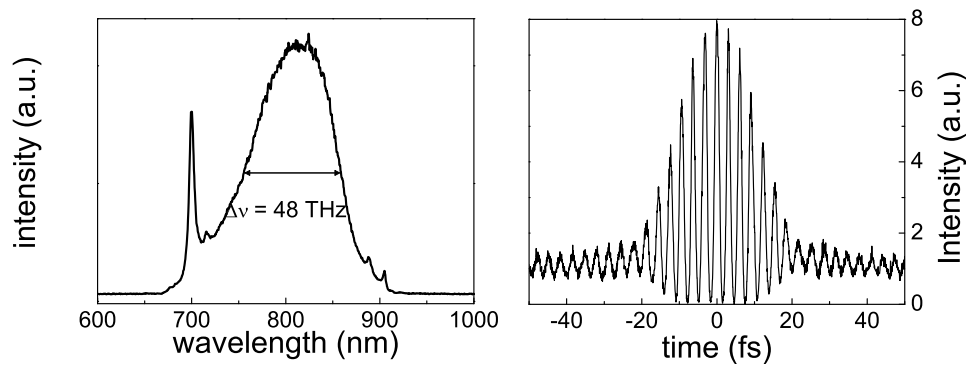


**Figure 4.22:** Power spectrum (left) and interferometric second-order autocorrelation trace (right) of the pulses delivered by the Ti:Sa laser. The spectrum exhibits a FWHM of 105 nm, while the measured pulse duration is 10.7 fs. The sharp line in the spectrum results from cw-spontaneous emission and does not contribute to the infrared pulse.

by phase matched difference frequency mixing in a GaSe crystal of spectral components within the ultrabroad spectrum of single 10-fs near-infrared laser pulses.

The advantage of this technique, which was developed by Kaindl *et al.* in 1998 [105, 106], lies in its inherent simplicity. While conventional methods for the generation of pulses in the 8-18  $\mu\text{m}$  range use the combination of a high-power Ti:Sapphire amplifier, an optical parametric oscillator, and a subsequent difference frequency mixing stage, the method discussed here uses only a single nonlinear conversion step.

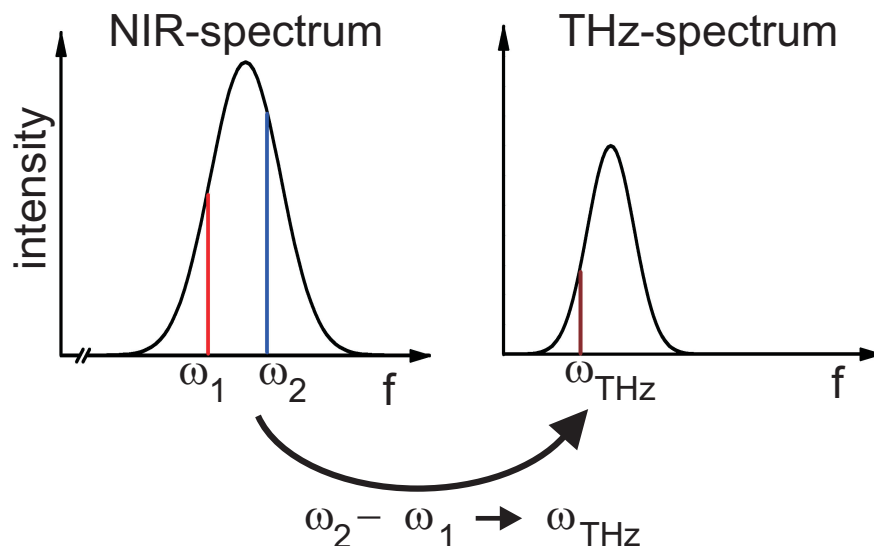


**Figure 4.23:** Schematic principle of difference frequency generation of 10-fs laser pulses. THz pulses are generated by mixing of spectral components within the ultrabroad spectrum ( $\Delta\nu=48$  THz) of the near-infrared laser pulse.

Difference frequency generation is a second order nonlinear process, where two electric fields  $E_1(\vec{r}, \omega_1)$ ,  $E_2(\vec{r}, \omega_2)$  induce the second order polarization in a nonlinear medium [107]

$$P_i^{(2)}(\vec{r}, \omega_0) = 2\epsilon_0 d_{ijk}^{(2)}(\omega_0; \omega_1, \omega_2) E_j(\vec{r}, \omega_1) E_k(\vec{r}, \omega_2) \quad (4.10)$$

where  $d_{ijk} = \frac{1}{2}\chi_{ijk}$  and  $\chi_{ijk}$  is the second order susceptibility. The induced polarization can be calculated via the wave equation, here shown in the frequency domain for convenience.

$$\nabla \times \nabla \times \vec{E}(\vec{r}, \omega) - \frac{\omega^2}{c^2} \underline{\epsilon}(\omega) \vec{E}(\vec{r}, \omega) = \frac{\omega^2}{c^2 \epsilon_0} P^{(2)}(\vec{r}, \omega) \quad (4.11)$$

Here  $\underline{\epsilon}(\omega)$  denotes the frequency-dependent dielectric tensor:  $\underline{\epsilon}(\omega) = \underline{1} + \underline{\chi}(\omega)$ . Assuming a plane wave  $\vec{E}(\vec{r}, \omega) = \vec{E}_0 \cdot e^{i(\vec{k}(\omega)\vec{r} - \omega t)}$ , inserted in Eqn.(4.11) then yields the following relation between the wave-vector  $\vec{k}(\omega)$  and the electric field  $\vec{E}$ :

$$k^2(\omega) E_i - k_i(\omega) k_j(\omega) E_j = \frac{\omega^2}{c^2} \epsilon_{ij}(\omega) E_j \quad (4.12)$$

The generation of mid-infrared pulses in a difference frequency mixing process involves three different electric fields ( $E_{NIR}(\omega_1)$ ,  $E_{NIR}(\omega_2)$ ,  $E_{THz}(\omega_1 - \omega_2)$ ) that have to fulfill the wave equation (4.11) simultaneously since all waves interact in the nonlinear crystal. Therefore we have to solve three coupled wave equations. For the solution of this problem, we make the ansatz of plane waves with a common  $\vec{k}$ -direction (collinear phase matching) parallel to the  $z$ -axis of the crystal (compare Fig. 4.18).

$$\begin{aligned} E_1(z, \omega_1) &= \text{Re}(A_1(z, \omega_1) e^{ik_1(\omega_1)z}) = \frac{1}{2} A_1(z, \omega_1) e^{ik_1(\omega_1)z} + c.c. \quad (4.13) \\ E_2(z, \omega_2) &= \frac{1}{2} A_2(z, \omega_2) e^{ik_2(\omega_2)z} + c.c. \\ E_{THz}(z, \omega_1 - \omega_2) &= \frac{1}{2} A_{THz}(z, \omega_1 - \omega_2) e^{ik_{THz}(\omega_1 - \omega_2)z} + c.c. \end{aligned}$$

Here  $A_{1,2}(\omega, z)$  is a complex amplitude, *slowly* varying in the  $z$ -coordinate. For convenience we now define  $\Delta\omega = \omega_1 - \omega_2$  as the difference frequency, assuming  $\omega_1 > \omega_2$ . Inserting the ansatz above into the wave-equation (4.11), we find for the THz-amplitude  $A_{THz}$ :

$$\frac{\partial}{\partial z} A_{THz}(z, \Delta\omega) + c.c. = \frac{i(\Delta\omega)^2 d}{2c^2 k_{THz}(\Delta\omega)} A_1(z, \omega) A_2^*(z, \omega + \Delta\omega) e^{i\Delta k z} + c.c. \quad (4.14)$$

where we use the slowly varying envelope approximation, indicating that the spatial change of  $A_{THz}(z, \Delta\omega)$  on the scale of one wavelength is negligible:

$$\left| \frac{\partial^2}{\partial z^2} A_{THz}(z, \Delta\omega) \right| \ll \left| k_{THz}(\omega) \frac{\partial}{\partial z} A_{THz}(z, \Delta\omega) \right| \quad (4.15)$$

Additionally we have introduced the phase-mismatch  $\Delta k$ , defined as:

$$\Delta k = k_2(\omega + \Delta\omega) - k_1(\omega) - k_{THz}(\Delta\omega). \quad (4.16)$$

The generated THz field amplitude is much weaker than the NIR electrical fields  $E_{1,2}(\omega, z)$ . Hence, the coupled differential equations for them can be neglected, since they can be

assumed to be constant along the crystal length  $L$ . The resulting amplitude at the exit of the crystal can then be obtained from the integration of Eqn.(4.14) over the crystal length:

$$A_{THz}(z, \Delta\omega) = \frac{(\Delta\omega)^2 d}{2c^2 k_{THz}(\Delta\omega)} A_1(\omega) A_2^*(\omega + \Delta\omega) \left( \frac{e^{i\Delta k L} - 1}{\Delta k} \right) \quad (4.17)$$

However, in our case the difference frequency generation takes place within a single pulse-spectrum, containing many frequency doublets  $(\omega_1, \omega_2)$ . Therefore we have to integrate over the full spectrum of the incident laser pulse to obtain the resulting THz-field amplitude:

$$A_{THz}(z, \Delta\omega) = \frac{(\Delta\omega)^2 d}{2c^2 k_{THz}(\Delta\omega)} \int A_1(\omega) A_2^*(\omega + \Delta\omega) \left( \frac{e^{i\Delta k L} - 1}{\Delta k} \right) d\omega \quad (4.18)$$

Eqn.(4.16) already introduced the phase-matching condition for difference frequency generation. As mentioned in Sec.(4.2.2), this condition implies that the phase velocity of the generated THz pulse  $v_{THz}^{Phase} = \Delta\omega/k_{THz}(\Delta\omega)$  has to match the group velocity of the NIR-pulses  $v_{NIR}^{group} = \partial\omega/\partial k$  along the length of the crystal. Otherwise THz pulses generated at different positions in the crystal would interfere destructively. From this view (and by Eqns.(4.17-4.18) it is clear that the phase-matching condition is most critical for long crystals, while it becomes less important in short ones.

In GaSe, phase matching can be achieved by tilting the optical axis with respect to the polarization of the extra-ordinary beam, resulting in the phase-matching angle  $\theta$  (compare Sec.(4.2.2) and Fig. 4.18). Generally, there are two types of possible phase-matching, type I and type II [93]. In case of difference frequency generation, type-I phase matching in a negatively uniaxial crystal like GaSe requires an extraordinary beam with the frequency  $\omega_1$  that is mixed with an ordinary beam of  $\omega_2$ , generating the difference frequency beam with ordinary polarization ( $eo - o \rightarrow o$ ). In type-II phase matching, the generated difference frequency beam has extraordinary polarization ( $eo - o \rightarrow eo$ ). The different types of phase matching and the orientations are shown in Fig. 4.24.

The nonlinear coefficient tensor  $d_{ijk}$  introduced in Eqn.(4.10) can be reduced to a  $3 \times 6$  matrix, if Kleinmans symmetry condition is fulfilled, meaning that the indices  $(i, j, k)$  are freely permutable [43]. In GaSe, belonging to the  $\bar{6}m2$  crystal-group, the only non-vanishing elements are:

$$d_{12} = d_{16} = -d_{22} \quad (4.19)$$

where  $d_{22} = 54 \pm 11$  pm/V, which is relevant for the difference frequency generation<sup>7</sup>. The effective nonlinear coefficient additionally depends also on the relevant angles  $\theta$  and  $\phi$ , where  $\theta$  is the azimuthal angle between the propagation vector  $k$  and the  $xz$  crystalline plane (see Fig. 4.18) and therefore differs slightly for the two types of phase matching:

$$\text{Type I: } d = d_{22} \cos(\theta) \sin(3\phi) \quad (4.20)$$

$$\text{Type II: } d = d_{22} \cos^2(\theta) \cos(3\phi)$$

<sup>7</sup>Note that  $d$  can be assumed to be frequency-independent, which is justified since we consider only frequencies far away from any resonances in the crystal.

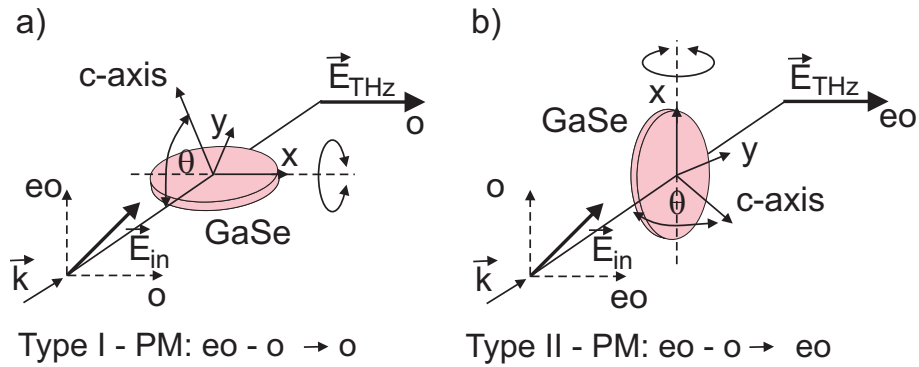


**Figure 4.24:** Schematic principle of the two different types of phase matching. Since we are generating the difference frequency within a single broadband pulse, the NIR-polarization has to be rotated by  $45^\circ$ , in order to provide an ordinary and extraordinary beam component. (a) shows the case of type-I phase matching, where an ordinary beam is generated. If the crystal is turned by  $90^\circ$ , the same polarization can be generated in type-II process, now being an extraordinary beam (b).

Now, by adjusting the phase-matching angle  $\theta$ , the central frequency of the THz-pulse can be adjusted, limited only by the spectral width of the NIR-laser pulse towards higher frequencies and by the reststrahlenband for low frequencies. In long crystals, the dependency of the central frequency on the phase-matching angle is more pronounced since the phase-matching condition is more critical, eventually leading to reduction of the spectral width of the generated THz-pulse (FWHM 4-5 THz). Hence, they are suitable for probing at a rather fixed photon energy. In case of thin crystals, the spectral width extends to a FWHM of more than 15 THz, providing ultrashort THz radiation for time and frequency-resolved spectroscopy *within a single pulse*.

### 4.3.3 Method of detection and characterization of ultra-broadband THz pulses

In this section we want to discuss different methods to characterize the ultrashort THz pulses. First, an interferometric method is used and is then compared to two different types of electro-optical sampling.

#### Interferometric cross-correlation

Fourier transform spectroscopy is clearly the most efficient technique for measuring the spectrum of THz and mid-IR radiation. It relies on the acquisition of the interferometric autocorrelation of the incident beam in a Michelson interferometer, followed by the numerical computation of its Fourier transform. This yields the square of the modulus of the electric field in the frequency domain, i.e. the power spectrum  $|E(\omega)|^2$ . This method is widely used in the form of Fourier transform infrared (FTIR) spectrometers, where simply a glowbar provides infrared radiation ranging from 1-100  $\mu\text{m}$ . Both beams of the Michelson interferometer are then focused collinearly onto an efficient detector. However,

Fourier transform spectroscopy can also be successfully adapted to the measurement of pulsed sources, as demonstrated by Greene *et al.* [108]. Ralph and Grischkowsky developed an improved setup that has no moving parts for the THz radiation [109]. They used a set of two identical emitters where the time delay between the two THz pulses is scanned by varying the time delay between the two exciting optical femtosecond pulses. This method was further developed by Joffre *et al.* [110], where only a single emitter is used.

However, the main drawback of these techniques is that the information on the spectral phase gets lost since only the power spectrum is recorded. For instance, the information about the phase is an important measure in spectroscopy, mandatory to identify and interpret recorded spectra correctly, since both, the real and imaginary parts of the dielectric function of the sample can be measured. Additionally, any chirp present in the THz pulses will remain undetected, leading to possible misinterpretation of the pulse duration. To obtain phase information, other techniques must be used. The method presented here is a variant of the autocorrelation technique, where two different emitters are used. In such a linear cross-correlation a quasi-single-cycle THz pulse acts as a reference to characterize an unknown THz pulse with a longer duration [111, 112]. This technique provides directly the electric field of a given THz pulse.

The setup of the interferometric cross-correlation is shown in Fig. 4.25. The 10 fs NIR pulses are first split into two parts with a 50% beamsplitter and each of them is focused on an individual THz emitter. The resulting THz pulses are recombined on a Si-wafer and then collinearly focused on an HgCdTe (MCT) detector where they interfere. To enhance the signal-to-noise ratio of the experiment, the incoming laser beam can be modulated by a mechanical chopper with frequencies from 300 Hz up to 4 kHz. This frequency acts as a reference signal for the Lock-In amplifier, connected to the MCT-detector. By use of the linear stage, the optical path of the pulses in the right arm can be varied, resulting in a variable time delay with respect to the left arm. By variation of the temporal delay, the intensity measured by the detector reads:

$$P(\tau) \propto \int_{-\infty}^{\infty} [E_1(t) + E_2(t + \tau)]^2 dt \quad (4.21)$$

and the part varying with  $\tau$  is

$$A(\tau) \propto \int_{-\infty}^{\infty} E_1(t)E_2(t + \tau)dt = E_1(\tau) \text{ for } E_2(t + \tau) \approx \delta(t - \tau) \quad (4.22)$$

From Eqn.(4.22) it can be seen that in order to obtain the electric field of the first emitter it is necessary that the reference pulse can be assumed to be  $\delta$ -function like. This can be achieved only by quasi single-cycle THz pulses. For this purpose we have two possibilities: the single-cycle THz pulse can either be generated by non-phase matched optical rectification in  $\langle 110 \rangle$  oriented GaAs or by difference frequency generation in an extremely thin GaSe emitter ( $L \approx 25 \mu\text{m}$ ) where also ultrabroad pulses are generated, exceeding the

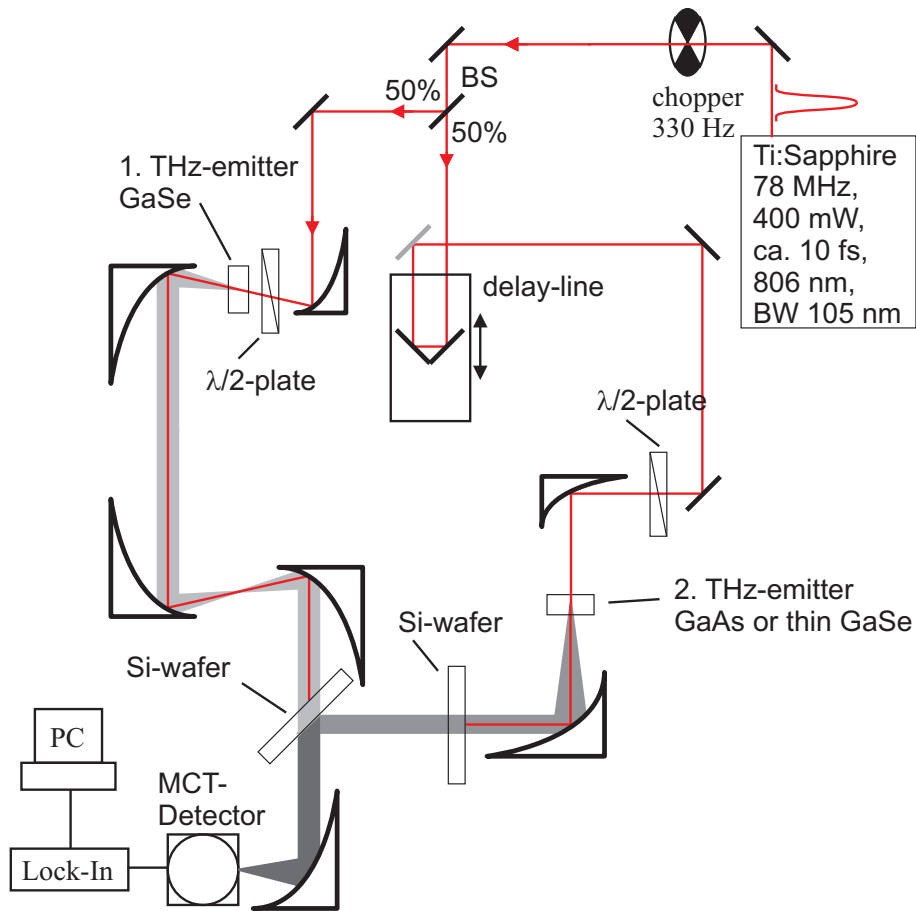


**Figure 4.25:** Setup for characterization of the THz pulses by interferometric cross-correlation. The 10 fs pulses are split into 2 pulses with a ratio of 50% and are focused onto individual THz emitters. The beams are recombined at a Si-wafer and are then focused on the MCT-detector, where they interfere. By varying the time delay between the two NIR pulses, the interferogram can be recorded. By use of a quasi single-cycle THz pulse generated with the second THz-emitter (GaAs or ultrathin GaSe), the recorded signal is proportional to the electric field of the first emitter.

spectral width of the first emitter. While optical rectification in  $\langle 110 \rangle$ -GaAs for sure gives the shortest pulses (if all spectral components of the NIR pulse are in phase), the thin GaSe emitter has to be verified with respect to its spectral bandwidth to confirm its  $\delta$ -like shape in time. This was achieved by a slight variation of the cross-correlation setup. Now the second pulse is (non-collinearly to the first) focused onto the same emitter, and both beams are then focused on the MCT-detector. This setup can be described as a non-collinear autocorrelator, where two identical pulses interfere at the detector. This technique was first introduced by Joffre *et al.* [110]. With this setup, the spectral width of the THz pulses generated in a only 25  $\mu\text{m}$  thin GaSe crystal could be determined. For comparison, a spectrum of a 55  $\mu\text{m}$  thick crystal was also recorded. The results are shown in Fig. 4.26. The recorded power spectrum of the thin emitter exhibits a FWHM of more than 17 THz, somewhat limited by the low-frequency cutoff of the detector used in the experiment. For comparison, the spectral width of the 55  $\mu\text{m}$  thick crystal is only 10 THz.



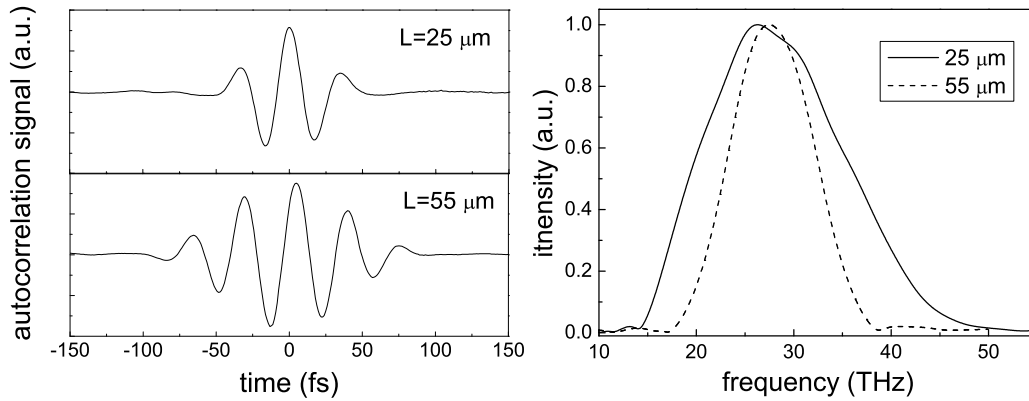


**Figure 4.26:** Autocorrelation signals (left) and power spectra (right hand side) of a 25  $\mu\text{m}$  and 55  $\mu\text{m}$  thick GaSe-emitter under a phase-matching angle of  $60^\circ$ . The extracted spectral (FWHM) width for the 25  $\mu\text{m}$  thick crystal is more than 17 THz and 10 THz for 55  $\mu\text{m}$  thick one, respectively. Note that the cutoff at low frequencies (16 THz) is due to the detector used in the experiment. Due to this cutoff the actual width of the power spectrum of the 25  $\mu\text{m}$  emitter is larger than the measured value.

Due to its enhanced spectral width, its pulse-length can be expected to be short enough to serve as a  $\delta$ -function for the cross-correlation experiments to characterize the THz pulses generated by thicker crystals ( $L > 55 \mu\text{m}$ ). Since the emitted power of the 25  $\mu\text{m}$  thick crystal was measured to be about 10 times larger than of a  $\langle 110 \rangle$ -GaAs emitter, we will use the 25  $\mu\text{m}$  thick GaSe-crystal as a reference emitter in the following characterization and in the time- and frequency-resolved experiments.

Fig. 4.27 shows a typical THz pulse measured by the cross-correlation technique. In the shown case, the emitted field from a 55  $\mu\text{m}$  thick GaSe crystal is sampled with a quasi single-cycle THz pulse from a 25  $\mu\text{m}$  GaSe-emitter, which acts as the reference pulse. Both emitters are tilted to a phase-matching angle  $\theta \approx 60^\circ$ . The cross-correlation signal can be interpreted as a direct measure of the electric field from the 55  $\mu\text{m}$  thick crystal. Its envelope can be approximated by a Gaussian with a width of 79 fs, corresponding to a pulse duration of only 56 fs, respectively. Fig. 4.27(b) shows its corresponding power spectrum  $|E(\omega)|^2$ , obtained by a Fourier-transform of the recorded waveform and its phase (lower part). The power spectrum has a full width at half maximum of 9.4 THz, which yields a time-bandwidth product of 0.53, which is close to transform-limited Gaussian pulses that have a TBP of 0.441. The operation close to the transform limit is confirmed by the analysis of the spectral phase which almost stays constant along the main spectral parts of the pulse, indicating that all spectral components have equal phase.

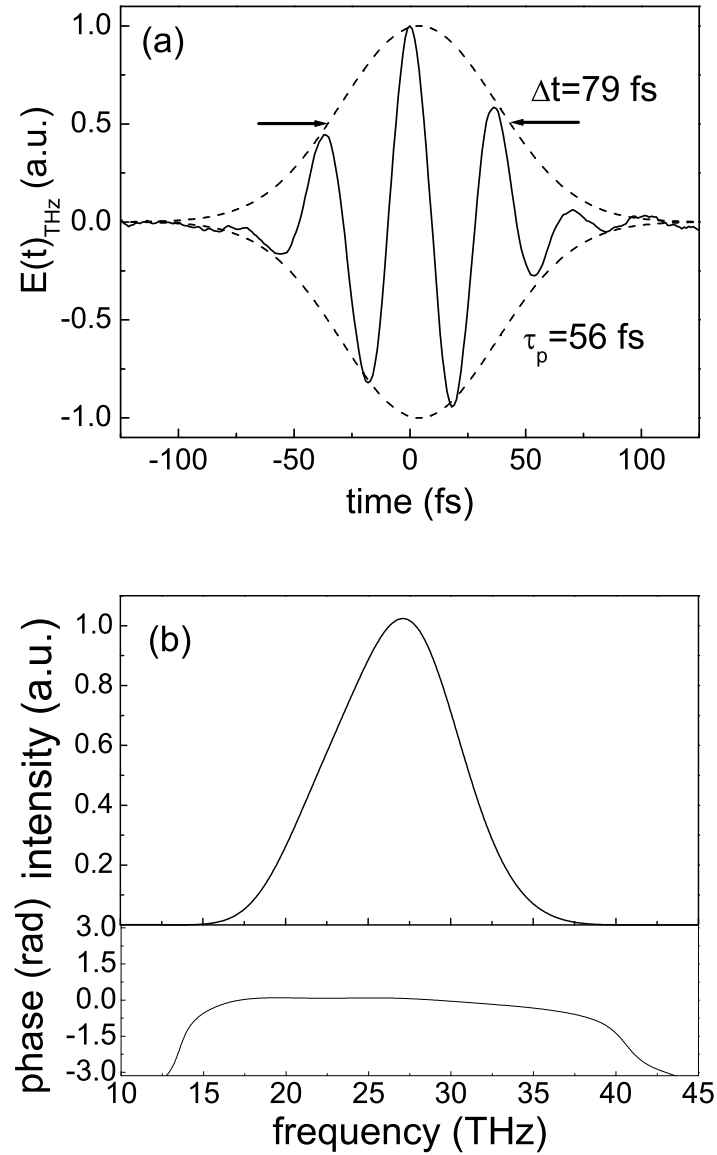


**Figure 4.27:** Cross-correlation signal (a) obtained from a THz pulse of a  $55 \mu\text{m}$  thick GaSe crystal sampled with a quasi single-cycle pulse from a  $25 \mu\text{m}$  thick GaSe-crystal. Both crystals were tilted to a phase-matching angle of  $60^\circ$ . The dashed line corresponds to a Gaussian envelope with a pulse duration of 56 fs. (b) Fourier transform of the recorded waveform  $|E(\omega)|^2$  and its corresponding phase, which is almost constant along the main spectral components within the pulse (lower part in (b)). The spectrum exhibits a FWHM of 9.4 THz, yielding a time-bandwidth product of 0.53.

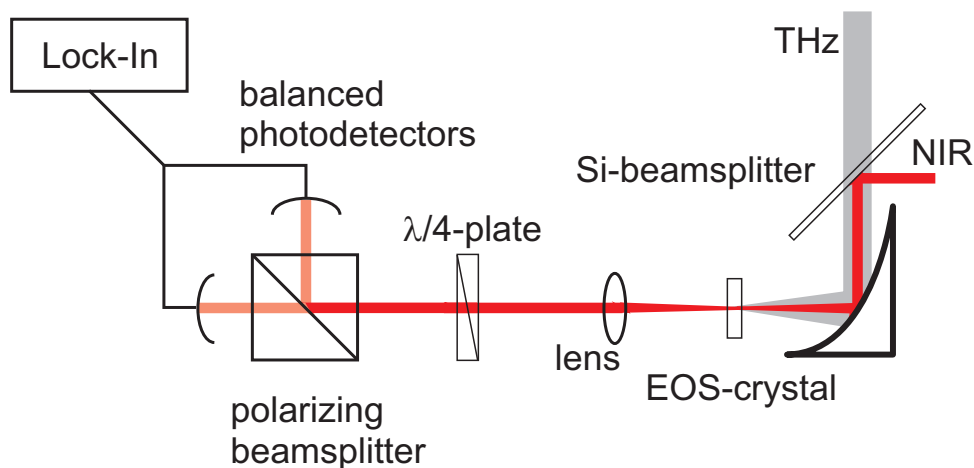


**Figure 4.28:** Principle of measurement of the electric field of a mid-infrared pulse using electro-optic sampling. The mid-infrared beam and the near-infrared reference beam are collinearly focused onto the electro-optic crystal. The reference beam passes a  $\lambda/4$  wave plate and a polarizing beamsplitter before it is measured with a pair of balanced photodetectors.

### (Phase-matched) electro-optic sampling

In this section we will address another method to characterize ultra-broadband THz pulses, namely the electro-optic detection [113, 114, 115, 116]. Free-space electro-optic sampling has developed into a powerful method to characterize ultrashort THz pulses, as it measures directly the electric field. Thus the complete spectral information of the field transient can be obtained (power spectrum and phase). Today, electro-optic sampling has become a standard technique in THz spectroscopy [117, 118, 119, 120, 121], and has been applied for the detection of ultrafast pulses with central frequencies of up to 41 THz [122, 123].

The basic idea of electro-optic sampling is that an electric field induces a (change of) birefringence in a crystal via the electro-optic effect, i.e., it generates a change in the index ellipsoid of the crystal. This is known as the Pockels effect and gives an instantaneous response to an electric field present in the crystal. Thus, it is also applicable to ultrafast electric field-transients of THz pulses. There an ultrashort linearly polarized probe pulse co-propagates inside the crystal with the THz beam, and its phase is modulated by the birefringence induced by the electric field of the THz pulse. The resulting phase retardation is converted into an intensity change by a polarization analyzer. For this a suitable material, i.e. with a broad transmission range and a large electro-optic coefficient, has to be selected. A very common electro-optic crystal is ZnTe in  $\langle 110 \rangle$  orientation, and will be used here as well. However, we will also use GaSe crystals for this experiment.

The schematic setup for electro-optic sampling is shown in Fig. 4.28. A silicon beamsplitter combines the THz beam and the near-infrared probe beam collinearly and they are both focused by an off-axis parabolic mirror onto the sensor crystal. Behind the crystal, a quarter-wave plate is inserted in the NIR-beam before it passes a polarization-sensitive beamsplitter. The two resulting beams are then focused onto balanced photodetectors.

Without the THz-field applied, the photodetectors are balanced by turning the  $\lambda/4$ -plate by 45 degrees. If an electric field is present at the time the probe beam passes the electro-optic crystal, it will undergo a phase retardation that can be detected by the polarization-resolved detection. To increase sensitivity, the THz beam is mechanically chopped at 4 kHz and the difference signal is recorded with a Lock-In amplifier.

This phase retardation  $\Gamma$  is directly proportional to electric field, as we will show below. Therefore we assume a linearly polarized probe beam in  $z$ -direction,  $\vec{E}_{in} = \frac{1}{\sqrt{2}}\vec{E}_0 e^{i(\omega t - kz)}$ , incident to an electro-optic crystal in the  $x$  and  $y$  plane. Then we find for the outgoing beam after the EOS-crystal and the  $\lambda/4$  plate [107]:

$$\begin{aligned} \vec{E}_{probe}^{out} &= 1/2 M_{\lambda/4} M(\Gamma) \vec{E}_{in} + c.c. \quad (4.23) \\ &= \frac{1}{2} \frac{1}{\sqrt{2}} \begin{pmatrix} 1 & e^{i\frac{\pi}{2}} \\ e^{i\frac{\pi}{2}} & 1 \end{pmatrix} \begin{pmatrix} \cos\left(\frac{\Gamma}{2}\right) & e^{i\frac{\pi}{2}} \sin\left(\frac{\Gamma}{2}\right) \\ e^{i\frac{\pi}{2}} \sin\left(\frac{\Gamma}{2}\right) & \cos\left(\frac{\Gamma}{2}\right) \end{pmatrix} \begin{pmatrix} E_{in} \\ E_{in} \end{pmatrix} + c.c. \\ &= \frac{1}{2} \frac{E_0}{\sqrt{2}} \begin{pmatrix} \cos\left(\frac{\Gamma}{2}\right) - \sin\left(\frac{\Gamma}{2}\right) \\ e^{i\frac{\pi}{2}} [\sin\left(\frac{\Gamma}{2}\right) + \cos\left(\frac{\Gamma}{2}\right)] \end{pmatrix} e^{i(\omega t - kz)} + c.c. = \begin{pmatrix} E_{out}^x \\ E_{out}^y \end{pmatrix} \end{aligned}$$

The balanced photodetectors now measure the time-averaged difference signal of their intensities  $\Delta$ :

$$\begin{aligned} \Delta &= \lim_{T \rightarrow \infty} \frac{1}{T} \int_0^T [(E_{out}^y)^2 - (E_{out}^x)^2] dt \\ &= \frac{E_0^2}{2} \left[ \left( \sin\left(\frac{\Gamma}{2}\right) + \cos\left(\frac{\Gamma}{2}\right) \right)^2 - \left( \cos\left(\frac{\Gamma}{2}\right) - \sin\left(\frac{\Gamma}{2}\right) \right)^2 \right] \\ &= E_0^2 \sin \Gamma \quad (4.24) \end{aligned}$$

Since  $|\Gamma| \ll 1$  is valid for most cases, we find that the normalized difference signal  $\Delta_E = \Delta/E_0^2$  detected at the balanced photodiodes reflects the electrical field inside the electro-optic crystal.

$$\Delta_E = \Gamma \propto E_{THz} \quad (4.25)$$

With  $\langle 110 \rangle$ -oriented ZnTe as an electro-optic crystal, the electric field can directly be retrieved from the measured signal  $\Delta_E$ :

$$E_{THz} = \frac{\lambda^{probe}}{2\pi} \frac{\Delta_E}{d_{41}} \frac{1}{n^3 L} \quad (4.26)$$

where  $d_{41} = 3.9 \frac{pV}{m}$  is the electro-optic coefficient and  $L$  is the length of the crystal. Eqn.(4.26) implies that the thicker the electro-optic crystal, the larger is the effect on the photodiodes. However, broadband velocity matching over the whole THz range (0.3 - 30 THz) is not possible due to varying indices of refraction at the respective wavelengths. Therefore, a sensor crystal with proper thickness is a crucial condition for the optimization

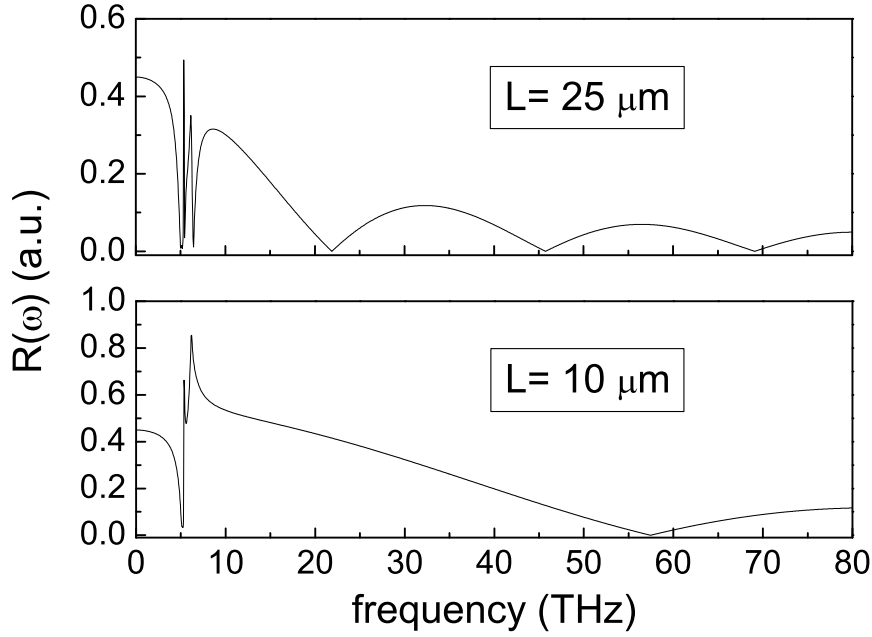


**Figure 4.29:** Normalized response function for a 25  $\mu\text{m}$  and a 10  $\mu\text{m}$  thick ZnTe crystal. Due to the increasing velocity mismatch at thicker crystals the frequency response exhibits several minima in the shown range.

of the THz pulse detection [117, 116]. Since the electro-optic sampling process is equivalent to a sum-frequency or a difference-frequency mixing process of the optical pulse and the THz pulse, this trade-off condition can be expressed by the phase-matching condition:

$$\Delta k = \omega_1 n_1 + \omega_{THz} n_{THz} - \omega_2 n_2 \equiv 0 \quad (4.27)$$

As for the phase-matched difference frequency generation described above (see Sec.(4.3.2)), this condition implies that the electro-optic effect is most efficient when the intensity profile of the optical pulse travels through the crystal at exactly the same speed as the electric field of the THz pulse. However, since ZnTe is an isotropic material it cannot be phase-matched by variation of a phase-matching angle as GaSe. When these velocities differ, the probe pulse averages over several oscillations of the THz field, which leads to a strong reduction of the electro-optic signal. In order to calculate the respective response function, we consider a  $\delta$ -function-like probe pulse centered at  $\lambda^{probe}$  and a monochromatic THz wave with a frequency of  $\omega_{THz}$ . Then, the group-velocity mismatch time accumulated along the crystal length reads

$$\delta(\omega_{Thz}) = \frac{n_{gr}(\omega^{probe}) - n(\omega_{THz})}{c} L \quad (4.28)$$

The time average of the electric field across the group-velocity mismatch time is given by

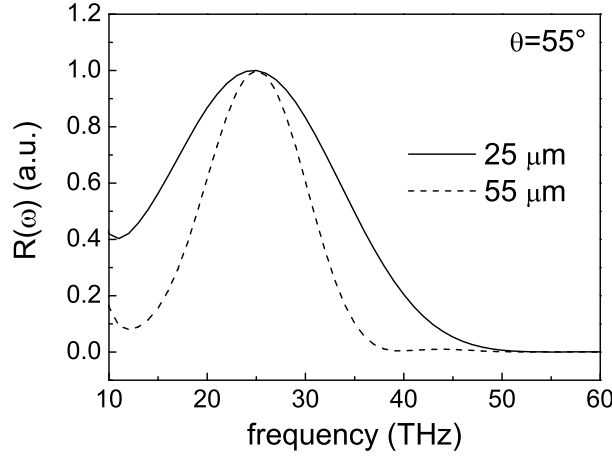


**Figure 4.30:** Normalized response function for a 25  $\mu\text{m}$  and 55  $\mu\text{m}$  thick GaSe crystal under a phase-matching angle of  $\theta = 55^\circ$ . The bandwidth of the 25  $\mu\text{m}$  thick crystal extends the bandwidth of the 55  $\mu\text{m}$  crystal by a factor of two, making it a suitable sensing crystal.

[117, 116]

$$G(\omega_{THz}) = \frac{T(\omega_{THz})}{\delta(\omega_{THz})} \int_0^{\delta(\omega_{THz})} e^{i2\pi\omega_{THz}t} dt = T(\omega_{THz}) \frac{e^{i2\pi\omega_{THz}\delta(\omega_{THz})} - 1}{i2\pi\omega_{THz}\delta(\omega_{THz})} \quad (4.29)$$

where  $T(\omega_{THz}) = 2/(n(\omega_{THz}) + 1)$  is the Fresnel transmission coefficient. For the resulting frequency response function  $R(\omega)$ , also the frequency dependence of the electro-optic coefficient (mainly around the LO- and TO-phonon resonances) has to be taken into account. Additionally the response is proportional to the crystal length, as shown in Eqn.(4.26).

The frequency response has been calculated for two different thicknesses of a ZnTe crystal. The result is shown in Fig. 4.29, where the response function is normalized to the crystal thickness. Due to the increasing velocity mismatch, the response function of the 25  $\mu\text{m}$  thick crystal exhibits several minima compared to the 10  $\mu\text{m}$  thick crystal. So there clearly exists a tradeoff between long interaction lengths and broadband sensitivity.

To alleviate this drawback, we choose a material that is phase-matchable in the respective wavelength range. Then thicker crystals can be used enhancing the electro-optic effect. Similar to the cross-correlation method, it has to be assured that the bandwidth of the frequency response is broader than the spectral width of the sampled THz pulse. This method, which can be called phase-matched electro-optic sampling, has been realized with a GaSe crystal ( $d=25 \mu\text{m}$ ) as electro-optic crystal for sensing THz pulses emitted from thicker GaSe crystals ( $d=55, 200 \mu\text{m}$ ). Its principle is fully equivalent to regular electro-optic sampling with ZnTe, now with the advantage that thicker EOS-crystals can be used in the high frequency range [121]. The response functions of a 25  $\mu\text{m}$  and a 55  $\mu\text{m}$  thick GaSe crystal under a phase-matching angle of  $\theta = 55^\circ$  are presented in Fig. 4.30.

Again, the response functions are normalized. As expected, we find that the bandwidth of the 25  $\mu\text{m}$  thick crystal is much larger compared to the 55  $\mu\text{m}$  one, making it a suitable sensing crystal for THz pulses generated at thicker GaSe emitters.

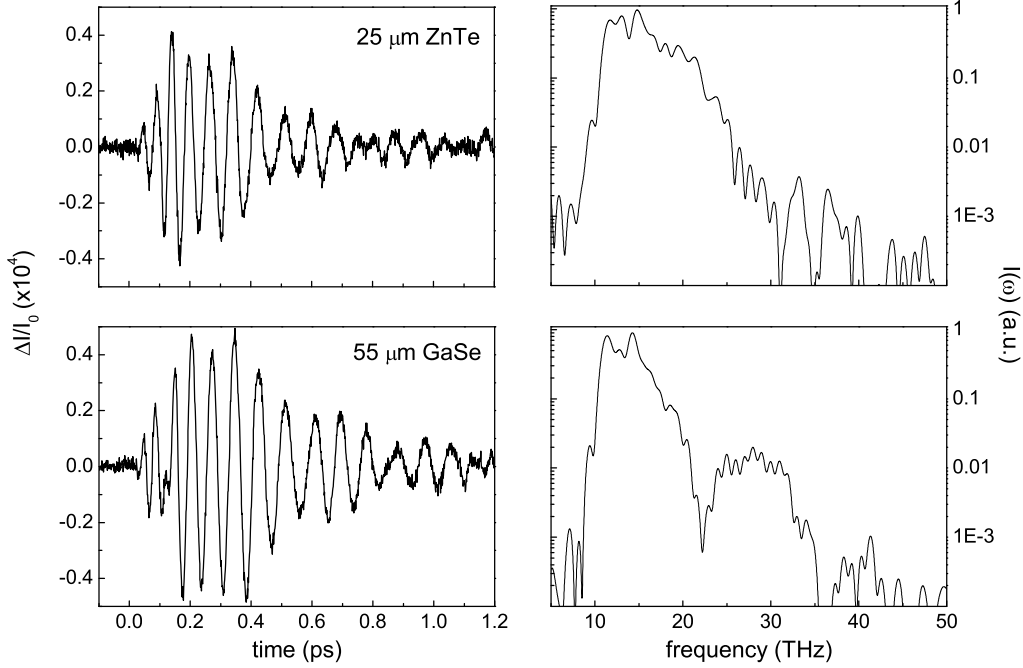


**Figure 4.31:** Electro-optic signals obtained from a 200  $\mu\text{m}$  thick GaSe crystal detected with a 25  $\mu\text{m}$  thick ZnTe crystal (upper part) and with a 55  $\mu\text{m}$  thick GaSe crystal under normal incidence (lower part).

To compare the two methods of electro-optic sampling, a 200  $\mu\text{m}$  thick GaSe crystal was used as a emitter under normal incidence ( $\theta = 0^\circ$ ) to obtain the lowest frequencies. The transients and their respective power spectra are shown in Fig. 4.31. We find that at these low frequencies the ZnTe sensor works well and no frequency cutoff is observable. On the other hand, sensing with GaSe involves phase-matching processes in generation and emission that eventually lead to a reduced sensitivity around 22 THz, where a sharp dip is observed in the power spectrum. However, this behavior is in agreement with the calculated emission spectrum and the response function. Both transients show a long pulse duration which is typical at this phase-matching angle [123], and demonstrates the suitability of GaSe as an electro-optic crystal.

From Eqn.(4.26) we can estimate a peak electric field strength of the pulses on the order of 20 V/cm.

Of course, the main advantage of phase-matched electro-optic sampling only appears at higher frequencies, where the signal-to-noise ratio and thus the sensitivity should be higher. This is demonstrated in Fig. 4.32. Here the THz pulse generated in a 55  $\mu\text{m}$  thick GaSe

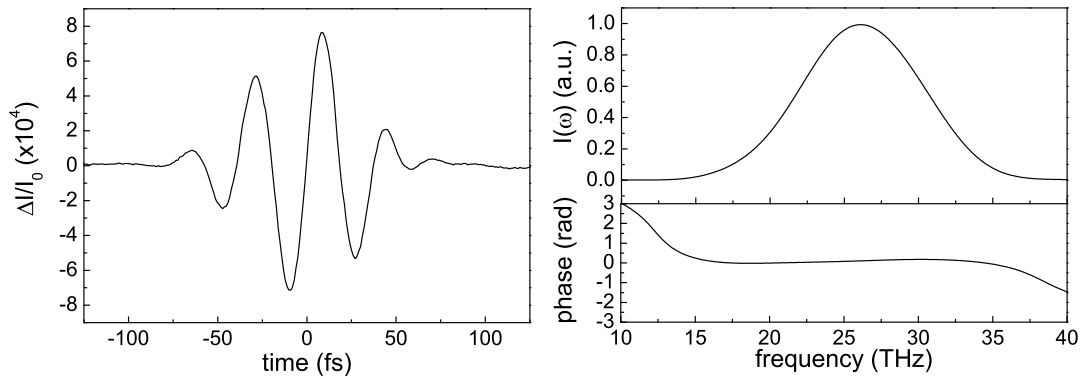


**Figure 4.32:** Electro-optic signal obtained from a 55  $\mu\text{m}$  thick GaSe crystal detected with a 25  $\mu\text{m}$  thick GaSe crystal (left). Both crystals were tilted to a phase-matching angle of  $\theta = 58^\circ$ . The right part shows its corresponding power spectrum and its phase, respectively.

crystal is sampled in a 25  $\mu\text{m}$  GaSe crystal. Both crystals were tilted under a phase-matching angle of  $\theta = 58^\circ$ , ensuring a good spectral overlap of the emitted pulse and the detection bandwidth.

From the THz-transient, shown on the left side of Fig. 4.32, a pulse duration of the order of 50 fs can be estimated. The power spectrum (right-hand side), obtained by a Fourier transform of the recorded waveform, exhibits a FWHM of 10 THz and clearly has a Gaussian profile. The time-bandwidth product is 0.50, indicating transform-limited Gaussian pulses. The operation near to the Fourier-limit is verified by an analysis of the phase of the respective frequencies, shown below the power spectrum. We find that the phase almost remains constant along the main frequency parts of the investigated THz pulse, leading to the conclusion that all frequencies in the pulse have nearly the same phase.

If we now compare the results from electro-optic sampling with results obtained by the cross-correlation experiments, we find an excellent agreement. Both methods show nearly the same results, confirming our earlier assumption that THz pulses generated in a 25  $\mu\text{m}$  thick GaSe crystal only consist of a single optical cycle. Hence they provide an ideal reference pulse for interferometric cross-correlation experiments. Overall we are able to generate nearly Fourier-transform limited pulses with pulse durations down to 50 fs in a 55  $\mu\text{m}$  thick GaSe crystal, providing an ideal tool for pump-probe experiments with a high temporal resolution as well as THz time-domain spectroscopy.

#### 4.3.4 Tunability

As already mentioned above, the extraordinary index of refraction  $n_{eo}(\omega, \theta)$  can be tuned by the external phase-matching angle  $\theta$  to some extent. Hence, the point of perfect phase matching can be tuned to different central frequencies of the generated THz pulse. In principle, this tunability is limited only by the spectral width of the incident near-infrared



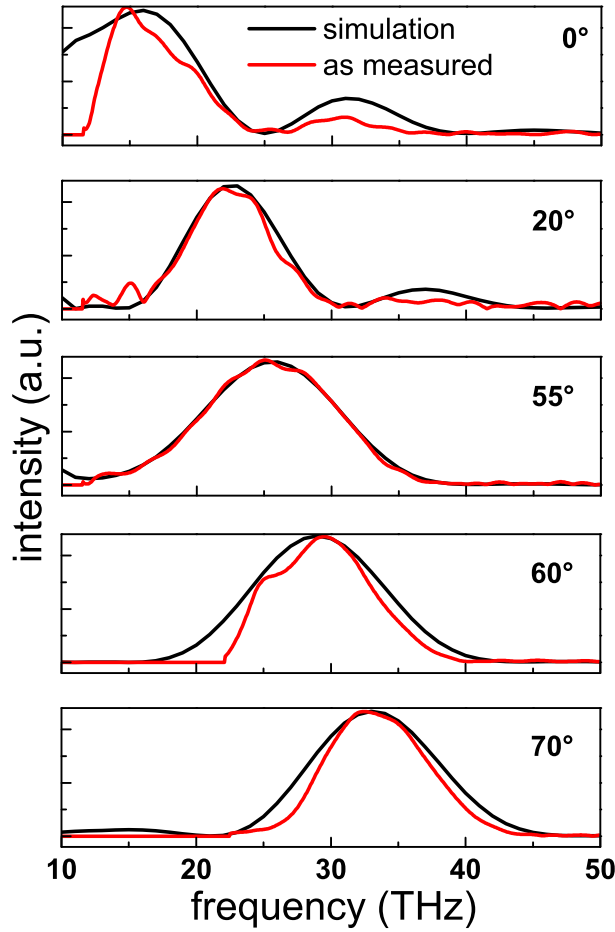


**Figure 4.33:** Measured (red) and calculated (black) power spectra from a  $55 \mu\text{m}$  thick GaSe crystal for different phase-matching angles as indicated.

pulse and the maximum achievable phase-matching angle. Usually, the latter is limited to about  $70^\circ$ - $75^\circ$ . To demonstrate the tunability of our setup, we used a  $55 \mu\text{m}$  thick GaSe crystal and rotated it from  $0^\circ$  up to  $70^\circ$  in the cross-correlation setup. For small phase-matching angles, an MCT detector with a frequency-cutoff at 11.2 THz ( $26 \mu\text{m}$ ) was used. Since MCT detectors become much less sensitive with longer-wavelength cutoffs, an MCT detector with a cutoff at  $14 \mu\text{m}$  was used for the larger phase-matching angles. The results are shown in Fig. 4.33. For comparison, we have calculated the emission spectra based on Eqn.(4.18) and the assumption of a Type II phase-matching process. By tuning the phase-matching angle  $\theta$ , we find that we can tune the central frequency of the THz pulses from 17 up to 33 THz ( $9$ - $18 \mu\text{m}$ ) with spectral components ranging even down to 11 THz and up to 40 THz. The observed power spectra also agree well with the simulation, which is clearly seen.

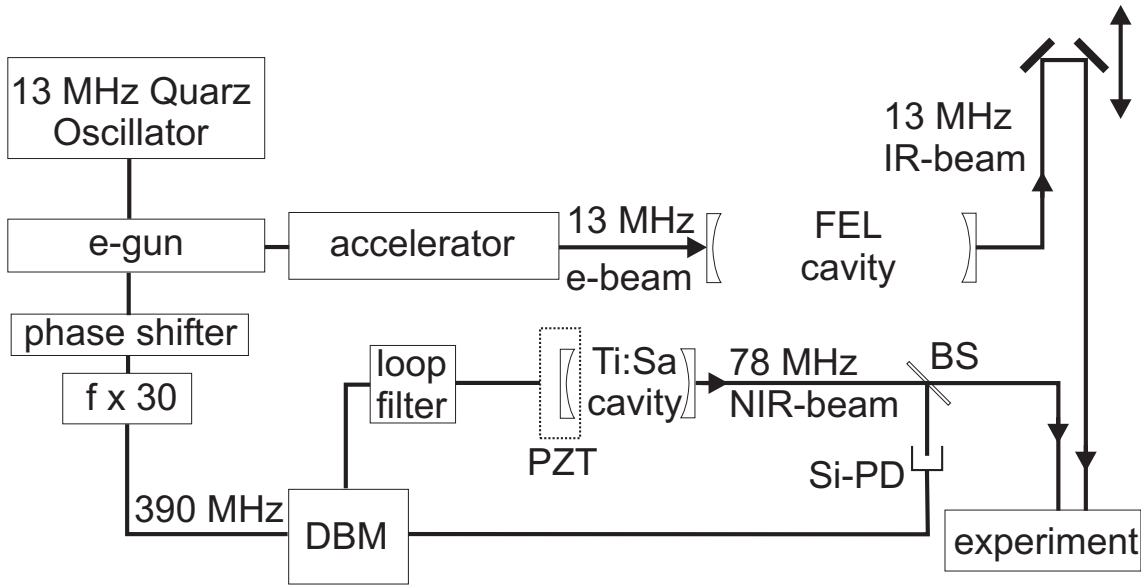


**Figure 4.34:** Schematic layout of the synchronization electronics and optics. An ultrastable rf clock running at 13 MHz first drives the electron gun. The resulting electron train is then accelerated and subsequently pumps the FELs. A rf splitter after the gun splits the 13 MHz signal into several optical links. One arm is first multiplied by a factor of 30 and serves as the reference clock input for the double-balanced mixer (DBM) at 390 MHz. A fast silicon diode (Si-PD) detects the 78-MHz Ti:Sapphire pulses behind a 2% beamsplitter (BS). This signal is mixed with the 390 MHz clock in the double-balanced mixer, yielding the phase difference. The resulting error signal is sent to a piezoelectric transducer (PZT) driver for adjustment of the Ti:Sa cavity length. A phase shifter and a mechanical delay stage is used to control the temporal overlap for the experiments.

### 4.3.5 Synchronization to external light sources

With the broadband THz-setup described above, we are now able to perform THz time-domain spectroscopy in a large tuning range. However, the aim is to involve other ultrashort light pulses in the experiments to, for instance, monitor the absorption behavior after or during a strong excitation by a different laser. In our case, this of course includes the Rossendorf FELs, which provide strong infrared light pulses from 4 to 200  $\mu\text{m}$ , but also other table-top lasers such as Ti:Sapphire oscillators. Therefore, the involved lasers have to be synchronized with a high accuracy. Since in our setup every NIR pulse generates a THz pulse, the most intuitive way for a good synchronization it to match the repetition frequency of the 10 fs laser to an external clock. As shown in Fig. 4.21, the optical cavity of the used Ti:Sapphire oscillator contains a synchronization unit, consisting of a picomotor-stage and a piezo-electric drive, where the output-coupler is mounted to. While the picomotor serves for rough adjustment of the repetition rate, the piezo-drive acts as a real-time synchronizer and is connected to high-speed electronics. The schematic layout of the synchronization electronics is shown in Fig. 4.34, where the synchronization to the FELs is sketched. This method was first introduced in 1998 at FELIX [101].

For monitoring the 78-MHz near-infrared pulse train we use a fast Si photodiode. The 390-MHz component of this signal and a reference signal of the 390 MHz clock of the FELs

are combined in a double-balanced mixer; its output serves as the error signal for driving the piezoelectric transducer. The unity-gain bandwidth of the loop was 1 kHz, determined primarily by the piezoelectric-transducer drive electronics and the loop filter. The use of the 5th harmonic of the 78-MHz round-trip frequency in the feedback loop provides better locking because of the reduced influence of amplitude-phase-noise ratio in the control-loop [124, 125, 126]. When the FEL and the Ti:Sapphire laser were frequency locked to each other, the temporal overlap can be found by use of a phase shifter and fine-tuned by a mechanical delay stage.

To demonstrate the frequency-locking of the Ti:Sapphire laser to the FELs we set up a simple two-color pump-probe experiment. A semi-insulating GaAs sample was excited with the near-infrared pulse, which introduces free carriers in the conduction band. The lifetime of this interband excitation is usually of the order of nanoseconds. After excitation of free carriers in the conduction band, the amount of free-carrier absorption can now be monitored by an infrared pulse which will partially be absorbed, depending on its wavelength and the carrier concentration. This process can be described by a simple Drude model. The dynamic conductivity reads

$$\sigma(\omega, \tau) = \sigma_0 \frac{1}{(1 - i\omega\tau)} \quad (4.30)$$

where  $\tau$  is the Drude-relaxation time,  $\omega$  the frequency of the incoming radiation and  $\sigma_0$  the DC conductivity. In bulk GaAs,  $\tau$  has a typical value of only 76 femtoseconds. The real part of the conductivity  $\sigma(\omega)$  is proportional to the absorption, which is quadratically increasing with the wavelength. Hence, the strongest absorption is expected at long wavelengths.

This free-carrier absorption was then monitored by the transmission of an infrared pulse from the FEL ( $\lambda \approx 11 \mu\text{m}$ ) whose time delay with respect to the NIR pump pulse was varied with a mechanical delay stage. A typical pump-probe curve is shown in Fig. 4.35, having the long decay time of the interband-relaxation. Note that the FEL pulse was heavily attenuated (-38 dB) to avoid any self-modulation of its transmittance. A scan with higher time resolution around zero time delay is shown on the right hand side of Fig. 4.35. The two scans were made within an interval of 5 minutes and no variation of the zero time delay was observed. However, a long term drift of 3-4 ps within 30 minutes was measured due to thermal variations within the long distances in the optical path of the FEL and the synchronization wiring. The rise time of the pump-induced absorption is determined by the pulse length of the FEL pulses, which is usually in the range of 1.5-5 ps at this wavelength, and the short-term phase jitter of the synchronization unit. On the right hand side of Fig. 4.35 we also show a simulated pump-probe signal, calculated from an instantaneous excitation from the 10 fs oscillator and a pulse duration of 2 ps for the FEL pulses. This fit shows good agreement with the measured data, indicating that the phase jitter of our synchronization unit is on the order of 1-2 ps, which lies within the range of the shortest FEL pulses achievable. Therefore, in an approximation, two-color

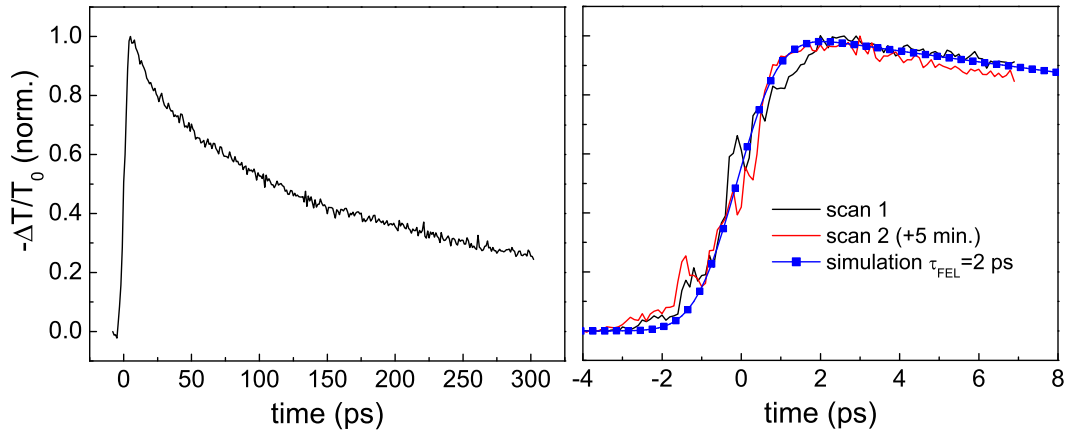


**Figure 4.35:** Decay of interband excitation in GaAs monitored by free-carrier absorption of an FEL-pulse (left hand side). Two high-resolution scans within a time interval of 5 minutes around zero time delay exhibit good stability a short term jitter of 1-2 picoseconds.

experiments can be expected to have a time resolution determined only by the pulse width of the FEL pulses. However, these experiments should be performed within a time frame of 10 to 20 minutes to avoid thermal drift effects.

Overall, in combination with phase matched difference frequency generation, we have now a full two-color setup that operates at a high repetition rate, promising very sensitive measurements with two independently tunable infrared light sources. In contrast to OPA systems, the use of ultra-broadband THz radiation allows spectrally resolved experiments without the drawback of beam displacement. In addition, the wavelength-range of the THz setup can easily be extended towards even longer wavelengths, simply by choosing different THz emitters such as photoconductive switches, that exhibit high electric-field transients up to 1kV/cm when pumped by a Ti:Sa oscillator.

## 5 Ultrafast dynamics of inter- and intra-miniband transitions in doped superlattices

In this section we will investigate the relaxation dynamics of interminiband transitions in doped GaAs/AlGaAs superlattices. This involves single-color pump-probe measurements to explore the dynamics at different wavelengths, which will be done only by use of the Rossendorf free-electron laser, providing picosecond pulses in a range from 3-200  $\mu\text{m}$ . In these experiments, a fast bleaching of the interminiband transition is observed followed by thermalization and subsequent relaxation, whose time-constants are determined. This is followed by an additional component due to carrier cooling in the lower miniband. In the second part, we will perform two-color pump-probe measurements, involving the FEL as the pump source and a table-top broadband tunable THz light source described above (Sec.(4.3)) for probing the transmission changes. These measurements allow a separate specification of the cooling times after a strong excitation. In addition, the dynamics of excited electrons *within the minibands* will be explored.

Parts of this chapter have been published in *Applied Physics Letters* **88**, 151108 (2006).

### 5.1 Single color pump-probe results

The relaxation and cooling behavior of electrons in semiconductors and their heterostructures is of crucial importance for most optoelectronic devices [19]. As a prime example the intersubband relaxation dynamics in quantum wells have to be known and well understood for the design of quantum cascade lasers [127, 128, 129]. Many such investigations have been performed over the past two decades in quantum structures based on different materials systems, and an impressive level of insight has been obtained [31]. Yet semiconductor superlattices (SL), while representing a key model system of an artificial semiconductor structure, have been much less investigated in this respect, although they provide the basis of SL cascade lasers [130] or Bloch oscillators [28, 29]. Compagnone *et al.*[33] have calculated the interminiband relaxation rates and the stationary electron distribution function using a Monte Carlo technique, but no time resolved experiments have been performed to the best of our knowledge.

The first superlattice we investigated is sample G757, the same as discussed in Sec.(3.6).

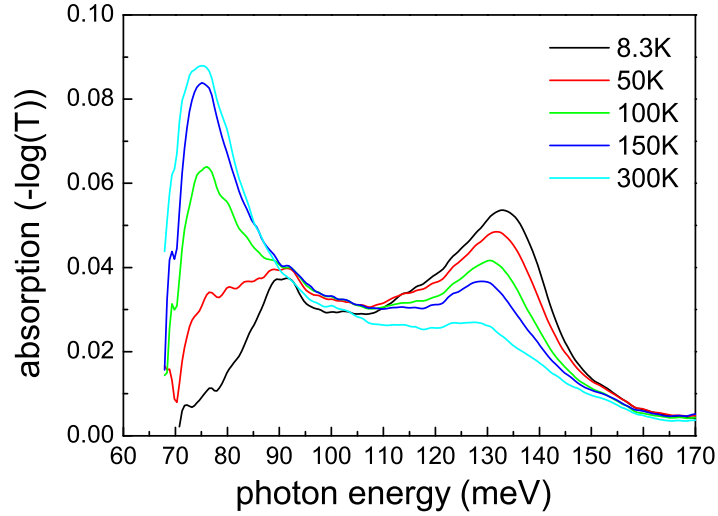


**Figure 5.1:** Linear absorption spectrum of the superlattice G757, recorded for different temperatures.

The detailed growth parameters are listed in Table 2.1. The linear interminiband absorption spectrum, measured on a sample with  $45^\circ$  polished facets and one total internal reflection, is shown in Fig. 5.1 for different temperatures. The absorption spectra (measured in a Fouriertransform spectrometer, *Bruker Equinox 55*) are obtained by normalizing the  $p$ -polarized signal by the  $s$ -polarized one.

At high temperature, the spectra reflect the van Hove singularities of the joint density of states at the center and edge of the mini-Brillouin zone, at low temperature they are dominated by impurity transitions (see Sec.(3), [70]). Note that the impurity nature of the transition at low temperature is not expected to change the dynamics observed in this experiment, since the excited impurity band largely overlaps with the excited miniband. We would like to point out that the strong temperature dependence of the absorption spectrum provides a means for measuring the effective temperature of the electron system [71]. In a quantum well, where the shape of the intersubband transition hardly changes with temperature, this is not possible.

For the time-resolved experiments the above sample was placed into a LHe flow cryostat equipped with KRS-5 windows and excited with the free-electron laser (FEL), which provided bandwidth limited Gaussian pulses [85][84] with a full width at half maximum (FWHM) between 1 and 2.5 ps (depending on the wavelength) at a 13 MHz repetition rate. This high repetition rate results in a far superior signal-to-noise ratio compared to macropulsed FELs or kHz optical parametric amplifier systems. The maximum pulse energy used for excitation was 50 nJ, corresponding to 650 mW average power, taking the sample geometry and attenuation of the cryostat windows into account. Under these

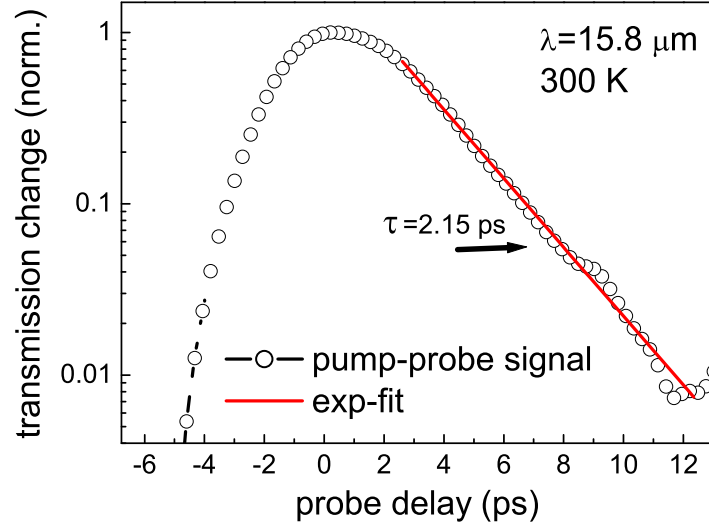


**Figure 5.2:** Pump-probe signal recorded for a wavelength of  $15.8 \mu\text{m}$  and a lattice temperature of 300 K. The interminiband transition is bleached, leading to a fast rise of the transmission. The subsequent can be fitted to an exponential decay with a time-constant of  $2.15 \pm 0.05$  ps.

conditions the lattice temperature of the samples increases by a few Kelvin. A fraction of the laser beam was split off using a Mylar beam splitter and served as the probe beam. Both pump and probe were focused onto the sample using a 10 cm focal-length off-axis parabolic mirror, taking care that the focal spot of the pump was larger than that of the probe. Behind the sample the transmitted probe beam was detected with a LN<sub>2</sub> cooled mercury-cadmium telluride (MCT) detector. As described in Sec.(4.2.1), the signals were recorded by chopping the pump beam mechanically at 350 Hz and measuring the probe signal using a lock-in amplifier at this frequency for high sensitivity. The pump-probe delay was achieved using a mechanical delay line.

Let us first analyze the pump-probe signal recorded at a wavelength of  $15.8 \mu\text{m}$  at room temperature, shown in Fig. 5.2. The FEL spectrum exhibited a FWHM of  $\Delta\lambda = 0.16 \mu\text{m}$ , which corresponds to a pulse duration of 2.2 ps for bandwidth-limited Gaussian pulses. In the recorded signal we find a fast bleaching of the respective interminiband transition, leading to a positive change in transmission. Subsequently, the electrons relax back to the ground miniband. The time constant gives a measure of the lifetime of the carriers that have been promoted to the second miniband. Fitting the observed decay signal with a single-exponential decay yields a decay-time of  $2.15 \pm 0.05$  ps. Although the pulse duration has a very similar value, from the clear asymmetric transient it is evident that we are able to determine confidently the corresponding relaxation rate. The value agrees reasonably well with calculations for interminiband relaxation via optical-phonons [33], which is the dominant relaxation channel in (quasi) two-dimensional heterostructures. Although these calculations were performed for InGaAs/InAlAs, it indicates that electron-

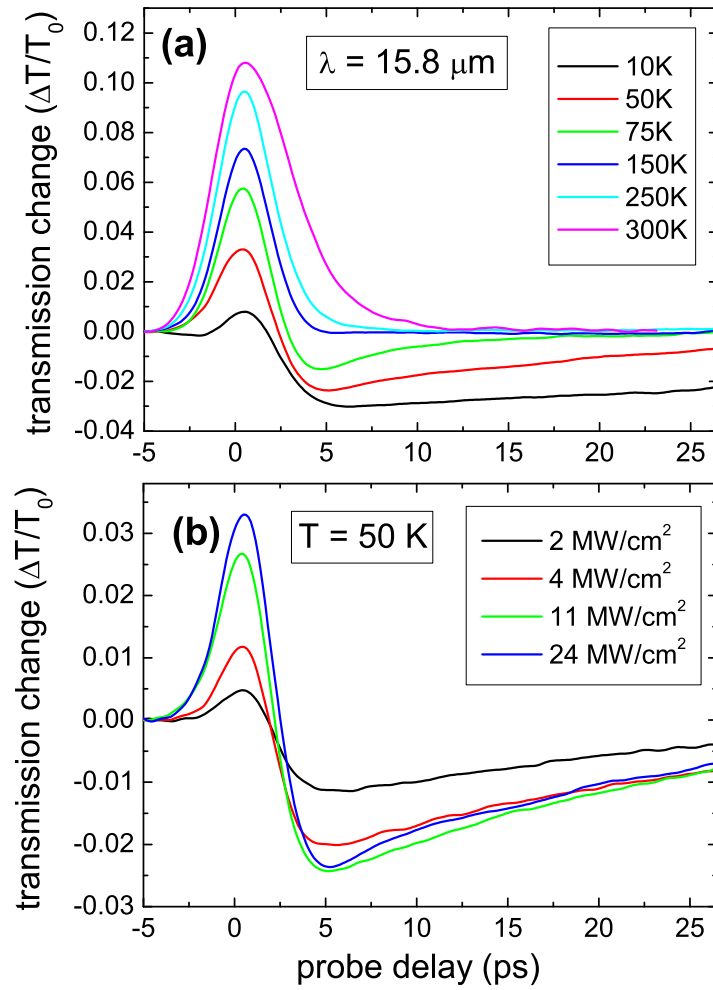


**Figure 5.3:** Probe transmission as a function of pump-probe delay recorded at  $15.8 \mu\text{m}$  for different temperatures (a) and different pump intensities at  $T=50 \text{ K}$  (b). Note that the intensity values are only accurate up to a factor of two approximately, while their relative values are accurate within 10%. The inset illustrates the sample geometry.



electron scattering cannot be much faster than the observed interminiband relaxation time. By varying the lattice temperature (Fig. 5.3(a)) and the pump power (Fig. 5.3(b)) we observe drastic changes of the transient behavior. At low temperatures the induced transmission first rises due to bleaching of the transition, then decreases again within a few ps and even goes negative, corresponding to induced absorption. This latter component relaxes on a much longer time scale. The fast bleaching component recovers by interminiband relaxation as well as by thermalization due to electron-electron scattering, which leads to a carrier distribution thermalized at a temperature higher than the lattice temperature. Exactly this is the reason for the negative (i.e. induced absorption) signal: from the linear absorption spectrum in Fig. 5.1 we know that at a wavelength of  $15.8 \mu\text{m}$  the absorption rises significantly with temperature. Thus an increase of the electron temperature leads to an increased absorption at this wavelength. The subsequent slower decay corresponds to the cooling of the electron distribution down to the lattice temperature. At higher temperature it is observed that

(i) the bleaching component becomes stronger, which is simply due to the fact that the linear absorption is larger, and

(ii) the thermalization/cooling component becomes weaker and faster. This is because at higher temperature the optical-phonon related energy loss rate of the electrons increases [71], but also there is more energy absorbed according to the spectra in Fig. 5.1. On the other hand the amplitude of the signal gets weaker, because at higher temperature the linear absorption does not change so much anymore (i.e., the intrinsic “thermometer” becomes less sensitive). The cooling time changes from 50 ps at  $T=10$  K to 6 ps at  $T=75$  K. At 250 K the fast relaxation and slower cooling component nearly cancel each other, and at  $T=300$  K a single exponential interminiband relaxation of 2.15 ps is observed.

The observations in Fig. 5.3(b), which shows the intensity dependence of the signal at a constant lattice temperature of 50 K, are consistent with the above picture: at higher pump intensity both the positive bleaching and the negative thermalization/cooling signal get larger and the cooling speeds up due to the larger temperature increase. Note that the vertical scale in Fig. 5.3 is essentially quantitative: the bleaching at the highest pump power reaches 3%, which corresponds to full saturation when compared with the vertical scale of the linear absorption spectrum shown in Fig. 5.1 (at 50 K and  $15.8 \mu\text{m}$ ). The negative heating signal reaches 2.4%, which corresponds to a rise from 50 K to approximately 100 K when again compared to Fig. 5.1. Fitting an exponential decay on the cooling curve (not shown) yields cooling times from 40 ps for the lowest to 18 ps for the highest pump intensity.

We performed similar pump-probe measurements at two other wavelengths: one at the high-energy peak of the absorption spectrum at  $\lambda = 9.3 \mu\text{m}$ , which corresponds to transitions near the center of the mini-Brillouin zone, and at an intermediate wavelength of  $13.75 \mu\text{m}$ . From the laser spectrum we could estimate the pulse length to 1.5 ps for  $9 \mu\text{m}$ . The intensity-dependent results for  $9.3 \mu\text{m}$  are shown in Fig. 5.4. The measured

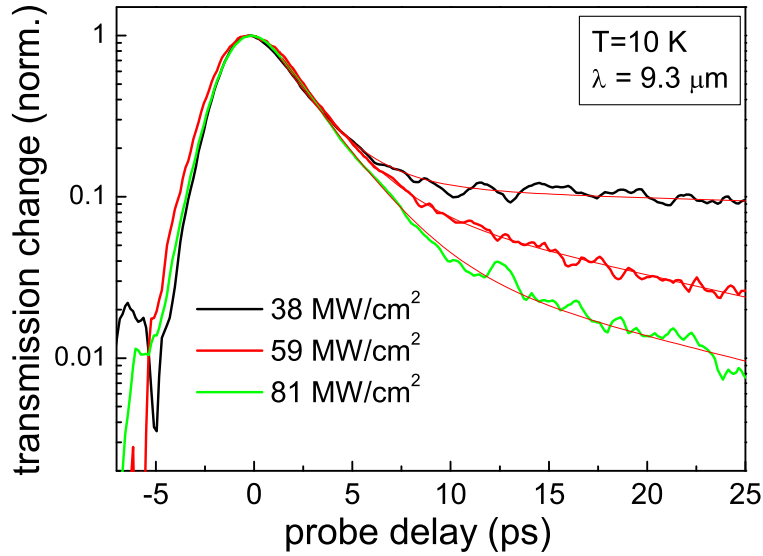


**Figure 5.4:** Probe transmission as a function of pump-probe delay recorded at  $9.3 \mu\text{m}$  for different pump intensities at  $T=10 \text{ K}$ . All curves exhibit a clear bi-exponential decay. While the short time-constant has an almost constant value of  $2.2 \text{ ps}$ , the longer time-constant, attributed to cooling of the electron gas, shortens from  $29 \pm 4 \text{ ps}$  to  $14 \pm 2 \text{ ps}$  with increasing pump intensity.

curves have been normalized for clarity. In contrast to the mono-exponential decay as in Fig. 5.2, we now observe a clear bi-exponential decay for all pump intensities with positive transmission change for all probe delays. The resulting best fits are shown as thin solid red lines for each pump-probe signal. While the fast decay reflects a combination of the inter-miniband relaxation and thermalization times of the excited electrons and only slightly increases from  $2.1$  to  $2.4 \text{ ps}$ , the slower component can be attributed to the subsequent cooling of the hot electron gas in the lower miniband. By increasing the pump intensity we find that the cooling times drop from  $29 \pm 4 \text{ ps}$  to  $\approx 14 \pm 2 \text{ ps}$  at a pump intensity of  $78 \text{ MW/cm}^2$ , respectively. This behavior is in agreement with the observed data for  $15.8 \mu\text{m}$ , where the cooling times decrease for higher pump intensities. This is again due to the fact that at higher electron temperatures the optical-phonon related energy loss rate of the electrons increases.

In Fig. 5.5 we show the pump-probe signals recorded for three different wavelengths: one at the high-energy peak of the absorption spectrum at  $\lambda = 9.0 \mu\text{m}$ , where the largest positive component related to cooling is expected, and at an intermediate wavelength of  $13.75 \mu\text{m}$  as well as for  $15.8 \mu\text{m}$ . The used pump intensities were  $40 \text{ MW/cm}^2$  at  $9 \mu\text{m}$ ,  $20 \text{ MW/cm}^2$  at  $13.75 \mu\text{m}$ , and  $24 \text{ MW/cm}^2$  at  $15.8 \mu\text{m}$ , respectively. In all cases, the lattice temperature was set to  $10 \text{ K}$ . We clearly see the difference of the recorded signals: with shortening the wavelength, the induced absorption (at  $15.8 \mu\text{m}$ ) first becomes much smaller and finally turns into a strong induced *transmission* in the case at  $\lambda = 9.0 \mu\text{m}$ . However, this behavior

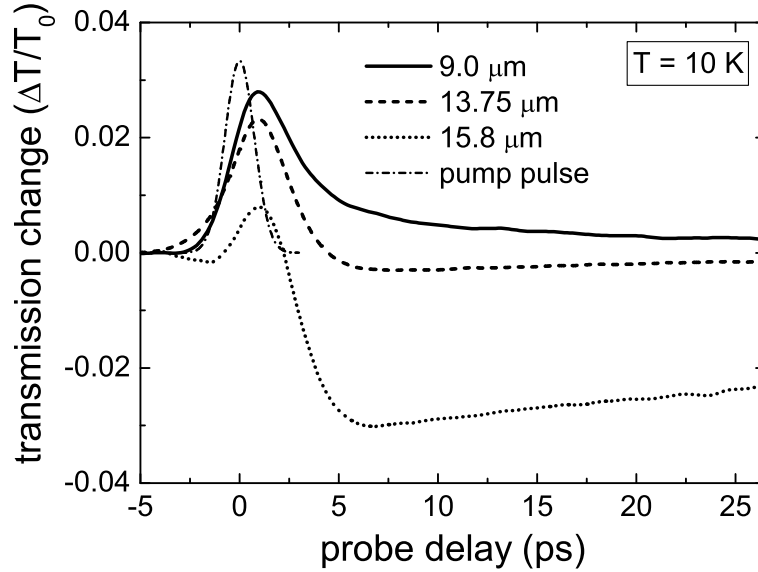


**Figure 5.5:** Probe transmission as a function of pump-probe delay recorded at  $T = 10$  K for different wavelengths as indicated. Also shown is the temporal pulse shape used to extract the decay times.

is again completely consistent with the temperature dependence of the linear absorption spectra (Fig. 5.1). At  $13.75 \mu\text{m}$ , the temperature change of the absorption is very small, e.g. we see a very small negative (i.e. induced absorption) signal (in other words, the intrinsic thermometer is not sensitive at this wavelength). At  $\lambda = 9.0 \mu\text{m}$ , it is obvious from Fig. 5.1 that the absorption decreases at higher temperatures. As a consequence now also the slow cooling transient is completely positive at all times.

Due to the large spectral spreading of the interminiband absorption in a superlattice and its temperature dependence it is thus possible to clearly separate different contributions of the electron dynamics. In isolated quantum wells this is not possible due to the parallel dispersion of the subbands, or at least to a much lesser degree: Lutgen *et al.*[46] were actually able to observe similar though much weaker effects in quantum wells due to the finite nonparabolicity of the subbands.

A similar behavior – positive and negative pump-probe signals – has also been observed by Woerner *et al.*[131] for the inter-valence band absorption in p-Ge. However, they ascribed both signal components to a change of carrier temperature (possible due to a nonmonotonic dependence of the absorption on the carrier temperature and a very fast hole-hole scattering) and excluded a real bleaching of the transition. Since in the present case the absorption depends monotonically on temperature for each wavelength, the fast signal must result from saturating the transition.

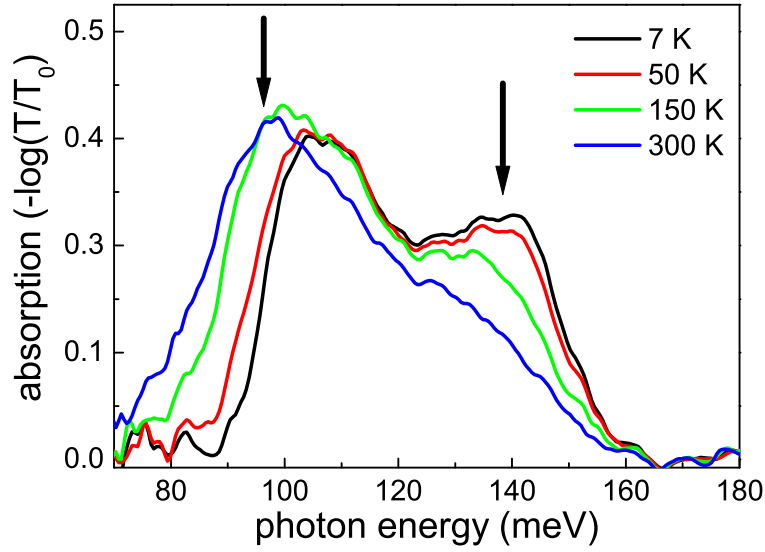


**Figure 5.6:** Linear absorption spectrum of the superlattice G999 that was used for the room-temperature pump-probe experiments, shown for different temperatures. The arrows indicate the excitation wavelengths.

At room temperature, where no contributions from cooling are expected, we studied the interminiband relaxation separately from cooling with a different GaAs/Al<sub>0.3</sub>Ga<sub>0.7</sub>As superlattice sample (G999). This sample consists of 300 periods with a well width of 85 Å and a barrier width of 31 Å, respectively. The resulting widths of the minibands are 9 meV for the lower and 41 meV for the upper (for details, see Table 2.1 on page 22). In order to provide electrons for interminiband absorption, the sample was doped in the center of the wells with a doping density of  $1 \times 10^{11} \text{cm}^{-2}$  per quantum well. With this sample, which is relative highly doped, we want to investigate the saturation behavior and the intensity dependence of the miniband transitions and its relaxation time. Therefore, the sample was prepared in a 38° waveguide geometry to obtain an electric field component parallel to the growth axis of the superlattice structure (see inset of Fig. 2.8(a)) and a high coupling efficiency to the interminiband transition. All experiments were done at a temperature of 300 K.

The linear absorption spectra, recorded at different temperatures, are shown in Fig. 5.6. At room temperature, the spectrum exhibits two maxima, reflecting the van Hove singularities at the center ( $\hbar\omega=135$  meV) and at the edge ( $\hbar\omega=95$  meV) of the mini-Brillouin zone. However, at low temperatures the spectrum has changed due to depopulation of the zone edge, and only transitions from the zone center ( $\hbar\omega =135$  meV) and impurity-related transitions (at 105 meV and 140 meV), are observed. We have studied the relaxation behavior at  $\lambda=13 \mu\text{m}$  (95 meV) and  $\lambda=8.9 \mu\text{m}$  (140 meV).

The results at a wavelength of 13  $\mu\text{m}$  are shown in Fig. 5.7. Here, the normalized

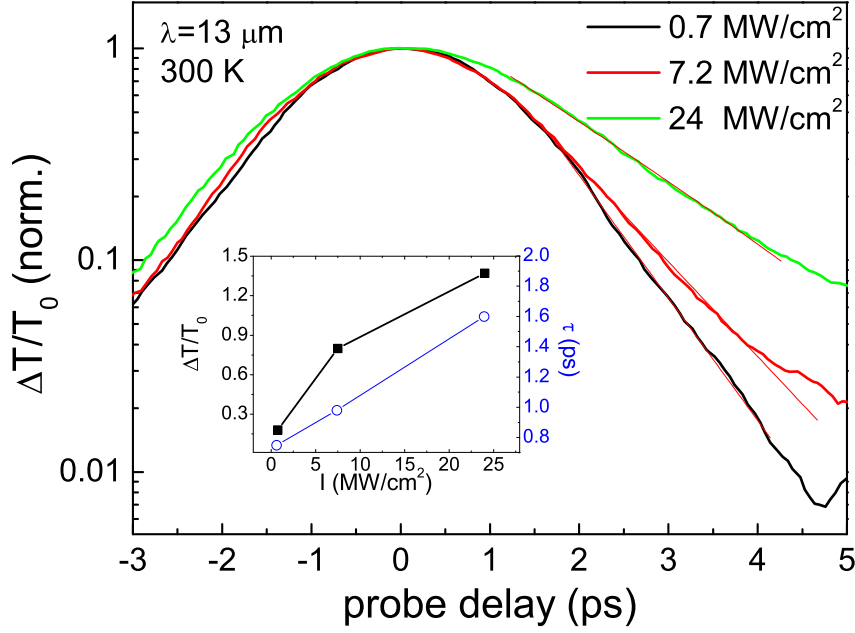


**Figure 5.7:** Normalized pump-probe signals recorded at a wavelength of  $13 \mu\text{m}$  and a lattice temperature of  $300 \text{ K}$ . The pump intensity was varied from  $0.7$  to  $24 \text{ MW/cm}^2$ . The solid red lines represent a best mono-exponential fit to the measured decay. The inset shows the change of transmission (black) and the extracted decay-times (blue) in ps.

pump-probe signal is depicted for different excitation densities, ranging from  $0.7$  up to  $24 \text{ MW/cm}^2$ .  $\Delta T$  denotes the change of transmission with and without pump light  $\Delta T = T(I) - T(I = 0)$  and  $T_0 = T(I = 0)$  is the bare probe transmission. At the lowest intensity, we measure an almost symmetric pump-probe transient. This implies a very short decay time, yielding a value of only  $0.8 \text{ ps}$ . However, this value surely is afflicted with an error of  $20 \%$ , due to the limited time-resolution from the FEL pulses. At the medium pump intensity of  $7.5 \text{ MW/cm}^2$  we find a longer decay time, now being  $1 \text{ ps}$ . The longest decay time is observed at the highest pump intensity. The best mono-exponential fit gives a relaxation time of  $1.6 \text{ ps}$ . The different decay times are shown in the inset of Fig. 5.7 as the blue circles. There seems that the decay time increases linearly with the pump intensity; this effect will be discussed later.

Also shown in the inset of Fig. 5.7 is the change in transmission, calculated from the transmission of the probe pulse with and without pump excitation. At the highest pump-intensity, we reach a value which is  $> 1$ . This, in fact, is due to the strong absorption at this respective wavelength, as shown in Fig. 5.6. Taking this absorption into account, we then can deduce the degree of saturation of the respective interminiband transition, where we find that the interminiband absorption is bleached to  $85 \%$ . Note that this saturation behavior is very sensitive to the absorption rate at the respective wavelength.

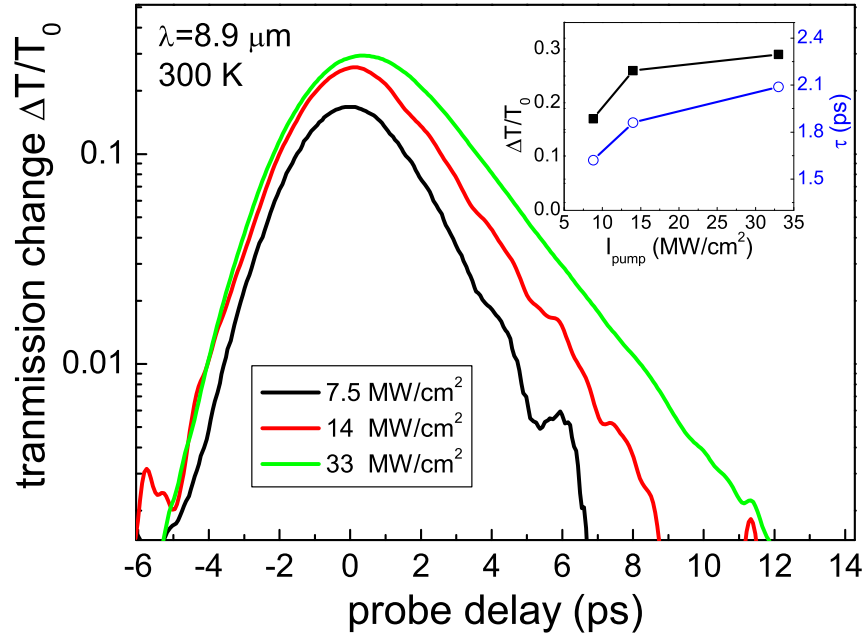


**Figure 5.8:** Pump-probe signals recorded at a wavelength of  $8.9 \mu\text{m}$  and a lattice temperature of 300 K. The pump intensity was varied from 7.4 to  $33 \text{ MW/cm}^2$ . The inset shows the extracted decay-times (blue) from a mono-exponential fit to the decay and the transmission change (black squares) as a function of the pump intensity.

We performed the same experiments of the interminiband transition at the center of the mini-Brillouin zone, which, in this case is resonant at a wavelength of  $8.9 \mu\text{m}$ , as seen in Fig. 5.6. The measured pump-probe curves are shown in Fig. 5.8, recorded for three different pump intensities, ranging from 7.4 to  $33 \text{ MW/cm}^2$ . Again, a fast rise of the signal is observed, corresponding to the bleaching of the interminiband transition. Its rise time is essentially given by the duration of the FEL pulses, which is 1.5 ps in this case. The subsequent decay can be approximated by a mono-exponential decay. As observed in the case of a pump wavelength of  $13 \mu\text{m}$ , the decay time increases for larger pump-intensity. We deduce a relaxation time of 1.6 ps for the lowest, and of 2.1 ps for the highest pump intensity, respectively. This change is illustrated in the inset of Fig. 5.8, given by the blue open circles. Due to the decreased oscillator strength at this wavelength, it is expected that saturation occurs on a somewhat larger pump-intensity than in the case of  $13 \mu\text{m}$ . The change of transmission is given in the inset of Fig. 5.8, represented by full black squares. Comparing the change in transmission to the absorbance, we find that the interminiband transition is bleached to 90 % at the highest pump-intensity. This result is in contrast to our expectations. But on the other hand, the relaxation time increased at this wavelength, leading to a reduced saturation intensity, as will be discussed later.

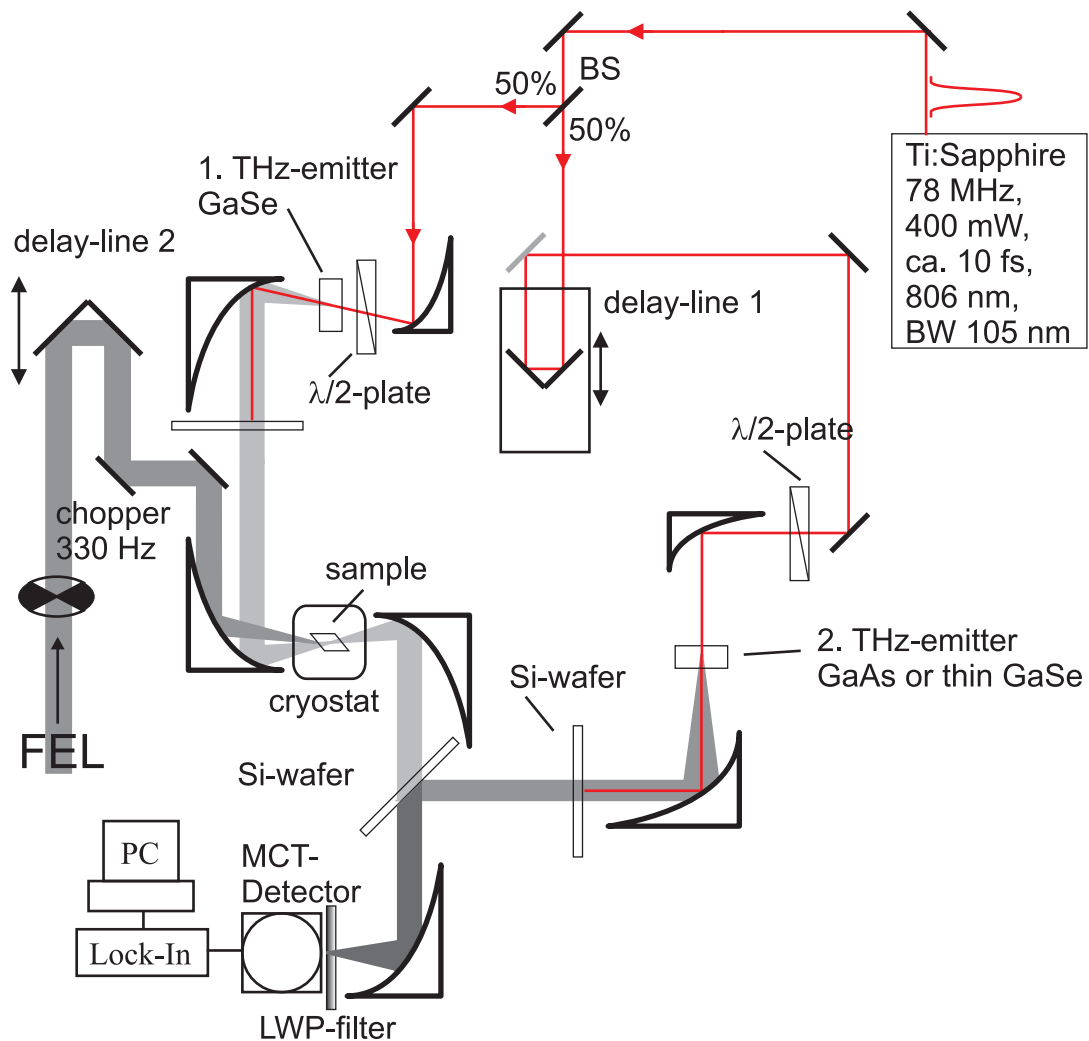


**Figure 5.9:** Schematic setup for the FEL-pump broadband THz-probe experiments. The probe beam is focused once more between two off-axis parabolic mirrors, where the sample, mounted on a cold finger cryostat, can be inserted. The FEL pulses undergo a separate adjustable delay and are focused non-collinearly with the probe beam onto the sample. The temporal change of transmission is measured by changing the delay of the FEL pulse, additionally its spectral changes can be obtained by an interferometric cross-correlation with the reference beam.

## 5.2 FEL-pump broadband THz-probe experiments

Up to this point we were using solely the infrared pulses from the FEL to investigate the dynamics of interminiband transitions in superlattices. Thus the pump pulse and the probe pulse had the same wavelength, they were degenerate. In an isolated two-level system exhibiting only a single sharp resonance, this method is the appropriate technique. However, superlattices, as shown before, have a broad absorption range, resulting from the strong coupling of the electronic states due to the thin barriers between the individual quantum wells. In the previous degenerate pump-probe measurements, the effect of electron heating influences the carrier density not only at the respective  $k_z$ -value but all over the mini-Brillouin zone. Therefore it is of large interest to observe spectral changes along the mini-Brillouin zone  $k_z = [0..π/d]$  after a resonant excitation, for instance at the zone-center,  $k_z = 0$ . At this respective  $k_z$  position, electrons excited to the second miniband can relax either directly back to their ground state in the lower miniband, or relax *within* the second miniband towards  $k_z = π/d$  by various scattering mechanisms (compare Fig. 5.10). Thus, it is desirable to observe the transmission change at  $k_z = π/d$ , while tuning the excitation to  $k_z = 0$ . By this technique, transients from direct interminiband relaxation can be separated from the cooling components, actually representing *intraminiband* transitions.

For such experiments, the above described methods of degenerate pump-probe experiments and the generation of broadband THz pulses are combined to a FEL-pump and (broadband) THz probe experiment. As a unique feature this method allows to measure the temporal *and* spectral change with a single THz pulse at a high repetition rate, resulting in a superior signal-to-noise ratio compared to table-top systems that typically operate at 1 kHz. The schematic setup for these experiments is shown in Fig. 5.9. Here a synchronized Ti:Sapphire laser that delivers 10 fs near-infrared pulses is used to generate ultrashort THz pulses from 12 to 33 THz with a spectral width ranging from 5 to 15 THz, serving as probe pulses for time-resolved experiments. The THz- and FEL pulses then are focused non-collinearly onto the sample, which can be placed in a LHe cold-finger cryostat. The time evolution of the probe pulse is measured by varying the delay of the FEL pulse, using delay stage 2. The frequency changes within the probe pulse are then recorded by a cross-correlation with a quasi single-cycle THz pulse, which is focused on an MCT detector collinearly with the probe pulse. By variation of the time delay between probe and reference pulse, the electric field of the probe pulse is obtained. If the FEL pulses and the THz-probe pulses are spectrally well separated, we insert a suitable edge-filter in front of the detector, which reduces noise due to scattered pump light. The sensitivity can be enhanced by placing a mechanical chopper into the FEL beam path and using a Lock-In amplifier, giving the temporal transmission change of the probe pulse. A major benefit of this method is that the redundant THz pulses that do not coincide with the pump pulses



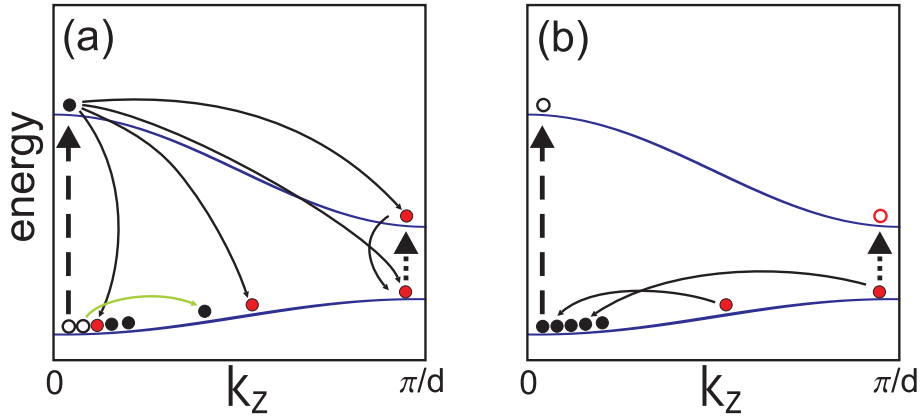


**Figure 5.10:** Relaxation processes and the wavelength configuration used in the two-color experiments: (a) illustrates the excitation process at low temperatures and the fast relaxation (black arrows) and thermalization (green) that lead to transmission change of the probe pulse. The right part (b) shows the relaxation paths for cooling within the lower miniband.

are filtered out. Consequently, since we are using a slow MCT detector that measures the time-integrated THz signal, the obtained change of transmission has to be multiplied by six, resulting in the absolute transmission change ( $f_{\text{THz}}^{\text{rep}} = 6 \times f_{\text{FEL}}^{\text{rep}}$ ). Also the *spectral* change of the probe beam can be measured by Lock-In detection, simply by performing a cross-correlation, which gives the spectral change of the THz pulse that coincides with the FEL pulse.

We start first with the cooling behavior which is analyzed for three different superlattice samples, i.e. sample G998, H175 and H171 (see Table 2.1). Whereas the doping concentration was nearly the same for all samples, the width of the respective minibands was varied by choosing different structure parameters. Here we investigate the cooling dynamics in the ground-state minibands with a width of 11, 25, and 45 meV, respectively. All interminiband-absorption spectra show a strong temperature dependence reflecting the electron distribution within the lowest miniband. The electron temperature was monitored by the absorption strength at the edge of the mini-Brillouin zone, while exciting the sample at the zone-center transition. This is illustrated in Fig. 5.10, in combination with possible relaxation paths directly after the pump pulse (a) and the relaxation that leads to cooling (b). The change of transmission of the probe pulse gives a direct measure of the temperature of the Fermi-distribution in the lower miniband after a strong excitation [71].

Let us start with the superlattice exhibiting the smallest miniband width. Its temperature-dependent absorption spectra and the respective pump-and probe configuration are shown in Fig. 5.11. The spectrum exhibits a strong temperature dependence, leading to a complete absence of absorption on the low energy side at a temperature of 6 K. The width of the lower miniband can be estimated from the difference of the impurity-peak at 105 meV and the low-energy miniband-transition at 94 meV ( $k_z = \pi/d$ ), resulting in a width of  $\Delta_1 = 11$  meV. This value is in reasonable agreement with the calculated value of 9

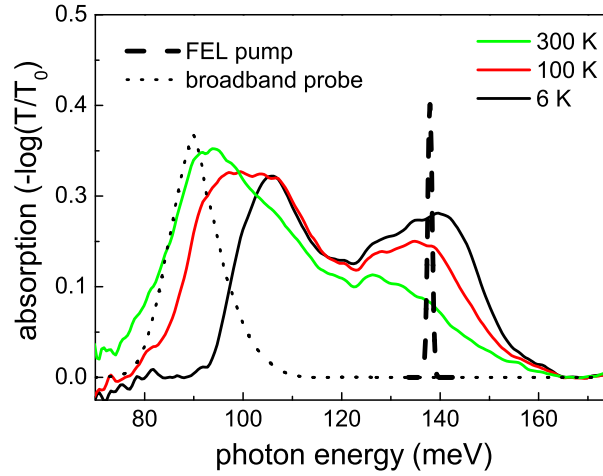


**Figure 5.11:** Linear absorption spectra of the superlattice sample G998, shown for different temperatures. Also shown is the configuration of the two-color pump-probe experiments. The dashed black line marks the spectral position of the FEL pump beam, while the dotted line represents the broad probe beam which is tuned to the range of maximum transmission change with temperature.

meV. For investigation of the cooling dynamics, the FEL was tuned to a photon energy of 138 meV ( $8.9 \mu\text{m}$ ) and the THz pulse to a central frequency of  $\hbar\omega = 90$  meV. At this energy the strongest change of transmission due to the electron temperature is expected. The results of the two-color pump-probe measurements are shown in Fig. 5.12. The sample was mounted on a LHe-flow cold-finger cryostat and the lattice temperature was kept constant at 6 K. In the upper part of Fig. 5.12, the negative change in transmission ( $-\Delta T/T_0$ ) is shown for different pump intensities. There we find a strong decrease of the transmission when the pump pulse arrives. Subsequently the transmission recovers on a long time scale. The origin of the negative differential transmission is the following: electrons are excited to the upper miniband, thermalize and relax back to the ground miniband on a picosecond timescale. Here they additionally heat up the electronic distribution by scattering mechanisms leading to an effective electron temperature higher than the lattice temperature. According to the linear absorption spectra shown in Fig. 5.11, this heat-up results in increased absorption (negative transmission). Note that in principle one would also observe the inter-miniband relaxation, identified as the rise-time of the observed signal. However, the time-resolution of the experiments was limited by a temporal jitter of the involved lasers, giving a time-resolution of about 3 ps. Thus, the inter-miniband relaxation time, which has been specified to 1-2 ps, cannot be resolved precisely and is also not the scope of this experiment.

By increasing the pump intensity, we find an increase of the induced absorption, however, quickly saturating at a pump intensity of about  $12 \text{ MW/cm}^2$ . Further increase of the pump intensity leads to no further transmission decrease, in fact, at the highest pump

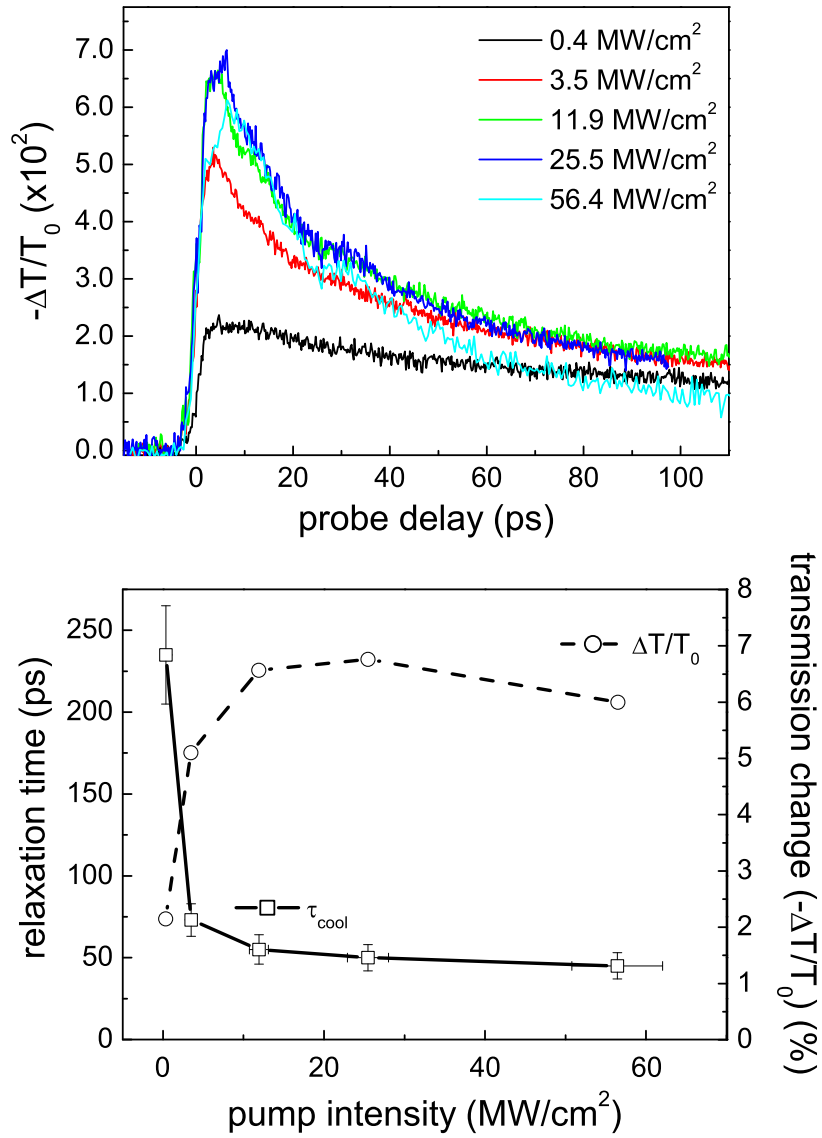


**Figure 5.12:** Two-color pump-probe signals from sample G998 at a lattice temperature of 6 K, recorded for different pump-intensities (top). On the bottom the extracted cooling times and absolute transmission changes are plotted as a function of the pump intensity.

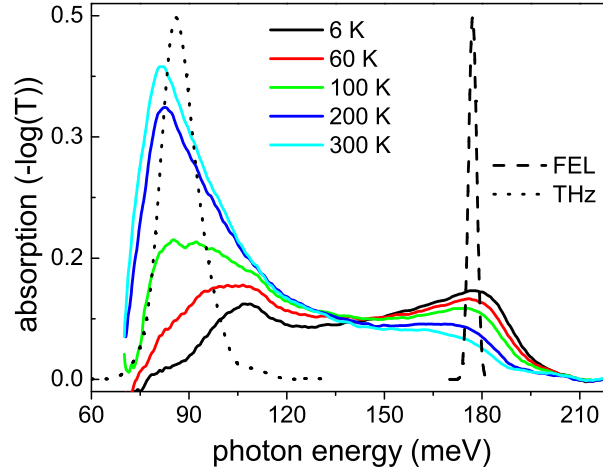


**Figure 5.13:** Linear absorption spectra of the superlattice sample H175, shown for different temperatures. Also shown is the configuration of the two-color pump-probe experiments. The dashed black line marks the spectral position of the FEL pump beam ( $\lambda = 7.0 \mu\text{m}$ ), while the dotted line represents the probe beam.

intensity the peak change in transmission even *decreases*. We also find that in all cases (except at the lowest intensity) the curves more or less merge together at a delay time of about 100 ps. Thus, regardless of the used pump intensity, the electron gas exhibits an equal temperature at this point. The spectrally integrated change of transmission is plotted in the lower part of Fig. 5.12, shown as the open circles. There we see a fast rise and saturation, and eventually a small drop of the induced transmission change. Also shown in this graph is the extracted cooling time as a function of the pump intensity. The times were manually extracted from the pump-probe curves and defined as the time the induced absorption drops to the  $1/e$ -part of its highest value. In this graph we find a very long decay time for the lowest intensity, having a value of  $230 \pm 20$  ps. With higher pump-intensity, the cooling time rapidly decreases and ends up in an almost constant value of  $50 \pm 5$  ps.

The pump-probe configuration of the second superlattice, having an intermediate lower miniband-width of 25 meV, is shown in Fig. 5.13. The growth parameters of this sample (H175) are shown in Table 2.1. Again, the spectrum exhibits a strong temperature dependence, suitable for investigation of the cooling dynamics in the lower miniband. From the spectra, we can extract a width of the lower miniband of 25 meV, somewhat larger than the calculated value (20 meV). Due to depopulation of the lower miniband at  $k_z = \pi/d$  for low temperatures, the absorption almost vanishes at this respective  $k_z$  position, whereas at high temperatures we observe a strong absorption signal. Thus, this spectral region is again ideal to study the evolution of the electron temperature after an excitation via the transmission change of the probe pulse. The pump pulse is tuned to the

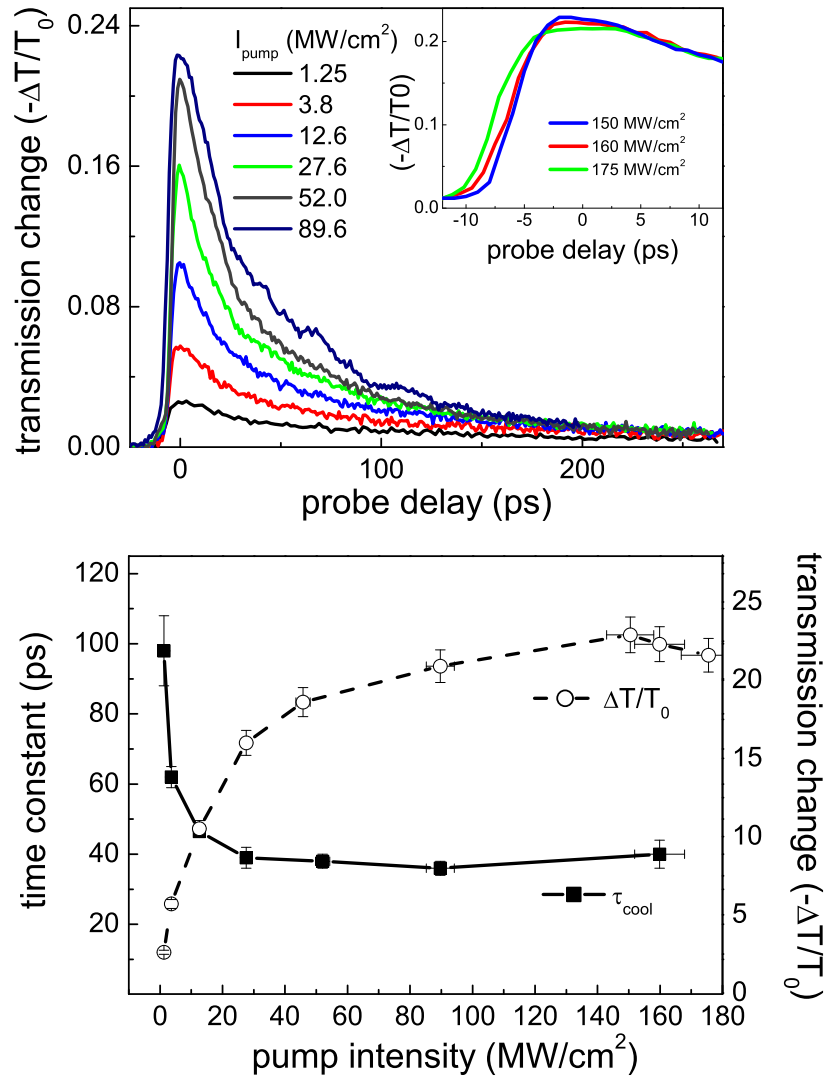
maximum absorption at 6 K, which is 177 meV ( $\lambda = 7.0 \mu\text{m}$ ). This absorption reflects the interminiband-transition at  $k_z = 0$ .

Fig. 5.14 shows the results for the pump-probe measurements, performed for different pump intensities. Note that the vertical scale is negative, thus we always have a negative change of transmission. Similar to the previous sample, a fast rise of the induced absorption is found. This is again due to the fast interminiband relaxation at the selected pump wavelength and the heating of the electron gas in the lower miniband due to scattering events. After this, the electron temperature relaxes back to the lattice temperature. Except for the lowest intensity, all pump-probe curves merge after about 200 ps, indicating an equal electron temperature for all pump intensities. From the linear absorption spectrum, we can estimate an electron temperature of about 30 K at this point. The absolute change of transmission is shown for a wide range of pump intensities (1.25-175 MW/cm<sup>2</sup>) in the lower part of Fig. 5.14. With increasing intensity, we find a fast saturation of the induced heating at an intensity of about 90 MW/cm<sup>2</sup>. At higher pump-intensities, the absolute change of transmission becomes smaller. This is also illustrated in the inset of the upper part of Fig. 5.14, where the pump-probe curve for the highest intensities are shown around zero time-delay. There we find a more and more flat peak-transmission change, during the direct temporal overlap of the pump- and probe pulse. Behind this point, the electronic temperatures are the same again and relax in the same way as for an intensity of 89 MW/cm<sup>2</sup>.

Also the intensity-dependent cooling times have been extracted from the measured data and are shown in the lower part of Fig. 5.14, represented as the open circles. For the lowest pump intensity, we find a long cooling time of about 100 ps. The cooling time drops quickly with increasing pump intensity, and above an intensity of 30 MW/cm<sup>2</sup>, the cooling time remains more or less constant at a value of 40 ps.

The interminiband absorption spectrum of the third superlattice investigated in this context (H171) is depicted in Fig. 5.15. This sample exhibits an extremely wide absorption spectrum, ranging from 70 meV up to 300 meV. This was achieved by choosing a thin coupling barrier. The growth parameters are listed in Table 2.1. It also has a remarkably different temperature dependence: starting at low temperatures, the absorption spectrum only slightly changes up to a temperature of 100 K. With further temperature increase a sharp resonance shows up at 82 meV, which denotes the zone-edge transition ( $k_z = \pi/d$ ). Simultaneously the absorption at the zone center (270 meV) decreases due to the different occupation within the first miniband. Due to the strong coupling, the lower miniband has a width of about 45 meV, in good agreement with the calculated value of 48 meV.

The temperature dependence is again used to monitor the time evolution of the electron temperature after a resonant excitation at the zone-center transition ( $\lambda = 4.5 \mu\text{m}$ ). The THz-probe pulse is tuned to 82 meV as the central frequency, sampling the electron temperature via the induced absorption due to occupation of the miniband edge after heating of the electron gas. The pump-probe signals were measured at a lattice temperature of 6 K



**Figure 5.14:** Two-color pump-probe signals from sample H175 at a lattice temperature of 6 K, recorded for different pump intensities (top). The inset shows a focused view around zero time delay for the three highest intensities. On the bottom the extracted cooling times and absolute transmission changes are plotted as a function of the pump intensity.

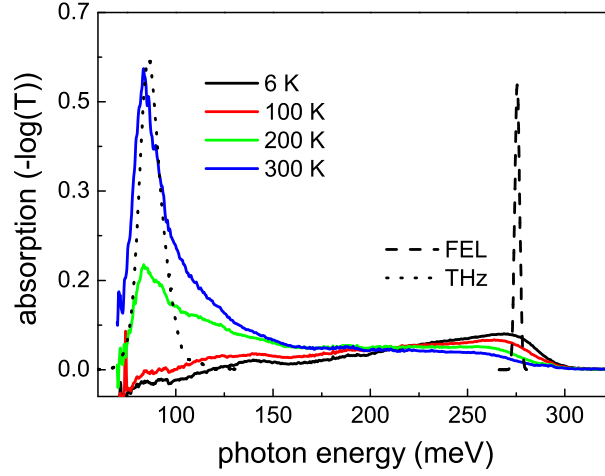


**Figure 5.15:** Linear absorption spectra of the superlattice sample H171, shown for different temperatures. Also shown is the configuration of the two-color pump-probe experiments. The dashed black line marks the spectral position of the FEL pump beam ( $\lambda = 4.5 \mu\text{m}$ ), while the dotted line represents the probe beam.

and were recorded for different pump intensities. The results are shown in Fig. 5.16. Also in this structure we find a negative transmission change for all applied pump intensities. However, the transient curves show a rapid decay, much faster than in the previous samples. The absolute transmission change and the relaxation times are plotted in the lower part of Fig. 5.16. Although we expect a strong transmission decrease at higher electron temperatures, the measured values are rather small, as the maximum transmission change is only 3 %. This is also because of the relative small oscillator strength at the pump wavelength at which we cannot observe a full saturation of the reduced transmission. However, at the highest pump intensity the onset of saturation is shown. Nevertheless, the electron temperature obviously does not rise at much as in the other samples. Also the observed cooling times are much shorter now, in fact, by more than one order of magnitude. Additionally, the cooling times stay constant at a value of about 3.5 ps, at least within the accuracy of our experiment. Thus, at this sample, having a miniband-width of 45 meV, the heating effects are less pronounced and the cooling appears on a much faster time scale than in the samples with a miniband width of 11 and 25 meV, respectively.

In the above measurements, investigating the cooling times in different superlattice samples at a lattice temperature of 6 K, we have found a more or less clear saturation behavior of the transmission change, induced by the heat-up of the electron gas. Moreover, in case of the samples G998 and H175, we have found that after saturation, the absolute change in transmission *decreases* again at the highest pump intensities. Thus it seems that once the electron temperature has increased to its maximum, additional processes within the

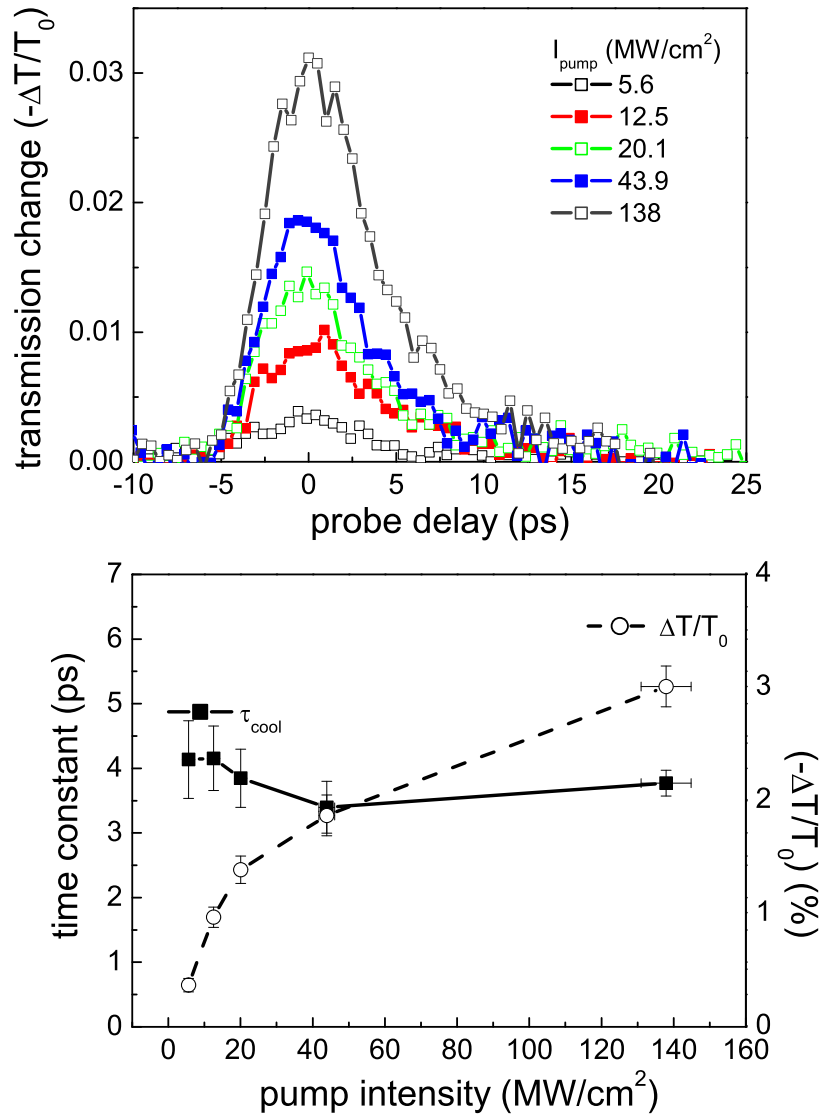


**Figure 5.16:** Two-color pump-probe signals from sample H171 at a lattice temperature of 6 K, recorded for different pump-intensities (top). On the bottom the extracted cooling times and negative transmission changes are plotted as a function of the pump intensity.



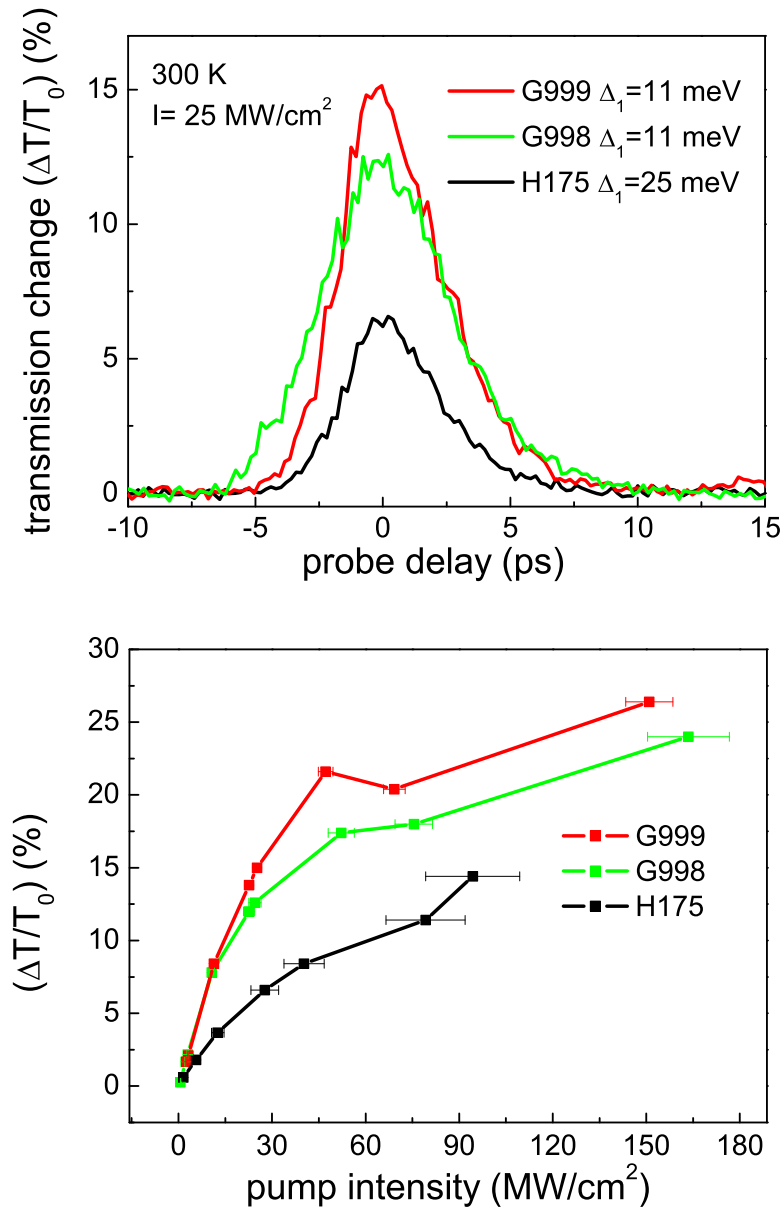


**Figure 5.17:** Room temperature two-color pump-probe signals of three different superlattice samples at a fixed pump intensity of  $25$  MW/cm<sup>2</sup> (top). The lower graph shows the transmission change as a function of the pump intensity.

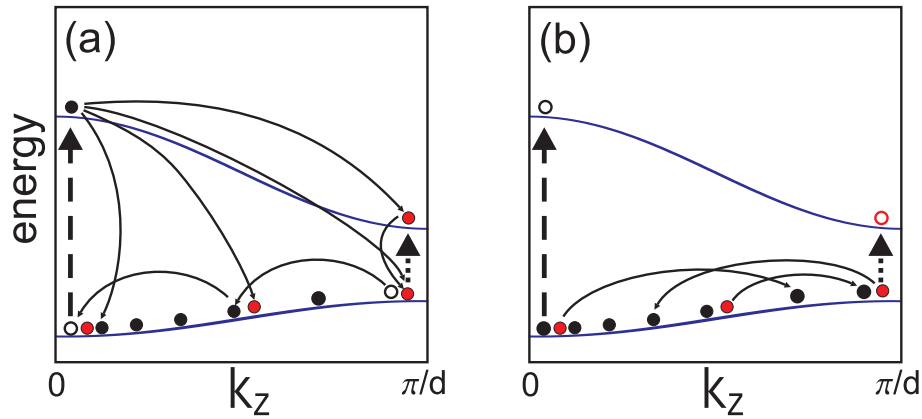


**Figure 5.18:** Relaxation processes and the wavelength configuration used in the two-color experiments at room temperature: (a) illustrates the excitation process and the fast relaxation that lead to transmission change of the probe pulse. In contrast to Fig. 5.10, we can now have relaxation towards the zone center, immediately after the pump pulse depleted the zone-center. The right part (b) shows the relaxation back to equilibrium, redistributing electrons within the lower miniband according to the Fermi distribution.

superlattice structure lead to a decrease of the negative transmission. To understand this process, the pump-probe measurements are carried out at room temperature, where the lower miniband is already occupied at the mini-Brillouin-zone edge ( $k_z = \pi/d$ ), due to the expanded Fermi distribution. In these experiments, heating effects should play a much smaller role and solely the reduced absorption should be measured when pumping at the zone-center transition. The measured transmission changes at a pump intensity of 25 MW/cm<sup>2</sup> are shown in the upper part of Fig. 5.17. For all investigated samples we now find a *positive* change in transmission, rising within the time resolution of the experiment and decaying on a timescale of a few picoseconds. Thus, at room temperature, excitation at the zone center transitions induces *reduced* absorption at the zone-edge transitions. This fact indicates that we not only have relaxation paths at the pump-wavelength, but also over the mini-Brillouin zone. In fact, with this positive transmission change we demonstrate that also relaxation *within* the upper and the lower minibands takes place.

As illustrated in Fig. 5.18, the positive pump-probe-signals can be attributed to two separate processes:

(i): electrons located at the lower miniband edge relax toward the miniband center, since electrons here are strongly excited to the upper miniband, leading to a depletion of the electron states at the mini-Brillouin zone center. However, in samples G998, G999, and H175 this process can be expected to have only a small contribution, since the widths of the lower minibands are well below the LO-phonon energy, making other (much less efficient) relaxation channels necessary.

(ii): electrons that have been promoted to the upper miniband can relax not only directly back at  $k_z = 0$ , but can also undergo relaxation towards the mini-Brillouin zone edge within the miniband. Once they have arrived there, they lead to a reduced absorption at

the probe-wavelength, either simply by Pauli-blocking or stimulated emission. Note that the latter process is the main mechanism for operation of superlattice quantum cascade lasers[130].

The change in transmission for the investigated samples is shown in the lower part of Fig. 5.17, where  $\Delta T/T_0$  is plotted for a series of different pump intensities. There we find that with increasing pump intensity the transmission rapidly increases, and also saturation behavior is observed. The sample with the largest absorption strength, of course, has the largest relative change of transmission. However, from the linear absorption spectra shown above we can deduce the degree of the suppressed absorption of the respective sample.

$$\begin{aligned} \Delta\alpha &= \frac{\alpha_{\text{pump}} - \alpha_0}{\alpha_0} = \frac{-\ln(T_{\text{pump}}) - (-\ln(T_0))}{-\ln(T_0)} \\ &\approx \frac{(1 - T_{\text{pump}}) - (1 - T_0)}{1 - T_0} = \frac{-T_{\text{pump}} + T_0}{1 - T_0} \end{aligned} \quad (5.1)$$

where  $T_0$  denotes the transmission without the pump pulse. This was done for pump intensities of 6.2 MW/cm<sup>2</sup> (in the linear regime) and at 80 MW/cm<sup>2</sup>, where saturation already sets in. From there find that at 6.2 MW/cm<sup>2</sup> in sample G999 the interminiband absorption integrated over the probe wavelengths was reduced by 4.5 %, whereas at sample G998 a value of 5 % is achieved. Sample H175 does not exhibit such a pronounced saturation behavior, since the oscillator strength is less at the pump wavelength. Consequently in this sample we determine that the absorption is quenched by 2 %. At an intensity of 80 MW/cm<sup>2</sup>, we reach values of 21 % for samples G999 and G999 and 11 % for sample H175, respectively. Overall the saturation behavior is different then at low temperatures, indicating that in the latter case we have competing processes such as heating of the electron gas which leads to a transmission decrease and the relaxation within the upper miniband, partially reducing this effect.

In these experiments, we clearly observed electronic relaxation within and in between the upper and the lower miniband. The two-color experiments at low temperature revealed the different cooling times for different superlattice samples. The cooling times depend strongly on the width of the lower miniband and on the pump intensity, and cooling times ranging from 230 down to 3 ps have been observed. In the samples with strong interminiband absorption at the pump-wavelength (G998, H175), a clear saturation of the transmission decrease was measured, which was even reduced for the highest pump intensities. The latter effect was explored by performing the same experiments at room temperature, where cooling effects do not play a role. There we found an always positive change in transmission, attributed to ultrafast relaxation *within* the upper and the lower miniband. These results and their conclusions will be discussed at the end of the next section.

### 5.3 Discussion

In order to evaluate the observed interminiband dynamics, we compare our results for the single-color experiments at room temperature to a two-level rate-equation model. With this model we can directly simulate the bleaching transients, verifying our approach that the interminiband relaxation can be extracted from pump-probe signals, where the duration of the exciting and probing pulse is of the same order as the observed relaxation times. With this model, also the saturation observed can be reproduced. After this we will shortly discuss the main scattering mechanisms that lead to a fast relaxation and cooling. Also the intensity dependence of the observed relaxation times will be addressed.

#### Two-level rate-equation model

A simple approximation of the interminiband absorption is a two-level model, of course only suitable for room temperature, where no cooling on longer-timescale mixes with the interminiband relaxation.

The coupled rate equations for the populations of a two-level system are given by:

$$\begin{aligned}\frac{dN_1}{dt} &= +W_{12}(N_2 - N_1) + \frac{N_2}{\tau_{21}} \\ \frac{dN_2}{dt} &= -W_{12}(N_2 - N_1) - \frac{N_2}{\tau_{21}}\end{aligned}\quad (5.2)$$

where  $W_{12} = \sigma\Phi$  is the transition rate calculated from Fermi's Golden Rule, given by the absorption cross section  $\sigma$  and the photon flux  $\Phi$ . An important condition is that the number of electrons has to be constant,  $N = N_1 + N_2 \equiv \text{const.}$ , allowing to eliminate  $N_1$  from the coupled equations:

$$\frac{dN_2}{dt} = -W_{12}(2N_2 - N) - \frac{N_2}{\tau_{12}} = -N_2 \left( \frac{1}{\tau_{12}} + 2W_{12} \right) + W_{12}N \quad (5.3)$$

Eqn.(5.3) can easily be solved by integration, giving the population of the second level. Note that in the case of pulsed excitation, the transition rate also becomes time-dependent and it linearly depends on the intensity of the exciting pulse

$$W_{12}(t) = \frac{I(t)\sigma}{\hbar\omega} \quad (5.4)$$

For our simulations, we assume a Gaussian pulse shape.

The absorption is generally proportional to the population in the second level subtracted from the population in the lower level, which can be simplified by use of  $N = N_1 + N_2 \equiv \text{const.}$ :

$$\alpha \propto (N_1 - N_2) = 2N_2 - N. \quad (5.5)$$

The transmission change is then obtained by

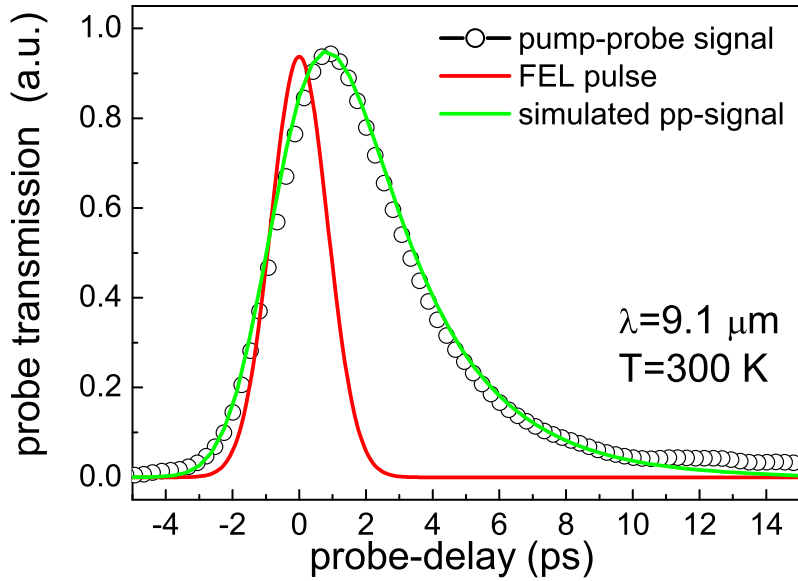


**Figure 5.19:** Room temperature pump-probe signal of sample G757 at  $\lambda = 9.1 \mu\text{m}$  and the result from a two-level rate-equation model.

$$\Delta T = (T_{\text{pump}} - T_0) \propto (e^{-\alpha x} - e^{-\alpha_0 x}) \quad (5.6)$$

where  $\alpha_0$  is the initial absorption. To simulate the change in transmission of a (weak) probe pulse, the obtained transmission change has to be convolved with its time envelope, which is again assumed to be Gaussian. This results in a simulated pump-probe curve comparable to the measured transients.

Let us now discuss the single-color-experiments. First we simulate the transient behavior at 300 K, recorded at a wavelength of  $9.1 \mu\text{m}$  at sample G757 with the rate-equation model described above. From the FEL spectrum, we deduced a pulse duration of 2 ps, and from an exponential fit to the decay we find a relaxation time of 2.5 ps. With these values we simulated the pump-probe signal at an intensity of  $50 \text{ MW}/\text{cm}^2$ . The results are shown in Fig. 5.19.

From there we find that the pump-probe signal rises during interaction with the pump pulse and then decays with the given decay time. The dotted curve is the experimental data, matching the simulating almost perfectly. Thus, even with pulse durations that are of the same order as the measured relaxation time, it is possible to extract the respective time-scales with good confidence.

As already mentioned above, the main relaxation mechanism for electrons in semiconductors is the relaxation by interaction with optical phonons [132]. Since LO-phonons exhibit only a small dispersion [133], it is necessary that the energy spacing between the investi-

gated electronic states is equal or larger than the optical phonon energy, which is 36 meV for the case of GaAs. At energy spacings below the optical phonon energy, interaction can only take place via their absorption or by other relaxation processes. Compagnone *et al.* [33] performed Monte Carlo simulations of the interminiband dynamics and identified LO-phonon interaction as the main relaxation mechanism for the interminiband relaxation. The Hamiltonian describing the interaction between electrons and phonons is given by:

$$H_{e-ph} = \sum_{\mathbf{q}} \left[ \alpha(\mathbf{q})(e^{i\mathbf{q}\mathbf{r}}b_{\mathbf{q}} + e^{-i\mathbf{q}\mathbf{r}}b_{\mathbf{q}}^{\dagger}) \right] \quad (5.7)$$

Here  $b_{\mathbf{q}}$  and  $b_{\mathbf{q}}^{\dagger}$  are creation and annihilation operators for a phonon mode  $\mathbf{q}$  and  $\alpha(\mathbf{q})$  is the electron-phonon interaction. For the polar optical phonons, the strength of this coupling via the Fröhlich interaction is [134]

$$|\alpha(\mathbf{q})|^2 = \frac{1}{\mathbf{q}^2} \frac{e^2 \hbar \omega_{\text{LO}}}{2\epsilon_0 V} \left( \frac{1}{\epsilon_{\infty}} + \frac{1}{\epsilon_z} \right) \quad (5.8)$$

where  $\epsilon_{\infty}$  and  $\epsilon_z$  are the high frequency and static dielectric constants of the quantum well system and  $V$  is the normalization volume. From the  $1/\mathbf{q}^2$ -dependence of the interaction strength it can be expected that the LO-phonon scattering rate decreases with increasing intersubband (or interminiband) spacing, since larger  $\mathbf{q}$ -values are required for relaxation. In case of interminiband transitions, this would lead to a faster decay at the mini-Brillouin zone edge than at its center. This was confirmed in a recent Monte Carlo simulation for interminiband relaxation, where a scattering rate of  $0.3 \text{ ps}^{-1}$  was found at the zone center and  $0.65 \text{ ps}^{-1}$  at the zone edge, respectively [33]. The corresponding photon energies at these positions were 320 meV and 175 meV. These photon energies are larger than the ones relevant in our single-color pump-probe experiments, where the interminiband absorption ranged from 90 meV to 140 meV for the sample G999. Thus, we expect that the relaxation times are somewhat shorter than in the Monte Carlo simulation. In fact, the relaxation times recorded at room temperature for the sample G999 show this typical behavior (see Figs. 5.7 and 5.8). At a pump intensity of  $15 \text{ MW/cm}^2$ , we find a relaxation time of about 1 ps for the zone-edge transition and 1.9 ps for the zone-center transition, respectively. The resulting scattering rates are larger than in the simulation ( $1 \text{ ps}^{-1}$  and  $0.52 \text{ ps}^{-1}$ ) which can be attributed to the reduced transition energy compared to the simulation [33]. However, consistent with the simulation, the scattering decreased by almost a factor 2. From this comparison, we can state that in our case the main relaxation of the interminiband transitions is due to LO-phonon interaction, whereas electron-electron scattering is expected to be on the same time scale or even slower.

This is also confirmed by the intensity dependence of the obtained relaxation times, where always an increase was found for higher pump intensity. In principle, a higher pump intensity results in a higher density of excited carriers in the upper miniband. However, the influence of the carrier density in the upper miniband was also investigated by the Monte Carlo simulation, and in fact, they found a reduction of the LO-phonon scattering

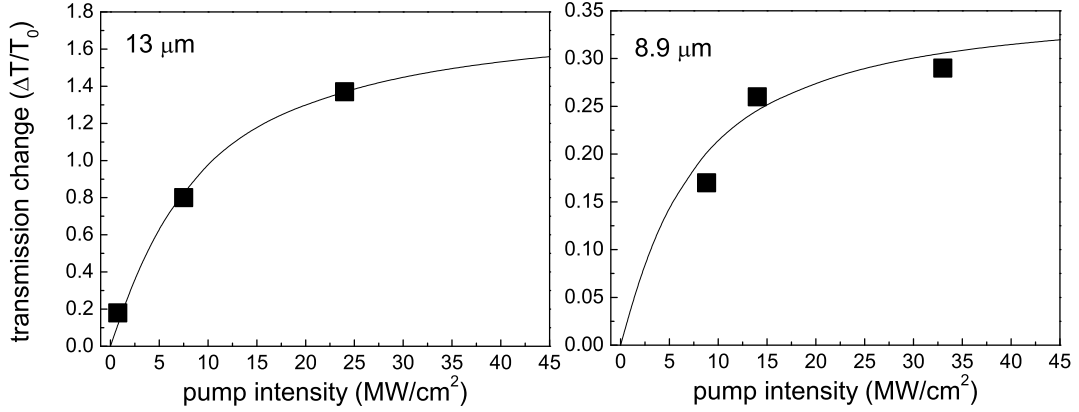


**Figure 5.20:** Saturation behavior of the two interminiband-transitions ( $\lambda=13\mu\text{m}$ ,  $8.9\mu\text{m}$ ) of the sample G999. The solid lines represent the simulated saturation obtained from the rate equation model.

rate by variation of the carrier density of about 10%. In our case, however, we found a much larger increase of the relaxation time. This can most likely be attributed to the existence of hot phonons [135]. At high excitation densities, a non-equilibrium LO-phonon distribution is generated by LO-phonon emission of the excited electrons. Then, the electron relaxation rate is reduced by reabsorption of non-equilibrium phonons that build up at the early stages of relaxation. Once most electrons have relaxed below the LO-phonon emission threshold, LO-phonon absorption and emission have almost the same rate. In this regime, the relaxation is dominated by the lifetime of the LO-phonons, which has a typical value of 5 ps in GaAs [136].

In the single-color experiments above, we have also studied the saturation behavior at two different wavelengths, representing the interminiband transition at the mini-Brillouin-zone center and its edge. The results are illustrated in Fig. 5.20. There we find that the transition at  $8.9\mu\text{m}$  saturates earlier than the transition at  $13\mu\text{m}$ , although the oscillator strength is smaller at this respective wavelength ( $f_{8.9\mu\text{m}} = 0.4$ ,  $f_{13\mu\text{m}} = 0.6$ ). However, not only the oscillator strength plays a role in the saturation dynamics, but also the relaxation time of the interminiband transition itself. In fact, as a result of the steady state solution of Eqn.(5.3), a larger relaxation time results in a faster saturation [137]. The observed difference in the relaxation times, where  $\tau_{8.9\mu\text{m}} > \tau_{13\mu\text{m}}$ , obviously compensates the difference in the oscillator strength, eventually leading to faster saturation. The solid lines in Fig. 5.20 represent the calculations from the two level rate equation model described above. For the case of  $8.9\mu\text{m}$ , we found that the saturation intensity is decreased by about 20% compared to a wavelength of  $13\mu\text{m}$ , almost perfectly matching with the estimation from the increased relaxation time and the reduced oscillator strength, giving a value of about  $\approx 25\%$ .

In case of the low-temperature pump-probe curves, a simple model like a two-level system cannot be applied anymore. In the single-color low-temperature measurements, we have observed fast interminiband relaxation and a slower component due to cooling of the heated electron gas. The interminiband relaxation can be attributed to electron-phonon scattering, and is of the same order as for the room temperature measurements (varied only by the phonon occupation number). To separate the bleaching component from the cooling effects, we have performed two-color pump-probe studies, where only cooling of the electron gas after a resonant interminiband excitation and relaxation could be observed. This was done for three different samples, that all had a strong interminiband absorption at high temperatures, which had vanished at a temperature of 6 K. However, the difference between the superlattices was the degree of coupling between the electronic states, that lead to different widths of the respective minibands. We found that the cooling time of the electron gas strongly depends on the width of the lower miniband as well as on the pump-intensity.

Let us first discuss the results from the first two superlattices with a miniband width of 11 meV and 25 meV, respectively. Both these values lie below the energy of optical phonons, which is 36 meV. During the heating process, electrons are promoted to the higher levels simply by a thermal activation due to scattering events after the interminiband excitation. Since the width of the lower miniband is smaller than the optical phonon energy, this relaxation channel is blocked and other scattering mechanisms become now dominant. In the simplest approximation, the lower miniband can be approximated by a system with discrete energy levels and only a small spacing. Thus, an analogy to the cooling experiment is a system of wide quantum wells, where the resonant two lowest subbands have an energy spacing below the optical phonon energy.

Such systems have been investigated over the last decade, due to the expectations of long relaxation times, compared to usual intersubband transitions in the mid-IR. As a suitable example, the relaxation time in wide quantum wells was studied by performing single-color pump-probe experiments in the far-infrared with an FEL [138, 139]. There they found relaxation times much longer than for usual quantum well samples ( $\tau \approx 50$  ps), that had also a strong dependence of the excitation power. On the other hand, it was found that the observed relaxation time was much shorter than what would be expected if only acoustical phonons are responsible for the slow relaxation. The results of these experiments were reconstructed by Monte Carlo simulations, taking all possible relaxation mechanisms such as electron-LO-phonon-, electron-electron-, electron-impurity-, and electron-acoustical phonon-scattering into account. While the latter does not play a significant role, all other scattering mechanism have to be taken into account for the observed relaxation. Fig. 5.21 shows the simulated fractional population for a wide quantum well with a subband-spacing of 18 meV after a resonant excitation with a FIR-laser pulse [134]. Note that the population of the second subband is already close to saturation. In this work, the authors have identified the following main scattering mechanisms, which are



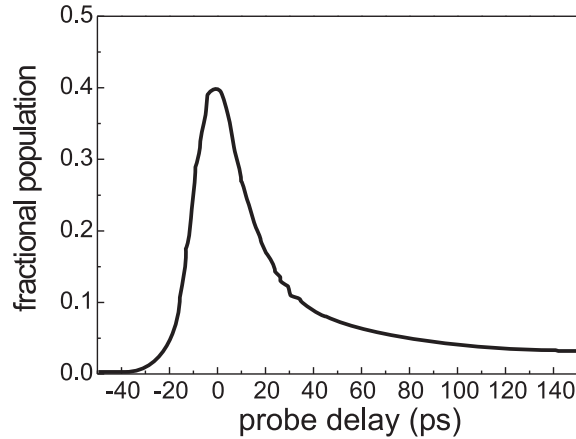


**Figure 5.21:** Simulated population of the second subband in a wide quantum well with a subband spacing smaller than the optical phonon energy after resonant excitation with a FIR-laser pulse. Graph reproduced from [134].

transduced to the case of intraminiband relaxation:

(i): The highest net intraminiband decay rate is due to ionized impurity scattering, reaching a value of  $0.3 \text{ ps}^{-1}$  at the used intensity. This is an elastic scattering mechanism and therefore does not allow energy relaxation of the excited electrons by itself. However, it is relevant for the dissipation process: After an electron has scattered from the edge of the lower miniband to its center, the scattered electron quickly thermalizes there with the other electrons through electron-electron scattering on a time scale much shorter than the intraminiband transition time back to the miniband edge. In this process, its excess kinetic energy is fed back into the whole electron system through carrier-carrier interactions. This process results in an additional heating of the entire distribution which enhances scattering due to polar optical phonons by promoting electrons above the phonon threshold along the whole lower miniband.

(ii): Once the electron gas has heated up, scattering due to polar optical phonons gives a significant contribution to the electron decay, and occurs primarily through phonon emission from the edge of the lower miniband to its center. The emission rates are reduced by the corresponding absorption rates caused by hot phonon effects [135]. Thus, as already discussed in the low-temperature single-color pump-probe part, the hotter the electron gas after excitation, the faster is the decay due to LO-phonon emission, since the tail of the Fermi-distribution extends stronger towards higher energies, thus promoting electrons above the threshold for LO-phonon emission.

After the pump pulse is over, impurity intraminiband scattering and electron-electron intraminiband scattering rapidly establish a quasi-equilibrium distribution with a common electron temperature and chemical potential. Because of the strong heating, there are still electrons above the lower-miniband edge. At this point, a form of steady state is reached with the number of electrons along the lower miniband determined by the common electron temperature. The large intraminiband scattering rates due to ionized impurity

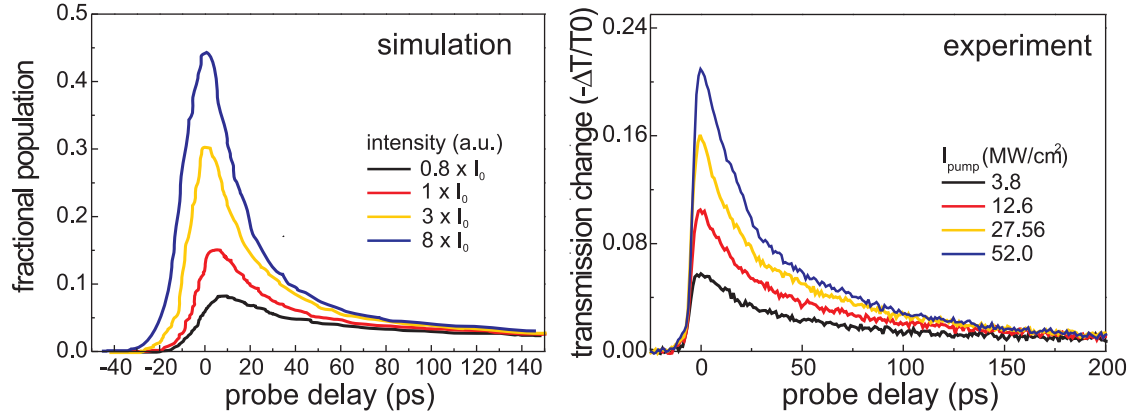


**Figure 5.22:** Left: simulated population of the second subband in a wide quantum well after resonant excitation with a FIR-laser pulse for different pulse intensities (reproduced from [134]). Right: cooling transient from the two-color pump-probe experiments of the sample H175 at 5 K.

scattering decrease as the number of electrons above the lower-miniband edge drops with the cooling of the electron temperature. The intraminiband decay is now limited by how fast the electron system can dissipate energy through inelastic scattering processes. Without photoexcitation, the tail of the distribution function shrinks and, therefore, fewer and fewer electrons are able to emit a polar optical phonon. As a result, the intraminiband decay in Fig. 5.21 slows down considerably for times larger than 40 ps. The emission process of optical phonons depends also on the energetic spacing of the involved states, making transitions closer to the optical phonon energy more likely than further away [134]. In fact, this is the reason for the different cooling time for the superlattice sample with a smaller miniband-width, where a cooling time of 50 ps was found in contrast to 40 ps of the sample H175, which had a width of 25 meV.

Also discussed by Dür *et al.* [134] is the dependence of the incident pump intensity. With increasing pump intensity, they find a decreasing cooling time, as we have observed for the cooling within the lower miniband. The results of the pump-variation, compared to our experimental results are shown in Fig. 5.22. The simulation shows the pump-induced fractional occupation of the upper subband in the wide quantum well, calculated for different intensities. Comparing these results with our experimental data exhibits a clear agreement of the observed behavior. With increasing pump intensity in both cases the cooling gets faster, and at longer delay times, all curves merge together indicating the same electron temperature for all pump intensities.

Due to the smaller fraction of electrons residing in the edge of the lower miniband at low pump intensities, the intraminiband scattering rates through polar optical phonons as well as electron-electron interaction contribute much less to the initial decay compared to high pump intensities. Thus, different relaxation mechanisms are dominant at a low excitation density, e.g. impurity-scattering and electron-electron scattering, the latter on much lower rate than at high intensities.

In their work they find out that, without impurity scattering included, the population at the miniband edge increases and, therefore, electron-electron scattering becomes important and limits the electron decay. In the presence of impurities, the electron system approaches a quasi-equilibrium distribution in a shorter time and the subsequent intraminiband relaxation begins to slow down sooner compared to the case when impurity scattering is absent, thus leading to a shorter time constant. However, the presence of Coulomb centers does not necessarily mean that the intraminiband decay beyond the peak population proceeds on a faster time scale.

As we have observed, the cooling behavior dramatically changed for the sample H171, having a lower-miniband width of 45 meV, well above the optical phonon energy. In this case optical phonon scattering dominates the relaxation. This is also confirmed by the fact that we observe almost no change of the cooling time with increasing pump intensity, in strong contrast to both other samples. The scattering rates due to LO-phonon scattering and electron-electron scattering in such a structure have been determined by a Monte Carlo simulation as well, giving a value of  $f_{11}^{LO} = 1.05 \text{ ps}^{-1}$  for LO-phonon scattering and  $f_{11}^{ee} = 1.35 \text{ ps}^{-1}$  for electron-electron scattering. This implies a cooling dynamics faster than the observed values and indicates that the observed negative change in transmission might not be due to heating of the electron gas in the lower miniband, but due to a different relaxation channel of the electrons that have been excited to the upper miniband. Also, the quantitative change of transmission, being only a few percent, indicates a different process than simply thermal filling of the states located near the edge of the lower miniband.

In principle, these excited electrons can undergo several relaxation paths within the miniband structure, including relaxation to the mini-Brillouin zone-edge, within the upper miniband as well as directly to the lower miniband (compare Fig. 5.10 on page 103). The first would correspond to transmission *increase*, giving rise to a stimulated emission of the incoming probe beam at this respective interminiband transition, while the latter would result in a transmission decrease, as was observed in our case. Eventually, we cannot make a final statement about the true origin of our observed transient. However, its time constant indicates that it is most likely due an interminiband relaxation, since relaxation *within* the minibands is expected to be faster.

In the room temperature experiments we observed, in strong contrast to the low temperature experiments, always positive transmission changes. Depending on the oscillator strength at the respective wavelengths of the different samples, the initial reduced transmission present without the pump pulse was quenched from 11% for sample H175 up to 21% for the samples G998 and G999 at an intensity of  $80 \text{ MW/cm}^2$ . As we have discussed earlier, two different relaxation mechanisms can lead to the reduced absorption. One is the de-population of the edge of the lower miniband due to relaxation towards its center and the second is increased population of the upper miniband at  $k_z = \pi/d$  due to relaxation

within the second miniband, leading to blocking of probed absorption or even stimulated emission of the incoming probe light.

The amount of quenching of the respective interminiband absorption at a fixed pump intensity depends on the oscillator strength at the pump wavelength. From the linear absorption spectra, we find for sample G998 an about 2 times larger oscillator strength at the pump-wavelength than for sample H175. Thus, assuming an equal homogeneous linewidth for both samples, one would expect less reduced absorption from the effect of relaxation within the upper miniband for the sample H175. And in fact, we observe at both intensities a factor of slightly larger than 2 in the reduced absorption signal. Since the width of the lower miniband is in both cases below the optical phonon energy of 36 meV, relaxation within the lower miniband of electrons towards the zone-center can be expected to be rather slow and inefficient. Hence, the main contribution to the reduced absorption must be due to relaxation of electrons within the *upper* miniband. Since in both cases, the width of the upper miniband is larger than the LO-phonon energy, relaxation can be assumed to be fast. Monte Carlo simulations [33, 140] showed that intra-miniband relaxation in the upper miniband can be on the order of 200 fs up to 1.2 ps, depending on the carrier density. Hence, it can be expected that a fraction of the excited electrons in the upper miniband relax towards the zone edge within a short time that cannot be resolved by our experimental setup. However, we can make an estimation of its efficiency. Therefore we consider the situation at low pump intensities. Regarding to the simulations with the simple rate equation model for sample G999, we can estimate a fractional population of about 0.2 after pump excitation at  $k_z = 0$  in the upper miniband. At the same time the interminiband absorption at  $k_z = \pi/d$  was reduced by about 4.5 %. As stated above, due to the small width of the lower miniband, the density at this respective  $k_z$  position remains nearly constant ( $n_{\pi/d}^{(1),p} \approx n_{\pi/d}^{(1),0}$ ). Since the absorption at  $k_z = \pi/d$  is proportional to difference of the occupations in the lower and the upper miniband, we can deduce the fractional population in the upper miniband at  $k_z = \pi/d$  to about 4.5 %:

$$\begin{aligned}
 \Delta\alpha &= \alpha_p - \alpha_0 & (5.9) \\
 &\propto n_{\pi/d}^{(1),p} - n_{\pi/d}^{(2),p} - \left( n_{\pi/d}^{(1),0} - n_{\pi/d}^{(2),0} \right) \\
 &= n_{\pi/d}^{(2),p} + n_{\pi/d}^{(2),0} \quad \text{with } n_{\pi/d}^{(1),p} \equiv n_{\pi/d}^{(1),0} \\
 &= n_{\pi/d}^{(2),p} \quad \text{with } n_{\pi/d}^{(2),0} = 0
 \end{aligned}$$

Hence, about 20% of the excited carriers in the upper miniband relax towards the zone edge where they increase the transmission of the probe pulse. This is valid for both samples and can be interpreted as the highest limit. In case carrier relax within a few hundred femtoseconds within the upper miniband, the density of excited electrons would be larger, since this time constant is faster than the usual pulse duration in our experiments. However, this value also agrees with the single-color measurements where at room temperature we could observe only a single decay time at both  $k_z$  positions. In fact the decay times at

$k_z = 0$  where always larger than at  $k_z = \pi/d$  indicating that the main relaxation path is directly at  $k_z = 0$ .

These results also bear consequences for the low-temperature measurements, where always decreased transmission was observed. The main contribution was the heating of the electron gas which has the strongest influence on the absorption. Although we expect also a small contribution due to heating in the room temperature measurements, the temperature change of the Fermi-Dirac occupation statistic has a much larger impact at low temperatures than at room temperature. Therefore, at 6 K, we observed only at large excitation densities the effect of relaxation within the upper miniband. Here the electron temperature was already heated up in such a way that a further increase leads only to a small absorption increase, whereas the competing process, e.g. relaxation within the upper miniband, showed stronger influence. This is also confirmed by the fact that the reduction of the induced absorption took place only during the temporal overlap with the pump pulse, whereas at later times all curves merged again (see Fig. 5.14).

In case of sample H171, where fast cooling due to LO-phonon scattering in the lower miniband was observed, heating had a much less effect, e.g. the amount of induced absorption was very small. However, it was not possible to overcome the heating by increasing the pump power. This can at least partially be attributed to the extremely low oscillator strength at the pump wavelength, which was only about 0.1 (compared to 0.44 for samples G998 and G999 and 0.26 for sample H175), leading to much smaller density of electrons after excitation at a fixed intensity. Obviously the density within the upper miniband was not large enough to compensate the induced absorption induced by carrier-carrier scattering. Due to the large photon energy of the pump pulse, the excited electrons have a large kinetic energy that can quickly dissipate within the electron gas by scattering events, eventually leading to a reduced transmission. Therefore, to achieve stimulated emission that compensates the losses due to heating one has to pump the interminiband transition  $k_z = 0$  much harder, which was not possible with our experimental setup. However, we have gained much information on the different relaxation paths between and within the minibands.

Note that the structure of sample H171 was designed similar to active regions in operating superlattice QCL's. However, in these devices electrons are injected *electronically* by applying a current along the growth direction. The electron injector regions are usually designed in such a way that electrons enter the active region *directly* in the upper lasing state, i.e. at  $k_z = \pi/d$ . Of course, this is not possible with optical excitation, and might be one of the main reasons for the absence of stimulated emission in our case. However, to confirm our quantitative results and for a thorough understanding of the competing processes it is desirable to perform Monte Carlo simulations, including all scattering mechanisms.

## 5.4 Outlook

In the present work, the interminiband and intraminiband relaxation has been studied, showing the fast interminiband relaxation due to LO-phonon scattering and the subsequent (cooling) dynamics within a single miniband that exhibited time constants from 230 ps down to 3 ps, strongly depending on the width of the respective minibands and the excitation density. While the interminiband relaxation could be evaluated and simulated with a rather simple model, intra-miniband relaxation showed a more complex behavior, involving many different scattering mechanisms. Since in the latter case the dynamics include various relaxation processes and also a quasi-continuum of electronic states in the minibands, it is not suitable to apply a model as simple as rate-equations. Therefore, for a complete quantitative description and understanding of the observed dynamics, it would be desirable to perform Monte Carlo simulations to understand the different processes involved. By comparison with results from former Monte Carlo simulations that investigated to some degree comparable systems, we partially found a good agreement, indicating that with this technique the observed dynamics could fully be recovered.

Another interesting experiment would be to determine the homogenous linewidth of the interminiband transitions which remains unknown due to the generally broad interminiband absorption spectrum, which derives from the different miniband dispersions. This could be measured by performing FEL-pump THz-probe experiments, where a single probing pulse fully covers the interminiband absorption. With such a spectral-hole burning experiment, the homogeneous linewidth of the excited interminiband transition could be measured, determined by the width of the bleached absorption [141].

Another aspect of FEL-THz pump-probe experiments is the presence of strong electric fields, oscillating with the center frequency of the FEL pulses. Since the FEL pulses exhibit an electric-field component in the growth direction, it also has a direct influence on the potential inside the heterostructure. This known as the AC-Stark effect.

For instance, in superlattices it has been predicted that the width of minibands inside the structure is affected by an alternating far-infrared field, eventually leading to a complete breakdown of the miniband structure (the so-called miniband-collapse) [142]. There, the FEL would be tuned to a long wavelength, ( $\lambda > 50\mu\text{m}$ ) and the miniband structure could be probed with a THz pulse, monitoring the expected change in the interminiband absorption spectrum.

## 6 Coherent dynamics of intersubband transitions in single quantum wells

Semiconductor quantum wells play an important role in modern solid state physics. The electrical and optical properties of such structures are strongly influenced by the microscopic carrier dynamics as well as by many-body effects. Ultrafast spectroscopy, in combination with tunable carrier densities, allows the time-resolved observation of those phenomena and thus provides direct insight into the microscopic dynamics [19]. A detailed understanding of these processes is fundamental for the development of novel electronic and optoelectronic devices.

Within the density matrix formalism (see Sec.(2.5)), the intersubband relaxation time, i.e.,  $T_1$ , describes the decay of the diagonal elements of the density matrix (relaxation of the populations). This parameter is important for the bandwidth of intersubband detectors or for the possibility of achieving population inversion between subbands. The decay of the non-diagonal elements of the density matrix, on the other hand, is described by the polarization or coherence decay time, i.e.,  $T_2$ . The coherence decay time is closely related to the linewidth of an intersubband transition. Thus, it is an important parameter for many applications. For example, narrow lines give rise to larger gain in intersubband lasers. Long coherence times are also important in experiments making use of the coherence between quantum mechanical energy levels such as coherent control experiments [143] and quantum information processing. This chapter deals with the dephasing of intersubband polarizations in symmetric quantum wells.

We present intersubband absorption experiments of photoexcited carriers in single quantum well structures, measured directly in the time domain, i.e., we are probing coherently the polarization between the first and the second subband. From the data we can directly extract the density and temperature dependence of the intersubband dephasing time between the two lowest subbands. This all-optical approach gives us the ability to tune the carrier concentration over an extremely wide range which is not accessible in doped quantum well samples. The influence of the carrier density on the dynamics of the intersubband polarization is studied, giving insight into many-body effects and their influence on the spectral position as well as on the lineshape of the investigated intersubband transition. Also the difference of excitonic interband excitation and free-carrier excitation is discussed, having a strong influence on the intersubband lineshape.

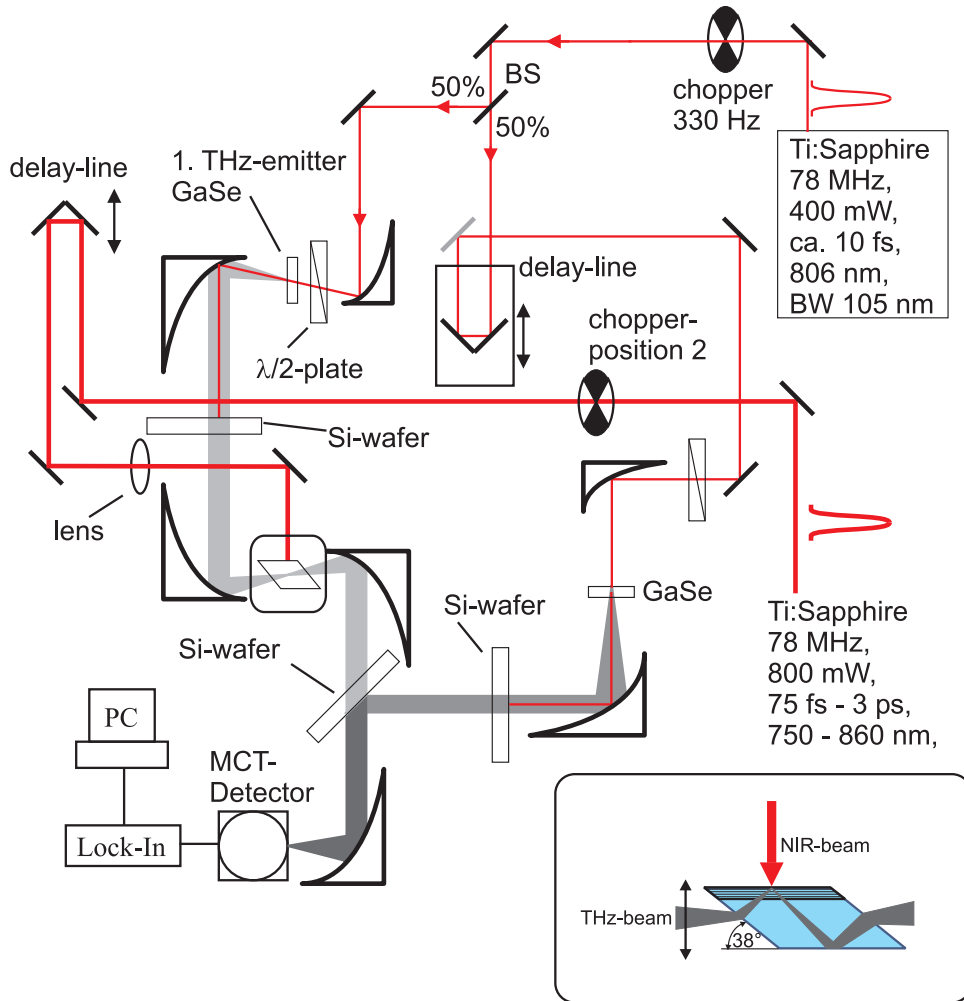


**Figure 6.1:** Experimental setup used for the collection of time-domain THz absorption spectra. A reference scan is recorded with the chopper in position 1, the photoinduced absorption scan is recorded with the chopper in position 2.

## 6.1 Experimental description and realization

A direct measurement of the polarization decay time in doped InGaAs/InAlAs quantum well samples has been performed by Kaindle *et al.* [45, 44] by time-resolved four-wave-mixing (TR-FWM) in the mid-IR regime. They found dephasing times between 118 fs and 320 fs, caused by electron-electron scattering. Vodopyanov *et al.* performed a two-color pump-probe experiment on a InGaAs/AlGaAs multiple quantum well structure [144]. They could not observe any spectral hole burning, indicating homogeneous broadening of the intersubband transition. From the linewidth of their sample (20 meV) one can estimate a dephasing time of 65 fs. These measurements were done only with doped samples, giving no information on the contribution of a free electron-hole plasma or excitons to the intersubband dephasing time. However, there has been work on undoped samples, measuring the intersubband *emission* of asymmetric or double quantum wells after an ultrashort



interband excitation, by coherently exciting into all relevant levels [145, 112, 146, 147, 148]. Müller *et al.*[149] also studied the absorption in asymmetric double quantum wells directly in the time-domain after an ultrafast optical excitation. In symmetric quantum wells, the emission process is not possible between the conduction band states due to symmetry reasons. However, it has been demonstrated between heavy and light holes [150].

The approach used here is to measure the coherent intersubband polarization and its decay, giving directly the dephasing time. The setup used for this experiment is shown in Fig. 6.1. First, charge carriers are generated by optical interband excitation. For this a second, synchronized Ti:Sapphire laser was used, which also oscillates at a repetition frequency of 78 MHz. The wavelength of this laser (*Spectra Physics Tsunami*) can be selected over a wide range. In principle, this laser has two different operation modes; one is the femtosecond mode, where the laser delivers transform-limited near-infrared pulses with duration of 30-80 fs, yielding a spectral width from 37 nm (70 meV) down to 11 nm (20 meV). In the second mode the laser operates in the picosecond regime, delivering transform-limited pulses with a duration of 2.1 up to 5 ps. This results in a very narrow spectral width, varying from 0.44 nm (0.85 meV) down to 0.18 nm (0.35 meV). Thus, with the first mode we can excite carriers within a large energy range in the quantum well system, whereas with picosecond excitation we are able to excite precisely into sharp resonances such as excitons.

Now having generated electrons (and holes) in the quantum well we probe the transmission with an ultra-broadband THz pulse, resonantly tuned to the expected intersubband absorption. These pulses typically exhibit a spectral width of more than 10 THz (41 meV) and thus represent an ideal tool for time-domain spectroscopy of intersubband resonances in quantum wells, that typically have a linewidth of 5-25 meV (in a GaAs/AlGaAs quantum well with a subband spacing of the order of 100 meV). This THz pulse induces a coherent polarization of the involved energetic states leading to a partial absorption of the THz probe pulse. As stated above, the temporal decay of the coherent polarization (e.g. the dephasing) usually occurs on timescales from 62 fs up to 1 ps. This requires an extremely high time resolution, that, in fact, is provided by the ultra-broadband THz pulses which usually have a duration of about 50 fs. Note that in FWM experiments, being a  $\chi^{(3)}$ -process, high pulse intensities are required, usually leading to longer pulses (>200 fs) and consequently to a lower time-resolution. Additionally the decay of the FWM-signal decays differently for homogeneously broadened ( $T_2 = 2\tau_{\text{hom}}^{\text{decay}}$ ) and inhomogeneously broadened systems ( $T_2 = 4\tau_{\text{inhom}}^{\text{decay}}$ ). These drawbacks can be alleviated by our approach<sup>1</sup>.

In our experiment, we create a coherent intersubband polarization by femtosecond intersubband excitation and monitor the decay of the macroscopic polarization via the electric field transient emitted from the sample: If a semiconductor quantum structure, which has

<sup>1</sup>With time-resolved four-wave mixing it is also possible to distinguish between homogeneously and inhomogeneously broadened systems. However, this technique is much more difficult than our approach.

a ground state  $E_1$  and an excited state  $E_2$  in the conduction band, is excited resonantly with a short THz pulse, such that the spectral components of the THz pulse exceeds the energy separation between the two states, the THz pulse excites a coherent superposition state  $|\psi(0)\rangle = 1/\sqrt{2}(|1\rangle + |2\rangle)$ , i.e., a linear superposition of the two conduction-band wavefunctions. This superposition state, however, is not stationary and its time evolution is

$$|\psi(t)\rangle = \frac{1}{\sqrt{2}} \sum_{n=1}^2 e^{-iE_n t/\hbar} |n\rangle \propto |1\rangle + e^{-iE_{12}t/\hbar} |2\rangle \quad (6.1)$$

where  $E_{12}$  is the level splitting between levels  $|1\rangle$  and  $|2\rangle$ . Since the eigenenergies of the two excited states are different, the phases of the two eigenstates will evolve at a different rate. As a result the excited electronic wavepacket oscillates with a frequency given by  $E_{12}/\hbar$ . Leo *et al.* [145] used a coupled double quantum well structure, consisting of a narrow well and a wide well, to study the wavepacket dynamics in semiconductors by time-resolved four-wave mixing and by interband pump-probe measurements. The modulation of the four-wave mixing signal and the pump-probe signal reflected the oscillatory behavior of the wavepacket, which was photoexcited in the structure.

Since the wavepacket is charged, the motion of the wavepacket gives rise to a time-dependent dipole moment and consequently emission of electromagnetic dipole radiation. This was first recognized by Roskos *et al.*[146]. They observed coherent THz emission from a double quantum well structure excited by a short optical pulse using THz time-domain spectroscopy. Their experiment is a direct proof of coherent charge oscillations in semiconductors, because it directly measures the time-dependent electric dipole moment. The wavepacket oscillation can be observed until phase relaxation destroys the coherence. Assuming the energy eigenstates as being homogeneously broadened, dephasing leads to an exponential damping of the oscillation with a damping rate  $\gamma_{12} = 1/T_2$  (compare Sec.(2.5)).

The experimental setup is illustrated in Fig. 6.1. The electric field of the THz probe pulse is obtained by a cross correlation with a quasi single-cycle THz pulse, having a sufficiently short duration and large spectral width (see Sec.(4.3)). For the absorption experiments, we first place the chopper in position 1, while blocking the interband excitation. This gives us the zero-absorption reference, since due to lack of carriers there is no intersubband absorption possible. The absorption measurement is then performed by placing the chopper in position 2, now modulating the interband excitation. By using Lock-In detection and keeping its phase locked to the one of the THz probe pulse, now the measured signal is negative, since we induce absorption on the measured signal with the interband-pump pulse. Performing now a cross correlation by variation of the delay of the probe- and reference pulse, yields the *direct electric field response* of the probe pulse due to the interband excitation. In fact, this electric-field response reflects the time evolution of the intersubband polarization. Therefore, in the time-domain experiments, we expect a rapid increase of the measured electric field, oscillating with the frequency of the intersubband

transition. After interaction with the probe pulse, the polarization freely decays due to dephasing, however, still oscillating at the resonance energy. As discussed in Sec.(2.5), this decay defines the dephasing time, directly correlated to the spectral width of the absorption-line.

Thus a Fourier-transform gives the amplitude spectrum of the photoinduced absorption, which is finally normalized to the reference spectrum taken when the interband excitation was absent.

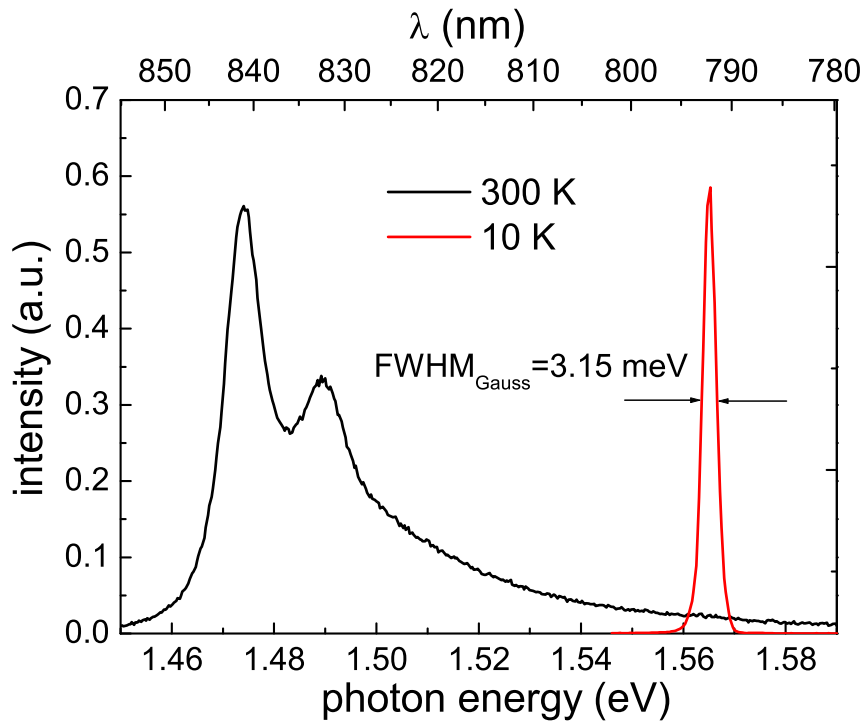


**Figure 6.2:** Photoluminescence taken from the undoped MQW sample at room temperature and a temperature of 10 K.

In this work we investigate the THz response of an undoped GaAs/AlGaAs multi-quantum well structure after interband excitation. The structure consists of 60 quantum wells with a thickness of 83 Å, separated by an Al<sub>0.3</sub>Ga<sub>0.7</sub>As barrier with a width of 196 Å, respectively. To provide a strong electrical field at the position of the quantum wells and the wavelength of the expected intersubband resonance, an Al<sub>0.3</sub>Ga<sub>0.7</sub>As spacer layer (which is transparent for the interband-excitation) with a thickness of 300 nm was grown on top and underneath the MQW structure (see Sec.(2.4) on page 19). The latter was inserted that in case the substrate is lifted off, the boundary conditions remain the same for the waveguide. The sample was polished to a single pass parallelogram with 38° facets to

provide an electric-field component in the growth direction, which is necessary for intersubband absorption. The interband pulse was focused on the active layer, leading to a spatial overlap of the pump pulse and the THz pulse directly behind the facet. This is illustrated in the inset of Fig. 6.1.

The photoluminescence (PL) spectra taken at 300 K and 10 K are shown in Fig. 6.2. There the sample was illuminated with a 5 mW HeNe laser ( $\lambda=632.8$  nm), with a spot size of about  $1 \text{ mm}^2$ , giving an excitation density of  $0.5 \text{ W/cm}^2$ . At room temperature, the PL shows two distinct peaks, overlapping with a long tail towards higher photon energies. The two peaks can be attributed to the recombination of the hh1-cb1 (1.474 eV) and the lh1-cb1 (1.490 eV) transition, respectively. The PL-spectrum changes at 10 K, where only a single sharp peak, corresponding to the hh1-cb1-transition, can be observed. The energy shift is due to the increased bandgap of GaAs at low temperatures.

## 6.2 Results

Fig. 6.3 shows the time-evolution of the induced polarization, 25 ps after interband excitation, recorded at room temperature. Note that interband relaxation is usually of the order of nanoseconds; therefore choosing a delay of 25 ps ensures a equilibrium distribution of the excited carriers in the conduction- and the valence band. The photoinduced electron density was set to  $3 \times 10^{10} \text{ cm}^{-2}$  per quantum well. The upper part shows the measured cross-correlation signal obtained in the absorption configuration. It can be interpreted as the time-dependent polarization of the system. There we find a rise of the signal within 200 fs, which afterwards monotonically decays to zero after 450 fs. Below this a simulation is shown, almost perfectly matching the measured curve. For this, a Gaussian pulse describing the rise time and an exponential decay are convolved. A decay time of 120 fs shows the best agreement to our data. The lower part of Fig. 6.3 shows the absorption spectra obtained from a Fourier transform of the measured waveform. The spectrum is normalized to a reference spectrum where interband excitation is switched off. The shape clearly shows a Lorentzian line, as indicated by the result of the simulation, where a Lorentzian lineshape results from the exponential decay of the polarization. By varying the excitation power, and thus the carrier density, we observe a strong change of the dephasing time, ranging from 130 fs for the lowest ( $n^{(2)} = 1 \times 10^{10} \text{ cm}^{-2}$ ) and 50 fs for the highest ( $n^{(2)} = 7.6 \times 10^{11} \text{ cm}^{-2}$ ) excitation density [151]. Correspondingly, the FWHM of the absorption line increases from 7.9 meV to 24.5 meV<sup>2</sup>. Thus the dephasing time depends strongly on the carrier density.

The measurements were also performed at low temperatures, i.e. at 80 K and at 4.2 K. The

<sup>2</sup>Note that for the spectral linewidth the complete interferogram has to be Fourier-transformed and the rise of the polarization is included. Therefore we find for short dephasing times, obtained from the time-domain data, a discrepancy between the spectral width and the dephasing time, since the rise of the polarization is not included in the simple dephasing model.

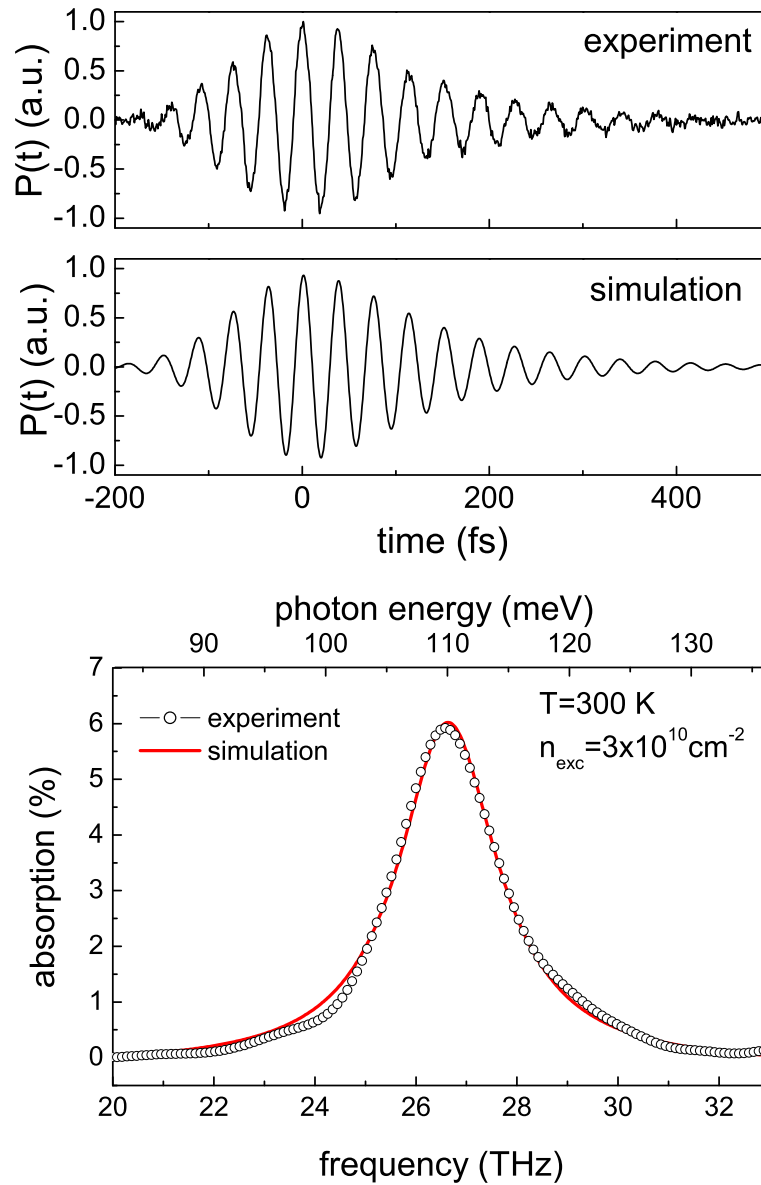


**Figure 6.3:** Upper part: time evolution of the induced polarization and a simulation. The lower graphs shows the measured absorption spectra, compared to the result of the simulation.

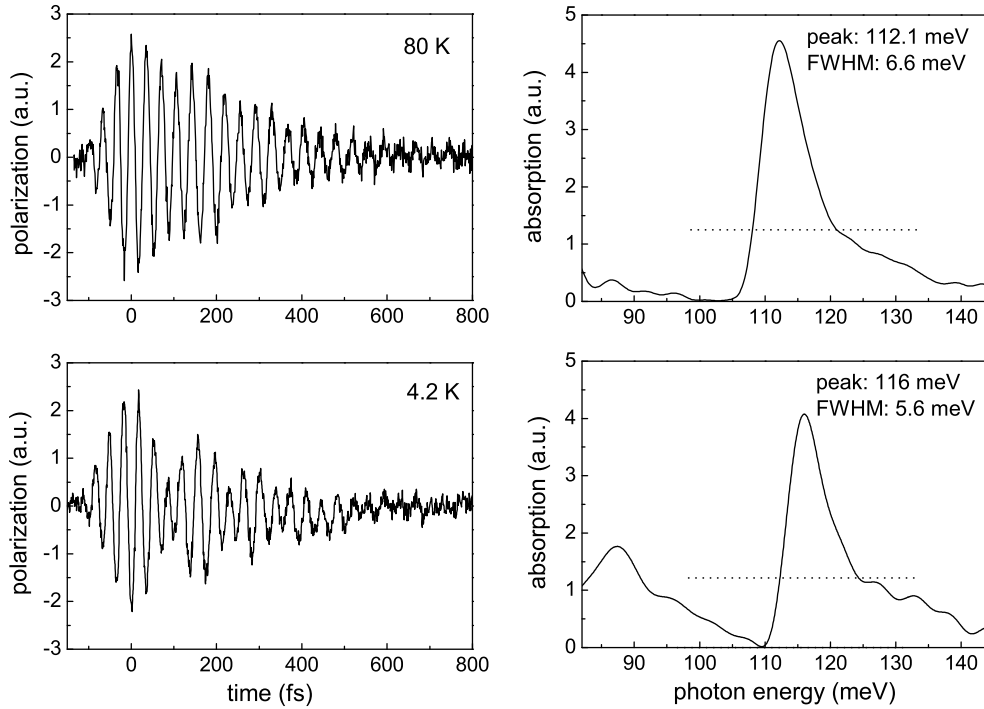


**Figure 6.4:** Left: time evolution of the induced polarization at different lattices temperatures and their corresponding absorption spectra (right-hand side). The excitation density was  $n^{(2)} = 3 \times 10^{10} \text{cm}^{-2}$  in both cases. The spectral widths have been determined from the peaks above the dashed lines.

results are shown in Fig. 6.4. Let us first analyze the left part, showing the interferograms obtained by the cross correlation, taken 25 ps after interband excitation. For both temperatures, the polarization rises within about 100 fs, oscillating with the resonance frequency. However, the subsequent decay differs significantly from the monotonic behavior observed in the room-temperature experiment. First, the decay time is longer, and we find that the polarization persists up to 800 fs in both cases. For the 80 K data, a dephasing time of 160 fs can be estimated, the same is found for the 4 K measurement. Secondly, we find a beating in the time-domain data, getting remarkably stronger in the 4 K measurement. The beating has a frequency of about 6.5 THz in both cases. This indicates that another resonance is present in the system, having either a 6.5 THz higher or lower frequency than the intersubband resonance, which results in a beating of the induced polarization. The corresponding absorption spectra are shown on the right side of Fig. 6.4. In contrast to the room-temperature data, both spectra exhibit a strong asymmetry, getting even stronger at a temperature of 4 K. The lineshapes are clearly no Lorentzian anymore: the main peak develops a broad shoulder at higher photon energies and drops rather sharply on the low energy side, where in both cases almost no absorption is found. Going further towards

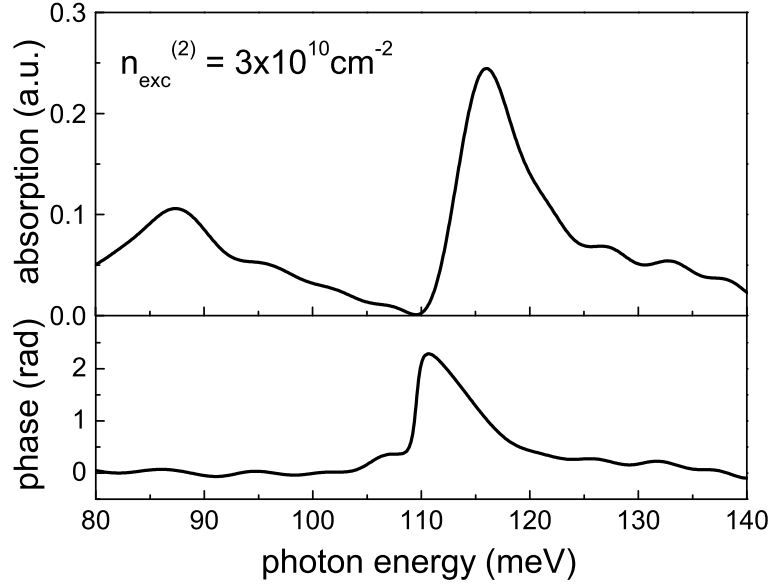


**Figure 6.5:** Top: absorption spectrum recorded at an excitation density of  $n_{\text{exc}}^{(2)} = 3 \times 10^{10} \text{ cm}^{-2}$  and a temperature of 4 K. The lower part shows the corresponding phase of the spectral components.

lower energies, the absorption rises again, being stronger for the case of 4 K. Here, we also see the indication of a small peak at 87 meV. This peak is separated from the main absorption feature by about 28 meV (6.8 THz), and could be interpreted as the reason for the strong beating signal. Interband-calculations [152] showed that a possible transition in this spectral region would correspond to a intra-valence-band transition between the two lowest light-hole states lh1 and lh2. In principle, by use of femtosecond interband excitation with a spectral width of 40 meV it is possible that light-hole states are occupied by free holes. However, the energetically lowest state in the valence band is the hh1 state, being separated by 19 meV from the lowest light-hole state and time-resolved photoluminescence studies showed no indication of the lh1-cb1 interband luminescence which would be expected if the light hole states are occupied [153]. Additionally, by variation of the time delay between the pump-pulse and the THz-probe pulse up to 250 ps, no change in the induced absorption is found. There the excitation density was as low as  $2 \times 10^{10} \text{ cm}^{-2}$  to ensure that the Fermi-level was well below the the lh1 state. Thus, although all carriers in the valence band should have relaxed to the heavy hole ground state, we still observe the strong beating signal. Hence it is not clear if the observed peak can be attributed to the lh1-lh2 transition.

However, the spectral shape of the observed absorption cannot be explained by the presence of an additional (independent) oscillator, since this would simply lead to two single Lorentzian lines in the spectrum. Also, the process of free-carrier absorption can be excluded for such low excitation densities, and, in fact, they would lead to a monotonic

background rising towards lower photon energies, in strong contrast to the vanishing absorption features on the low energy side of the main absorption peak<sup>3</sup>. Hence, a different mechanism must be responsible for the asymmetric lineshape of the photoinduced absorption.

In addition to the absorption-line, also the spectral phase can be retrieved from the time-domain data. For the measurement at 4 K, the corresponding spectral phase of an absorption spectrum taken at an excitation density of  $n^{(2)} = 3 \times 10^{10} \text{cm}^{-2}$  is shown in Fig. 6.5. Since the THz pulse is chirped when passing through the waveguide sample, the spectral phase of the reference pulse has been subtracted from the phase of the absorption spectrum. The result is shown in the lower part of Fig. 6.5. There we find that at the absorption *minimum*, located at 110 meV, the phase undergoes a drastic sharp change of 2.3 radians, corresponding to  $130^\circ$ . In the literature [154, 155, 156, 157, 158], similar lineshapes and spectral features have been observed in quantum well systems before and were attributed Fano resonances. However, this will be discussed later.

At low temperatures, carriers that have been excited by an interband excitation, do not necessarily have to appear as free carriers, but electrons and holes can form excitons [20]. This fact is of particular interest, and in a similar experiment it was claimed that the exciton-like state of electrons and holes leads to an enhancement of the intersubband absorption strength [159]. The resulting excitonic interband absorption lies usually a few meV below the band-to-band absorption, reduced by the exciton binding energy. In high quality samples, the linewidth of the excitonic absorption is in the order of 1 meV. Up to now we have generated carriers over a wide spectral range, injecting carriers probably into excitonic as well as free-carrier-type states. To change this we have performed the photoinduced absorption experiments with a ps-Ti:Sa-laser, with a small linewidth ( $< 1$  meV), enabling us to directly excite free carriers or excitons. This will allow us to avoid excitation of electrons into the lh1-state, and to draw conclusions from the comparison to the fs-excitation.

The cross-correlation signal, obtained for an interband excitation tuned to 791 nm, which marks the hh1-cb1-exciton absorption line, is shown in Fig. 6.6(a). The excitation density was set to  $n^{(2)} = 3 \times 10^{10} \text{cm}^{-2}$ , the delay between the optical pump pulse and the THz probe pulse was 25 ps. In strong contrast to the fs-excitation, we now observe almost no beating in the recorded signal, but a long lasting oscillation, generated by the induced polarization, which now decays monotonically. To extract the dephasing time, we have taken the absolute value of the waveform and removed the fringes by application of a low-frequency pass filter with a cut-off at 8 THz. The result is shown in the inset of Fig. 6.6(a), also showing a best mono-exponential fit to the data. This fit gives a dephasing time of 250 fs, which corresponds to FWHM of the absorption line of only 5.3 meV. The corresponding

---

<sup>3</sup>In addition, free-carrier absorption is expected to be only weakly temperature-dependent, and thus, should be present in the room temperature experiments as well.



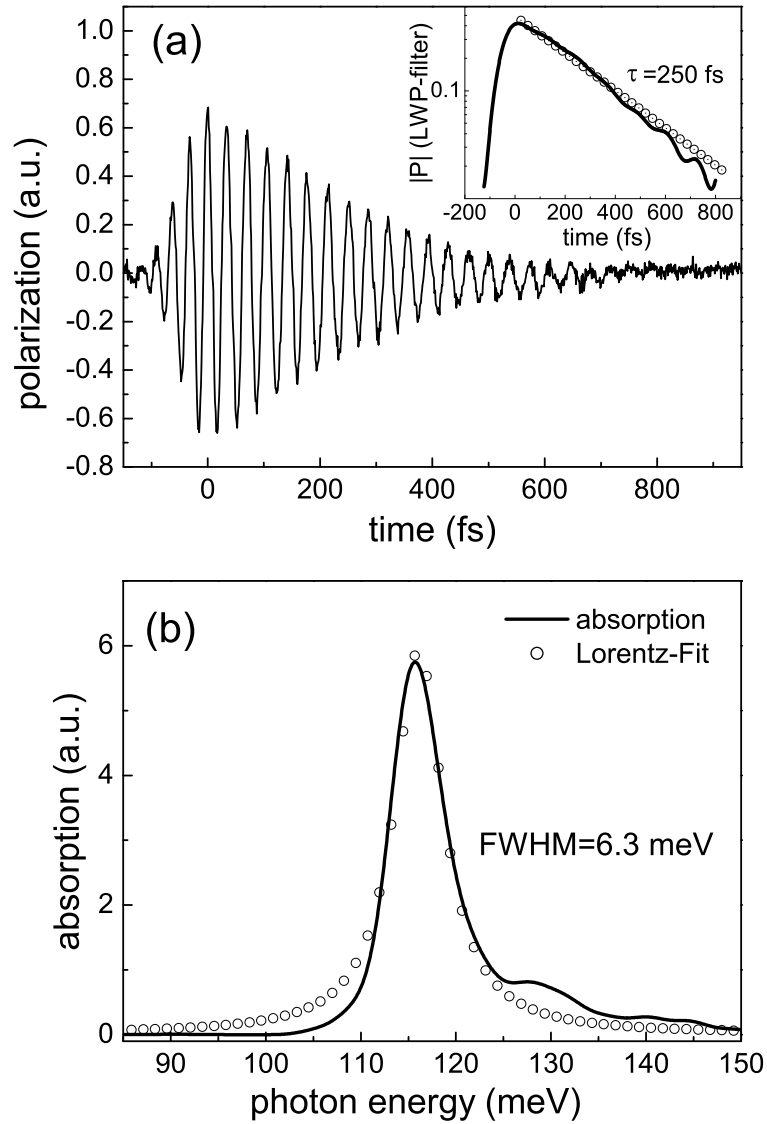


**Figure 6.6:** Waveform of the induced polarization recorded 25 ps after picosecond interband excitation at 791 nm and an excitation density of  $n^{(2)} = 3 \times 10^{10} \text{cm}^{-2}$ . The inset shows the absolute value, with fringes removed by a low-pass filter at 8 THz. The decay can be approximated by an exponential with a time-constant of 250 fs (open circles). The lower part shows the corresponding absorption spectrum and a fit with a Lorentzian.

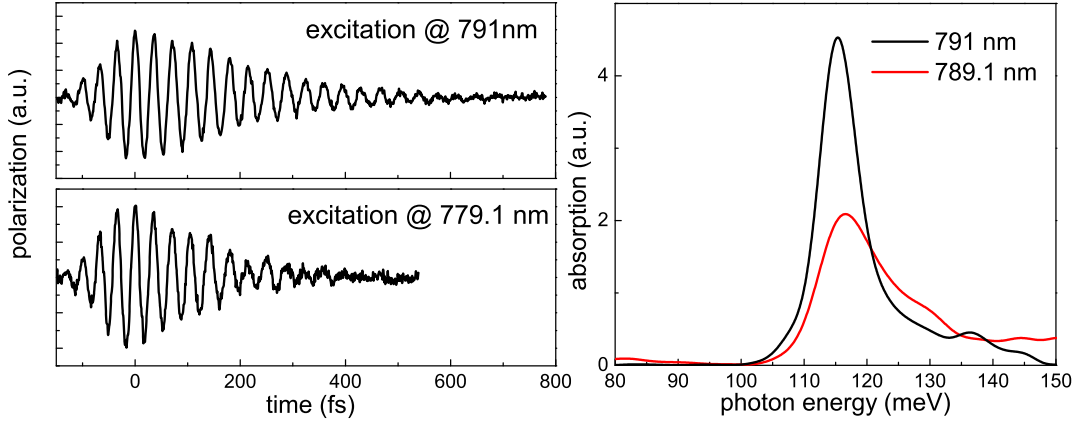


**Figure 6.7:** Waveform recorded at different pump wavelengths as indicated (left) and the corresponding absorption spectra. The excitation density was set to  $n^{(2)} = 3 \times 10^{10} \text{cm}^{-2}$ .

absorption spectrum, obtained by a Fourier transformation, is shown in Fig. 6.6(b). The spectrum exhibits a larger FWHM (6.3 meV) than obtained from the pure dephasing time, although the rise is included in the Fourier transformation. This discrepancy can most likely be attributed to a thermal drift of the probe- and the reference pulses during the measurement that is introduced by movement of the sample and/or other components in the setup. This drift leads to a slight variation of the oscillating frequency, eventually leading to a broader spectrum than expected. This effect can be eliminated only by a faster measurement. However, the decay of the polarization is much less sensitive to this drift, and therefore we estimate the obtained linewidth from the dephasing time. At larger excitation densities, where the dephasing time is shorter, this thermal drift becomes less important, allowing precise analysis of the lineshape (shown later). Nevertheless, although the spectrum is broader than expected, we can deduce some conclusions from it:

(i): with direct excitation into the lowest hh-state, we observe no absorption components in the region of 80-90 meV, where in case of fs-excitation absorption maybe due to light-hole transitions occurred. However, the absence is a strong indication that the strong beating in this case was due to the presence of the lh1-lh2- transition.

(ii): even though the spectrum is artificially broadened, we still find an asymmetric lineshape of the absorption, again with a pronounced shoulder at larger photon energies. However, this has to be verified by more accurate measurements that will be done in the near future.

To verify our assumption that in the case above we are dealing with electrons mostly present in the hh1-cb1 exciton, we have tuned the excitation wavelength towards higher photon energies. By this, we find a drastic change of the time-evolution of the infrared polarization and hence also in the corresponding absorption spectra. The result of excitation at 779.1 nm (slightly above the expected lh1-cb1-exciton resonance at 781 nm), compared

to excitation at the exciton-resonance located at 791 nm are shown in Fig. 6.7. There we find that the polarization decays much faster than in the case of resonant excitation. Additionally the cross-correlation signal for the higher photon energy shows a slightly non-monotonic decay. Correspondingly, the absorption spectra have a different shape. While the spectrum taken at 791 nm shows a sharp peak and a slight asymmetry, the spectrum recorded at 779.1 nm is much broader and exhibits small absorption components at around 83 meV and a more pronounced high-energy tail than for the 791 nm excitation.

Hence, this demonstrates that it *does* make a difference whether we excite directly into excitonic absorption resonances or at higher photon energies, where also free carriers are generated in the heavy-hole- as well as in the light-hole state.

### 6.3 Discussion

We will now address the mechanisms which induce the homogeneous dephasing of the (1-2) intersubband transition, as found in our experiments. In principle, the (1-2) intersubband polarization can decay due to (i) depopulation of the upper subband which occurs with the intersubband relaxation time  $T_1$  or (ii) by pure dephasing due to phase-breaking scattering processes which destroy the macroscopic polarization between the atomic dipoles of an ensemble, but do not change the population. This is described by the pure dephasing time  $T_2^{\text{deph}}$ . These two contributions add up in the following way to give the total dephasing time  $T_2$  (see Sec.(2.5) and [20]):

$$\frac{1}{T_2} = \frac{1}{2T_1} + \frac{1}{T_2^{\text{deph}}} \quad (6.2)$$

As already discussed in the previous chapter, intersubband relaxation in a quantum well with a subband spacing larger than the LO phonon energy is due to LO phonon scattering. However, typical values of the intersubband relaxation time in single quantum wells lie in the range of  $T_1 = 0.5$  ps and  $T_1 = 1$  ps, respectively [31, 160]. Assuming dephasing only due to depopulation, this would indicate a dephasing times between  $(2T_1)^{-1} = 1$  ps and 2 ps, being much longer than our measured values that range from 60 fs up to 250 fs. Hence, intersubband relaxation can have only a minor contribution to the fast dephasing times, and, in fact such fast scattering times can only be explained by intra-subband scattering. These processes cause an extremely fast exchange of energy and momentum of electrons which stay within their original band after scattering. In principle, there are a number of processes that can lead to dephasing between the macroscopic intersubband polarization, and the most important ones are:

(i): intra-subband electron-phonon scattering:

Scattering of electrons with optical or acoustic phonons can lead to the dephasing of the intersubband polarization. In the latter, however, it has been shown [160], that the scattering rate is on the order of  $\gamma_{12}^{AC} \approx 8 \text{ ns}^{-1}$ , since the interaction between electrons and

acoustic phonons is weak and can thus be neglected. For the case of optical phonons, the dephasing rate can be estimated from the same type of interaction as described above for intersubband (and interminiband) relaxation processes. Basically the scattering of an electron with an LO-phonon can take place either by emission or absorption. At low temperatures, however, LO-phonon emission can be neglected, since the electrons would have to overcome an energy-threshold of 36 meV within the upper subband by thermalization processes. At the low intensities of the probe-pulses used in the experiments, this is completely negligible. At higher lattice temperatures, however, this might have a small influence due to the decreased Fermi energy, leading to a partial occupation of the subbands at higher  $k$ -values. Phonon absorption does not obey such an energy threshold, and is, in principle possible for all electrons in the upper and lower subband. However, one has to account for the phonon occupation number, which is almost zero for lattice temperatures below 50 K and thus can be excluded for the low-temperature experiments.

(ii): electron-electron scattering:

Since – due to the low Fermi energy – LO-phonon scattering can not contribute to the dephasing at low temperatures, one remaining phase-breaking process is electron-electron scattering. Several theoretical works have calculated the electron-electron interactions for semiconductor quantum wells in various approximations. These studies, as already stated in Sec.(5.3), showed that this process is a very fast scattering mechanism with timescales similar what we have observed in our experiments. However, taking these processes into account is very complicated due to the many-body nature of the electron-electron interaction: the bare Coulomb interaction is strongly influenced by the presence of the other charge carriers in the plasma. Therefore, collective excitations as well as single particle-excitations have to be taken fully into account. This is equivalent to the calculation of the dynamically screened dielectric response  $\epsilon(\omega, \mathbf{q})$ , and we briefly discuss the equations that have to be solved. The matrix element due to Coulombs interaction, which has to be evaluated, is given by [161, 162]:

$$V_{i,i',j,j'}^s(\mathbf{q}, \omega) = V_{i,i',j,j'}^s(q) + \sum_{m,n} V_{i,i',n,m}^s(q) \lim_{\delta \rightarrow 0} \left[ \sum_{\mathbf{k}} \frac{n_{m,\mathbf{k}+\mathbf{q}} - n_{n,\mathbf{k}}}{E_{m,\mathbf{k}+\mathbf{q}} - E_{n,\mathbf{k}} - \hbar\omega - i\delta} \right] V_{i,i',n,m}^s(q) \quad (6.3)$$

for the scattering of two electrons with initial subband  $(i,j)$  into the final subband  $(i',j')$  and  $\mathbf{q}$  describing the momentum exchange. The shown sum over  $\mathbf{k}$  determines the mutual coupling in so so-called "random phase approximation" (RPA), which is widely used to solve these complicated problems.  $E_{n,\mathbf{k}}$  and  $n_{n,\mathbf{k}}$  are the energies and populations in the subband  $n$  at the wavevector  $\mathbf{k}$  and  $\hbar\omega$  is the energy exchange. The static Coulomb potential for a two-dimensional system is given by:

$$V_{i,i',j,j'}^s(q) = \frac{e^2}{2A\epsilon_s} \frac{1}{q} \int \int dz' dz \varphi_{i'}^*(z) \varphi_i(z) e^{-q|z-z'|} \varphi_{j'}^*(z') \varphi_j(z) \quad (6.4)$$

where  $\varphi_i(z)$  are the envelope wavefunctions,  $A$  is the normalization area and  $\epsilon_s$  represents the static dielectric function. Additionally, the Pauli-blocking of final states has to be taken into account, finally leading to the rate

$$\gamma_{i,\mathbf{k}}^{out} = \frac{2\pi}{\hbar} \sum_{i',j',q \neq 0, \mathbf{k}} |V_{i,i',j,j'}^s(\mathbf{q}, \omega)|^2 (1 - n_{i',\mathbf{k}-\mathbf{q}}) n_{j,\mathbf{k}'} (n_{j,\mathbf{k}'+\mathbf{q}}) \delta(E_{j',\mathbf{k}'+\mathbf{q}} - E_{j,\mathbf{k}} - \hbar\omega) \quad (6.5)$$

for scattering out of state  $i$  into any other state, obeying energy conservation. Hence, from the structure of Eqn.(6.4), we find that a change of subbands leads to a small rate, whereas intra-subband relaxation ( $i=i', j=j'$ ) becomes possible and efficient. Calculations show that there is usually a factor of ten for the different relaxation paths. Von Allmen [161] calculated the linewidth of intersubband transitions using a full dynamical screened RPA approach, from where a scattering rate of  $\gamma=1-6 \text{ ps}^{-1}$  was deduced for a temperature of 0 K. These rates lie in the same order of magnitude as our experimental results. Lee and Galbraith [163] have also calculated the electron-electron interaction, however, in a wide quantum well with a subband spacing of only 19.6 meV, which is well below the LO-phonon energy. At 4 K they find a value of  $\gamma= 3 \text{ ps}^{-1}$  at an electron density of  $n^{(2)} = 1 \times 10^{11} \text{ cm}^{-2}$ , corresponding to a dephasing time of 330 fs, respectively. They have also calculated the room-temperature scattering rate, being four times higher than at 4 K due to LO-phonon absorption:  $\gamma \approx 12-40 \text{ ps}^{-1}$ . However, such a strong increase is not observed in our data, where the scattering rate is on the order of  $\gamma \approx 9 \text{ ps}^{-1}$ . This might be because the intersubband-separation is much larger in our case, effectively reducing the LO-phonon scattering rate [132].

(iii): electron-hole scattering:

So far, the effect of the presence of holes in the quantum well systems have not been included in a theoretical treatment of intersubband dephasing. However, the electron-hole scattering rates have been calculated in the work of Meissner *et al.* [164], where the electron-hole scattering rate is  $< 0.1 \text{ ps}^{-1}$  even for excitation densities of  $n^{(2)} = 1 \times 10^{12} \text{ cm}^{-2}$ . These rates are much smaller than observed in our experiments. Hence electron-hole scattering is not expected to have a major contribution to the intersubband dephasing times.

Thus, the major fraction of intersubband dephasing observed at low temperatures can be well explained by typical electron-electron scattering rates of a two-dimensional electron plasma. For all excitation densities, even for extremely low excitation densities such as  $n^{(2)} = 0.25 \times 10^{10} \text{ cm}^{-2}$ , where a dephasing time of 400 fs was found (not shown), the dephasing cannot be fully attributed to the population decay. However, in this low excitation regime, population relaxation via LO-phonon does have a contribution of about 40%.

Above we have shown that electron-electron scattering has a main influence on the dephas-

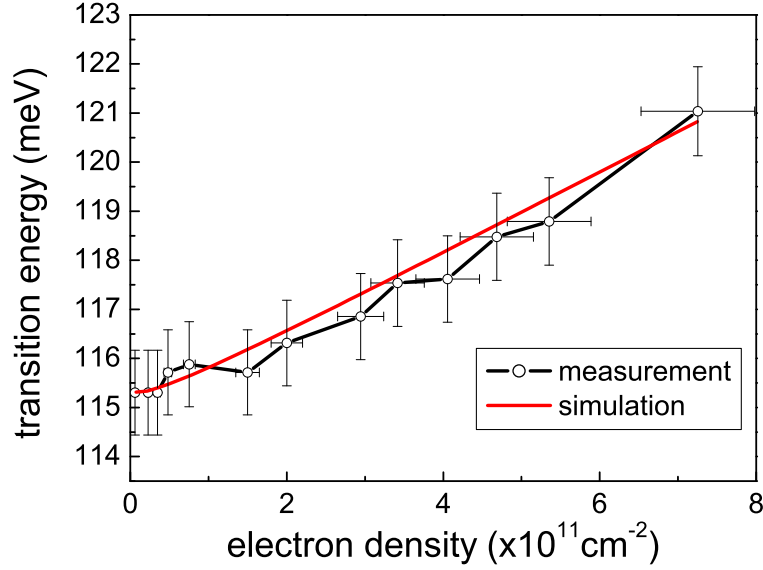


**Figure 6.8:** Experimental peak absorption energy and the result from a simulation as a function of the excited carrier density.

ing time, and thus on its linewidth. However, taking many-body interactions into account does not only lead to a change of the linewidth but also affects the spectral position of the main resonance[40]. This was also demonstrated for photoinduced intersubband absorption in single [165] and double quantum wells [166]. Apart from the dephasing times, we have also analyzed the change of the peak absorption with respect to the excitation density. These measurements were performed at 4 K under fs excitation, leading to a broader distribution within the valence band than with small-bandwidth excitation. The spectrum was taken 25 ps after interband excitation, thus a cold carrier distribution can be assumed. The results, where the carrier density was varied from  $n^{(2)} = 0.7 \times 10^{10} \text{ cm}^{-2}$  up to  $n^{(2)} = 7 \times 10^{11} \text{ cm}^{-2}$ , are shown in Fig. 6.8. There we find a large shift ( $\Delta E \approx 6$  meV) of the main absorption peak with increasing excitation density. The shift sets in at an excitation density of  $5 \times 10^{10} \text{ cm}^{-2}$ , for smaller values the peak absorption remains constant.

For a simulation of the observed peak shift, one has to take into account the following effects, having a static and dynamic effect on the intersubband resonance [37].

(i): Static band structure model:

In a first step, we compute the static band-structure of the QW self-consistently, considering only electrons ( $e$ ) and heavy holes ( $h$ ) of equal densities  $n=p$ . Mixing effects of light- and heavy-hole states are ignored; however, nonparabolicity of the conduction band is taken into account by an energy-dependent effective mass  $m^* = m^*(E)$ . The total effective potential  $V(z)$  acting on the electrons consists of the bare QW potential  $V_{\text{QW}}(z)$

– in our case a square well of width  $a=8.3$  nm and height  $U_e =297.8$  meV or  $U_h =174.9$  meV – and the direct Hartree term

$$V_H(z) = \frac{e^2}{\epsilon\epsilon_0} \int_{-\infty}^{\infty} dz' \int_{-\infty}^{\infty} dz \left[ n^{(3)}(z) - p^{(3)}(z) \right] \quad (6.6)$$

and the exchange-correlation correction within the local density approximation of density-functional theory [37]

$$V_{XC} = V_{xc}(n^{(3)}(z)) \quad (6.7)$$

where  $n^{(3)}(z)$  is the local three-dimensional charge density. Analogous equations hold, of course, for the holes. These equations are solved self-consistently with the Schrödinger equation, yielding the subband levels  $E_i$  and corresponding wave functions  $\psi_i(z)$  for a given 2D electron-hole plasma density  $n$ . We repeat the above local-density approximation calculation for a range of densities and thereby compute the renormalized electronic intersubband separation  $E_{12}(n) = E_2(n) - E_1(n)$  as a function of  $n$ . Note that this model simply accounts for the direct Coulomb interactions between electrons and holes, but neglects interband exchange processes – related to the Pauli exclusion principle and electron-hole correlations – for example, excitonic binding effects. Interband exchange is known to be small in most systems. On the other hand, the formation of excitons is a strong effect in the low-density regime, which gradually disappears with increasing excitation density due to efficient screening. From the viewpoint of the electrons, such correlations result in a further lowering of their energy levels, in addition to the Hartree attraction by the mean hole density distribution.

(ii): Dynamic electron-electron interactions:

With the static, self-consistent wavefunctions and subband energy levels from above, we then calculate the dynamic many-body corrections to the intersubband absorption spectrum. The intersubband absorption does not appear at frequencies corresponding to the self-consistent subband separation  $E_{nm}$ . Instead, the resonances are additionally shifted by the depolarization effect and by the exciton effect [40]<sup>4</sup>. The depolarization shift essentially comes from a time-dependent Hartree term. Each electron feels an effective field that is different from the external field by the mean Hartree field of the other electrons. Thus, the external field is screened by the quasi-two-dimensional electron gas. The depolarization shift can be calculated by using time-dependent perturbation theory and by introducing a self-consistent AC potential into the Schrödinger equation and evaluating the induced oscillating charge density self-consistently. The exciton interaction acts to reduce the resonance frequency and is due to the Coulomb interaction between the excited electron and the quasi-hole left behind in the ground subband. It corresponds to a reduction of the mean Hartree field around each electron due to exchange-correlation effects. In case of two-level system the final intersubband-transition energy is given by [37]

<sup>4</sup>Note that this is not to be confused with the interband exciton.

$$E_{res} = E_{12}\sqrt{1 + \alpha(n) - \beta(n)} \quad (6.8)$$

with  $\alpha(n) = 2I_{ee}n/E_{12}(n)$ , accounting for the depolarization shift and

$$\beta(n) = \frac{-2n}{E_{12}(n)} \int dz [\psi_1(z)]^2 [\psi_2(z)]^2 \frac{\delta V_{xc}(n^{(3)})}{\delta n^{(3)}}(z) \quad (6.9)$$

being its excitonic counterpart. The Coulomb integral  $I_{ee}$  in an homogenous system is given by:

$$I_{ee} = -\frac{e^2}{2\epsilon\epsilon_0} \int dz \int dz' \psi_2(z)\psi_1(z) |z - z'| \psi_2(z')\psi_1(z') \quad (6.10)$$

(iii):Dynamic electron-hole interactions:

Now we discuss shortly the possibility of dynamic interactions between electrons and holes. For a similar system this was implemented in the calculations by linearizing Eqn.(6.8) for the intersubband transitions in the conduction band as well as in the the valence band [165], e.g.

$$\begin{aligned} E_{lin}(n) &= E_{12}(n) + nT_{ee} \\ H_{lin}(p) &= H_{12}(p) + pT_{hh} \end{aligned} \quad (6.11)$$

where  $\beta$  was neglected and  $\alpha$  assumed being close to unity.

This treatment yields a system of two coupled oscillators, with the solution:

$$\hbar\omega_{1,2} = \frac{1}{2} [E_{lin}(n) + H_{lin}(p)] \pm \frac{1}{2} |E_{lin}(n) - H_{lin}(p)| \sqrt{1 + \gamma} \quad (6.12)$$

with the dimensionless coupling coefficient

$$\gamma = \left( \frac{\sqrt{np} T_{eh}}{E_{lin}(n) - H_{lin}(p)} \right)^2 \quad (6.13)$$

The result of this simulation is shown as the red full line in Fig. 6.8, calculated for a carrier density varying from  $n^{(2)} = 0.7 \times 10^{10} \text{cm}^{-2}$  up to  $n^{(2)} = 7 \times 10^{11} \text{cm}^{-2}$ . As observed experimentally, there is only a small shift of the intersubband resonance for low excitation densities, whereas with higher carrier densities the intersubband resonance shifts linearly towards higher photon energies. Note that there are essentially no fitting parameters included in the simulation, indication that this treatment gives a correct description of the energetic shift of the main resonance peak observed in the experiment. Note that in the work of Shtrichman *et al.*[165] it was shown that this treatment gives a better agreement than only the use of Eqn.(6.8), where the holes are neglected, but without the linearization used in Eqn.(6.11).

From the above model, the lineshape of the intersubband resonance cannot be deduced. At low temperatures, we have observed strongly asymmetric lineshapes, giving rise to a strong phase shift of the spectral phase of the induced polarization. Due to the limited



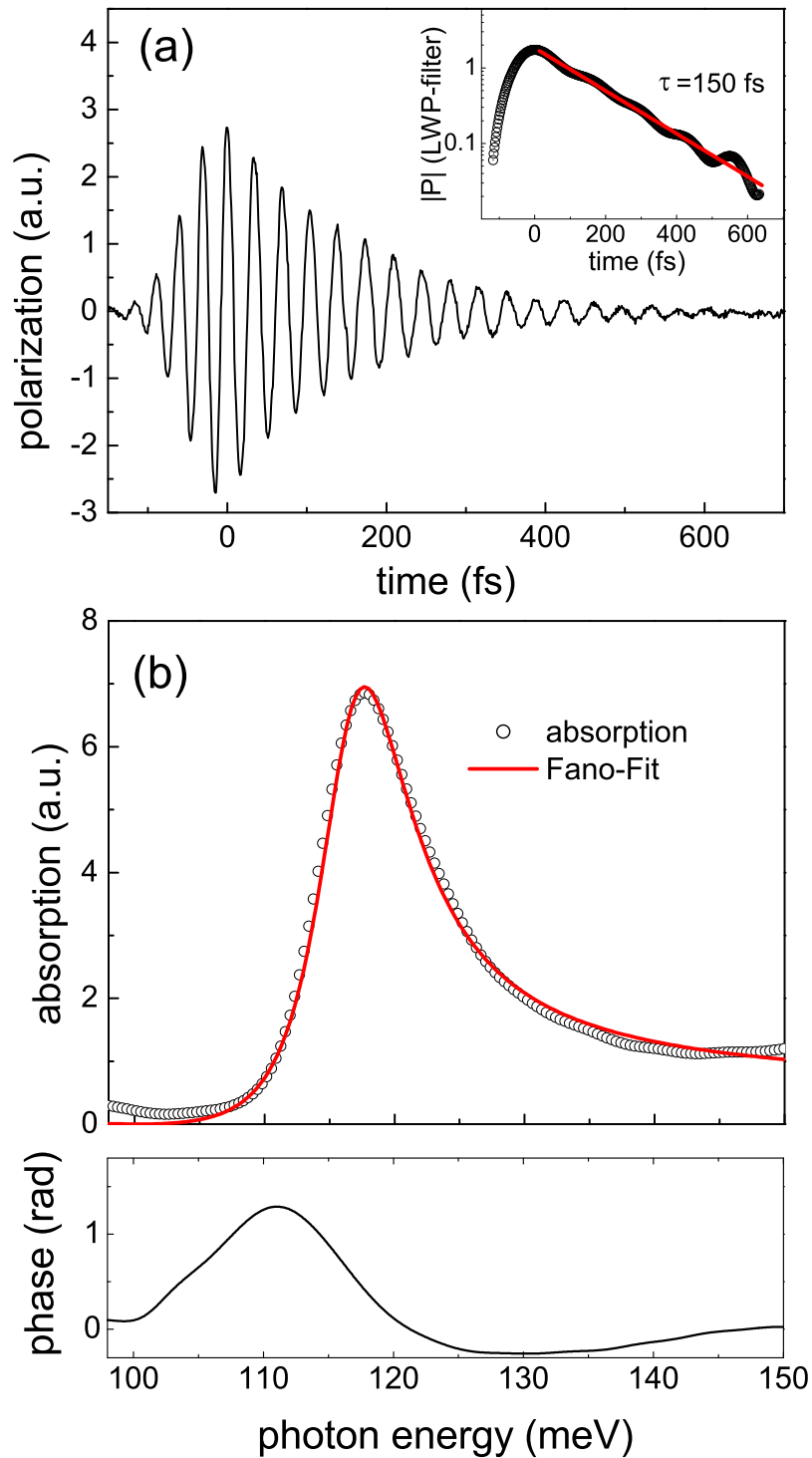


**Figure 6.9:** (a) Polarization waveform recorded at an excitation density of  $n^{(2)} = 2.5 \times 10^{11} \text{ cm}^{-2}$ . The inset shows the absolute polarization with fringes removed by a low pass filter and a mono-exponential fit to its decay. (b) Absorption spectrum and corresponding spectral phase. The solid red line represents the result of a typical Fano resonance calculated from experimental data and fit parameters (see details in the text).

accuracy in the experiments involving ps-interband excitation (due to thermal drifts, when long dephasing times are measured), this asymmetry was not pronounced as much as for the fs excitation. However, once the interferograms become shorter, thermal drifts become less important. Therefore we discuss now the lineshape of the photoinduced absorption taken at an excitation density of  $n^{(2)} = 2.5 \times 10^{11} \text{ cm}^{-2}$  by using ps-excitation at  $\lambda = 791 \text{ nm}$ . This excitation density is about ten times higher than used in the previous experiments (Figs. 6.6 and 6.7). The time-dependent polarization is shown in Fig. 6.9(a). As before, we observe a rapid increase of the induced polarization within about 100 fs, which subsequently decays and vanishes at a time of 600 fs. From the curve, we extract the dephasing time by taking the absolute value of  $P(t)$  and remove the fast oscillating parts with a low band-pass filter at 8 THz, as shown in the inset of Fig. 6.9(a). The decay of this signal can be assimilated mono-exponentially, resulting in a dephasing time of  $\tau = 150 \text{ fs}$ . From this dephasing time we can calculate the homogenous linewidth, being  $2\Gamma = 8.8 \text{ meV}$  as the full-width half maximum. The absorption spectrum, shown in Fig. 6.9(b) is obtained by dividing the Fourier spectrum of the recorded waveform by a reference spectrum, where the interband excitation is absent. The resulting spectrum exhibits a strong asymmetry around the main resonance at 118 meV. While towards lower photon energies the absorption line drops sharply, we observe a long absorption tail at higher photon energies. Below the absorption spectrum we also show the spectral phase of the absorption, where the phase of the reference spectrum (exhibiting a drift due to the chirp of the THz pulse within the waveguide) is subtracted to obtain a pure signal due to the presence of photo-generated carriers. Starting from the low-energy side, the phase increases linearly and exhibits a maximum at about 111 meV, which also marks the onset of the absorption peak. After this the phase drops back to zero, becomes slightly negative and finally recovers to zero at the end of the spectrum. Note that this behavior bears similarity to the phase change observed earlier (compare Fig. 6.5). However, it is not as sharp due to the larger linewidths involved at these excitation densities.

Note that in the common approach of the density-matrix formalism of a two-level system, such asymmetric lineshapes cannot be explained. Hence, a different mechanism with more levels included must be responsible for the observed lineshape. In fact, by comparison with data published earlier we found a strong similarity of the observed lineshape with absorption spectra recorded in systems exhibiting Fano resonances. Such Fano resonances are at the heart of quantum mechanics, since they show the presence of quantum interference in a discrete two-level system coupled to a continuum [167]. In principle, these quantum-interference effects appear once a discrete two-level system is *resonantly* coupled to a continuum of states. In most intersubband systems investigated so far, this coupling is provided by quantum-mechanical tunneling processes [158]. In fact, also in intersubband-absorption experiments, Fano resonances were demonstrated [154]. However, this and similar experiments involved a complicated conduction-band structure, where a continuum was formed within the conduction band of the specially designed heterostructure.

In our case, this cannot be the explanation for the asymmetric structure of the observed absorption line. But, on the other hand, also in systems exhibiting a confinement due to large magnetic fields [168] or semiconductor heterostructures such as quantum wells and quantum wires, the existence of Fano-resonances were predicted and eventually proven in the case of excitonic interband absorption [156, 169, 157]. In these works the resonances are explained by Coulomb coupling of the bound and scattering states of an exciton series belonging to different subband pairs but occurring at the same photon energy. Particularly, Glutsch *et al.* [170] theoretically predicted the presence of Fano resonances in a quantum well around the hh1-cb2-excitonic absorption line. However, it was predicted that this feature was rather small and only observable in the case of extremely small linewidths. But these works studied only the effects of interband light interaction with the quantum wells system. Sadeghi *et al.*[171] included a resonant infrared field in their calculations and found a strong enhancement of the Fano-like behavior in the photoluminescence spectra of single quantum wells. Thus, naturally, it can be expected that the reverse interaction leads to a similar effect on the cb1-cb2 transition itself.

For a simple approximation of the observed lineshape we therefore calculated the Fano-like absorption spectrum according to the original work of Fano in 1961 [167]. There, the absorption line can be assimilated by the following formula:

$$A(\hbar\omega) \propto \frac{(q + \epsilon)^2}{1 + \epsilon^2} = 1 + \frac{q^2 - 1 + 2q\epsilon}{1 + \epsilon^2} \quad (6.14)$$

where  $\epsilon = (\hbar\omega - E_{12})/(\Gamma/2)$  denotes the reduced photon energy and  $q$  is the parameter describing the asymmetry of the lineshape[167]. In an intersubband system with a high potential barrier, it was shown that  $q$  can be approximated by [154]

$$q^2 = \frac{\Gamma_{1 \rightarrow c} f_{1 \rightarrow 2}}{\Gamma f_{1 \rightarrow c}} \quad (6.15)$$

where  $2\Gamma_{1 \rightarrow c}$  is the range over which the absorption to the continuum is spread and  $f_{1 \rightarrow 2}$  and  $f_{1 \rightarrow c}$  are the oscillator strengths from the ground states to the first excited state of the two-level system and to the continuum, respectively. For the calculation of the lineshape, we take the experimental data from our measurements, which are 4.4 meV for the spectral width  $\Gamma$  and  $f_{1 \rightarrow 2} \approx 1$  for the oscillator strength of the intersubband transition. For the oscillator strength into the continuum, we also assume an oscillator strength of  $f_{1 \rightarrow c} \approx 1$ , which is arbitrary, since we do not know the correct energy- and wavefunction situation. For the width of the continuum transition, we choose a value  $\Gamma_{1 \rightarrow c} = 62.5$  meV, to come up with a comparable lineshape to what we observed in our experiment. Note that we principally just vary the ratio of  $\Gamma_{1 \rightarrow c}/f_{1 \rightarrow c}$  as a fitting parameter. The bare resonance energy  $E_{12}$  is chosen slightly lower than the maximum of the measured absorption spectrum, i.e. 116.5 meV.

The result of this simple approximation is shown as the full red line in Fig. 6.9(b). The displayed lineshape shows an amazingly good agreement with the experimental data, and the

overall spectral behavior can be reproduced in a way such that the main spectral features match with the experimental ones. However, only the agreement of spectral shapes does not give rise to the final statement that this is the reason for our asymmetric lineshapes, it just gives a strong indication. For the proof, it is necessary to fully account for all possible transitions in the system, which include collective electron transitions in the conduction band, their counterparts in the valence band as well as the effect that electrons and holes form an excitonic electron-hole system. In fact, especially the latter can be suspected to have a strong influence, since the asymmetric lineshapes occur only at low temperatures, where excitons can be formed.

Overall, we have shown that the all-optical time-resolved time-domain approach for investigations of intersubband transitions has revealed many interesting phenomena that are not accessible by different methods, such as with doped samples or by stationary experiments. As two prime examples, we were able to determine the influence of the carrier-density on the dephasing time within a single sample, which is, of course not possible in doped structures where for each electron concentration a different sample is needed<sup>5</sup>. Secondly, we observed strong deviations of intersubband absorption spectra recorded either at room temperature and a temperature of 4 K, indicating that the formation of excitons has a significant impact on the intersubband lineshape.

## 6.4 Outlook

As already mentioned, to prove the indication that the excitonic nature of the photo-generated carriers has a influence on the the shape of the observed intersubband transition, it is essential to take all possible energetic levels present in this quantum well system into account. This will include interband- as well as intersubband transitions. However, a full many-body theory for such conditions has not been developed yet, and in fact, we hope that we are able stimulate a progress in this field for further investigations.

To verify the claim that the generated electron and holes eventually are present as excitons at low temperatures, a direct probing of the intra-excitonic transition after photogeneration [172, 173] can be used. Therefore one has to probe at photon energies around 0.5-3 THz, which is a widely used frequency range for time-domain spectroscopy, since many efficient methods exist for the generation of spectrally sufficiently wide THz pulses. In our case, the GaSe-emitter would simply be replaced by such a low THz-frequency emitter, and electro-optic sampling would be needed for detection.

---

<sup>5</sup>A possibility to vary the electron density in doped samples is the use of a gate contact to deplete the quantum well. However, the strong electric field from the gate also influences the heterostructure potential, which is avoided by our approach.

## Bibliography

- [1] R. Chau, B. Boyanov, B. Doyle, M. Doczy, S. Datta, S. Hareland, B. Jin, J. Kavalieros, and M. Metz, *Physica E: Low-dimensional Systems and Nanostructures* **19**, 1 (2003).
- [2] R. Chau, S. Datta, M. Doczy, B. Doyle, B. Jin, J. Kavalieros, A. Majumdar, M. Metz, and M. Radosavljevic, *IEEE Trans. on Nanotechnology* **4**, 153 (2005).
- [3] Y. Arakawa and H. Sakaki, *Appl. Phys. Lett.* **40**, 939 (1982).
- [4] L. Esaki and R. Tsu, *IBM J. Res. Develop.* **14**, 61 (1970).
- [5] R. Dingle, W. Wiegmann, and C.H. Henry, *Phys. Rev. Lett.* **33**, 827 (1974).
- [6] L.C. West and S.J. Eglash, *Appl. Phys. Lett.* **46**, 1156 (1985).
- [7] J.H. Smet, L.H. Peng, Y. Hirayama, and C.G. Fonstad, *Appl. Phys. Lett.* **64**, 986 (1994).
- [8] M. Helm, F.M. Peeters, F. DeRosa, E. Colas, J.P. Harbison, and L.T. Florez, *Phys. Rev. B* **43**, 13983 (1991).
- [9] H. Schneider and H.C. Liu, *Quantum Well Infrared Photodetectors*, Springer Berlin (2006).
- [10] R. Köhler, A. Tredicucci, F. Beltram, H.E. Beere, E.H. Linfield, A.G. Davies, D.A. Ritchie, R.C. Iotti, and F. Rossi, *Nature (London)* **417**, 156 (2002).
- [11] C. Walther, G. Scalari, J. Faist, H. Beere, and D. Ritchie, *Appl. Phys. Lett.* **89**, 231121 (2006).
- [12] J. Faist, F. Capasso, D. L. Sivco, C. Sirtori, A.L. Hutchinson, and A.Y. Cho, *Science* **264**, 5158 (1994).
- [13] M.P. Semtsiv, M. Wienold, S. Dressler, and W.T. Masselink, *Appl. Phys. Lett.* **89**, 211124 (2006).
- [14] J. Devenson, D. Barate, O. Cathabard, R. Teissier, and A.N. Baranov, *Appl. Phys. Lett.* **89**, 191115 (1998).

- [15] S.G. Carter, V. Birkedal, C.S. Wang, L.A. Coldren, A.V. Maslov, D.S. Citrin, and M.S. Sherwin, *Science* **310**, 651 (2005).
- [16] K.v. Klitzing, G. Doerda, and M. Pepper, *Phys. Rev. Lett.* **45**, 494 (1980).
- [17] S.D. Tsui, H.L. Störmer, and A.C. Gossard, *Phys. Rev. Lett.* **48**, 1559 (1982).
- [18] E.O. Göbel and K. Ploog, *Prog. Quant. Electron.* **14**, 289 (1990).
- [19] J. Shah, *Ultrafast Spectroscopy of Semiconductors and Semiconductor Nanostructures*, Springer New York (1999).
- [20] H. Haug and S.W. Koch, *Quantum Theory of the Optical and Electronic Properties of Semiconductors*, World Scientific Singapore (1994).
- [21] D.S. Chemla, *Ultrafast Transient Nonlinear Optical Processes in Semiconductors* volume 58 of *Semiconductors and Semimetals*, Academic Press San Diego (1999).
- [22] S.W. Koch, M. Kira, G. Khitrova, and H.M. Gibbs, *Nature Materials* **5**, 523 (2006).
- [23] L.V. Butov, A. Zrenner, G. Abstreiter, G. Böhm, and G. Weimann, *Phys. Rev. Lett.* **73**, 304 (1994).
- [24] D. Snoke, *Science* **298**, 1368 (2002).
- [25] M. Helm, *Semicond. Sci. Technol.* **10**, 567 (1995).
- [26] K. Unterrainer, B.J. Keay, M.C. Wanke, S.J. Allen, D. Leonard, G. Medeiros-Ribeiro, U. Bhattacharya, and M.J.W. Rodwell, *Phys. Rev. Lett.* **76**, 2973 (1996).
- [27] K. Leo, *High-Field Transport in Semiconductor Superlattices*, Springer New York (2003).
- [28] N. Sekine and K. Hirakawa, *Phys. Rev. Lett.* **94**, 57408 (2005).
- [29] P.G. Savvidis, B. Kolasa, G. Lee, and S.J. Allen, *Phys. Rev. Lett.* **92**, 196802 (2004).
- [30] T. Elsaesser, J.G. Fujimoto, D.A. Wiersma, and W. Zinth, editors, volume XI of *Ultrafast Phenomena*, Springer Berlin (1998).
- [31] T. Elsaesser and M. Woerner, *Phys. Rep.* **312**, 253 (1999).
- [32] T. Elsaesser, S. Mukamel, M.M. Murnane, and N.F. Scherer, editors, volume XII of *Ultrafast Phenomena*, Springer Berlin (2001).
- [33] F. Compagnone, A. DiCarlo, and P. Lugli, *Appl. Phys. Lett.* **80**, 920 (2002).
- [34] G. Bastard, *Phys. Rev. B* **24**, 4714 (1981).

- [35] G. Bastard, *Wave mechanics applied to semiconductor heterostructures*, Halsted Press New York (1988).
- [36] R.L. Greene and K.K. Bajaj, *Phys. Rev. B* **31**, 4006 (1985).
- [37] M. Helm, *The Basics Physics Of Intersubband Transitions: Physics and Device Applications*, In H.C. Liu and F. Capasso, editors, *Semiconductors and Semimetals* volume **62** chapter 1. Academic Press San Diego 2000.
- [38] K.L. Campman, H. Schmidt, A. Imamoglu, and A.C. Gossard, *Appl. Phys. Lett.* **69**, 2554 (1996).
- [39] M. Zaluzny, *Phys. Rev. B* **43**, 4511 (1991).
- [40] T. Ando, A.B. Fowler, and F. Stern, *Rev. Mod. Phys.* **54**, 437 (1982).
- [41] M. Helm, W. Hilber, T. Fromherz, F.M. Peeters, K. Alavi, and R.N. Pathak, *Phys. Rev. B* **48**, 1601 (1993).
- [42] K.L. Vodopyanov, V. Chazapis, C.C. Phillips, B. Sung, and J.S. Harris Jr., *Semicond. Sci. Technol.* **12**, 708 (1997).
- [43] R.W. Boyd, *Nonlinear Optics*, Academic Press London (1992).
- [44] R.A. Kaindl, S. Lutgen, M. Woerner, T. Elsaesser, B. Nottelmann, V.M. Axt, T. Kuhn, A. Hase, and H. Künzel, *Phys. Rev. Lett.* **80**, 3575 (1998).
- [45] R.A. Kaindl, K. Reimann, M. Woerner, T. Elsaesser, R. Hey, and K.H. Ploog, *Phys. Rev. B* **63**, 161308 (2001).
- [46] S. Lutgen, R.A. Kaindl, M. Woerner, T. Elsaesser, A. Hase, and H. Künzel, *Phys. Rev. B* **54**, R17343 (1996).
- [47] D.M. Finlayson, editor, *Localization and Interaction in Disordered Metals and Semiconductors*, Inst. Phys. Publications Bristol, UK (1986).
- [48] D. Romero, S. Liu, and H.D. Drew, *Phys. Rev. B* **42**, 3179 (1990).
- [49] M.C. Maliepaard, M. Pepper, R. Newbury, and G. Hill, *Phys. Rev. Lett.* **61**, 369 (1988).
- [50] H.C. Liu and F. Capasso, editors, *Intersubband Transitions in Quantum Wells: Physics and Device Applications* volume 62 of *Semiconductors and Semimetals*, Academic Press, San Diego (2000).
- [51] C. Mailhot, Y C. Chang, and T.C. McGill, *Phys. Rev. B* **26**, 4449 (1982).

- [52] R. Chen, J.P. Cheng, D.L. Lin, B.D. McCombe, and T.F. George, *J. Phys.: Condens. Matter* **7**, 3577 (1995).
- [53] A. Bruno-Alfonso, G.Q. Hai, F.M. Peeters, T. Yeo, S.R. Ryu, and B. D. McCombe, *J. Phys.: Condens. Matter* **13**, 9761 (2001).
- [54] J.P. Cheng and B.D. McCombe, *Phys. Rev. B* **42**, 7626 (1990).
- [55] T.A. Perry, R. Merlin, B.V. Shanabrook, and J. Comas, *Phys. Rev. Lett.* **54**, 2623 (1985).
- [56] X. Marcadet M. Carras, V. Berger and B. Vinter, *Phys. Rev. B* **70**, 233310 (2004).
- [57] S. T. Yen, *Phys. Rev. B* **68**, 165331 (2003).
- [58] C. Priester, G. Allan, and M. Lannoo, *Phys. Rev. B* **29**, 3408 (1984).
- [59] A. Ghazali and J. Serre, *Phys. Rev. Lett.* **48**, 886 (1982).
- [60] J. Serre and A. Ghazali, *Phys. Rev. B* **28**, 4704 (1983).
- [61] J. Serre, A. Ghazali, and A. Gold, *Phys. Rev. B* **39**, 8499 (1989).
- [62] J. Kortus and J. Monecke, *Phys. Rev. B* **49**, 17216 (1994).
- [63] M. Hofmann, M. Bockstedte, and O. Pankratov, *Phys. Rev. B* **64**, 245321 (2001).
- [64] B.S. Monozon and P. Schmelcher, *Phys. Rev. B* **71**, 085302 (2005).
- [65] C. Metzner, M. Hofmann, and G.H. Döhler, *Phys. Rev. B* **58**, 7188 (1998).
- [66] R.N. Riemann, C. Metzner, and G.H. Döhler, *Phys. Rev. B* **65**, 115304 (2002).
- [67] M.C. Wanke , private communication.
- [68] H. A. Fertig and S. Das Sarma, *Phys. Rev. B* **42**, 1448 (1990).
- [69] S. Liu, K. Karrai, F. Dunmore, H.D. Drew, R. Wilson, and G.A. Thomas, *Phys. Rev. B* **48**, 11394 (1993).
- [70] D. Stehr, C. Metzner, M. Helm, T. Roch, and G. Strasser, *Phys. Rev. Lett.* **95**, 257401 (2005).
- [71] W. Hilber, M. Helm, F.M. Peeters, K. Alavi, and R.N. Pathak, *Phys. Rev. B* **53**, 6919 (1996).
- [72] J.J. Lee, N. Georgiev, T. Dekorsy, and M. Helm, (unpublished).
- [73] P.W. Milonni and J.H. Eberly, *Lasers*, John Wiley & Sons Inc. New York (1988).



- [74] K. Wille, *Physik der Teilchenbeschleuniger und Synchrotronstrahlungsquellen*, Teubner Studienbücher Stuttgart, Germany (1992).
- [75] T.C. Marshall, *Free Electron Lasers*, MacMillan New York (1985).
- [76] C.A. Brau, *Free Electron Lasers*, Academic Press Boston (1991).
- [77] L.M.J. Madey, *Nuovo Cimento* **B50**, 64 (1979).
- [78] G. Margaritondo, *Elements of Synchrotron Light*, Oxford University Press New York (2002).
- [79] G.M.H. Knippels, *The Short-Pulse Free-Electron Laser: Manipulation of the Gain Medium*, PhD thesis Vrije Universiteit, Amsterdam 1996.
- [80] G. Dattoli and A. Renieri, *Experimental and theoretical aspects of the free-electron laser* volume 4 of *Laser Handbook*, North-Holland Amsterdam (1985).
- [81] D.A. Jarosznvski, D. Oepts, A.F.G. van der Meer, F.W. van Amersfoort, and W.B. Colson, *Nucl. Instrum. & Methods Phys. Res. A* **296**, 480 (1990).
- [82] D.J. Bradley and G.H.C. New, Ultrashort pulse measurements, *IEEE J. Quantum Electron.* **62**, 313 (1974).
- [83] G.M.H. Knippels, R.F.X.A.M. Mols, A.F.G. van der Meer, D. Oepts, and P.W. van Amersfoort, *Phys. Rev. Lett.* **75**, 1755 (1995).
- [84] P. Michel, F. Gabriel, E. Grosse, P. Evtushenko, T. Dekorsy, M. Krenz, M. Helm, U. Lehnert, W. Seidel, R. Wunsch, D. Wohlfarth, and A. Wolf, Proceedings of the 26th International FEL Conference Trieste (2004), <http://accelconf.web.cern.ch/accelconf/f04/papers/MOAIS04/MOAIS04.pdf>.
- [85] U. Lehnert, P. Michel, W. Seidel, D. Stehr, J. Teichert, D. Wohlfarth, and R. Wunsch, Proceedings of the 27th International FEL Conference Stanford (2005), <http://accelconf.web.cern.ch/AccelConf/f05/PAPERS/TUPP030.PDF>.
- [86] D.A. McArthur and D.H. Alexander, *Appl. Opt.* **10**, 2566 (1971).
- [87] C.J. Johnson, G.H. Sherman, and R. Weil, *Appl. Opt.* **8**, 1667 (1969).
- [88] A.M. MacLeod, X. Yan, W.A. Gillespie, G.M.H. Knippels, D. Oepts, A.F.G. van der Meer, C.W. Rella, T.I. Smith, and H.A. Schwettman, *Phys. Rev. E* **62**, 4216 (2000).
- [89] C.W. Rella, G.M.H. Knippels, D.V. Palanker, and H.A. Schwettman, *Optics. Commun.* **157**, 335 (1998).
- [90] P. Evtushenko, *Electron Beam Diagnostic at the ELBE Free Electron Laser*, PhD thesis Forschungszentrum Dresden-Rossendorf 2004.

- [91] D. Martin, *Polarizing (Martin-Puplett) interferometric spectrometers for the near- and sub-millimeter spectra*, Infrared and Millimeter Waves. Academic Press New York (1991).
- [92] K.L. Vodopyanov and L.A. Kulevskii, *Opt. Commun.* **118**, 375 (1995).
- [93] V.G. Dmitriev, G.G. Gurzadyan, and D.N. Nikogosyan, *Polarizing (Martin-Puplett) interferometric spectrometers for the near- and sub-millimeter spectra, 3rd Edition* volume **64** of *Springer Series in Optical Sciences*, Springer Berlin (1999).
- [94] J.M. Auerhammer and E.R. Eliel, *Opt. Lett.* **21**, 773 (1996).
- [95] B.N. Murdin, K. Litvinenko, D.G. Clarke, C.R. Pidgeon, P. Murzyn, P.J. Phillips, D. Carder, G. Berden, B. Redlich, A.F.G. van der Meer, S. Clowes, J.J. Harris, L.F. Cohen, T. Ashley, and L. Buckle, *Phys. Rev. Lett.* **96**, 96603 (2006).
- [96] S. Lutgen, R.A. Kaindl, M. Woerner, T. Elsaesser, A. Hase, H. Kunzel, M. Gulia, D. Meglio, and P. Lugli, *Phys. Rev. Lett.* **77**, 3657 (1996).
- [97] C. Kolano, J. Helbing, M. Kozinski, W. Sander, and P. Hamm, *Nature (London)* **444**, 469 (2006).
- [98] A. Leitenstorfer, C. Fürst, and A. Laubereau, *Opt. Lett.* **20**, 916 (1995).
- [99] T.R. Schibli, J. Kim, O. Kuzucu, J.T. Gopinath, S.N. Tandon, G.S. Petrich, L.A. Kolodziejski, J.G. Fujimoto, E.P. Ippen, and F.X. Kaertner, *Opt. Lett.* **28**, 947 (1995).
- [100] For example, see manual for Spectra-Physics Synchronisation unit Lock-To-Clock.
- [101] G.M.H. Knippels, M.J. van de Pol, H.P.M. Pellemans, P.C.M. Planken, and A.F.G. van der Meer, *Opt. Lett.* **23**, 1754 (1998).
- [102] R. Prazeres, F. Glotin, C. Insa, D.A. Jaroszynski, and J.M. Ortega, *Eur. Phys. J. D* **3**, 87 (1998).
- [103] C. Spielmann, P.F. Curley, T. Brabec, and F. Krausz, *IEEE J. Quantum Electron.* **30**, 1100 (1994).
- [104] T. Brabec and F. Krausz, *Rev. Mod. Phys.* **72**, 545 (2000).
- [105] R.A. Kaindl, D.C. Smith, M. Joschko, M.P. Hasselbeck, M. Woerner, and T. Elsaesser, *Opt. Lett.* **23**, 861 (1998).
- [106] R.A. Kaindl, F. Eickemeyer, M. Woerner, and T. Elsaesser, *Appl. Phys. Lett.* **75**, 1060 (1999).

- [107] F. Eickemeyer, *Ultrafast dynamics of coherent intersubband polarizations in quantum wells and quantum cascade laser structures*, PhD thesis Humboldt-Universität zu Berlin (2002).
- [108] B.I. Greene, J.F. Federici, D.R. Dykaar, R.R. Jones, and P.H. Buckbaum, *Appl. Phys. Lett.* **59**, 893 (1991).
- [109] S.E. Ralph and D. Grischkowsky, *Appl. Phys. Lett.* **60**, 1070 (1992).
- [110] M. Joffre, A. Bonvalet, A. Migus, and J.-L. Martin, *Opt. Lett.* **21**, 964 (1996).
- [111] J.N. Heyman, R. Kersting, and K. Unterrainer, *Appl. Phys. Lett.* **72**, 644 (1998).
- [112] A. Bonvalet, J. Nagle, V. Berger, A. Migus, J.-L. Martin, and M. Joffre, *Phys. Rev. Lett.* **76**, 4392 (1996).
- [113] Q. Wu and X.-C. Zhang, *Appl. Phys. Lett.* **67**, 3523 (1995).
- [114] A. Nahata, D.H. Auston, and T.F. Heinz, *Appl. Phys. Lett.* **68**, 150 (1996).
- [115] Q. Wu and X.-C. Zhang, *Appl. Phys. Lett.* **68**, 1604 (1996).
- [116] Q. Wu and X.-C. Zhang, *IEEE Jour. of Sel. Topics in Quantum Electronics* **3**, 693 (1996).
- [117] Q. Wu and X.-C. Zhang, *Appl. Phys. Lett.* **70**, 1784 (1997).
- [118] Z. Jiang and X.-C. Zhang, *Appl. Phys. Lett.* **72**, 1945 (1998).
- [119] G. Gallot, J. Zhang, R.W. McGowan, T.-I. Jeon, and D. Grischkowsky, *Appl. Phys. Lett.* **74**, 3450 (1999).
- [120] C. Winnewisser, P.U. Jepsen, M. Schall, V. Schyja, and H. Helm, *Appl. Phys. Lett.* **70**, 3069 (1997).
- [121] C. Kübler, R. Huber, S. Tübel, and A. Leitenstorfer, *Appl. Phys. Lett.* **85**, 3360 (2004).
- [122] A. Leitenstorfer, S. Hunsche, J. Shah, M.C. Nuss, and W.H. Knox, *Appl. Phys. Lett.* **74**, 1516 (1999).
- [123] R. Huber, A. Brodschelm, F. Tauser, and A. Leitenstorfer, *Appl. Phys. Lett.* **76**, 3191 (2000).
- [124] D. von der Linde, *Appl. Phys. B* **39**, 201 (1986).
- [125] D.E. Spence, W.E. Sleat, J.M. Evans, W. Sibbet, and J.D. Kafka, *Opt. Commun.* **101**, 286 (1993).

- [126] M.J.W. Rodwell, D.M. Bloom, and K.J. Weingarten, *IEEE J. Quantum Electron.* **25**, 817 (1989).
- [127] C. Gmachl, F. Capasso, D.L. Sivco, and A.Y. Cho, *Rep. Prog. Phys.* **64**, 1533 (2001).
- [128] M.S. Vitiello, G. Scamarcio, V. Spagnolo, B.S. Williams, S. Kumar, Q. Hua, and J.L. Reno, *Appl. Phys. Lett.* **64**, 111115 (2005).
- [129] M. Troccoli, G. Scamarcio, V. Spagnolo, A. Tredicucci, C. Gmachl, F. Capasso, D.L. Sivco, A.Y. Cho, and M. Striccoli, *Appl. Phys. Lett.* **64**, 1088 (2000).
- [130] G. Scamarcio, F. Capasso, C. Sirtori, J. Faist, A.L. Hutchinson, D.L. Sivco, and A.Y. Cho, *Science* **276**, 773 (1997).
- [131] M. Woerner, T. Elsaesser, and W. Kaiser, *Phys. Rev. B* **41**, 5463 (1990).
- [132] R. Ferreira and G. Bastard, *Phys. Rev. B* **40**, 2 (1989).
- [133] J.L.T. Waugh and G. Dolling, *Phys. Rev.* **132**, 2410 (1963).
- [134] M. Dür, S.M. Goodnick, and P. Lugli, *Phys. Rev. B* **54**, 17794 (1996).
- [135] P. Lugli and S.M. Goodnick, *Phys. Rev. Lett.* **59**, 716 (1987).
- [136] M.C. Tatham and J.F. Ryan, *Phys. Rev. Lett.* **63**, 1637 (1989).
- [137] M. Helm, T. Fromherz, B.N. Murdin, C.R. Pidgeon, K.K. Geerinck, N.J. Hovenyer, W.Th. Wenckebach, A.F.G. van der Meer, and P.W. van Amersfoort, *Appl. Phys. Lett.* **63**, 3315 (1993).
- [138] B. N. Murdin, W. Heiss, C.J.G.M. Langerak, S.-C. Lee, I. Galbraith, G. Strasser, E. Gornik, M. Helm, and C.R. Pidgeon, *Phys. Rev. B* **9**, 1551 (1994).
- [139] B.N. Murdin, G.M.H. Knippels, A.F.G. van der Meer, C.R. Pidgeon, C.J.G.M. Langerakts, M. Helm, W. Heiss, K. Unterrainer, E. Gornik, K.K. Geerinck, N.J. Hovenier, and W.Th. Wenckebach, *Semicond. Sci. Technol.* **55**, 5171 (1997).
- [140] S. Tortora, F. Compagnone, A. Di Carlo, P. Lugli, M.T. Pellegrini, M. Troccoli, and G. Scamarcio, *Physica B* **272**, 219 (1999).
- [141] Z. Wang, K. Reimann, M. Woerner, T. Elsaesser, D. Hofstetter, E. Baumann, F.R. Giorgetta, H. Wu, W.J. Schaff, and L.F. Eastman, *Appl. Phys. Lett.* **89**, 151103 (2006).
- [142] M. Holthaus, *Phys. Rev. Lett.* **69**, 351 (1993).
- [143] C.W. Luo, K. Reimann, M. Woerner, T. Elsaesser, R. Hey, and K.H. Ploog, *Phys. Rev. Lett.* **92**, 47402 (2004).

- [144] K.L. Vodopyanov, V. Chazapis, and C.C. Phillips, *Appl. Phys. Lett.* **69**, 3405 (1996).
- [145] K. Leo, J. Shah, E.O. Göbel, T.C. Damen, S. Schmitt-Rink, W. Schäfer, and K. Köhler, *Phys. Rev. Lett.* **66**, 201 (1991).
- [146] H.G. Roskos, M.C. Nuss, J. Shah, K. Leo, D.A.B. Miller, A.M. Fox, S. Schmitt-Rink, and K. Köhler, *Phys. Rev. Lett.* **68**, 2216 (1992).
- [147] P.G. Huggard, C.J. Shaw, S.R. Andrews, and J.A. Cluff, *Phys. Rev. Lett.* **84**, 1023 (2000).
- [148] T. Müller, W. Parz, G. Strasser, and K. Unterrainer, *Appl. Phys. Lett.* **84**, 64 (2004).
- [149] T. Müller, R. Bratschitsch, G. Strasser, and K. Unterrainer, *Appl. Phys. Lett.* **79**, 2755 (2001).
- [150] P.C.M. Planken, M.C. Nuss, I. Brener, K.W. Gossen, M.S.C. Luo, L. Chuang, and L.N. Pfeiffer, *Phys. Rev. Lett.* **69**, 3800 (1992).
- [151] M. Wagner, *Erzeugung, Charakterisierung, und Anwendung ultrakurzer THz-Pulse*, Master Thesis University of Konstanz (2006).
- [152] M. Kira, private communication.
- [153] D. Stehr, M. Wagner, H. Schneider, and M. Helm, (unpublished).
- [154] J. Faist, C. Sirtori, F. Capasso, S.-N.G. Chu, L.N. Pfeiffer, and K.W. West, *Opt. Lett.* **21**, 985 (1996).
- [155] L.A.O. Nunes, L. Ioriatti, L.T. Florez, and J.P. Harbison, *Phys. Rev. B* **47**, 13011 (1993).
- [156] D.Y. Oberli, G. Böhm, and G. Weimann, *Phys. Rev. B* **49**, 5757 (1994).
- [157] U. Siegner, M.A. Mycek, S. Glutsch, and D.S. Chemla, *Phys. Rev. B* **51**, 4953 (1995).
- [158] H. Schmidt, K.L. Campman, A.C. Gossard, and A. Imamoglu, *Appl. Phys. Lett.* **70**, 3455 (1997).
- [159] M. Olszakier, E. Ehrenfreund, E. Cohen, J. Bajaj, and G.J. Sullivan, *Phys. Rev. Lett.* **62**, 2997 (1989).
- [160] R.A. Kaindl, *Ultrafast mid-infrared studies of low-energy excitations in solids*, PhD thesis Humboldt-Universität zu Berlin (2000).
- [161] P. v. Allmen, *Phys. Rev. B* **46**, 13351 (1992).
- [162] S.-C. Lee and I. Galbraith, *Phys. Rev. B* **55**, R16025 (1997).

- 
- [163] S.-C. Lee and I. Galbraith, *Phys. Rev. B* **59**, 15796 (1999).
- [164] K. Meissner, B. Fluegel, H. Giessen, G. Mohs, R. Binder, S.W. Koch, and N. Peyghambarian, *Phys. Rev. B* **50**, 17647 (1994).
- [165] I. Shtrichman, C. Metzner, E. Ehrenfreund, D. Gershoni, K.D. Maranowski, and A.C. Gossard, *Phys. Rev. B* **65**, 35310 (2001).
- [166] T. Müller, W. Parz, G. Strasser, and K. Unterrainer, *Phys. Rev. B* **70**, 155324 (2004).
- [167] U. Fano, *Phys. Rev.* **123**, 1866 (1961).
- [168] S. Glutsch, U. Siegner, M.-A. Mycek, and D.S. Chemla, *Phys. Rev. B* **50**, 17009 (1994).
- [169] C.P. Holfeld, F. Löser, M. Sudzius, K. Leo, D.M. Whittaker, and K. Köhler, *Phys. Rev. Lett.* **81**, 874 (1998).
- [170] S. Glutsch, D.S. Chemla, and F. Bechstedt, *Phys. Rev. B* **51**, 16885 (1995).
- [171] S.M. Sadeghi and J. Meyer, *J. Phys.: Cond. Mat.* **9**, 7685 (1997).
- [172] R. Huber, F. Tauser, A. Brodschelm, M. Bichler, G. Abstreiter, and A. Leitenstorfer, *Nature (London)* **414**, 286 (2001).
- [173] R. Huber, R.A. Kaindl, B.A. Schmid, and D.S. Chemla, *Phys. Rev. B* **72**, R161314 (2005).

# Publications

## Journal papers

- [J1] T. Grange, E.A. Zibik, R. Ferreira, G. Bastard, P.J. Phillips, D. Stehr, S. Winnerl, M. Helm, M.J. Steer, M. Hopkinson, J.W. Cockburn, M.S. Skolnick, and L.R. Wilson, *Singlet and Triplet Polaron Relaxation in Doubly Charged Self-Assembled Quantum Dots*, submitted to Phys. Rev. B (2007).
- [J2] S. Schneider, J. Seidel, S. Grafström, L.M. Eng, S. Winnerl, D. Stehr, and M. Helm, *Impact of optical in-plane anisotropy on near-field phonon polariton spectroscopy*, Appl. Phys. Lett. **90**, 143101 (2007).
- [J3] S. Menzel, E. A. Zibik, P. Aivaliotis, B. A. Carpenter, D. Stehr, S. Winnerl, M. Helm, M. J. Steer, M. Hopkinson, J. W. Cockburn, and L. R. Wilson, *Electron intraband capture and relaxation in self-assembled InAs/GaAs quantum dots*, phys. stat. sol. (c), in print (2007).
- [J4] D. Stehr, M. Helm, C. Metzner, and M. C. Wanke, *Microscopic theory of impurity states in coupled quantum wells and superlattices*, Phys. Rev. B **74**, 085311 (2006).
- [J5] D. Stehr, S. Winnerl, M. Helm, T. Dekorsy, T. Roch, and G. Strasser, *Pump-probe spectroscopy of interminiband relaxation and electron cooling in doped superlattices*, Appl. Phys. Lett. **88**, 151108 (2006).
- [J6] D. Stehr, C. Metzner, M. Helm, T. Roch, and G. Strasser, *Resonant Impurity Bands in Semiconductor Superlattices*, Phys. Rev. Lett. **95**, 257401 (2005).
- [J7] C. Metzner and D. Stehr, *Mesoscopic dots as collective terahertz oscillators*, Phys. Rev. B **70**, 195433 (2004).

## Refereed Conference proceedings

- [P1] S. Winnerl, D. Stehr, O. Drachenko, H. Schneider, M. Helm, W. Seidel, P. Michel, S. Schneider, J. Seidel, S. Grafström, L.M. Eng, T. Roch, G. Strasser, T. Maier, and M. Walther, *FELBE Free-Electron Laser: Status and Application for Time Resolved Spectroscopy Experiments*, Conference digest of the 2006 IRMMW-THz 2006, 1-4244-0399-5, 159-159 (2006).
- [P2] P. Michel, H. Buettig, F. Gabriel, M. Helm, U. Lehnert, Ch. Schneider, R. Schurig, W. Seidel, D. Stehr, J. Teichert, S. Winnerl, and R. Wuensch, *The Rossendorf IR-FEL ELBE*, Proceedings of the 28<sup>th</sup> International FEL Conference at BESSY (2006). (<http://cern.ch/AccelConf/f06/PAPERS/TUCAU02.PDF>)
- [P3] W. Seidel, S. Friebel, R. Jainsch, M. Justus, K.-W. Leege, D. Proehl, D. Stehr, H. Weigelt, S. Winnerl, and D. Wohlfarth, *Remote Controlled IR-Diagnostic Station for the FEL at Rossendorf*, Proceedings of the 28<sup>th</sup> International FEL Conference at BESSY (2006). (<http://cern.ch/AccelConf/f06/PAPERS/TUPPH015.PDF>)
- [P4] D. Stehr, M. Helm, C. Metzner, and M.C. Wanke, *Theory of Impurity States in Coupled Quantum Wells and Superlattices and Their Infrared Absorption Spectra*, AIP Conference Proceedings **893**, 243 (2007).
- [P5] D. Stehr, S. Winnerl, M. Helm, A. M. Andrews, T. Roch, and G. Strasser, *Relaxation Dynamics of Interminiband Transitions and Electron Cooling in Doped GaAs/AlGaAs Superlattices* AIP Conference Proceedings **893**, 485 (2007).
- [P6] S. Winnerl, A. Dreyhaupt, F. Peter, D. Stehr, M. Helm, and T. Dekorsy, *High-Intensity THz Radiation from a Large-Aperture Photoconductive Emitter*, Springer Proceedings in Physics **110**, 73 (2006).
- [P7] U. Lehnert, P. Michel, W. Seidel, D. Stehr, J. Teichert, D. Wohlfarth, and R. Wünsch, *Optical Beam Properties and Performance of the MID-IR FEL at ELBE*, Proceedings of the 27<sup>th</sup> International FEL Conference (Stanford, 2005). (<http://accelconf.web.cern.ch/AccelConf/f05/PAPERS/TUPP030.PDF>)



# Acknowledgement

The research work described in this thesis was carried out at the Forschungszentrum Dresden-Rossendorf and finally, I would like to acknowledge all those people who helped to make this thesis possible.

Firstly, many thanks to my supervisor, Manfred Helm, for his constant and kind support and patience throughout the last three years. Additionally he has initiated the international collaborations which were indispensable in the success of this thesis.

Many thanks to Harald Schneider for the fruitful discussions and support, the friendly working atmosphere, and the critical reading of the manuscript.

I am grateful to Thomas Dekorsy for many discussions and for his kind support during the first months of my PhD period.

I would also like to thank Gottfried Strasser, Tomas Roch and Max Andrews at the Technical University of Vienna for growing the samples.

It is particular a pleasure for me to thank Claus Metzner for the fruitful cooperations and many helpful discussions throughout this thesis.

I am grateful to Wolfgang Seidel for his continuous support concerning all kinds of issues with the FEL, to Peter Michel and the whole ELBE team for their dedicated support.

I would also like to thank my laboratory colleagues, Stephan Winnerl, Martin Wagner, and Marcel Krenz for all the discussions and fun we had when working together in the lab.

I am grateful to Mike Wanke for the fruitful collaboration and providing me with his results on "strange absorption features" in a quadruple quantum well sample for the impurity project.

It is also a pleasure to thank Andre Dreyhaupt, Steffen Sinning, Christiana Villas-Boas Grimm, Falk Peter, and all the other colleagues for creating a unique working atmosphere within our group.

A particular thanks to Uta Lucchsi for the technical support. I am indebted to Sybille Kirch, Ines Heidel, and Luise Post for the prompt settlement of any kind of administrative problem.

Finally, I want to thank Martina and my parents and for their kind support and patience during the years.



# Curriculum Vitae

## Address

Lauensteiner Straße 18  
01277 Dresden

Tel.: (0351)3125689  
E Mail: d.stehr@fzd.de

## Personal Data

Married to Martina Stehr since 14.7.2006  
Son Anton Stehr, born 30.10.2006

## Education

- 2004–present      PhD:  
Institute of Ion Beam Physics and Materials Research, Forschungszentrum Dresden-Rossendorf, Dresden, Germany  
Supervisor: Prof. M. Helm  
Topics: *Infrared studies of ultrafast carrier dynamics in semiconductor heterostructures; electronic properties of doped GaAs/AlGaAs heterostructures*
- Feb. 2004      Diploma in Physics
- 12.2003 – 1.2004      Diploma thesis at the Institute for Technical Physics 1, University of Erlangen (Prof. G.H. Döhler)  
Topic: *All-optically controlled, collective electron-dynamics in complex potentials*
- 1998 – 2004      Physics Studies at the University of Erlangen-Nürnberg, Germany
- 1998      Full High School Degree ("Abitur")
- 1989 – 1998      Secondary School "Gymnasium Fridericianum", Erlangen, Germany
- 1985 – 1989      Elementary School Spardorf, Germany

### **Other research activities (internship etc.)**

- 2.2001 – 3.2001 Undergraduate study as a research student at Old Dominion University, Norfolk, USA (Prof. K. H. Schoenbach)  
Topic: *Pulsed microhollow cathode discharges*
- 1998 – 2003 Undergraduate research assistant at SIEMENS, corporate technology, Power & Sensor Systems.  
Topics: *Magnetic field effects in high temperature superconductors*  
*Simulations of plasma discharges in high-power switches*
- 8.1995 – 2.1996 Exchange Student in Rockford, Illinois, USA

### **Academic activities**

- 7.2005 – 6.2006 Supervision of diploma student  
Topic: *Generation, characterization and application of ultrashort THz pulses*

# Versicherung

Hiermit versichere ich, dass ich die vorliegende Arbeit ohne unzulässige Hilfe Dritter und ohne Benutzung anderer als der angegebenen Hilfsmittel angefertigt habe; die aus fremden Quellen direkt oder indirekt übernommenen Gedanken sind als solche kenntlich gemacht. Die Arbeit wurde bisher weder im Inland noch im Ausland in gleicher oder ähnlicher Form einer anderen Prüfungsbehörde vorgelegt.

Ich erkenne die Promotionsordnung der Technischen Universität Dresden an.

Dresden, 18. April 2007

*Dominik Stehr*

Diese Arbeit wurde am Forschungszentrum Dresden-Rossendorf und unter wissenschaftlicher Betreuung von Prof. Dr. Manfred Helm angefertigt.

Manfred Helm ist Professor im Institut für Angewandte Physik der Fakultät Mathematik und Naturwissenschaften der Technischen Universität Dresden.